

Universidade do Minho
Escola de Ciências

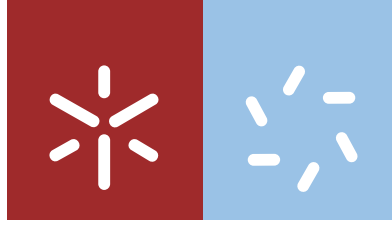
Paulo Ricardo Araújo Ferreira

Response of a water-Cherenkov detector to inclined muons at the Pierre Auger Observatory

Paulo Ricardo Araújo Ferreira **Response of a water-Cherenkov detector to inclined muons at the Pierre Auger Observatory**

UMinho | 2017

outubro de 2017



Universidade do Minho
Escola de Ciências

Paulo Ricardo Araújo Ferreira

**Response of a water-Cherenkov detector
to inclined muons at the Pierre Auger
Observatory**

Dissertação de Mestrado
Mestrado em Física Aplicada

Trabalho realizado sob orientação do
**Professor Doutor António Joaquim Onofre de Abreu
Ribeiro Gonçalves**
e do
Doutor Raul Cambraia Lopes Sarmiento Pereira

outubro de 2017

DECLARAÇÃO

Nome: Paulo Ricardo Araújo Ferreira

E-mail: ferreira@lip.pt

Telemóvel: +351917334831

Número de Identificação Civil: 14360118

Título da Tese: Response of a water-Cherenkov detector to inclined muons at the Pierre Auger Observatory

Orientadores: Professor Doutor António Joaquim Onofre de Abreu Ribeiro Gonçalves
Doutor Raul Cambraia Lopes Sarmiento Pereira

Ano de Conclusão: 2017

Designação do Mestrado: Mestrado em Física Aplicada

É AUTORIZADA A REPRODUÇÃO INTEGRAL DESTA TESE APENAS PARA EFEITOS DE INVESTIGAÇÃO, MEDIANTE DECLARAÇÃO ESCRITA DO INTERESSADO, QUE A TAL SE COMPROMETE.

Universidade do Minho, 6 de Outubro de 2017

Assinatura:

Acknowledgements

There is no other way to start this page if not by thanking to Raul Sarmento for all the support and guidance during the last four years. The journey of getting to know about Astroparticle Physics and Cosmic Rays, from my Bachelor project to my Master Thesis, would not have been possible without Raul's help.

I would like to thank to Professor Mário Pimenta, Professor Thomas Hebbeker and Professor Martin Erdmann for the opportunity to study at RWTH as an Erasmus student. My time in Aachen was a remarkable experience, both at the personal and professional levels.

Regarding my time in Aachen, I would like thank to all my colleagues for the shared moments but specially to Christine Peters for all the help and friendship. The quality of this dissertation would not have been the same without her help.

I must also thank to the Auger group of LIP, especially to Ruben Conceição, to Bernardo Tomé and to Pedro Assis.

To my colleagues from the University of Minho, who have accompanied me during the last years, a special thanks.

To my mother and to my father, a thanks with the highest gratitude for the permanent support and motivation given, so that I could follow my academic ambitions.

Finally, to all my friends and especially to Peter Nissen for all the support and friendship during the last years.



Abstract

Response of a water-Cherenkov detector to inclined muons at the Pierre Auger Observatory

Recent studies performed to highly inclined (with zenith angle larger than 60°), hybrid events collected by the Pierre Auger Collaboration show disagreements between data and simulations, with a deficit on the muon content between 30% and 80%, depending on the hadronic interaction model used. However, large uncertainties (11%) were still associated with the muon measurements at inclined angles.

Following the need to have an accurate study of the response of the water Cherenkov detectors (WCD) to inclined muons, a new experimental campaign with the RCP hodoscope at the Gianni Navarra test tank took place. The data acquisition was monitored and analysed in detail, allowing to study the behaviour of the RPCs in these conditions.

A sample of muons with a zenith angle distribution between $[62, 68]^\circ$ was collected and studied. Unaccounted background sources (possibly electrons and small showers) were found in the data, that made the analysis of the response of the WCD complex. Nonetheless, the charge peak variation with the reconstructed track length is compatible between data and simulation, in the premise that the former is rescaled to take into account the bias introduced by the background contaminations. Additionally, direct light effects to one PMT were also studied and some discrepancies were found. These differences were discussed in the context of the ageing effects and of the background found in the data.

Resumo

Resposta de um tanque de Cherenkov do Observatório Pierre Auger a muões inclinados

Estudos recentes feitos com eventos híbridos e bastante inclinados (com ângulo zenital maior que 60°), colectados pela Colaboração Pierre Auger mostram desacordos entre dados e simulações, com um déficit no número de muões entre 30% e 80%, dependendo do modelo de interação hadrónica utilizado. Contudo, incertezas elevadas (11%) permanecem associadas às medidas de muões inclinados.

Seguindo a necessidade de estudar com precisão a resposta do tanque de Cherenkov a muões inclinados, foi iniciada uma nova aquisição de dados com o hodoscópio de RPCs colocado sobre o tanque de teste Gianni Navarra. A aquisição foi monitorizada e analisada em detalhe, permitindo estudar o comportamento das RPCs nestas condições.

Uma amostra de muões, com uma distribuição em ângulo zenital entre $[62, 68]^\circ$, foi colectada e analisada. A presença de fontes de fundo não contabilizadas (possivelmente electrões e pequenos chuveiros) tornaram a análise da resposta do tanque de Cherenkov complexa. Não obstante, a variação no pico de carga com o comprimento reconstruído do trajecto dos muões dentro do tanque é compatível entre dados e simulação, na condição de que os dados sejam renormalizados de forma a considerar a influência do fundo. Adicionalmente, foram também feitos estudos da luz de Cherenkov directa para um dos PMTs e algumas discrepâncias foram encontradas. Estas diferenças foram discutidas no contexto de possíveis efeitos de envelhecimento do tanque e da contaminação pelos fundos nos dados.

Contents

Acknowledgements	iii
Abstract	v
Resumo	vii
Introduction	1
1 Historical Review	3
1.1 The beginning	4
1.2 From balloons flights to Pierre Auger Observatory	11
2 Cosmic Rays	15
2.1 Energy Spectrum	15
2.2 Composition	17
2.3 Acceleration Mechanisms	20
2.4 Sources	22
2.5 Anisotropy	23
2.6 Direct Measurements: Balloons and Satellites	25
2.7 Indirect Measurements	26
2.7.1 Atmosphere	27
2.7.2 Extensive Air Showers	29
2.7.3 Heitler’s Model	32
2.7.4 Shower Profiles	36
2.7.5 Hadronic Interactions	37
2.7.5.1 Quantum Chromodynamics	38
2.7.5.2 Hadronic Models	40
2.7.5.3 Extensive Air Showers Simulations	41
2.7.6 Radiation Emissions	42
2.7.6.1 Cherenkov Light	43
2.7.6.2 Fluorescence Light	44
2.7.7 Inclined Showers	46
2.7.8 Muon Content in Inclined Showers	47
2.7.8.1 Muon Number	48
2.7.8.2 Muon Production Depth	50
2.7.8.3 Testing Hadronic Interactions	53
2.7.8.4 Implications and Motivation	55
3 Pierre Auger Observatory	57
3.1 Hybrid Design	58
3.1.1 Fluorescence Detector	59
3.1.2 Surface Detector	61
3.1.2.1 Water Cherenkov Station	62
3.1.2.2 Photomultipliers	62

3.1.2.3	Direct Cherenkov Effects	63
3.2	Enhancements	65
3.3	AugerPrime	67
3.4	The MARTA Project	67
3.4.1	Resistive Plate Chambers	68
4	Experimental Setup	71
4.1	RPC Hodoscope	72
4.1.1	Triggers	73
4.2	Simulation of Atmospheric Particles	74
4.2.1	Offline Software Framework	74
4.2.2	Atmospheric Muons	74
4.2.3	Detector Simulation	76
4.3	Previous Analyses	76
4.3.1	First Results	77
4.3.2	VEM Calibration	78
4.4	New Acquisition	78
4.4.1	Geometric Description	80
4.4.2	Acquisition Time Estimative	84
5	Data Acquisition and Monitoring	89
5.1	Monitoring Data	89
5.2	RPC Monitoring and Analysis	93
5.3	Rates Analysis	100
5.4	Overview	102
6	Analysis of inclined atmospheric muons	105
6.1	Data	105
6.1.1	Data Alignment	107
6.1.2	Data Selection	108
6.1.3	Muon Trajectory Reconstruction	111
6.1.4	Features on the Data Signal	113
6.1.5	AoP and Charge relation	114
6.2	Simulation	117
6.2.1	Geometry verification	117
6.2.2	Simulation Procedure	118
6.2.3	Charge distribution for single muons	118
6.3	Discussion	123
6.3.1	Peak of events for low charge	123
6.3.1.1	Hodoscope triggers from single electrons	123
6.3.1.2	Muon Decay in the Tank	124
6.3.1.3	Random triggers and single electrons	125
6.3.2	High Charge Events	126
6.3.2.1	Zenith Angle Dependency	127
6.3.2.2	The influence of large deflections	129
6.3.2.3	Possible contamination by Small Showers	129
6.3.3	Response of the water-Cherenkov detector	131
6.3.3.1	WCD Response to Inclined Muons	131
6.3.3.2	WCD Response to Direct Cherenkov Effects	134
6.4	Final Notes	136

Conclusion	137
A Kolhörster and Bothe’s Coincidence Experiment: probability of two electrons to be produced by a gamma ray	139
B Calculation of the GZK energy limit	141
C Semi-Analytical Monte Carlos simulation for the hodoscope geometric efficiency determination	143
D Monte Carlo Calculation: Hodoscope geometric efficiency with small showers	145
Bibliography	147

List of Figures

1.1	On the left: Victor Hess preparing for a balloon flight. On the right: Measurements of the variation of the ionisation with altitude made by Hess in 1912.[2] . . .	5
1.2	Representation of a Wilson Chamber [8](left) and a picture of a positron took by Anderson (on the right) using this type of detector. The positron entered from below with an energy of 63 MeV and left the lead plate with an energy of circa 23 MeV [9].	7
1.3	On the left: Karlsruhe, Germany. Picture of KASCADE-Grande. On the right: Fly's Eye, Utah (USA). [21, 22]	13
2.1	Energy spectrum of cosmic rays measured by different collaborations (direct and indirect measurements are shown). The flux is scaled by $E^{2.65}$ to highlight the structures [23].	16
2.2	Variation of the mean energy of a proton propagating through the Universe due to the interaction with the CMB photons for different initial energies [35].	18
2.3	Fluxes of primary cosmic rays as function of their kinetic energy [37].	19
2.4	Average X_{\max} , obtained by different experiments, as function of the energy of the primary. Simulations for proton and iron are shown for comparison, according to the hadronic interaction model QGSJET 01 (solid line), QGSJET II-3 (dashed line), SIBYLL 2.1 (dotted line) and EPOS 1.6 (dash-dotted) [38].	20
2.5	The mean value and the standard deviation of the measured X_{\max} distributions (left and right, respectively) as function of the energy, by the Pierre Auger Observatory. For comparison also the results for air shower simulations induced by proton and iron are presented [39].	20
2.6	Hillas diagram. Different astrophysical objects are represented with respect to their size and magnetic field. The lines represent the correlation needed between L and B to accelerate protons or an iron nucleus to the energies shown in the plot (assuming that $\beta_c = 1$). Objects below the line cannot accelerate the particles to these energies. Adapted from [49]	23
2.7	The pictures represent the results from the Pierre Auger Observatory and Telescope Array (TA) collaborations. On the left the Auger results for energies higher than 5.6×10^{18} eV are shown in galactic coordinates, as well as the Swift AGNs brighter than 10^{44} erg s $^{-1}$ and closer than 130 Mpc, represented by the red circles [50]. On the right the results from TA for energies higher than 57 EeV are displayed in equatorial coordinates [53]. The color scale represents σ	24
2.8	Cosmic rays flux in equatorial coordinates smoothed with a 45° top-hat function. In dashed the galactic plane is represented and is marked the center of the galaxy with an asterisk [56].	25
2.9	Spectrum of electrons plus positrons (only electrons for PAMELA) multiplied by E^3 . The line in black represents the spectrum for proton multiplied by 0.01 [37].	26
2.10	Schematic representation of AMS-02. The different layers to detect cosmic rays particles are shown. [36].	27
2.11	Variation of the atmospheric vertical depth (or column density) with the altitude [18].	28

2.12	Schematic evolution of an extensive air shower in the atmosphere. The three main components (hadronic, muonic and electromagnetic) are represented. The purple dashed lines represent the transfer of energy for neutral pions (1/3 of the energy), while the blue solid lines represent the charged pions (2/3 of the energy) [62].	30
2.13	Schematic representation of an electromagnetic cascade according to the Heitler's model. The photons produce e^-e^+ pairs, while the last ones will emit photons through <i>bremsstrahlung</i> radiation. The cascade continues its development until the critical energy is reached.	32
2.14	Schematic representation of a hadronic cascade according to the adaptations of Heitler's model by Matthews. At each interaction, one third of the energy will result in π^0 and the rest 2/3 will be charged pions. The cascade continues its development until the critical energy is reached.	34
2.15	Representation of the 1σ contour of the correlation between the X_{\max} and the number of muons (N_μ). The simulated showers were induced for proton, Helium, Nitrogen and Iron with an energy of 5×10^{19} eV and fixed zenith angle of 38° [67].	36
2.16	Examples of a longitudinal and a lateral distributions (left and right, respectively) obtained by the Pierre Auger Observatory. On the left, a longitudinal profile of an event measured by the fluorescence detectors is represented, the red line is the Gaisser Hillas fit and the vertical axis represents the the energy loss rate $\frac{dE}{dX}$ in the atmosphere (see Section 2.7.6.2). On the right, a lateral profile of an event measured by the surface detector of the Pierre Auger Observatory is shown. The figure represents the detector signal as function of the distance to the axis of the shower. The circles are candidate stations and colours are related with the arrival time. The solid line is the fit of the lateral distribution made by the adapted version of the NKG equation for Auger [38].	38
2.17	Schematic representation of Cherenkov effect [36].	43
2.18	Fluorescence spectrum in air when excited by a current of $\sim 10 \mu\text{A}$, with 3 MeV electrons at a pressure of 800 hPa [87].	45
2.19	Variation of the atmospheric thickness at the sea level crossed by the shower as function of its zenith angle [18].	47
2.20	Variation of the particle densities with the atmospheric depth [18].	47
2.21	Left: Average muon content as a function of the shower energy, in double logarithmic scale. The data is represented in black circles and the black line is the respective fit. The grey band is the uncertainty associated with the fit. The brackets show the systematic errors of the measurements and their diagonal offset represents the correlated effect of systematic shifts in the energy scale. For comparison, the predictions for iron and proton are drawn (in both plots) to $E = 10^{19}$ eV and $\theta = 67^\circ$ using two different hadronic models. Right: $\langle R_\mu \rangle$ as a function of the $\langle X_{\max} \rangle$ for the data and predictions from different models [88].	50
2.22	Left: Comparison between Auger data and different model predictions of the mean logarithmic muon content $\langle \ln R_\mu \rangle$, for $E = 10^{19}$ eV. The predictions are made at $\theta = 67^\circ$ for proton, iron and a shower with a mix composition that matches the $\langle X_{\max} \rangle$ of the data. The uncertainties are represented by the black brackets. Right: Analogous comparison as in the left figure but for $d\langle \ln R_\mu \rangle/d \ln E$ between 4×10^{18} eV and 5×10^{19} eV [88].	51
2.23	Average value of the maximum depth of the muon production $\langle X_{\max}^\mu \rangle$ as a function of the shower energy E . The data is represented in black dots and the numbers above represent the total number of events for each bin. For comparison, the predictions for proton and iron are drawn based on two different hadronic models [89].	52

2.24	Results of $\langle \ln A \rangle$ from $\langle X_{\max}^{\mu} \rangle$ and $\langle X_{\max} \rangle$. The hadronic models QGSJETII-04 (left) and EPOS-LHC (right) are used as reference [89].	53
2.25	Left: Measured longitudinal profile and curves for iron and proton simulations with QGSJETII-04. Right: Observed and simulated lateral distribution function for the same events [90].	54
2.26	Best values fitted for R_E and R_{had} with the hadronic models EPOS-LHC and QGSJETII-04, for a pure proton (solid symbols) and mixed composition (open symbols). The grey area represents the systematic uncertainties and the black ellipse gives the area for the 1σ statistical uncertainties [90].	54
3.1	Google Earth view of the Pierre Auger Observatory. The scale and the north direction are displayed in the right down corner. The Auger Central Campus is located in Malargüe and the yellow points represent the default position of the water Cherenkov stations. The positions of the four fluorescence stations are also marked. The location of the cities of Malargüe and San Rafael can be seen in the left down corner and right upper corner, respectively. Developed by Stéphane Coutu in 2006.	58
3.2	Left: Water Cherenkov station in high flat lands of the province of Mendoza, near Malargüe. Right: Picture of a fluorescence station of the observatory. The pictures were taken by Guillermo Sierra in 2007 and have public access at the Auger website [106].	59
3.3	Left: schematic representation of the components of a telescope from the FD, with a person for scale. Right: picture from inside of one of the telescopes, with the aperture on the left side and the PMTs at the center and the mirrors on the right side [107].	60
3.4	Water Cherenkov station and the respective components necessary for its autonomous operation [108].	61
3.5	Photography and schematic drawing of the XP1805 PMT used on the water Cherenkov stations of the Pierre Auger Observatory. The measurements on the right are in mm. These PMTs are produced by Photonis. Pictures taken from HZC Photonis website [110].	63
3.6	Schematic representation of the water Cherenkov tank, in blue, and a PMT, in green. A muon (path represented by a red dashed line) hits the tank with a zenith angle of θ_{μ} . If the muon is energetic enough, it will emit radiation in the form of Cherenkov photons, with an angle θ_C	64
3.7	MC calculation. It represents the dependence of the probability of at least one of the three PMTs being hit with direct Cherenkov-light as function of the zenith angle. The non-zero fraction below the critic angle results from particles which cross the tank close to a PMT (without intersecting it). A 1000000 points were simulated on the top of the tank for each integer number of θ_{μ}	66
3.8	On the left: variation of the probability of having direct Cherenkov light emission for each PMT, P , with the zenith angle of the muons. On the right: variation of P for each PMT with the azimuth.	66
3.9	Picture and schematic representation of a water Cherenkov station with a scintillator detector at its top [115].	67

3.10	Particle detection by a RPC. The development being in the top left picture with the passage of a charged particle (dashed line) which provokes the ionization of the gas. The electrons will move in the opposite direction of the electric field E_0 (picture top right) while the positive ions will move in the direction of the electric field. The electrons will reach the anode (bottom left) before the ions reach the cathode (bottom right). When the electrons reach the anode, it will produce deformations in the electric field which can be measured and will confirm that a particle crossed the plates. After a few hundreds picoseconds the gas and the electric field will return to the initial stage [119].	68
4.1	Picture of the experimental setup of Gianni Navarra in Malargue, Argentina. The large cylinder is the water Cherenkov station and the box on the top is one of the RPCs (the other one is not visible in this picture, since is located under the tank). .	72
4.2	Lateral view of the experimental setup configuration. The blue rectangle represents the tank, while the grey ones represent the RPCs. The dashed red line represents the muon trajectory.	73
4.3	Representation of the main structures of the Offline Software Framework [127]. .	74
4.4	Energy distribution for atmospheric particles at Pierre Auger Observatory used to produced the simulation [125].	75
4.5	Zenith distribution of the flux of atmospheric particles used in the simulation. . .	75
4.6	Results of the total charge peak variation with the reconstructed track length for the data and for the respective simulation for muons with a zenith distribution within $[20^\circ, 55^\circ]$ [125].	77
4.7	Variation of the total charge peak (sum of all PMTs) with the distance to the center of the tank for nearly vertical muons [129].	78
4.8	Three-dimensional representation of the experimental setup configuration for the inclined muons analysis.	79
4.9	Theodolite referential.	80
4.10	GAP-2015-033 referential.	80
4.11	Offline referential.	81
4.12	Graphic representation of a RPC. Each RPC, $\xi \times \kappa \text{ m}^2$, contains 64 pads, distributed in a 8×8 matrix. Each pad (of dimensions $a \times b$) is separated from each other, vertically and horizontally, by d . L , R , B and T represent the borders. Those are sections of the RPC without pads (non active space). The dimensions of each segment can be seen in Table 4.2. The red dot in the center represents the center of the active area of the RPC. The number 1 represents the Corner 1, also used as reference.	82
4.13	Definition of the top (left) and bottom (right) RPCs rotation over the z-axis. The smaller side of the top RPC is parallel to the x-axis before being rotated by an angle of ϕ_t . While in the bottom RPC the longer side is parallel to the x-axis before being rotated by an angle of ϕ_b	83
4.14	Top view of the test tank configuration for the study of higher angles ($> 50^\circ$). The PMTs are represented inside the tank accordingly to the Offline referential. The red dots over the grey areas mark the center of the used pads. At the upper side, the bottom RPC is drawn, with 6 active pads. At the lower of the picture, the top RPC is shown, with 9 active pads. The blue dots represent the intersections with the top surface of the tank ($9 \times 6 = 54$).	85
4.15	Lateral view over the RPC hodoscope. The tank is represented by the blue rectangle and the RPC by the grey ones. The red points represent the exit points of the particles from the tank.	86

5.1	Example of a calibration histogram.	91
5.2	Calibration values of the PMTs 1,2 and 3 during a week of data acquisition tank.	91
5.3	Up: Mean values for the background rates of the top and bottom RPCs. Down: Number of active pads for both RPCs, from a total of 9 at the top and 6 at the bottom RPC, for the same period of acquisition.	92
5.4	Variation of the monitored parameters of the top RPC as a function of time. From the upper to the lower picture: current, temperature, applied voltage and pressure.	94
5.5	Variation of the monitored parameters of the bottom RPC as a function of time. From the upper to the lower picture: current, temperature, applied voltage and pressure.	95
5.6	Correlation between the reduced electric field and the efficiency in a RPC [133]. In the legend, TdF means "Terra del Fogo", which is in Argentina. The differences between the curves from Coimbra and from Terra del Fogo arrive from different atmospheric conditions (mostly the pressure).	95
5.7	Comparison of the time variation of the mean background rate, the reduced electric field and the efficiency on the top RPC.	96
5.8	Comparison of the time variation of the mean background rate, the reduced electric field and the efficiency on the bottom RPC.	97
5.9	Up: Relation between the temperature and the mean background rates for both RPCs. Down: Relation between the temperature and the current values for RPC top (blue) and bottom (red).	98
5.10	Up: Variation $(E/N)'$ as a function of time for RPC top (blue) and bottom (red). Down: Variation $(E/N)''$ as a function of time for both RPCs.	99
5.11	Estimated random coincidences rate (in green), estimated rate for muons (in red), measured trigger rate before cuts (in blue) and the rate after the data selection (in red) as a function of time.	101
5.12	Hodoscope efficiency variation as a function of time.	101
6.1	Example of a high-gain trace (from PMT 2).	106
6.2	Distribution of the time-bin position of the peak signal for sum of all PMTs traces.	109
6.3	Charge distributions for PMT 3 before the data selection (in black), the signal in the trigger cut (in blue), the restriction to signal hits (in green), no saturation and no baseline oscillations (in purple) and the final distribution, after the charge errors (in red).	110
6.4	Area over Peak distributions for PMT 3 before the data selection (in black), the signal in the trigger cut (in blue), the restriction to single hits (in green), no saturation and no baseline oscillations (in purple) and the final distribution, after the charge errors (in red).	111
6.5	Track Length (L) distribution.	112
6.6	Left: Zenith angle (θ) distribution. Right: Azimuth angle (ϕ) distribution.	112
6.7	Relation between the zenith angle and the track length of the particles trajectories of this setup. The color represents the number of events that have the respective L and θ relation.	112
6.8	Left: Coordinates of the points of intersection of the muons when entering the tank at its top (see Figure 4.14 for reference). Right: Coordinates of the points of intersection of the muons when exiting the tank, from the side (see Figure 4.15 for reference).	113
6.9	Charge distribution for PMT 1.	114
6.10	Charge distribution for PMTs 2 and 3.	114
6.11	Charge vs AoP for PMTs 2 (Left) and 3 (Right).	115
6.12	Charge vs AoP for PMTs 1.	116

6.13	Up: Track length distributions for the simulated Sample A in comparison with the data. Down: Zenith angle distributions for the simulated Sample A in comparison with the data.	120
6.14	Comparison between data (in black) and simulation (in color) of the charge distributions for PMTs 1 (up), 2 (middle) and 3 (down).	121
6.15	Comparison between data (in black) and simulation (in color) of the AoP distributions for PMTs 1 (up), 2 (middle) and 3 (down).	122
6.16	Average trace for events with less than 0.4 VEM in PMT1, in comparison with the average traces (of the same events) for PMTs 2 and 3. The baseline was removed in all traces for a better perception.	125
6.17	Charge distributions (normalized to PMT1's first peak of charge) for electrons crossing the top RPC (in color) in comparison with the data (in black) for PMTs 1 (up), 2 (middle) and 3 (down).	126
6.18	Number of events for each pads combination. The numbers in the axis give respect to the pads identification. The vertical axis marks the identification of the bottom pads and the horizontal axis marks it for the top pads. The color points the number of events of each combination.	127
6.19	Comparison of a trace of 6.9 VEM and a trace with 0.86 VEM (normalized to the peak of the former).	128
6.20	Variation of the frequency of high charge events with the zenith angle. The color shows the fraction that each angle and charge combination occurred in the data samples.	128
6.21	P_z variation between bottom and top RPCs in Sample A.	129
6.22	Correction between the charge distribution of PMTs 2 and 3.	130
6.23	Average trace signal of PMT 2 for different intervals of track length.	132
6.24	Example of a charge distribution of PMT 2 for a track length range between 0.8 and 0.9 m and the adjusted fit.	132
6.25	Variation of the peak of charge with the length reconstructed track inside the WCD for data (in black) and simulation (in color) for PMTs 2 (up) and 3 (down).	133
6.26	Comparison between data and simulation of the charge peak's variation with the reconstructed length of the path inside the WCD for PMT 2 (up) and 3 (down), with the data normalized to the first point of the simulation.	134
6.27	Comparison between Data and Simulation of the Charge vs AoP distributions of PMT 1.	135
6.28	Normalized charged distributions for PMT1 for events with AoP < 2 and Charge > 2 VEM.	135
A.1	Illustration of a γ ray producing two electrons [4].	139
C.1	Representation of the Gianni Navarra configuration, by a top view. In the right is represented the top RPC and in the left the bottom one. The blue circle represents the Water-Cherenkov Tank. We considered trajectories that cross a pad on the top RPC and we will determine the fraction that reaches a selected pad of the bottom RPC.	143
D.1	Single hits trigger efficiency of the hodoscope as a function of the number of particles. The total hodoscope geometric efficiency is represented in black.	146

List of Tables

2.1	Refractive index and Cherenkov angle in air, water and standard glass.	44
4.1	Rotation angles to change between the different referential. (Consult horizontally. For example, to go from the Offline referential to Theodolite, one must rotate 60° over the z axis).	81
4.2	Dimensions of the segments of the RPC, defined in Figure 4.12.	81
4.3	Measured values for center of the RPC (in Theodolite referential), the rotation angle for the each RPC (over its center) and the inclination angle relatively to the xy-plane. The rotation angles are defined in Figure 4.13.	82
4.4	Coordinates for the center of the RPCs, in the Offline referential.	83
4.5	Coordinates of each corner for both RPC, in the Offline referential. The Corner 1 is represented in Figure 4.12, the others were randomly chosen.	84
5.1	Values of the constants of Equation 5.4.	94
6.1	Statistics of the data collected by the different detectors and the alignment between them.	108
6.2	Number of events after each cut and respective percentage left in relation to the aligned data.	108
6.3	Restrictions of the input file used to produce Sample A.	119
6.4	Events statistics for Sample A.	119
6.5	Restrictions of the input file used to produce Sample B.	124
6.6	Events statistics for Sample B.	124

List of Abbreviations

AoP	Area over Peak
CR	Cosmic Rays
PMT	PhotoMultiplier Tube
RPC	Resistive Plate Chamber
VEM	Vertical Equivalent Muon
WCD	Water Cherenkov Detector

And it is only 4% ...

Introduction

Recent studies conducted by the Pierre Auger Collaboration about the muon content of extensive air showers have shown a muon deficit in the simulations larger than 30%. However, these analyses still have larger uncertainties associated, mainly with the energy scale and the WCD response to inclined muons. A detailed analysis of the response of the water Cherenkov stations of the Surface Detector to muons aims to reduce the systematic errors and to verify if the simulations used by the Pierre Auger Collaboration are representing well the performance of these detectors.

To answer these questions, a test tank unattached from the Surface Detector, was equipped with a hodoscope created by two resistive plate chambers. The hodoscope allows to select limited angular distributions for muons crossing the tank and to reconstruct their trajectories. The response of the test tank to muons with zenith angles shorter than 55° had already been successfully performed and the simulations are in agreement with the collected data.

In this work, a new hodoscope configuration was implemented in the hodoscope to enable the study of inclined muons ($\theta > 60^\circ$).

This thesis is divided in six Chapters. In the first Chapter, the most important discoveries and projects of Cosmic Rays are described, by chronological order.

Chapter 2 covers the state of the art of the field of ultra-high energy cosmic rays. The spectrum and its features are explained and the composition and the arrival directions of primary cosmic rays are discussed. The difference between direct and indirect measurements is explained, and a detailed description of different aspects of measurements of air showers is made. Chapter 2 ends with the discussion of the analyses that motivated this thesis.

The Pierre Auger Observatory is shortly described in Chapter 3. The main features of the surface and the fluorescence detectors are exposed, as well as the enhancements of the observatory. The detectors used for the hodoscope experiment, resistive plate chambers, are also explained in this Chapter.

In Chapter 4, the configuration of the hodoscope and test tank are described and the previous analyses are explained. The geometry for the new analysis is described and the acquisition time is estimated.

The monitoring of the acquisition, including the description of the output parameters given by the detectors, is made in Chapter 5. The stability of the data acquisition is studied to guarantee the quality of the data.

Chapter 6 addresses the response of the water Cherenkov tank by an analysis to single muons in comparison with simulations.

Chapter 1

Historical Review

“The time has now arrived, it seems to me, when we can say that the so-called cosmic rays definitely have their origin at such remote distances from the Earth that they may properly be called cosmic, and that the use of the rays has by now led to results of such importance that they may be considered a discovery of the first magnitude.” - Arthur Compton

Somewhere in the Universe, nuclei, with one or several nucleons, are, somehow, accelerated at very high energies and then released into space. Some of those nuclei will eventually reach Earth and interact with its atmosphere. That interaction will produce many secondary particles which will interact, as well, in the atmosphere, producing other particles, and so on, until they lose enough energy that they become more likely to decay than to interact and produce more particles¹. These particles are known by Cosmic Rays. To the first particle, the one that had an extraterrestrial origin, we call it primary cosmic ray.

The term *Cosmic Ray* has a wide definition and it can be subdivided into different groups, for example: primary cosmic rays, solar cosmic rays, secondary cosmic rays and terrestrial cosmic rays. Primary cosmic rays are energetic particles which reach the top of the Earth’s atmosphere. Solar cosmic rays are primary cosmic rays produced by the Sun (usually by solar winds). Secondary cosmic rays are the particles produced in the atmosphere that resulted from the interaction of the primary cosmic rays with the atoms of the atmosphere and terrestrial cosmic rays accounts for the secondary particles which reach the Earth’s surface. However, those groups can be resumed into primary and secondary cosmic rays, which will be the used terms from now on. Primary cosmic rays, then, account for all particles accelerated in the Universe that reach Earth, which includes electrons and positrons and different type of nuclei². Secondary cosmic rays are the particles produced in the atmosphere due to the interaction of primary cosmic rays. Any ambiguous mention to simply cosmic rays is also used for the purpose of including all particles, to mention the field itself, or situations where the distinction between primary and secondary is not relevant.

The primary cosmic rays have a very large spectrum of energy, covering around fourteen orders of magnitude, from 10^6 eV to hundreds of exa-electronvolts ($\sim 10^{20}$ eV). Their flux at Earth is related to their energy. A higher flux is observed for less energetic particles, which allows us to measure them directly. However, the flux of cosmic rays decreases with energy and at energies higher than 10^{14} eV becomes complicated to measure them directly. Above this limit, our study needs to be focused on the secondary particles that are produced in the atmosphere.

The discoveries and the studies around cosmic rays had a big impact in Physics, such that its discoverer, Victor Hess, was rewarded for it in 1936 with the Nobel Prize in Physics by the Royal Swedish Academy of Science. However, the

¹Not all particles decay before they reach the Earth’s surface.

²The particles are not available for all energies. Electrons, for example, are not found with high energies.

discovery of cosmic rays involved more scientists than just Hess. It is important to have a wide view of the history of a field, not only to honour those who made important contributions, but also to understand the steps that were made to reach the knowledge that we possess today. This Chapter is divided in two sections. Firstly, the first steps that gave birth to Cosmic Rays studies are narrated. Important achievements which led to the creation of Particle and Astroparticle Physics are described, such as the discovery of the antimatter by Anderson. The earlier studies about the energy spectrum are presented as well as the consequence of the CMB in this field. In the second part an approach accordingly to the energy spectrum was taken. Experiments from balloon flights, for direct measurements of low energetic primaries, to detector arrays of large dimensions, for the study of the extremely high energetic particles, are described.

1.1 The beginning

It started with the French physicist Charles-Augustin de Coulomb (1736-1806). In 1785, he found that his electroscope could spontaneously discharge by merely being exposed to air [1]. This was the first registered scientific experiment linked to cosmic rays, although they kept unknown until the 20th century.

More than one hundred years later, in 1896, Henri Becquerel (1852-1908) discovered the spontaneous radioactivity. A few years later, Marie Curie (1867-1934) and her husband, Pierre Curie (1859-1906), proved that Polonium and Radium suffer radioactive decays. When we approach radioactive materials to a charged electroscope, it will become immediately uncharged. It follows that the discharge happens because radioactive materials emit charged particles. This discovery reopened the discussion about the spontaneous discharge of electroscopes in air discovered by Coulomb. The scientists of the time were puzzled about the natural radioactivity. There must be a natural flux of charged particles that provokes the spontaneous discharge of the electroscopes, arising the question: where does the flux come from?

Around 1900, Julius Elster and Hans Geitel in Germany and independently Charles Wilson in Scotland improved the insulation of a gold leaf electroscope, in order to increase its sensibility and to allow measurements of the rate of the observed spontaneous discharge. They concluded that the particles responsible for this phenomenon come, indeed, from outside the electroscope and that some of those particles were highly penetrating (they could ionize the air inside the electroscope shielded by a few centimetres of a metal)[2].

The question was still open. Where does the radiation come from? At that time there were three possibilities discussed: either they originate from within Earth or from some phenomenon from the atmosphere or they could have an extraterrestrial source. In 1909, the Jesuit priest Theodor Wulf (1868-1946) built an electroscope even more sensitive and easier to transport than the gold leaf electroscope. Using this detector, he took measurements at different locations in Germany, Belgium and the Netherlands and he concluded that the penetrating radiation was coming from the Earth. To prove his theory, he wanted to measure the variation of the radioactivity with height. If the flux was originating from Earth, it should decrease strongly with height. Wulf travelled to Paris to measure the ionization rate at the top and at the bottom of the Eiffel Tower. If the radiation was coming from within Earth's crust, the radiation at the top of the tower

(~ 300 m) should be just a few percent of the ground level, due to the absorption in the air. He verified a decrease in the rate at the top but not enough to prove his theory. Thus, the origin of the radiation kept unknown for more a few years [2].

Then, balloon flights were used by researchers to measure the ionizing radiation far from Earth's surface. In 1910, Albert Gokel (1868-1927) measured the ionization rate at 3000 m and he found that it did not decrease with height, which means that it could not have an exclusive source at Earth's crust. Domenico Pacini (1878-1934) questioned the idea that the radioactivity had an origin at Earth. To explore his doubts he took measurements of the radiation on the ground at different elevations and underwater. He found, through his underwater measurements in the Genoa gulf, that the ionization rate was about 20% lower three meters underwater than at the ground level. He concluded that the radioactivity could not have a source within Earth's crusts. However, Pacini's studies could not prove if the origin was in the atmosphere or if it was extraterrestrial.

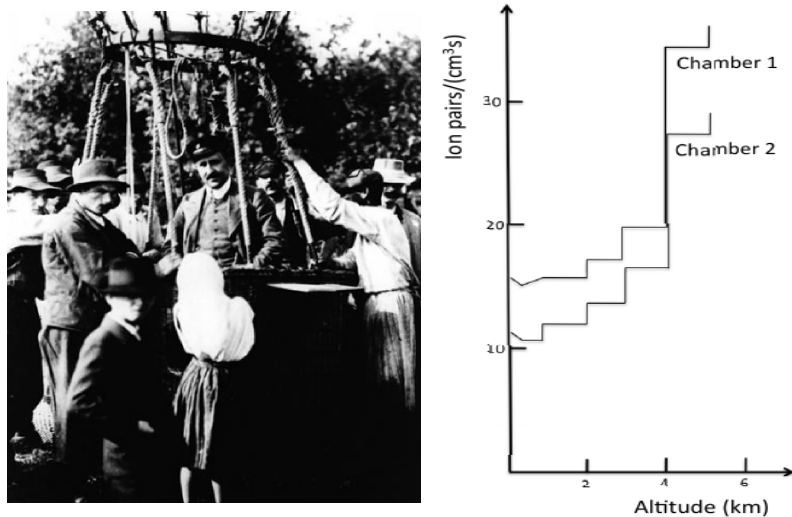


FIGURE 1.1: On the left: Victor Hess preparing for a balloon flight. On the right: Measurements of the variation of the ionisation with altitude made by Hess in 1912.[2]

During the years of 1911 and 1912, the Austrian Victor Hess (1883-1964) performed measurements for different heights, using balloons. On figure 1.1 Hess is shown preparing for one of his balloon flights (left) and measurements made by him (right). From his results, it follows that the radiation increases with altitude. Therefore, the experiment of Hess ended the doubts about the source of the natural radioactivity. It comes from outer space.

However, it took some time until the scientific community came to an agreement about the origin of cosmic rays. Hess received his Nobel Prize 24 years after his experiments. Werner Kolhörster (1887-1946), a German physicist, repeated the experiment of Hess, in 1913, because he was not convinced. He measured the radiation up to 9300 m and his results confirmed Hess's experiment. The radiation increases with height. [3]

Robert Millikan (1868-1953) was also not convinced by Hess's results. He and G. Harvey Cameron took measurements, in 1926, of the radiation rate for different altitudes and also underwater but they had to conclude that the radiation had

an extraterrestrial source. The name itself, *Cosmic Rays*, was coined by Millikan.

Another puzzling question was about the properties of this cosmic radiation. In the beginning of the 1920s, it was believed that cosmic rays were gamma radiation, due to their capacity to penetrate matter. In 1927 and 1928, Jacob Clay (1882-1955) conducted different measurements of the ionization between the Netherlands and Java (Indonesia). He found that the radiation increases with the latitude. This means that the intensity of cosmic rays is lower near the Equator. Kolhörster and Walther Bothe (1891-1957) made an experiment in 1929 using a Geiger-Müller counter.

The Geiger-Müller counter was developed, in 1928, by Hans Geiger and Walter Müller (a PhD student of Geiger). The detector consists of a tube filled with gas which is ionized when charged particles cross it. In their experiment, Kolhörster and Bothe used two Geiger-Müller tubes, placing one above the other, to count coincidences. When a particle passes both detectors we have a coincidence, which gives us information about its path. With their experiment, Bothe and Kolhörster pored about the nature of the radiation measured at Earth's surface and they concluded that the radiation detected at surface was mostly corpuscular. They pointed out two possibilities: gamma rays or charged particles. In order to have a coincidence, a gamma ray would have to emit two electrons, by Compton effect, one for each counter³. Since the probability of this situation is too small to justify the number of coincidences, they concluded that "each coincidence signifies the passage of one and the same corpuscular ray through both counters". [4]

Bothe and Kolhörster's experiment told us that the secondary radiation has charge. The nature of the primary radiation came a few years later after. In 1932, Arthur H. Compton (1892-1962) performed measurements of the cosmic radiation similar to Clay's experiment and he also obtained different values for different latitudes. Based on this it follows that cosmic rays interact with Earth's geomagnetic field, which implies that they must be charged particles. In the following year, three independent experiments were made, by Compton [5], Thomas H. Jonhson and by the Italian Bruno Rossi (1905-1993) [6], and all discovered that we were receiving more cosmic rays from West than from East. These results showed that cosmic rays were mostly positive charged particles⁴. By now, the idea that cosmic rays were gamma rays was completely rejected. However, we need to wait until 1940s when Marcel Schein, William P. Jesse and Ernest O. Wollan, in the Ryerson Physical Laboratory at the University of Chicago, came to the conclusion that the primary positively charged particles were mostly protons [7].

The progress of this field is deeply attached to detectors and their evolution through time. The development of electroscopes and electrometers⁵, especially their insulation, was fundamental for the discovery of cosmic rays. Later, new detectors were built providing additional and more precise information, which led to new discoveries.

In 1911, the already mentioned Scottish physicist, Charles Wilson, presented his new detector: the cloud chamber (also known as Wilson's chamber, see Figure 1.2 left). This device was very important for the development of experimental particle physics, between 1920s and the end of the Second World War. The cloud

³In Appendix A it is shown how one can calculate this probability.

⁴The East-West asymmetry, at the Equator, of the cosmic rays occurs due to the interaction with the Earth's magnetic field.

⁵The difference between electrometers and electroscopes is very narrow. Usually, electrometers are defined as a device which allows to perform a quantitative measurement of electrostatic charge, while electroscopes allow qualitative measurements.

chamber consists of a supersaturated vapour⁶ inside a vessel. When charged particles go through it, they leave a trail due to the ionization that they induce in the vapour. Wilson was awarded with the Nobel Prize of Physics for his invention.

This detector is known for some remarkable discoveries in the history of particle physics. In the early 1920s, this chamber was used to study the track of particles by Wilson himself and by Blackett. In 1932, Carl Anderson (1905-1991) discovered, at the California Institute of Technology (Caltech), the positive electron - positron. If a magnetic field is applied inside the Wilson's Chamber, we will photograph curved tracks for the charged particles. By analysing the curvature, we can calculate the mass of the particle. This was what Anderson and his professor, R. Millikan, used for their experiments with cosmic radiation. What Anderson found in his photographs (as represented in 1.2 right) was a track with similar curvature to the electron one, but curved in the other direction, which means that the charge had to be positive. Carl Anderson just discovered the anti-matter. This experiment earned him the Nobel Prize of Physics, shared with Victor Hess (1936). Previously, Dimitry Skobeltzyn, a Soviet physicist, also used a cloud chamber to observe tracks left by electrons emitted by radioactive decays, in 1929. Some of the tracks he observed were identified as secondary electrons produced in the atmosphere. These were the first observations of cosmic rays tracks.

In 1937, Seth Neddermeyer (1907-1988) and Carl Anderson published their

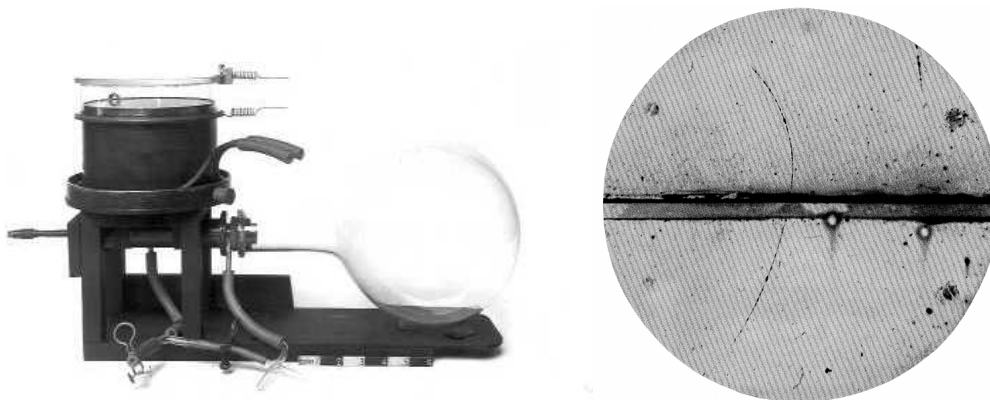


FIGURE 1.2: Representation of a Wilson Chamber [8](left) and a picture of a positron took by Anderson (on the right) using this type of detector. The positron entered from below with an energy of 63 MeV and left the lead plate with an energy of circa 23 MeV [9].

work about the discovery of the muon, using the same method [10]. This time, the curvature told them that they observed a particle heavier than the electron but lighter than the proton. At the beginning it was called the mu meson because it was believed to be the particle predicted by Yukawa in 1935, due to its mass. As we will see later, muons are very important for the study of Cosmic Rays in modern times.

The theoretical particle predicted by the Japanese Yukawa (1901-1981) was discovered 10 years later, in 1947, by César Lattes, Giuseppe Occhinalini and C.F. Powell [11]. These three physicists, while working together at the University of

⁶When a charged particle crosses the chamber, it condenses the supersaturated vapour on its path, allowing the user to observe it.

Bristol (England), discovered the charged pi mesons (also known as pions). A meson is a hadronic particle composed by a quark and an anti-quark, bounded by the strong interaction. The pions were the first mesons to be discovered but by the end of the same year, the K meson (kaon) was discovered by Clifford Butler and George Rochester, also through cosmic rays studies. This last meson also marks the discovery of strangeness. In 1950, Hopper and Biswas [12] discovered the neutral lambda baryon. After World War II, scientists started to use particle accelerators, which marked the separation of Particle Physics and Astroparticle Physics.

However, even at our time, cosmic rays are the only way to study extremely high energies. Nowadays, many important studies of this field are focused on particles at the limit of the energy spectrum. But, as previously mentioned, the flux at such energies is low, which makes direct observation impractical. To perform direct observation of cosmic rays at such energies detectors of dimensions nearly impossible to build by humankind or tremendously long measurement times would be required to collect enough statistics, which would block developments on this subject. So, how are researchers able to study cosmic rays at these energies? In the 30s of the last century, a very important discovery was made – Extensive Air Showers.

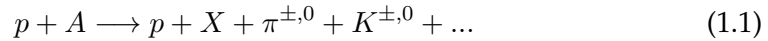
The progress of detectors and the capacity to combine them were fundamental for this discovery. A crucial moment was the development of the coincidence technique by Bothe, in 1929, as mentioned above, for which he was rewarded with the Nobel Prize, in 1954. His circuit had resolving time of 1.4 ms. Resolving time, or dead time, is the time that a system needs to be able to register another measurement.

In 1930, the Italian Bruno Rossi designed a coincidence circuit which could connect more than just two Geiger-Müller counters and had a dead time around 0.4 ms. Later, in 1932, Blackett and Occhialini used two Geiger-Müller counters to trigger a cloud chamber, allowing them to have a better efficiency on the observation of particles. These developments were fundamental for the discovery of extensive air showers. In 1933, Rossi realized that he obtained more coincidences in his detector if he placed some centimetres of lead above it. He concluded that secondary particles were produced when cosmic rays crossed the material. In the year after, the Italian physicist made the first register of extensive air showers. He made some experiments in Eritrea with his counters and he realized that he was obtaining more coincidences than expected. He observed the same phenomenon even when he raised the distance between the detectors. He concluded that he should be in the presence of a shower of secondary particles [13]. Nonetheless, this discovery did not receive much attention from the scientific community around the world. At this time, scientists published their work mostly in their native language, which compromised the spread of new results. Not only that but Rossi had also to stop his works in Italy, because he needed to leave the country, in 1938, due to the raise of anti-Semitism.

In 1938, two German groups – Schmeiser and Bothe and the group of Kolhörster – also took measurements of the rate of coincidences as function of the distance of the counters. However, the discovery of extensive air showers is usually assigned to Pierre Auger (1899 - 1993) and his team. Roland Maze, a colleague of Auger, was able to reduce the resolving time of a coincidence circuit to 5 μ s. At the Swiss Alps, in 1938, Auger and his team managed to separate the detectors as far as 300 meters and still obtained coincidences. This was justified by the

presence of secondary particles produced by a primary particle with an incredibly high energy.

By the early 1950s, we knew that cosmic rays are mostly protons that interact in the atmosphere and produce a shower of secondary particles, like electrons, positrons, muons, pions, kaons and others. We can express the interaction of a primary proton with an atom from the atmosphere with the following equation:



Where X represents the fragmented nucleus. The proton on the right side of the equation is called leading particle and usually carries about 50% of the total energy (which corresponds to the elasticity). Further interactions will happen in the atmosphere until it reaches a critical energy. The first explanations for the processes that occur in an atmospheric shower of particles appear in the 1930s. In 1934, Hans Bethe (1906 - 2005) and Walter Heitler (1904-1981) wrote the basic concepts of the multiplications occurring in extensive air showers [14]. Later, these processes were formulated as pair-production and bremsstrahlung by Homi Bhabha and Heitler [15]. Carlson and J. R. Oppenheimer, from the University of California, also contributed to these first theoretical approaches to extensive air showers, by acknowledging the energy losses of electrons by ionisation. All of this led to the first theoretical model for electromagnetic cascades, known as Heitler's model. Although it fails to describe with high accuracy all the processes in an electromagnetic cascade, it still gives us the correct notions that the number of produced particles is proportional to the energy of the primary (the energy of the cosmic ray, E_0) and that the depth at which the shower reaches its maximum development, X_{\max} , in the atmosphere is logarithmically proportional to that same energy E_0 . Nowadays, physicists use Monte Carlo simulations to obtain more detailed and accurate descriptions of these interactions and particle production in the atmosphere.

Parameters measured from air showers, such as the X_{\max} and the number of muons (N_{μ}), are important to know the composition of the primaries. Data collected from air showers is compared with simulations, in order to study the energy and the composition of cosmic rays. This requires a detailed knowledge of the processes and interactions that occur in the atmosphere.

After World War II, new experiments with arrays of Geiger-Müller counters emerged in the United Kingdom and in the USSR [15]. In the 1950s, T. Cranshaw and W. Galbraith from the UK Atomic Energy Research Establish, assembled an array of 91 Geiger counters in Culham, England. The detectors covered an area of circa 0.5 km^2 and were distributed on a triangular grid with a separation of 99 m from each other, at an altitude close to the sea-level. Although it had technological limitations, the studies of the anisotropy of cosmic rays performed with this array were enough to discard the theory that the Sun is a major source of cosmic rays. This theory emerged in the end of the 1940s and would lead to an isotropic distribution due to the Earth's magnetic field.

In the USSR experiments were performed at high altitudes and at the sea-level. The first studies at high altitude were performed in the Pamir Mountains and in the late 1950s they were moved to Tien Shan. The studies at the sea-level were developed by the Moscow State University, using several groups of hodoscoped Geiger counters, covering an area of 0.8 km^2 . In 1958, the Moscow group made an important discovery – a structure in the energy spectrum of cosmic rays. Khristiansen and Kulikov found that the flux of cosmic rays steeps

around 10^{15} eV. They argued that the reason behind it could be an extragalactic origin for protons (and other light cosmic rays) with energies above 10^{16} eV. Nowadays this structure is known as “knee” and the general consensus is that it marks the transition between galactic and extra-galactic sources for light nuclei (heavier nuclei, such as iron, can still be accelerated in our galaxy above this energy).

The era of Geiger-Müller counters came to an end in the late 1950s and new experiments emerged, using photomultipliers as detectors. The first photomultiplier tubes (PMT) were developed in the 1930s and they put in practice two physical concepts: photoelectric effect and secondary emission of electrons. Those detectors were used in the last years of the Culham array, which introduced the studies of extensive air showers through Cherenkov radiation.

Cherenkov radiation was discovered in 1934, by the Russians Pavel Cherenkov (1904-1990) and Sergey Vavilov (1891-1951). When charged particles travel faster than light in a medium, they emit photons in the visible and ultra-violet wavelength regimes. Cherenkov was, for his discovery, awarded in 1958 with the Nobel Prize.

In the Pic du Midi, Pyrenees, France, in 1953, Bill Galbraith and John Jelley discovered Cherenkov radiation produced in the atmosphere, confirming predictions made by Patrick Blackett. Initially they started the investigations at Culham. During nights of clear and moonless sky, they pointed a mirror which focused the light onto a PMT, searching for air Cherenkov light, using the Geiger counters as triggers for the PMT. Since their study relied on weather conditions, they moved it to the Pyrenees and they were able to demonstrate the existence of air Cherenkov radiation.

Another development made in Culham with PMTs was the water Cherenkov tank. In order to study air showers, we can use water as a medium to make charged particles to emit Cherenkov light, which is more easily detected than air Cherenkov. A water Cherenkov tank is a volume filled with water and equipped with PMTs inside to detect the radiation. Later, similar tanks would be used for the experiments at Haverah Park and at the Pierre Auger Observatory. The Culham array was closed in 1958.

In the decades that followed, several small arrays of detectors were developed to study cosmic rays between 10^{14} and 10^{17} eV, located in different countries, such as Australia, Germany, India, Italy, Japan, Poland, UK, the USA and the URSS. However, in the whole history of Astroparticles Physics, there are not many arrays of detectors to study extremely high energetic cosmic rays. Due to their low flux and the large extension of their air showers, cosmic rays with energies above 10^{17} eV require arrays with a large area. With areas over 1 km^2 , there has been seven surface arrays. Of those, four are already closed: Volcano Ranch, Haverah Park, SUGAR and AGASA; and three are still operating: Telescope Array (TA), Pierre Auger Observatory and the Yakutsk array.

The first large detector was installed in Volcano Ranch, New Mexico, USA (at an altitude of 1770 m, with an atmospheric depth of 834 gcm^{-2}), under the leadership of John Linsley. During most of its operating time, it had 19 units with scintillation counters spaced by 884 m, resulting in a total area of 8.1 km^2 . Volcano Ranch emerged from the works of the MIT group, led by Bruno Rossi, which used a smaller array of detectors (Agassiz). This experiment made several contributions for the understanding of air showers at high energies and it was the first to detect an ultra-high energy cosmic rays. In 1962 an event was detected with 10^{20} eV. Volcano Ranch was operated from 1959 to 1978.[15]

In the 1960s, two new large arrays of detectors appeared: Haverah Park and

SUGAR. Under the coordination of the University of Durham, Leeds and London, the Haverah Park experiment was constructed near Harrogate (North Yorkshire, England) and covered an area of circa 12 km^2 . The water Cherenkov tanks developed at the ending stage of the Culham array by N. Porter were used as principal detectors. Haverah Park collected data from 1967 to 1987 and was designed to study cosmic rays above 10^{15} eV . The first studies of inclined showers were performed at Haverah Park, such as studies about the time structure of the air shower front. A remarkable achievement was the capability to keep the water inside the tanks free of bacteria. In fact, the modern water Cherenkov tank is very similar to the one designed by Porter.

In 1968, the Sydney University Giant Air Shower Recorder – SUGAR – was built near Narrabri, Australia, covering an area of approximately 70 km^2 with more than 40 stations. An innovation introduced by this experiment was the independence of each station in relation to the others. Each station recorded the data and the time in an autonomous way, while in previous arrays the detectors were connected via cables, making experiments (at such dimensions) more practical and less expensive. Until its closure in 1979, the SUGAR experiment made several measurements of the directions of cosmic rays above 10^{18} eV but no anisotropy was found.

The accidental discovery of the Cosmic Microwave Background (CMB), in 1964, by Arno Penzias and Robert Wilson had a significant impact on this field. In 1966, Kenneth Greisen and, independently, the Russians Vadim Kuzmin and Georgiy Zatsepin predicted that the energy spectrum of cosmic rays should have a strong steepening above $4 \times 10^{19} \text{ eV}$ due to an effect that became known as GZK effect. They argued that the interaction of high energy protons with the photons from the CMB would result in photopion production, reducing the energy of the protons. For heavy nuclei, they argued that, at high energies, they would photodisintegrate.

On the first large detector arrays this proposal of the ending of the cosmic ray spectrum had no influence, since they were planned before, but this served as motivation for more recent detectors, such as Fly's Eye, AGASA and the Pierre Auger Observatory. Although there are not enough proves to support the GZK effect, the suppression at such energies was confirmed in 2007, by both HiRes and the Pierre Auger Observatory.

1.2 From balloons flights to Pierre Auger Observatory

With such a large energy spectrum and different structures on its flux (such as the knee or the suppression), as well as the need to cover all sky (since cosmic rays arrive from all directions), one can easily understand the need of different detectors and experiments to cover everything. For the lower energies, experiments with satellites and balloons were performed, where direct measurements are possible. Above 10^{14} eV , different arrays of detectors, with different configurations, were built for the study of air showers.

Cosmic rays with energies below 10^{14} eV have been, until today, well studied by several experiments with balloon flights and measurements with satellites. Some famous balloon flights were already mentioned, like Hess or Kolhörster in

the 1910s. In decades that followed, other researchers performed similar experiments with balloons, like Robert Millikan or Martin Pomerantz. In the 1950s, pioneer experiments with rockets and spacecraft were conducted. However, it was since the last 30 years that most research of direct cosmic rays has been done. In 1992 the satellite SAMPLEX and the balloon-borne IMAX were launched, which studied the flux and the composition of galactic cosmic rays. In the same decade, other important balloon-borne experiments were launched, such as JACEE (an American and Japanese collaboration), BESS, MASS, RunJob, TRACER and others. In 1997 the satellite ACE (Advancer Composition Explorer) was launched in order to collect data about the composition of matter from different astrophysical origins. In 2011, the Alpha Magnetic Spectrometer, AMS, was incorporated on the International Space Station. Other balloon flights (TIGER, CREAM, ATIC, etc) and satellites (PAMELA, LUCID, etc) were launched, contributing with studies of the flux and of the chemical composition of cosmic rays up to energies of circa 10^{14} eV.[16, 17]

Above this limit, we enter in the field of indirect measurements of cosmic rays. As we have seen, the study of air showers requires large arrays of detectors. The dimensions and spacing between the detectors are so chosen that the best performance for the desired range of energies is achieved. The range of energies between 10^{14} and 10^{17} eV have been studied since the 1950s by several experiments - from the early experiments in England and the URSS to very precise measurements made in Germany by KASCADE. Some of those experiments are: Agassiz (operated during the 1950s, under the coordination of the Harvard University), Cornell (founded by Kenneth Greisen, in the 1950s, at the Cornell University), INS (Institute for Nuclear Studies, Japan), Kiel (Germany), CASA-MIA (in Utah, USA, from 1992 to 2001), GRAPES (in Ooty, India, still operating as GRAPES 3), HEGRA (in La Palma, Spain, from 1987-2002), EAS-TOP (in Italy, with 35 scintillators covering an area of circa 0.1 km^2 , operating between 1989 and 2000) and others.[15, 18]

Most of the small and medium size arrays of detectors that were constructed after the middle of the 1980s were largely motivated by an unexpected and uncertain measurement made in Kiel. In 1983, the collaboration of Kiel reported an observation who suggested that the X-ray binary system Cygnus X-3 (at 11 kpc from Earth) was a source of cosmic rays. One of those experiments was KASCADE.

KASCADE (KArlsruhe Shower Core and Array DEtector) started in 1996, in Karlsruhe, Germany. In Figure 1.3 left a picture of the array is shown. It consisted of 252 detectors spaced by 13 meters from each other, studying air showers of energies from 10^{14} eV up to 10^{17} eV. Later, the experiments of KASCADE and EAS-TOP were merged into KASCADE-Grande, covering a total area of 0.5 km^2 . The collaboration at Karlsruhe reported the existence of a knee-like structure in the energy spectrum of the heavy component of cosmic rays around 80 PeV, known as the second knee [19].

Another structure on the spectrum is the ankle, located around $2 - 8 \times 10^{18}$ eV, and the origin of cosmic rays above this limit is, most likely, extragalactic [20]. We can now summarize all the known structures on the energy spectrum: the (first) knee, at $\sim 10^{15}$ eV, the second knee, at $\sim 10^{17}$ eV, the ankle, $\sim 10^{18}$ eV, and the suppression above $\sim 10^{19}$ eV.

A new technique for the study of air showers was developed in the 1960s. So far we talked about studying air showers through the detection of charged particles (either by using Cherenkov radiation and PMTs or through gas detectors



FIGURE 1.3: On the left: Karlsruhe, Germany. Picture of KASCADE-Grande. On the right: Fly's Eye, Utah (USA). [21, 22]

who become ionized when crossed by charged particles). Another alternative is to study the fluorescence radiation emitted by the nitrogen atoms in the atmosphere, when these are excited by charged particles. An important experiment (and also one of the pioneers) which used this effect to study air showers was Fly's Eye (see Figure 1.3 (right)). In the early 1970s a prototype detector, Fly's Eye I, was assembled in Utah (USA) which consisted of 67 camera units with PMTs. Fly's Eye I was able to collect data of air showers beyond 10^{18} eV. Later, in 1986, a similar structure, Fly's Eye II, was built circa 3.5 km away from Fly's Eye I. The duty cycle of this type of detection is extremely limited by external conditions. Only in nights with clear sky and without moon light it is possible to use it. The Fly's Eye experiment gave origin to HiRes (High Resolution Fly's Eye) with the construction of HiRes I, in 1997, and HiRes II in 1999, both in Utah. Several improvements were applied from Fly's Eye to HiRes, such as in the data acquisition, which allowed more precise measurements of the longitudinal shower profile. HiRes collected data until 2006 and its biggest achievement was the confirmation of the suppression of the energy spectrum at the GZK limit.[15]

The highest energies are covered by the large arrays of detectors, which were already mentioned and some already described (Volcano Ranch, Haverah Park and SUGAR). In the end of the 1960s the Yakutsk array was developed, which consisted of a surface array of detectors, including 35 PMTs for the detection of air-Cherenkov. During its prime, the Yakutsk covered more than 17 km^2 but nowadays it is confined to an area of circa 10 km^2 . The Yakutsk array is still operating and is designed for the study of cosmic rays above 10 PeV.

Before the construction of Auger and TA, the largest surface array of detectors was AGASA (Akeno Giant Air Shower Array), which was constructed in Akeno, Japan. The AGASA experiment had been operating since 1990 to 2004 and consisted of 111 scintillators, spaced by 1 km from each other, covering an area of circa 100 km^2 . The suppression at the GZK limit was questioned due to 11 events, recorded by AGASA, with an energy higher than 10^{20} eV. Later it was shown that there were deficiencies in the energy reconstruction of those events.

Even before the construction of AGASA, scientists already knew that they would need a very large array of detectors – over 1000 km^2 - to study the limits of energy spectrum of cosmic rays. Following this idea, in 1992, Jim W. Cronin and Alan Watson proposed the creation of the largest array ever built, initializing the concept of the Pierre Auger Observatory. The construction started in 2000 at Mendoza, Argentina, and was officially finished in 2008. It is based on the hybrid detection technique, combining 27 fluorescence telescopes with more than 1600

water-Cherenkov tanks that cover around 3000 km². A similar hybrid observatory was created in the northern hemisphere, in Utah (USA), the Telescope Array. TA emerged from a collaboration between the teams of AGASA and HiRes. It consists of 38 fluorescence telescopes and 507 scintillators surface detectors with a total area of about 730 km².

Another type of experiments exploring the field of Astroparticles are experiments for the detection of neutrinos with an extra-terrestrial source. The mechanism of acceleration of cosmic rays and sources which can accelerate them at such high energies are still unknown. One possible mechanism was proposed by the Italian Enrico Fermi, in 1949, called Fermi acceleration or diffusive shock acceleration. Shortly, he proposed that charged particles are accelerated through several collisions with moving interstellar clouds. However, the level of uncertainty on this part of Cosmic Rays Physics is still too high and that is why experiments with astrophysical neutrinos and high energy gamma rays are very important. Since neutrinos are chargeless and nearly massless, it makes them the best particles to study the arrival direction (due to their absence of charge, they are not deflected by magnetic fields). By studying astrophysical neutrinos, one can perform anisotropy studies and research about sources which can accelerate particles at very high energies. Baikal Deep Underwater Neutrino Telescope (in Lake Baikal, Russia), Antares (in the Mediterranean Sea, near France) and IceCube (buried in the ice, at the South Pole) are some examples of experiments which are focused on the detection of neutrinos. Until now, no significant discoveries about anisotropy were made.

We have now covered the most significant marks of Cosmic Rays history. From the early flights of Hess to the construction of Auger and TA, we now know, among other things, that cosmic rays are nuclei (mostly protons) who arrive to Earth with high energies. However, there are several questions which remain unanswered, especially in terms of the energy spectrum. Although it is clear that there is a suppression on the flux above 10¹⁹ eV, it is yet not proved why it happens (either being the GZK effect or the absence of sources for higher energies). It also remains to be answered how primary cosmic rays are accelerated at such high energies and which sources are able to do it. The mass composition at higher energies is also an open question and it led to the construction of AugerPrime, the on-going upgrade of the Pierre Auger Observatory, with the goal to collect new information about air showers.

Another open question, which will be further discussed in detail in this thesis, is the excess of the number of muons when compared to the current simulations.

Next in this thesis, we shall focus on the physics of cosmic rays, covering with more detail the energy spectrum of cosmic rays, extensive air showers and other important points. We will also describe in detail the Pierre Auger Observatory, its detectors and main results obtained from the studies of extensive air showers in Argentina.

Chapter 2

Cosmic Rays

“On what can we now place our hopes of solving the many riddles which still exist as to the origin and composition of cosmic rays?” - Victor Hess

Since the discovery of the spontaneous discharge of electroscopes by Coulomb in the 18th century, the knowledge about Cosmic Rays has grown massively, especially in the last one hundred years.

In this Chapter the energy spectrum and the change in the flux after each known structure (knee, second knee, ankle and suppression), as well as the chemical composition of primary cosmic rays will be explored. The acceleration of cosmic rays and their propagation until Earth will also be covered and the techniques and processes of direct and indirect measurements will be explained. Since this thesis is embedded in the context of the Pierre Auger Observatory, the main focus is on indirect measurements of cosmic rays through extensive air showers. The different processes that occur in the atmosphere will be reviewed and the excess of muons measured in inclined showers will be explored and discussed why it is important to study such particles.

2.1 Energy Spectrum

Primary cosmic rays cover a large range of energies, with their interaction in the atmosphere reaching center of mass energies nearly 100 times higher than those which are currently possible at the LHC (Large Hadron Collider). As referred in the previous Chapter, the flux of cosmic rays decreases with energy. The range of energies starts at some MeV and extends to energies up to 10^{20} eV. At 100 GeV (10^{11} eV), the flux on Earth is on the order of a few particles per m^2 per second. Around 10^{15} eV, the flux is reduced to around one particle per m^2 per year and at the highest energy limits it is below 1 particle per km^2 per century.

In Figure 2.1 the energy spectrum is shown for energies higher than 1 TeV. For energies below a few GeV, the flux is modulated by solar winds, with an anti-correlation between the flux and periods with higher solar activity [24]. The flux for these lower energies is affected by Earth’s magnetic field. Above a few GeV, the energy spectrum of primary cosmic rays $J(E)$ can be described by a power law:

$$J(E) = \frac{dN}{dE} \propto E^{-\gamma} \quad (2.1)$$

where N represents the number of particles and γ is the spectral index. The changes of the value of γ create the structures in the energy spectrum. As mentioned before, there are four visible features: knee, second knee, ankle and the suppression.

From, approximately, 10^9 to 10^{15} eV the spectral index is $\gamma = 2.7$. At an energy

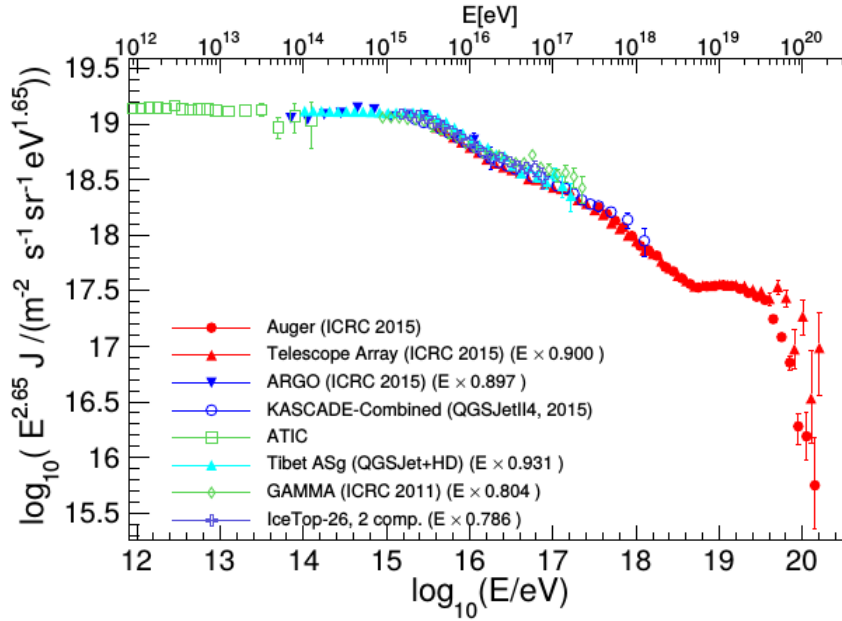


FIGURE 2.1: Energy spectrum of cosmic rays measured by different collaborations (direct and indirect measurements are shown). The flux is scaled by $E^{2.65}$ to highlight the structures [23].

of $\sim 3 \times 10^{15}$ eV, as reported by KASCADE [25], the index changes to $\gamma = 3.1$. This is the first feature observed on the energy spectrum and is known as the knee. Around 8×10^{16} eV, another knee-like structure was found by the KASCADE collaboration [19]. This point is called second knee and the spectral index increases again, $\gamma \sim 3.3$, implying a decrease on the spectrum. There are still not enough proofs to explain these phenomena but the prevailing opinion is that, these features mark the transition from galactic to extragalactic sources. For this range of energies, the capacity of the galactic sources to accelerate nuclei is dependent on Z , such that lighter nuclei reach their energy limit at lower energies. This means that primary cosmic rays of higher energies have an extragalactic origin, since galactic source reached their limit. Therefore, it is expected that the first knee marks the transition limit between galactic and extragalactic sources for lighter nuclei (such as proton) and the second knee establishes the limit for heavier nuclei (iron).

The next change in the spectral index occurs for $\sim 5 \times 10^{18}$ eV at the ankle structure, where $\gamma \sim 2.7$. More strictly, Auger indicates an ankle energy of $(4.8 \pm 0.1(\text{stat}) \pm 0.8(\text{sys})) \times 10^{18}$ eV while TA points to $(5.2 \pm 0.2) \times 10^{18}$ eV [26]. There is no scientific consensus for the reasons behind this feature in the spectrum. Some astrophysical models, known by ankle models [27], suggest that it occurs due to the transition from the galactic to the extragalactic sources, while others, like dip models [28], suggest that the ankle is a consequence of the energy loss by the protons via electron-positron pair production after the interaction with CMB. The results from TA and Auger point for a light composition around the ankle region [29].

Above 10^{19} eV the suppression region starts and there is no value for the spectral index due to lack of statistics. The suppression has been confirmed by the experiments of HiRes and Pierre Auger Observatory. The collaboration of HiRes indicated that this region starts at $(5.6 \pm 0.5(\text{stat}) \pm 0.9(\text{sys})) \times 10^{19}$ eV [30]. The latest result published by the Auger collaboration points to $(4.2 \pm 0.2(\text{stat}) \pm$

$0.8(\text{sys}) \times 10^{19}$ eV [31].

The two most likely explanations for the suppression of cosmic rays at the highest energies are the GZK effect [32, 33] or the exhaustion of sources. The last one is self explanatory. It presupposes that there are no cosmic rays with higher energies because there are no sources which can accelerate particles beyond this point. The other one, the GZK effect, as briefly referred before, implies that the primary cosmic rays interact with the photons from the CMB, resulting in photo-pion production.

According to the GZK effect, the most likely decay products from a proton-photon interaction are:

$$p + \gamma_{CMB} \rightarrow p + \pi^0 \quad (2.2)$$

$$\rightarrow n + \pi^+ \quad (2.3)$$

$$\rightarrow p + \pi^+ + \pi^- \quad (2.4)$$

$$\rightarrow p + e^+ + e^- \quad (2.5)$$

The protons lose energy through this process, therefore it becomes unlikely to detect cosmic rays at Earth with an energy higher than the GZK limit. For heavier nuclei it is expected that they lose their energy through photo-disintegration.

In Appendix B, the calculation of the GZK energy limit is shown, as well as the value for the mean free path for photo-pion production. In Figure 2.2, the mean energy of a proton propagating through the Universe is shown for three different initial energies. Due to the interaction with the CMB, it is expected that (according to the GZK effect) after the protons had travelled ~ 100 Mpc their energy would be below 10^{20} eV, no matter their initial energy. Under this principle, in order to detect at Earth cosmic rays more energetic than this threshold, the source must be less than 100 Mpc away from Earth.

A shift on the energy is visible in Figure 2.1 between the data from TA (red triangles) and Auger (red circles). These differences on the energy scale rise from the energy determination from the fluorescence detectors, with different related uncertainties. There are not only internal parameters associated with the experiments, such as differences on the detectors performance and the techniques used for the analyses, but also other factors related with general properties of the showers, like the invisible energy (see Section 2.7.3) and fluorescence yield (see Section 2.7.6.2). More details about the energy scale comparison between the two experiments can be found in [34].

2.2 Composition

From photons (γ -rays) to neutrinos or electrons, or from proton to iron, the primary cosmic rays have a large variety of particles and their abundance is dependent on their energy.

The flux is dominated by nucleons. Beneath the knee, between 1 GeV and 100 TeV, around 80% are free protons and around 15% are He nuclei [36]. In Figure 2.3 the fluxes of different types of primary cosmic rays are shown for this range of energies. Although not very abundant in the Universe, Lithium, Beryllium and Boron have a relatively high flux in the cosmic rays composition. This lack of proportionality is explained by spallation of heavier nuclei into lighter nuclei. Due to this, it can be argued that Li, Be and Bo are not primary cosmic rays but rather secondary cosmic rays and, therefore, they are not shown in Figure 2.3. However, since this detail is not relevant to the purpose of this thesis and to keep simplicity,

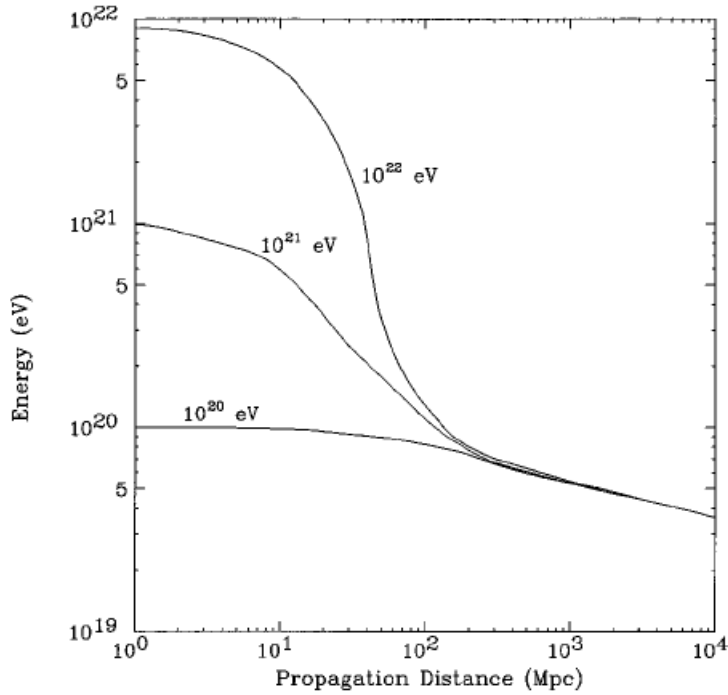


FIGURE 2.2: Variation of the mean energy of a proton propagating through the Universe due to the interaction with the CMB photons for different initial energies [35].

the distinction of primary and secondary cosmic rays used will continue to be the one given in first Chapter (i.e., extra-terrestrial particles and particles produced in the atmosphere, respectively).

Measurements of the chemical composition below the energy of the knee can be performed directly, like the ones represented in Figure 2.3. However, as referred before, above this energy the fluxes become too low for direct measurements and it is required to study secondary particles. The chemical composition of primary cosmic rays has, then, to be inferred from analysing extensive air showers.

In Section 2.7 are described the processes that occur in these cascades of particles. There are two main possibilities for studying the mass composition of primary cosmic rays through secondary particles. Either the number of particles at the ground is determined, or the development of the cascade in the atmosphere is studied. Both scenarios can be correlated with the mass of the primary since they are proportional to the mean logarithmic mass, $\langle \ln A \rangle$:

$$\langle \ln A \rangle \propto \log_{10} \frac{N_{\mu}}{N_e} \quad (2.6)$$

$$\propto X_{\max}^{-1}, \quad (2.7)$$

where N_{μ} and N_e account for the number of muons and electrons at surface, respectively, and X_{\max} represents the depth at which the shower reaches is maximum development (see Section 2.7.3).

In Figure 2.4 the variation of the results of the mean X_{\max} with the energy of the primary is shown for energies above 10^{14} eV. This variation is correlated with the structures observed in the energy spectrum. As explained above, the changes in the spectral index are mainly assumed to happen due consecutive breaks on

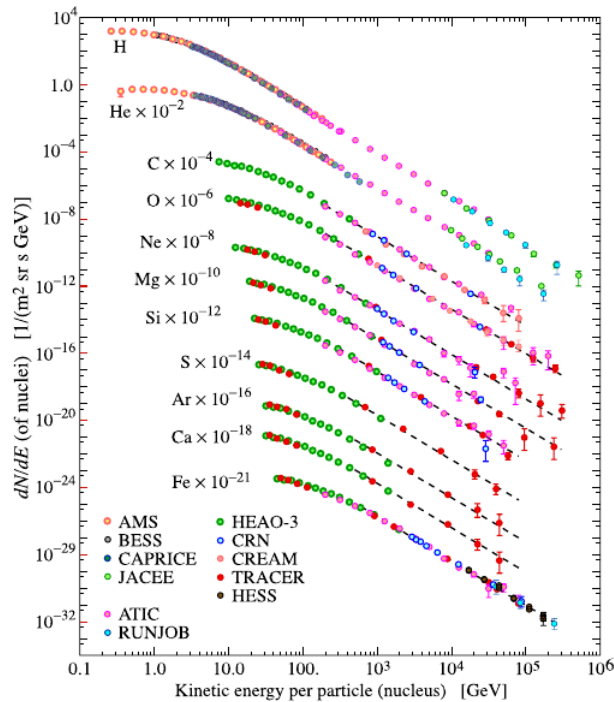


FIGURE 2.3: Fluxes of primary cosmic rays as function of their kinetic energy [37].

the acceleration of nucleons with the increase of the mass, either for primaries with galactic or extra galactic origin. At the knee region, $\sim 3 \times 10^{15}$ eV, the X_{\max} is closer to the simulations for heavier nuclei but it approaches to lighter nuclei at the second knee energy.

For extremely high energies the chemical composition is still unclear. In Figure 2.5 the results of the Pierre Auger collaboration for the mean value of X_{\max} and the respective standard deviation are displayed as function of the energy. For comparison the predictions of hadronic simulations (EPOS-LHC, QGSJetII-04 and Sibyll2.1) induced by a proton and by a iron nucleus are also shown. The theoretical curves for showers induced by proton and iron are often used for data comparison, since these are the lighter and the heavier limits for the type of primary cosmic rays. From this graphic it can be seen that below the ankle, from 10^{17} eV to $\sim 10^{18.3}$ eV, the average value for the maximum depth, $\langle X_{\max} \rangle$, is increasing more strongly than predicted in the case that the mass composition would be constant. After this point, the mean value of X_{\max} increases at a lower rate than predicted for a constant mass composition. From a mass composition point of view, this implies that at $10^{18.3}$ eV the composition of primaries should be light nuclei and after this point it would change to heavier nuclei. Further studies of the chemical composition at these energies are required. For this reason, the ongoing upgrade of the Pierre Auger Observatory (AugerPrime) aims to improve the measurements of the number of muons (N_{μ}), which is also a solution to study the mass composition, as explained above. By combining both parameters, X_{\max} and N_{μ} , it becomes easier to disentangle the mass composition of primaries, as we will see in Section 2.7.

The data collected by TA, if included the low energy extensions, starts above

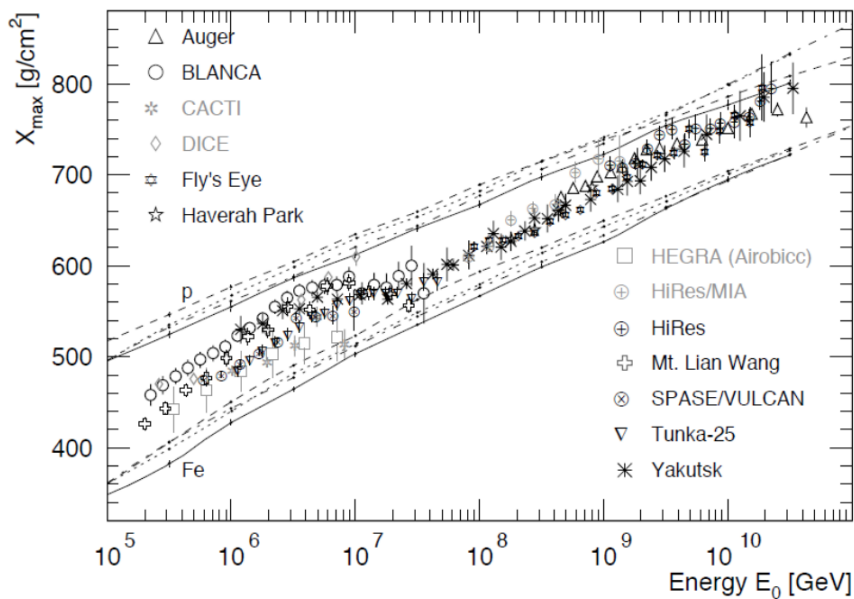


FIGURE 2.4: Average X_{\max} , obtained by different experiments, as function of the energy of the primary. Simulations for proton and iron are shown for comparison, according to the hadronic interaction model QGSJET 01 (solid line), QGSJET II-3 (dashed line), SIBYLL 2.1 (dotted line) and EPOS 1.6 (dash-dotted) [38].

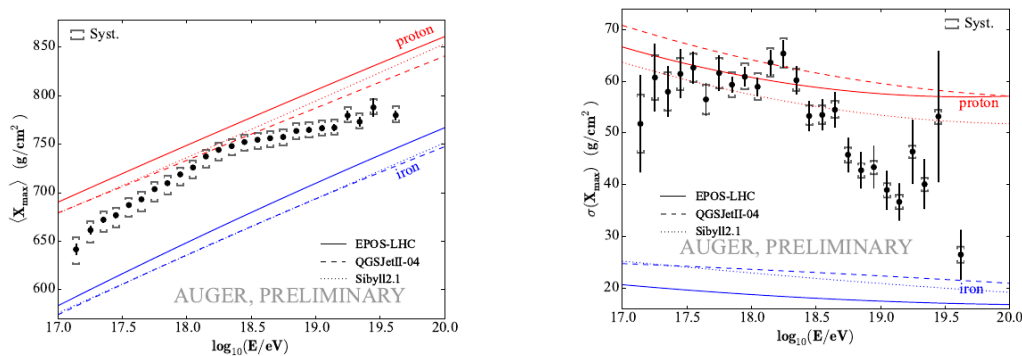


FIGURE 2.5: The mean value and the standard deviation of the measured X_{\max} distributions (left and right, respectively) as function of the energy, by the Pierre Auger Observatory. For comparison also the results for air shower simulations induced by proton and iron are presented [39].

the first knee, at 4×10^{15} eV, to the extremely high energies [40]. In terms of composition, for energies above 10^{18} eV, TA results are in agreement with Auger, within the systematic uncertainties [41].

2.3 Acceleration Mechanisms

The sources of primary cosmic rays of the highest energies and how they are accelerated are still open questions. An explanation for an acceleration mechanism has to account for different features. The mechanism has to reproduce an energy spectrum which follows a power law, as we saw in the beginning of this

Chapter. Furthermore, it needs to be able to accelerate particles until energies up to 10^{20} eV and the chemical abundance of primary cosmic rays must be correlated with the abundance of each element in the Universe [42].

There are two groups of models which aim to describe how particles are accelerated at such energies: Bottom-Up and Top-Down theories. The first ones assume that the (charged) particles are accelerated by some mechanism while the other ones claim that primary cosmic rays are sub-products of even more energetic particles.

Bottom-Up models establish a scenario where particles are originally produced with a lower energy and then are accelerated to higher energies, by an external process. Therefore its name refers to an energy transfer process, beginning at *bottom* energies and then *up* to higher energies. The most known mechanism is the stochastic acceleration, proposed by Enrico Fermi [43] (in 1949, as we saw in the Chapter 1).

There are two different approaches to Fermi's mechanism: first order Fermi's acceleration and second order Fermi's acceleration. The first one was later proposed by Blandford and Ostriker in the 1970s [44] and it assumes that the acceleration process occurs through shock waves. In the second order Fermi's mechanism, the interactions of charged particles with magnetic clouds, while propagating through interstellar space, are suggested as a process to accelerate particles to high energies. A detailed explanation for both versions can be seen in [45].

The particles are confined to a region of acceleration. They enter the region with an initial energy E_0 and the increase of energy happens in a stochastic way. The amount of energy dE that a particle gains in each collision can be described by β , where $\beta = V/c$, being V the velocity of the cloud or of the shock wave. After n collisions inside this region, the energy of the particle E_n is given by:

$$E_n = E_0(1 + \beta)^n. \quad (2.8)$$

Let the probability of a particle escaping from this region be given by P_{esc} . From this, it follows that the probability for a particle to reach the energy E_n is given by $(1 - P_{\text{esc}})^n$. So, after n collisions, there are $N = N_0(1 - P_{\text{esc}})^n$ particles with energy equal or higher than E_n , where N_0 is the initial number of particles. By dividing both equations we can remove the n from the calculation and it follows that:

$$\frac{\ln(N/N_0)}{\ln(E/E_0)} = \frac{\ln(1 - P_{\text{esc}})}{\ln \beta} \quad (2.9)$$

Which implies that

$$\frac{N}{N_0} = \left(\frac{E}{E_0} \right)^{\ln(1 - P_{\text{esc}})/\ln \beta}. \quad (2.10)$$

From this equation follows:

$$N(E)dE \propto E^{-1+(\ln(1 - P_{\text{esc}})/\ln \beta)} dE. \quad (2.11)$$

Which means that a stochastic process for the acceleration of particles describes the energy distribution with a power law, which is what is observed for the energy spectrum of primary cosmic rays.

The biggest difference between both scenarios is that, for the second order the gain of energy per collision, $\langle \Delta E \rangle / E$, is proportional to β^2 while the first is linearly proportional to β (hence, it is called *first order* Fermi acceleration). Since the cloud shocks velocity is non-relativistic it follows that $\beta \ll 1$, which implies that

the second order mechanism is less efficient than the first order process.

Although the first order Fermi's acceleration is an improvement in relation to the original version, it still is not a rapid process and there is an upper limit of energy that particles can be accelerated to, which is much lower than the GZK threshold.

Other mechanisms for the acceleration of primary cosmic rays are the Top-Down models. These theories assume that the primary cosmic rays have origin in particles even heavier ($> 10^{20}$ eV). These mechanisms avoid the need for an acceleration process because they are based on the annihilation or decay of particles to reproduce the energy spectrum of primary cosmic rays. These particles could be topological defects, super heavy dark matter, QCD fragmentation or Z-burst model [46]. This type of models predict a large flux of photons at extremely high energies which has not been seen by any of the experiments for this range of energies [47]. Due to this reason, Top-Down models are seen as less likely than Bottom-Up models, and many of them are already ruled out.

2.4 Sources

The Bottom-Up models like the Fermi's mechanisms described above, are limited to an acceleration region. The particles can only be accelerated as long as they remain inside that region, i. e., while their Larmor radius r_L is smaller than the size L of the acceleration region. The Larmor radius of a cosmic particle with charge Ze is given by:

$$r_L \approx \frac{110E/10^{19}}{eZB_{\mu G}} \text{ [kpc]} \quad (2.12)$$

Where $B_{\mu G}$ is the magnetic field B in μG and E is the energy in eV. Considering β_c as the velocity of the medium, the maximum energy that a particle can reach is:

$$E_{\max} \approx 2\beta_c ZeB_{\mu G}r_L = \beta_c ZeB_{\mu G}L \quad (2.13)$$

This equation relates the magnetic field and the size of the acceleration region. This was summarized by A. Hillas in his famous diagram [48]. The Hillas diagram is displayed in Figure 2.6, where different types of astrophysical structures are represented with respect to their size and their magnetic field. The lines for proton and iron acceleration to 10^{20} eV are also shown, assuming extreme values of $\beta_c = 1$.

There are different objects which can be a source of extremely high energetic cosmic rays, either due to its huge size, its strong magnetic field or both. As referred in the first section of this Chapter, the sources change with the energy of the primaries. Above 10^{16} eV the primary cosmic rays have an extra-galactic origin while below they have mainly a galactic source. Electrons and positrons detected at the top of Earth's atmosphere are also expected to be of galactic origin, given the fact that they cannot propagate for long distances, due to losses of energy through synchrotron radiation¹ and inverse Compton².

The Sun is the nearest cosmic rays source and responsible for the lowest energetic particles, usually not reaching energies higher than a few hundred MeVs

¹When charged particles are accelerated perpendicularly to the direction of their velocity, they emit synchrotron radiation. It is estimated that losses due to this effect are proportional to E^2 [42].

²The interaction of high energy electrons with photons can result in transference of energy through inverse Compton, resulting in losses of energy of the electron [42].

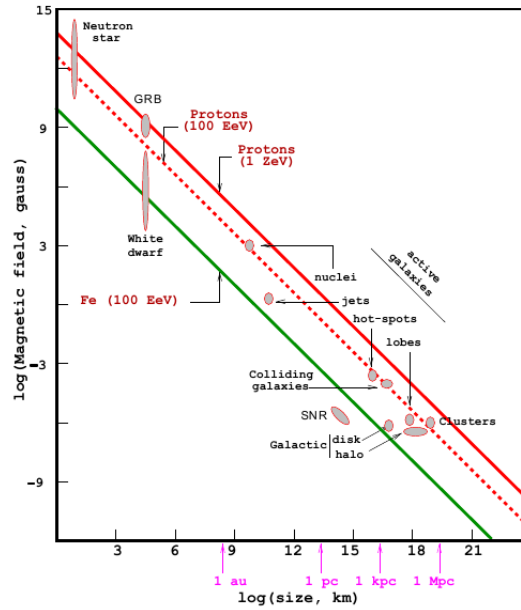


FIGURE 2.6: Hillas diagram. Different astrophysical objects are represented with respect to their size and magnetic field. The lines represent the correlation needed between L and B to accelerate protons or an iron nucleus to the energies shown in the plot (assuming that $\beta_c = 1$). Objects below the line cannot accelerate the particles to these energies. Adapted from [49]

[24] (although in more violent phenomena they can reach energies around 10 GeV). Other close sources of galactic origin follow, which are responsible to accelerate particles until $10^{15} - 10^{17}$ eV (depending on particle's mass). Neutron stars are an example of the possible sources within the Milky Way. As one can verify by Figure 2.6, although they are not too large ($L \sim 10$ km) they have a strong magnetic field ($B \sim 10^{12}$ G) and an angular velocity of 50 Hz, which allows them to be able to accelerate particles up to 10^{20} eV. Pulsars, supernova remnants or binary systems are other possible galactic sources.

As for the extremely high energetic particles, the possible sources are located beyond the Milky Way. Active galactic nuclei (AGN), gamma ray burst (GRB) or radio galaxies are some of the possible sources of primary cosmic rays. All examples are listed in Figure 2.6. Active galactic nuclei contain at the center a super massive black hole. Their magnetic field is around 5 G but the size of an AGN extends up to 10^{-2} pc, turning these astrophysical objects as favourable source for the extremely high energetic primaries [36].

2.5 Anisotropy

The identification of possible sources of primary cosmic rays can be performed by studying the distribution of arrival directions of the primaries at Earth. These studies are currently done by the collaborations of Pierre Auger Observatory and Telescope Array (TA), which are the biggest cosmic rays experiments in the southern and the northern hemisphere, respectively.

Studies about the origin of extremely high energy cosmic rays is not an easy task, since the flux of extremely high energy primaries is low and they suffer from

deflections in magnetic fields, while propagating throughout space. Nonetheless, analysing the distribution of arrival directions can still point to possible sources. Low-mass primary cosmic rays with energies around or higher than the GZK threshold are the favourable particles to allow to perform such studies. Assuming a scenario where the suppression at the GZK limit occurs precisely due to the GZK effect, cosmic rays which arrive at Earth with higher energies than this threshold must have a source not too far (> 100 Mpc, as we saw in Section 2.1). This implies that such particles would be less vulnerable to deflections or other effects that could happen during their propagation in interstellar space and, therefore, have arrival directions which point back to the source [50].

The arrival directions of charged primary cosmic rays is generally isotropic, explainable by the effect of the galactic magnetic field. However, some small anisotropies at the level of 10^{-3} were found by some experiments, including Ice-Cube [51] and Milagro [52], for cosmic rays with energy of a few TeV, probably related to nearby sources (due to their low energy). At the high energy limits, the results of Auger and TA do not show significant anisotropies of the arrival directions for small scales. In Figure 2.7 left the arrival directions of primaries detected by Auger are shown, together with AGNs closer than 130 Mpc (represented by red circles) but no significant correlation was found. Nonetheless, a possible correlation was found with the region of the galaxy Centaurus A, which is located about 4 Mpc from Earth (but not yet statistical significant). On the same figure (on the right) the results from the northern hemisphere, by the TA collaboration, are presented in equatorial coordinates. For events with an energy higher than 57 EeV a hotspot was observed in the direction of the Ursa Major constellation with a diameter of 30° to 40° , but no significant correlation with AGNs was observed [36]. The detected hotspot resulted from 19 collected events when the background expectation was 4.49. This excess has a significance level of 3.4σ .

At large scale above 8×10^{18} eV a dipole was found, with a significance level

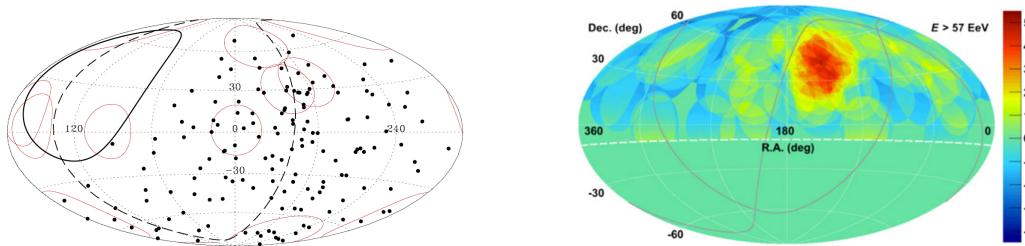


FIGURE 2.7: The pictures represent the results from the Pierre Auger Observatory and Telescope Array (TA) collaborations. On the left the Auger results for energies higher than 5.6×10^{18} eV are shown in galactic coordinates, as well as the Swift AGNs brighter than 10^{44} erg s^{-1} and closer than 130 Mpc, represented by the red circles [50]. On the right the results from TA for energies higher than 57 EeV are displayed in equatorial coordinates [53]. The color scale represents σ .

of 5.4σ , for the arrival direction of primaries to Earth, by the Auger Collaboration. The results are presented in Figure 2.8 in equatorial coordinates. Through comparisons of these results with phenomenological predictions, it was found that the magnitude and directions of this anisotropy supports the hypothesis of extragalactic sources as the origin of the more energetic primaries. Details of this result can be found in [54]. TA and Auger joined data at large scale of the arrival

directions also seems to point for an anisotropy represented by a dipole for energies above 10 EeV [55].

Further studies and more statistics, as well as more information about the type of particles arriving, are needed to better understand the anisotropies.

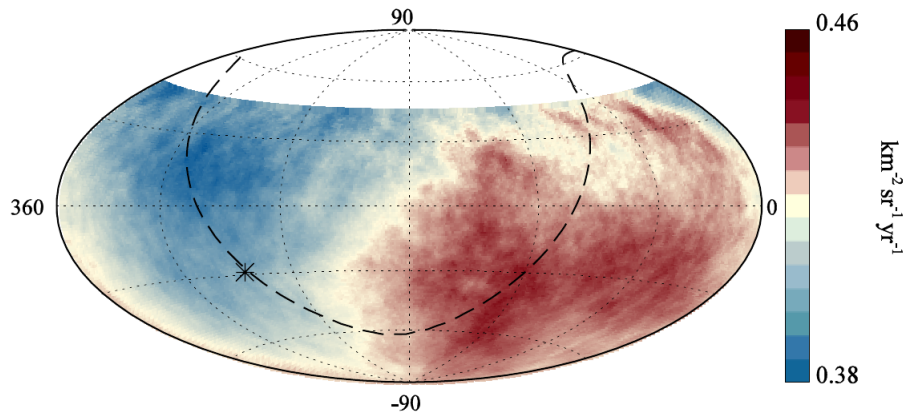


FIGURE 2.8: Cosmic rays flux in equatorial coordinates smoothed with a 45° top-hat function. In dashed the galactic plane is represented and is marked the center of the galaxy with an asterisk [56].

Until this point the general known properties of primary cosmic rays were discussed, including their energy spectrum, chemical composition and possible sources. The next subsections focus on the detection of cosmic rays at Earth divided between the two main possibilities of measurement: direct and indirect.

2.6 Direct Measurements: Balloons and Satellites

Direct detection of charged primary cosmic rays can be performed by balloon flights or satellites for the lower orders of energy (below a few dozens TeV). Some experiments performing direct measurements were already mentioned in the last Chapter, like ACE, PAMELA or AMS. These types of experiments allow to obtain a improved understanding of the chemical composition, as it was illustrated in Figure 2.3.

Such experiments are used not only for determining the energy spectrum for different nuclei, but also for other particles like electrons and positrons. ATIC and others took measurements of the flux of electrons plus positrons until energies of the order of TeV. The results for this measurement at the top of the atmosphere are displayed in Figure 2.9. The results show that the spectrum of electrons steepens one order around 5-10 GeV, as expressed in the figure by the change of the slope. After this point the energy spectrum of electrons can be expressed as power law with index ~ 3 . The feature of the electron spectrum is related to close sources, of galactic origin, since due to synchrotron radiation and inverse Compton effects during the propagation it is not possible for extra-galactic electrons to be detected at Earth. More information about the spectrum of high energy electrons can be found in [37, 57, 58].

Another direct measurement performed by satellites is the ratio anti-proton to proton, \bar{p}/p . This ratio was measured to be at the level of 10^{-4} [59]. Antimatter of heavier nuclei, antideuteron or antihelium for example, has not been detected until now.

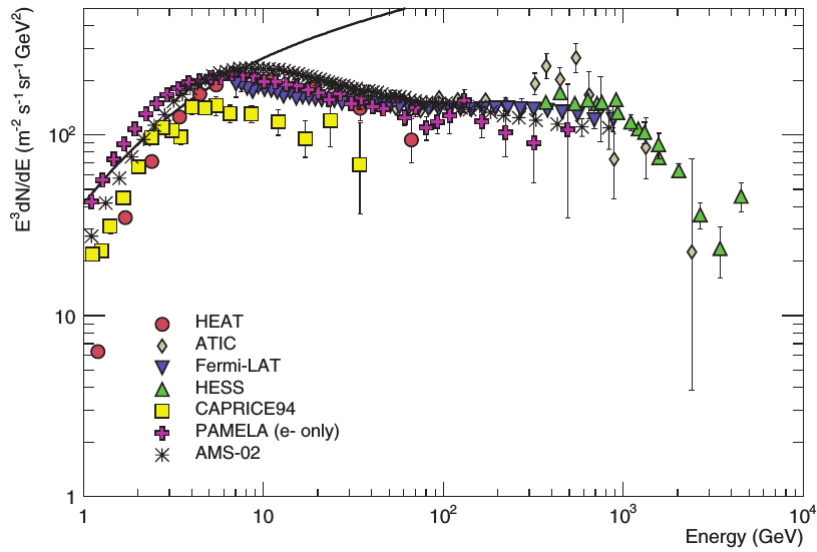


FIGURE 2.9: Spectrum of electrons plus positrons (only electrons for PAMELA) multiplied by E^3 . The line in black represents the spectrum for proton multiplied by 0.01 [37].

One of the most important experiments currently operating is the AMS-02 (Alpha Magnetic Spectrometer, Figure 2.10), installed in May 2011 on the International Space Station. AMS-02 is capable of measuring charged particles, either leptons or nuclei, from energies of a few MeV to TeV. It contains nine plates of precision silicon tracker, a Transition Radiation Detector (TRD), four planes of Time Of Flight counter (TOF, s1, s2, s3 and s4 in the Figure), a magnet, an array of Anti-Coincidences Counter (ACC), a Ring Imaging Cherenkov Detector (RICH) and an Electromagnetic CALorimeter (ECAL) [60]. The combination of these layers allows to perform precise measurements of primary cosmic rays. Measuring the flux of cosmic rays and searching for antimatter and dark matter are the main goals of AMS.

2.7 Indirect Measurements

The interaction of a primary at the top of the atmosphere results in the production of a cascade of particles, whose depth and size is dependent on the energy and mass of the primary. As established in Chapter 1, the particles which result from this interaction are called secondary particles, which can be measured at Earth and analysed in order to understand, indirectly, the properties of the primary. For energies above the knee ($E > 300$ TeV), indirect measurements are the only possible solution of cosmic rays studies, due the low fluxes. In Chapter 1, the most important experiments about measurements of secondary cosmic rays were mentioned, including the largest surface arrays ever built. Currently, the most important experiments of extremely high energetic cosmic rays are the Telescope Array and the Pierre Auger Observatory.

The descriptions that follow in this section aim to give an overview of the processes that occur in an extensive air shower produced in the atmosphere. The importance of the Earth's atmosphere and the main processes that occur during the development of an air shower are explained. Hadronic interactions are also

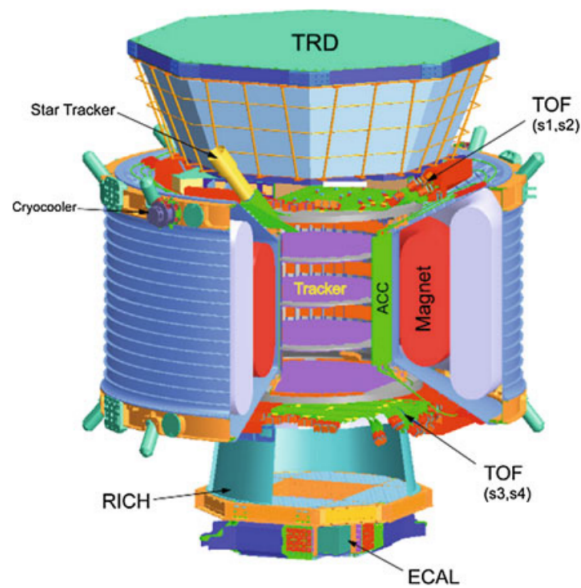


FIGURE 2.10: Schematic representation of AMS-02. The different layers to detect cosmic rays particles are shown. [36].

covered with focus on the properties of extensive air showers that allow to distinguish primary cosmic rays by their mass and their energy. The two main physical processes that are used for the detection of secondary particles are also reviewed (Cherenkov radiation and fluorescence light). At last, the section is completed with a discussion focused on the main theme of this thesis, with a description of inclined air showers ($\theta > 60^\circ$) as well as the properties of atmospheric muons.

2.7.1 Atmosphere

The atmosphere of the planet Earth is fundamental for the survival of life as we know it. It is composed by a thin layer of gases chained by Earth's gravity, which allows the planet to have a soft variation of the temperature between day and night (contrary to the gradient of temperature that occurs at Mercury, which has no atmosphere). Additionally, its capacity to reflect high energy light arriving from the Sun made life a possibility on Earth. Notwithstanding, the atmosphere plays also an important role on the studies of extremely high energy cosmic ray physics. As Greisen put it in the Annual Review in 1960: "Primary cosmic rays with many ergs of energy are so rare that to study them without taking advantage of the atmospheric magnification of their cross section would require prohibitively large detectors or excessive patience" [61].

Earth's atmosphere is a large volume of gas whose density varies with the distance from the surface. At the sea level, the density is on the order of 10^{19} particles per cm^3 and then gradually decreases with height. Due to this gradual decrease, there are no fixed boundary to the atmosphere. Usually, the boundary between the atmosphere and the outer space is marked by the Kármán line, at 100 km above the sea level. In the case of cosmic rays, the first interaction of the primary in the atmosphere generally occurs between 15 km and 35 km of altitude. The atmosphere of the Earth has a mass around 5.15×10^{18} kg but 75% of it is accumulated in the first 11 km.

Although the chemical composition of the atmosphere has changed during time and keeps changing, the dominant element is, by far, Nitrogen (as a diatomic gas N_2). Nitrogen accounts for circa 78% of the atmosphere, Oxygen (O_2) $\sim 20\%$ and Argon (Ar) $\sim 1\%$. The rest of the constituents have a smaller fraction, such as carbon dioxide, Helium, Neon or vapour of water (H_2O). Nitrogen plays an important role in analysis of air showers, since the interaction of the shower charged particles results in emission of fluorescence light, which can be detected by telescopes.

The description of the atmospheric depth is commonly given by the vertical column density X , which is expressed in $g\ cm^{-2}$ [18]. This parameter refers to how much matter was crossed in the atmosphere. The mathematical expression for X is:

$$X(h) = X(h = 0)e^{-h/h_s} [g\ cm^{-2}], \quad (2.14)$$

Where h is the altitude, $X(h = 0)$ is the atmosphere depth at the sea level and $h_s = (kT/Mg)$ $[cm]^3$. The variation of the vertical column density with the distance to the sea level is represented in Figure 2.11.

The complete atmosphere, i.e, crossing it from the top down to the sea level,

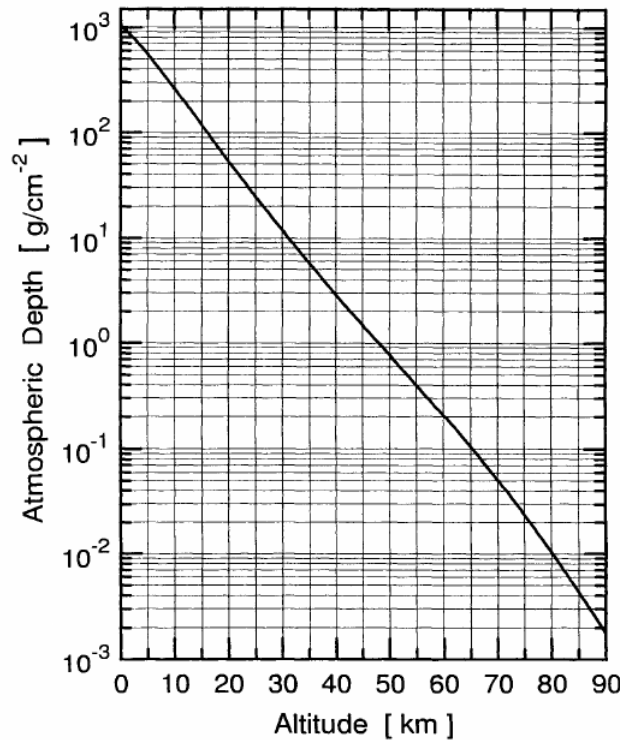


FIGURE 2.11: Variation of the atmospheric vertical depth (or column density) with the altitude [18].

has a depth of circa $1000\ g\ cm^{-2}$. This allows for around 27 radiation lengths⁴ and 11 hadronic interaction length⁵ [63]. By other words, it allows for a complete development of an extensive air shower. In Figure 2.5, it is shown that the

³ k is the Boltzman's constant, T is the temperature in Kelvin, M is the molecular weight and g is the gravitational acceleration.

⁴The radiation length is the mean path that a particle crosses until losing energy through the emission of electromagnetic radiation. For air, this value is usually $X_0 = 36.66\ g\ cm^{-2}$ [62].

⁵The interaction length for hadrons in the atmosphere is $\lambda = 90\ g\ cm^{-2}$.

value for X_{\max} of a proton-induced shower at extremely high energies⁶ is around 800 g cm^{-2} . Not only the atmosphere is deep enough to allow showers to reach their full development, but it is also not too deep, which would result in the complete absorption of the shower before reaching the Earth's surface. Experiments performed in mountains or in plateaus allow to take measurements closer to the maximum development of the shower. For example, the atmospheric depth for the Pierre Auger Observatory is 870 g cm^{-2} , which is close to the maximum depth for the showers produced by protons with extreme energies.

2.7.2 Extensive Air Showers

In an extensive air shower several particles (and of different type) are produced. The number of produced particles and the point where the shower reaches its maximum development (X_{\max}) are dependent on the energy and the type of the primary that initiated the shower. As described in Chapter 1, extensive air showers were discovered in the 1930s by the work of Pierre Auger and Roland Maze and, separately, by Bruno Rossi.

The propagation of the shower in the atmosphere has the same direction as the primary cosmic ray. The center of the shower is normally referred to as the shower core, which is given by the intersection of the shower axis with the surface plane. Given the shape of the showers, the particle distributions are divided into lateral and longitudinal distributions of particles. The longitudinal distribution accounts for the development of the shower in the atmosphere, i. e., the size of the shower⁷ as a function of the atmospheric depth, $N(X)$. The lateral (or transverse) distribution is expressed as $\rho(r)$, where r is the distance to the axis of the shower. This distribution represents the particle density in a plane perpendicular to the shower axis. Since the development of the shower is dependent on the energy and mass of the primary, these distributions will also be dependent on the same parameters. This means that the study of these distributions offers important information for the analysis of extensive air showers.

Several secondary particles result from the interaction of the primary with the nitrogen and oxygen molecules from the atmosphere. Electrons (e^{\pm}), muons (μ^{\pm}), photons (γ), pions (π^0, π^{\pm}), kaons (K), and other particles, are all products of these interactions. These particles can be divided into different components of an extensive air shower. The three main components are: the electromagnetic, the muonic and the hadronic component.

In Figure 2.12, the evolution of an air shower in the atmosphere is outlined. The interaction of the primaries in the atmosphere results in the production of high energy hadrons, mainly mesons (most of them pions and some kaons). These hadrons will interact again or decay, producing other particles. Generally, one third of the hadrons will decay into photons, originating (and constantly feeding) the electromagnetic cascade. The muonic component results from the charged hadrons which decay into muons and neutrinos.

The muons have a small mean lifetime ($\tau \sim 2.19 \mu\text{s}$, or $c\tau \sim 659 \text{ m}$ [64]) and they decay into electrons and neutrinos, feeding the electromagnetic cascade. However, since the muons produced in the shower are relativistic, most of them

⁶However, photon-induced showers would have a larger X_{\max} .

⁷The size of the shower is related to its number of particles.

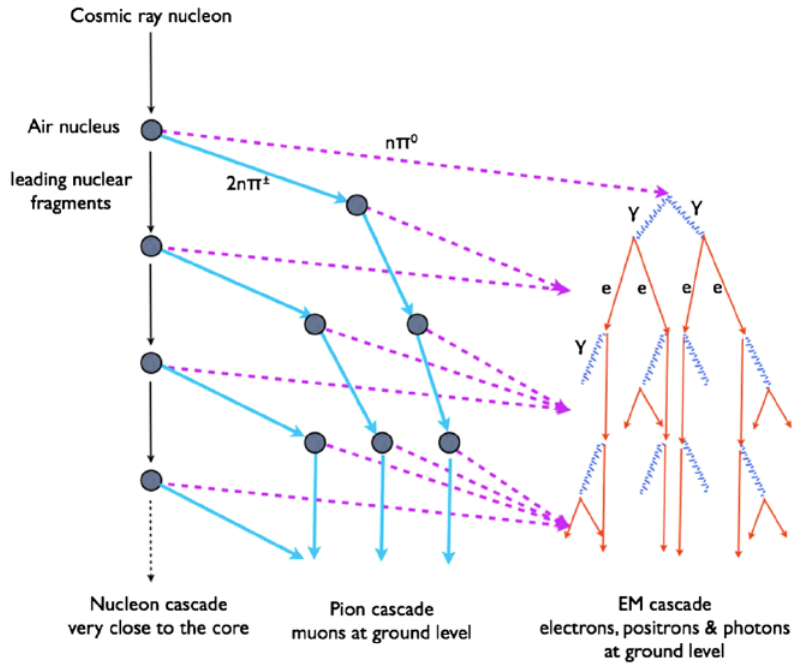
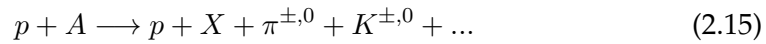


FIGURE 2.12: Schematic evolution of an extensive air shower in the atmosphere. The three main components (hadronic, muonic and electromagnetic) are represented. The purple dashed lines represent the transfer of energy for neutral pions (1/3 of the energy), while the blue solid lines represent the charged pions (2/3 of the energy) [62].

will hit the ground level⁸.

At the ground level, the number of hadrons of a shower is very small. Through the interaction of the primary cosmic rays, several hadrons will be produced. As it was expressed in Chapter 1 about the early developments on the phenomenology of extensive air showers, the interaction of a proton with atoms from the atmosphere can be describe as:



As previously referred, A represents an atom from the atmosphere and the p on the left represents the primary cosmic rays. On the right, the p is defined as the leading particle, the X is the fragmented nucleus and the rest of the particles are mesons and baryons (including others which are not described and can be neglected, such as Ω , Σ , Λ , etc). The majority of the products of this interaction are the pi mesons: the neutral (π^0) and the charged ones (π^\pm).

According to the Particle Data Group [64], the neutral pion ($\pi^0 : u\bar{u}$ or $d\bar{d}$) has a mass of $\sim 134.9 \text{ MeV}/c^2$ and a short mean life time ($\tau \sim 8.5 \times 10^{-17} \text{ s}$, or $c\tau \sim 25 \text{ nm}$). The main decay channel of this particle is into two photons ($\pi^0 \rightarrow \gamma + \gamma$). This decay has a branching ratio⁹ of 0.988. The decay into one photon and a

⁸The average energy for muons from air showers at the sea is 4 GeV, which implies that the muons are relativistic with a velocity $\sim 0.998c$. This means that the mean life of 2.19 μs is in relation to the muon referential. The Lorentz factor for this case is $\gamma \sim 15.81$, which implies that the mean life for muons in the Earth's referential is $\gamma \times \tau = 34.6 \mu\text{s}$. From another perspective, the muons can cross up to 10 km in the atmosphere until decaying into electrons.

⁹Branching ratio is the fraction of particles that should suffer such decay, i.e, the probability of a decay to occur.

electron-positron pair ($\pi^0 \rightarrow \gamma + e^- + e^+$) is also possible but much less likely (with a branching ratio of 0.0117). The other possible decays have a probability much smaller than 0.5%.

With such a small τ , the π^0 do not have time to interact and they decay nearly instantly into photons. This process initiates the electromagnetic cascade. The shower will continue its successive development and at each hadronic interaction, roughly one third of the energy goes into π^0 , which then decay into photons, feeding the electromagnetic cascade, sequentially.

Regarding the development of the electromagnetic cascade initiated by π^0 decay. The dominant processes are pair production of e^-e^+ and *bremsstrahlung*¹⁰ radiation. These processes are involved in a chain reaction - the photons will create a electron-positron pair and the last ones will emit photons through *bremsstrahlung* radiation. The electrons and photons will keep producing each other as long as there is enough energy available.

Both processes have a similar radiation length ($\sim 36.66 \text{ g cm}^{-2}$ [62]). After each interaction, the number of particles increases while the energy available per particle decreases. When the energy is low enough, the main processes of energy losses are ionization and collisions, since pair production or *bremsstrahlung* become less likely. After this point, the cascade has reached its maximum and starts to decrease, since the particles will be absorbed by the atmosphere. This energy is often defined as critical energy ξ_c and it is defined as the energy at which the losses due to *bremsstrahlung* equal the ones due to ionization (while previous to this point, the losses are dominated by *bremsstrahlung*). Then, for the electromagnetic cascade, the critical energy is $\xi_c^e \sim 86 \text{ MeV}$ [62].

The charged pi mesons (π^+ : $u\bar{d}$; π^- : $d\bar{u}$) resulting from the hadronic interactions suffer different processes. The π^\pm are slightly heavier than the neutral one, with a mass of $\sim 139.6 \text{ MeV}/c^2$ [64]. Their mean lifetime is also much larger ($\tau \sim 2.6 \times 10^{-8} \text{ s}$, or $c\tau \sim 7.8 \text{ m}$ [64]) which means that, contrary to the π^0 , they will interact before decaying. The charged pions will interact with the molecules and atoms of the atmosphere and produce new particles. Once again, a third of them will be essentially neutral pions and the other 2/3 will be charged pions. The π^0 will decay into photons and, once more, feed the electromagnetic cascade, as described above. As for the charged pions, they will redo the process. Analogously to the electromagnetic cascade, this process will flow until it had reached a critical energy. In this case, the critical energy occurs when it becomes more likely for the charged pions to decay than to interact. The typical critical energy for charged pions is $\xi_c^\pi \sim 20 \text{ GeV}$.

After reaching this critical point, the π^\pm will start to decay instead of interacting with the molecules of the atmosphere and the cascade of pions has reached its maximum development. The main decay of charged pions is into muons and muonic neutrinos:

$$\pi^\pm \rightarrow \mu^\pm + \nu_\mu/\bar{\nu}_\mu. \quad (2.16)$$

At the ground level, a vertical extensive air shower is largely dominated by photons and electrons. The rest of the particles are muons and at even smaller amounts, different types of hadrons. For example, for a vertical shower induced by a proton with energy around 10^{19} eV , 3×10^{10} particles are expected at the sea level. Of those, 99% are γ and e^\pm (at a ratio of 6 to 1). Their energy is usually ranged between 1 and 10 MeV and they account for 85% of the total energy of the

¹⁰Of German origin, from *bremsen* (to brake) and *Strahlung* (radiation). It can be resumed as the emission of photons due to the deceleration of charged particles (e^\pm , in this case).

shower. The μ^\pm account for circa 10% of the energy and the rest is called *invisible* energy and is divided between neutrinos, mesons and baryons [65].

2.7.3 Heitler's Model

The earlier attempts to describe an extensive air shower were performed in the end of the first half of the last century. A known model for a pure electromagnetic cascade is the Heitler's Model.

The Heitler's model assumes that the evolution of an electromagnetic cascade can be represented as a binary tree, where, at each step, all particles interact and each produce two new particles (electrons, positrons or photons) of equal energy. The process proceeds until the particles reach a critical energy. In this model, all cross sections are assumed as independent of the energy and the energy loss out to collisions is ignored. Furthermore, it is also considered that collisions between secondary particles of the cascade do not occur at all [66].

In Figure 2.13, a schematic representation of an electromagnetic cascade according to the Heitler's model is shown. The cascade is initiated by a photon (that resulted from a π^0 decay) which then produce a electron-positron pair. The energy will be equally divided between the two particles. Next, the e^\pm will emit a photon and lose energy through *bremsstrahlung*. By its turn, the photons emitted by the electrons will produce new electron-positron pairs, while the electrons will emit again a photon. And so on, until the particles have lost enough energy.

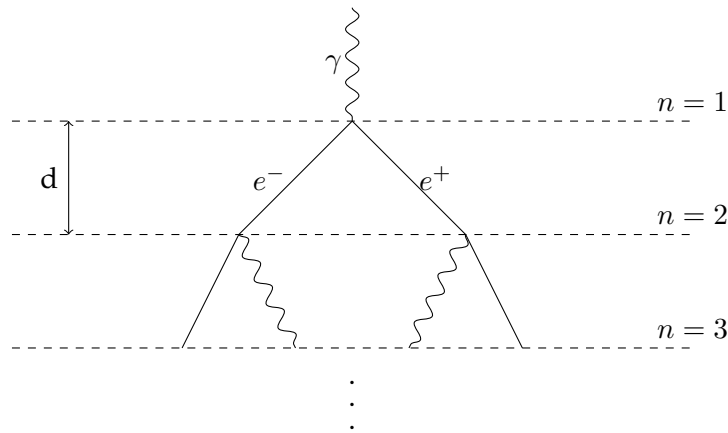


FIGURE 2.13: Schematic representation of an electromagnetic cascade according to the Heitler's model. The photons produce e^-e^+ pairs, while the last ones will emit photons through *bremsstrahlung* radiation. The cascade continues its development until the critical energy is reached.

The radiation length for both processes (pair production and *bremsstrahlung* radiation) is roughly equal, such as $X_0 \sim 36.66 \text{ g cm}^{-2}$. By definition, the radiation length is the average length for the energy of the electron be reduced to $1/e$ of its initial energy due to *bremsstrahlung* losses. Since the Heitler's model assumes that the electron lose half of the energy, the distance is instead defined as splitting length and expressed as $d = \ln 2 X_0$ ¹¹. This is the distance that the particles in the

¹¹The energy loss for electrons due to *bremsstrahlung* can be obtain through the Bethe formula and reduced to $-\frac{dE}{dx} = \frac{E}{X_0}$, where X_0 is, as described, the radiation length. By deriving this equation, follows that $E(x) = E_0 e^{-x/X_0}$. According to the Heitler's model, the energy is split equally onto

electromagnetic cascade travel before splitting into two particles.

After n splitting lengths, the shower has a length of $x_n = n \ln 2 X_0$ [g cm⁻²] and the size of the shower, i.e, total number of particles is given by $N = 2^n = e^{x_n/X_0}$. The development of the shower ends when the critical energy is reached (for this case, $\xi_c^e \sim 86$ MeV). Since this model assumes that the particles are equally divided after each splitting, it implies that the sum of all particles at each generation has to be equal to the energy E_0 of the photon that started the shower. If at the maximum development of the shower there are N_{\max} particles, then the initial energy is given by:

$$E_0 = \xi_c^e N_{\max} \quad (2.17)$$

Defining n_c as the number of divisions until the critical energy is reached, then the maximum number of particles is $N_{\max} = 2^{n_c}$. From equation 2.17 follows that $n_c = \frac{\ln(E_0/\xi_c^e)}{\ln 2}$. The depth of the shower maximum for the electromagnetic cascade, X_{\max}^γ is, therefore, given by:

$$X_{\max}^\gamma = n_c X_0 \ln 2 = X_0 \ln \left(\frac{E_0}{\xi_c^e} \right). \quad (2.18)$$

The increase of the maximum depth with the energy E_0 is given by the elongation rate Λ . For an electromagnetic cascade described by the Heitler's model, it is expressed as:

$$\Lambda^\gamma = \frac{dX_{\max}^\gamma}{d \log_{10} E_0} = 2.3 X_0 \sim 85 \text{ g cm}^{-2}. \quad (2.19)$$

This means that the value of X_{\max}^γ increases ~ 85 g cm⁻² per decade of energy increase of E_0 .

The value for the X_{\max} and the ratio of electrons over photons is overestimated by this model, since the absorptions on the atmosphere and other collisions are neglected. Additionally, the electrons lose energy faster than the photons and more than just one electron is emitted through *bremsstrahlung*. Nonetheless, albeit limited, the Heitler's model correctly tell us that the size of an electromagnetic shower is proportional to the energy of the primary and the depth maximum of the shower, X_{\max} , increases logarithmically with energy.

The principles of this model can be applied analogously for a hadronic cascade induced by a proton, as it was performed by Matthews in [66]. Now, instead of pair production and *bremsstrahlung* radiation, hadronic interactions occur which result in the production of several secondary particles. One third of the particles are π^0 , which will decay into photons, and two thirds are charged pions, which will interact again. This cascade is represented as a scheme in Figure 2.14.

In a similar way, this process happens after a certain distance travelled by the pions, given by the hadronic interaction length. Being the hadronic length $\lambda = 120$ g cm⁻², the splitting length for the hadronic cascade is then $d = \lambda \ln 2$.

At each interaction, N_m new particles will be produced. This implies that $N_m/3$ there will be produced by π^0 and $\frac{2}{3}N_m$ by π^\pm . After n hadronic interactions (or n atmospheric layers), the number of pions is given by:

$$N_{\pi^\pm} = \left(\frac{2}{3} N_m \right)^n. \quad (2.20)$$

both particles, i.e., $E(x) = E_0/2$. Replacing this in the previous equations, follows that $x = \ln 2 X_0$, which is the splitting length d [42].

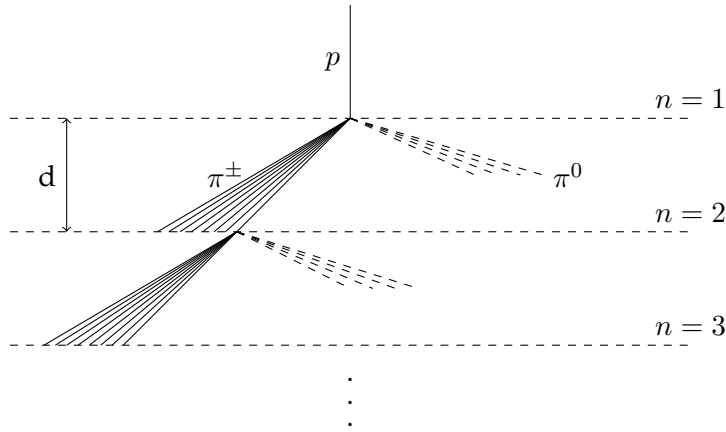


FIGURE 2.14: Schematic representation of a hadronic cascade according to the adaptations of Heitler's model by Matthews. At each interaction, one third of the energy will result in π^0 and the rest $2/3$ will be charged pions. The cascade continues its development until the critical energy is reached.

Being the energy of the initial proton E_0 and since this model assumes that the energy is equally divided between the particles, at the layer n , each charged pion will have an energy equal to:

$$E_{\pi^\pm, \pi^0}(n) = \frac{E_0}{N_m^n}. \quad (2.21)$$

The cascade will stop its development after n_c interactions, where n_c is the layer where the critical energy is reached. As mentioned above, for this cascade, the critical energy is $\xi_c^\pi \sim 20$ GeV. By other words, the n_c layer is the point where $E_{\pi^\pm, \pi^0}(n_c) = \xi_c^\pi$. From this, follows that $n_c = \frac{\ln(E_0/\xi_c^\pi)}{\ln N_m}$.

Once the charged pions reach this point, they will decay instead of interacting again. Since the branching ratio of the charge pions into muons is higher than 99.9%, it is a good approximation to assume that the number of muons produced in the shower is the same as the maximum number of charged pions:

$$N_\mu = N_\pi^\pm = \left(\frac{2}{3}N_m\right)^{n_c}. \quad (2.22)$$

By having in consideration the expression for n_c , the number of muons can be obtain as function of the initial energy:

$$\ln(N_\mu) = \ln(\ln N_\pi^\pm) = n_c \ln\left(\frac{2}{3}N_m\right) \implies N_\mu = \left(\frac{E_0}{\xi_c^\pi}\right)^\beta, \quad (2.23)$$

Where $\beta = \frac{\ln(\frac{2}{3}N_m)}{\ln(N_m)}$.

The exponential β is then dependent on the parameter N_m , which is the number of particles produced after each interaction. This is defined as multiplicity. If the multiplicity ranges between 10 and 100, then β will be between 0.85 and 0.92.

The depth of the shower maximum for a shower induced by a proton, X_{\max}^p , is the atmospheric depth at which the electrons and the photons reach their maximum number. Therefore, this value can be calculated in a similar way as the X_{\max}^γ for the pure electromagnetic cascade. The electromagnetic component of the hadronic cascade is generated by the decays of π^0 alongside the shower.

For a proper evaluation of X_{\max}^p , all sub-electromagnetic showers should be considered independently and then summed up together. However, such calculation is beyond the purpose of a simple model as the Heitler's model. As an alternative approximation, only the first shower is considered and is treated as a pure electromagnetic shower like the one described above.

Additionally, the depth for the first hadronic interaction ($X_0^p = \lambda \ln 2 \sim 61 \text{ g cm}^{-2}$) is considered, which will then result in pion production. After the interaction of the proton in the atmosphere, $N_m/3$ neutral pions will be produced from one third of the total energy. Each one of the π^0 will decay into two γ , so there will be $2N_m/3$ electromagnetic showers developing in parallel through the atmosphere, all with an energy equal to $E_0/2N_m$.

In short, the X_{\max} will be given as a sum of the depth of the first interaction of the proton X_0^p with energy E_0 with the X_{\max}^γ for a pure electromagnetic shower with energy $E_0/2N_m$:

$$X_{\max}^p = X_0^p + X_0 \ln \left(\frac{E_0}{2\xi_c^e N_m} \right) = X_0^p + X_{\max}^\gamma - X_0 \ln(2N_m). \quad (2.24)$$

The consequences of neglecting the contributions of the other sub-showers and assuming an equal distribution of energy at each hadronic interaction result in an underestimation for X_{\max}^p by about 100 g cm^{-2} (independently of the energy), giving an error of $\sim 10\%$ to 20% .

According to this calculation, the elongation rate for proton showers will then be

$$\Lambda^p = \Lambda^\gamma + \frac{d}{d \log_{10} E_0} [X_0^p - X_0 \ln(2N_m)] \sim 58 \text{ g cm}^{-2} \text{ per decade}. \quad (2.25)$$

This value is lower than the elongation rate for photons, due to the increase of the multiplicity (N_m) and the increase of the cross section (X_0^p), as it can be observed from the equation above. The reductions of Λ^γ due to the multiplicity and the cross section are 17 g cm^{-2} and 10 g cm^{-2} , respectively.

Another important parameter that is neglected due to the approximations required to keep the model simple is the energy available for particle production. This model wrongly assumes that the initial energy is completely available for particle production, ignoring that the leading particle of the shower will still carry a significant part of the energy after the first interaction in the atmosphere. In hadronic interactions, the inelasticity κ is the energy available for secondary particles production. By neglecting the energy of the leading particle, it is assumed that $\kappa = 1$. If instead we considered that $\kappa < 1$, the elongation rate would not be affected by it but the same is not valid for the depth of maximum. Including the inelasticity will alter the initial energy of the electromagnetic showers and, therefore, the point at which the X_{\max} is reached.

The final step of the adaptation of the Heitler's model to hadronic cascades is to address showers induced by nuclei with more than one nucleon. In the case of a nucleus with a mass number A , a superposition condition is assumed, by considering A different hadronic showers induced by a single nucleon (by a proton), each with energy E_0/A , where E_0 is the energy of the primary nucleus. In this case, the number of muons can be expressed by:

$$N_\mu^A = \left(\frac{E_0}{\xi_c^\pi} \right)^\beta \cdot A^{1-\beta}. \quad (2.26)$$

As for the depth of the shower maximum, it follows that:

$$X_{\max}^A = X_{\max}^p - \lambda \ln(A). \quad (2.27)$$

This means that a shower induced by a nucleus with $A > 1$ will have a higher number of muons and a shorter X_{\max} than a proton-induced shower. Assuming that $\beta = 0.85$, it is expected that an iron-induced shower would produce $(A = 56)^{0.15} = 1.8$ times more muons than a proton-induced shower, and it would have a shorter X_{\max} by a difference of 150 g cm^{-2} .

As we saw in Section 2.2, the number of muons and the depth of the shower maximum are the two main parameters used to analyse extensive air showers, in order to distinguish which primary induced the shower. These calculations from a simplified model like Heitler's, show that both parameters are dependent on the properties of the primary mass. However, an entanglement of both parameters would increase the capacity of analysis the mass composition of the primaries, which is the aim for the ongoing upgrade of Auger. In Figure 2.15 the correlations between N_{μ} and X_{\max} obtained from simulations using the hadronic interaction model QGSjetII.04 for showers induced by different primaries is shown. By combining the number of muons and the depth of the shower maximum obtained from an air shower, one can increase its capacity of investigating the chemical composition of the primaries.

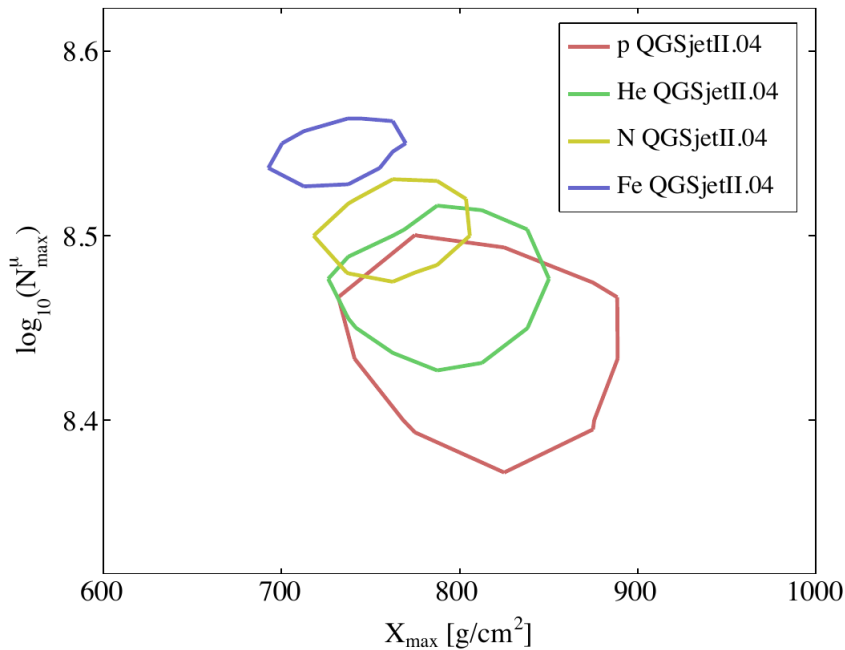


FIGURE 2.15: Representation of the 1σ contour of the correlation between the X_{\max} and the number of muons (N_{μ}). The simulated showers were induced for proton, Helium, Nitrogen and Iron with an energy of $5 \times 10^{19} \text{ eV}$ and fixed zenith angle of 38° [67].

2.7.4 Shower Profiles

Extensive air showers induced by a primary cosmic ray have a different distribution of particles alongside the shower development, but also a distribution perpendicular to the core of the shower, due to Coulomb scattering. In Figure

2.16 an example for the longitudinal and for the lateral distribution are displayed.

The longitudinal distribution of the shower can be parametrized by the Gaisser-Hillas function [68]. The number of particles, or size of the shower, N is given by this parametrization as function of the atmospheric depth X . I.e.,

$$N(X) = N_{\max} \left(\frac{X - X_0}{X_{\max} - X_0} \right)^{\frac{X_{\max} - X_0}{\lambda}} e^{-\frac{X_{\max} - X}{\lambda}}. \quad (2.28)$$

Where N_{\max} is the maximum number of particles (i.e., the number of particles when $X = X_{\max}$), X_0 corresponds to the effective first interaction point and λ is the interaction length. The fluorescence light emitted in the atmosphere is proportional to the number of electrons, which means that the longitudinal distribution can be obtained by studying the fluorescence emissions. This allows not only to find at which depth the X_{\max} occurs, but also to determine the total energy of the shower, since it is proportional to the integral of the Gaisser-Hillas function.

The lateral or transverse profile of a shower can be parametrized by the Nishimura, Kamata and Greisen (NKG) equation [61]. It is expressed in terms of the particle density $\rho(r)$, where r is the distance to the axis of the shower. The general expression for this function is:

$$\rho(r) = \frac{N_e}{2\pi r_M^2} \frac{\Gamma(4.5 - s)}{\Gamma(s) - \Gamma(4.5 - 2s)} \left(\frac{r}{r_M} \right)^{(s-2)} \left(1 + \frac{r}{r_M} \right)^{s-4.5}. \quad (2.29)$$

Where, N_e is the total number of electrons, Γ is the Gamma function, r_M is the Molière radius¹² and $s = \frac{3X}{X+2X_{\max}}$ which is called the shower age. The shower age s is a parameter of development of the shower expressed in terms of the shower maximum depth and the current depth X of the shower. At the beginning of the shower $s = 0$ and $s = 1$ when the shower reaches its maximum.

Different collaborations of surface arrays have used different adaptations of the NKG equation. Additionally, by choosing properly the values for s and r_M , the lateral distribution can be calculated individually for electrons, muons or hadrons.

The lateral distribution for the surface array of the Pierre Auger Observatory was adapted from the NKG function [69], and it is given by:

$$S(r) = S_{1000} \left(\frac{r}{r_{1000}} \right)^{\beta} \left(\frac{r + r_{700}}{r_{1000} + r_{700}} \right)^{\beta+\gamma}. \quad (2.30)$$

Where $r_{1000} = 1000$ m, $r_{700} = 700$ m and S_{1000} is the signal at 1000 m from the shower core and used as the energy estimator and calibrated with the fluorescence detector [70]. The exponent β is adjusted to the data and it is dependent on the zenith angle (it fits to a second order polynomial in $\sec(\theta)$) and γ is very close to zero. The lateral size of a shower, i.e., the number of particles per unit of area (density) as a function of the distance to the shower core, varies with the energy and the type of the primary.

2.7.5 Hadronic Interactions

Hadrons are particles composed by quarks bounded by the strong interaction. Hadrons can be grouped into baryons and mesons, which relate to their number

¹²The Molière radius (named after the German physicist Paul Molière) can be seen as the transverse distance that a particle, at the critical energy, travels before being absorbed. On average, 90% of the shower energy is contained in a cylinder with this exact radius r_M .

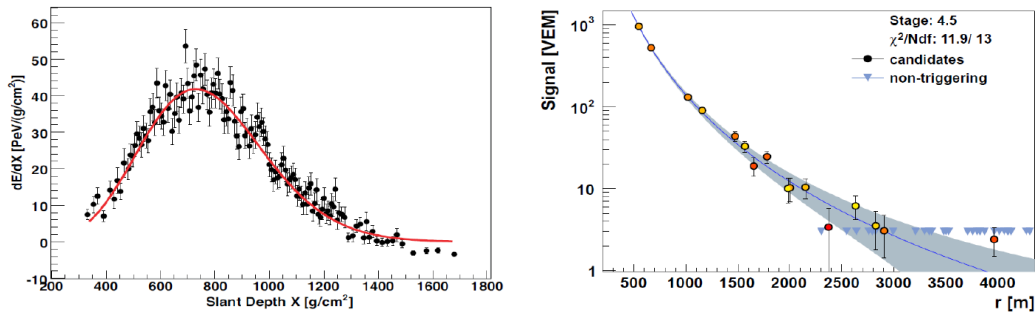


FIGURE 2.16: Examples of a longitudinal and a lateral distributions (left and right, respectively) obtained by the Pierre Auger Observatory. On the left, a longitudinal profile of an event measured by the fluorescence detectors is represented, the red line is the Gaisser Hillas fit and the vertical axis represents the the energy loss rate $\frac{dE}{dX}$ in the atmosphere (see Section 2.7.6.2). On the right, a lateral profile of an event measured by the surface detector of the Pierre Auger Observatory is shown. The figure represents the detector signal as function of the distance to the axis of the shower. The circles are candidate stations and colours are related with the arrival time. The solid line is the fit of the lateral distribution made by the adapted version of the NKG equation for Auger [38].

of quarks (three and two, respectively¹³). A proton is a baryon composed by two up quarks and one down quark and has a mass of $\sim 938.3 \text{ MeV}/c^2$ and is a stable particle¹⁴. An extensive air shower, as mentioned before, starts in the upper atmosphere after the first interaction of a primary cosmic ray with a molecule of the atmosphere. The successive production of pions during the shower development happens due to hadronic interactions.

Hadronic interactions are theoretically described by Quantum Chromodynamics¹⁵ (shortly known as QCD). This theory is implemented in hadronic models, such as QGSJET, SYBILL or EPOS, which describe different hadronic interactions at high energies. By their turn, these models are used in software for Monte Carlo simulations of air showers, like CORSIKA or CONEX, to simulate the propagation of particles in the atmosphere and their respective interactions.

2.7.5.1 Quantum Chromodynamics

Quantum Chromodynamics is a Yang-Mills theory of strong interactions between partons¹⁶ [36, 71]. A Yang-Mills theory is a gauge theory based on Special Unitary groups $SU(N)$. The symmetry group of these theories is non-abelian, i.e., the generators do not commute. QCD is based on the gauge group $SU(3)$, which is the Special Unitary group in three dimensions, where each dimension represents a color (*red*, *blue* and *green* by convention). This gauge theory implies a total of $3^2 - 1 = 8$ free parameters (or generators), which are the carriers of color, the gluons. In this gauge group, each one of the generators is a gauge boson and

¹³Hadrons with more than three quarks are exotic particles.

¹⁴Free protons do not decay spontaneous to other particles, contrary to free neutrons (a baryon composed 2 down quarks and 1 up quark) which has a mean life time of $\sim 880 \text{ s}$.

¹⁵Of Greek origin, chromo means color. Chromodynamics is related to the quantum property of the color of quarks.

¹⁶Partons are defined as *parts* of hadrons, i.e., quarks and gluons

represents a color exchange. The generators of SU(3) can be written in terms of the Gell-Mann matrices.

A general wave function for a quark can be written as a vector in the color space: $\psi = (\psi_{qR}, \psi_{qG}, \psi_{qB})$, where R, G and B refers to the color and q represents the quark. A quark is a fermion with spin 1/2. According to the Standard Model, there are 6 quarks (and their respective antiquarks): up (u), down (d), strange (s), charm (c), top (t) and bottom (b). The quarks up, charm and top have charge $+2/3$, while the other three have a charge of $-1/3$ (and the additive inverse of those charges for the antiquarks). Quarks carry not only electrical charge but also color charge - red (R), green (G) or blue (B) (and the respective anti-color). Color emerged as a new quantum state, exclusive of quarks, in order to explain the existence of baryons composed by the same quark. Baryons such as Δ^{++} (uuu) or Ω^- (sss) are constituted by three equal quarks, which seems to break the Pauli's exclusion principle, which says that two identical fermions cannot occupy the same state. However, if each one of the up quarks of the baryon Δ^{++} has a different color, the Pauli's exclusion principle is not violated.

There are no isolated particles with color. All quark combinations result in a colorless particle. Either the quarks have opposite color or they have an equal amount of each one of the three colors. A blue quark, for example, has one unit of blueness and zero of redness and greenness. Its respective antiparticle would come in negative units of redness, blueness and greenness. Therefore, a meson has to be constituted by a quark and a anti-quark which have opposite color charges, so it would be a colorless particle. A baryon, for instance, needs to be composed by three quarks of different color and the antibaryons of antiquarks of different anticolor. This explains why there are no quark-quark particles or baryons composed of quarks and anti-quarks combinations.

In addition, this also explains why isolated quarks are not observed in nature, since there are no colorless quarks. In QCD theory, this is called quark confinement. When two quarks, bounded by strong interaction, are separated they should results in two new pairs of quarks, since the energy of the gluon field is enough to create another quark pair. This means that quarks can never be isolated and to exist as a single particle. By other words, this means that the interaction between two quarks gets stronger as the distance between them increases. Or inversely, the interaction strength between the quarks becomes smaller as the distance becomes shorter. From this last point, emerges another property of QCD, asymptotic freedom.

The coupling strength α_s is the basic free parameter in QCD, which is the analogue to the fine structure constant α in QED (Quantum Electrodynamics). This coupling becomes stronger in regimes of larger distances or low momentum transfer interactions, meaning that the partons are confined. But, for short time intervals¹⁷, in short distance and high energy reactions, the gluons and the quarks interact weakly, behaving like a quark-gluon plasma, where all the partons behave like free particles, so they are assumed to be asymptotically free. I.e, $\alpha_s \rightarrow 0$ for momentum transfer $Q \rightarrow \infty$ [72].

The coupling constant of QCD can be expressed as a function of the momentum scale μ :

$$\alpha_s(\mu) = \frac{2\pi}{\beta_0 \ln(\mu/\Lambda_{QCD})}, \quad (2.31)$$

¹⁷In quantum physics, large distances correspond to values > 1 fm, low momentum transfers are related to $Q < 1$ GeV/c and short time intervals last less than 10^{-24} s [72].

Where β_0 is a β -function and $\beta_0 = 11 - 2n_f/3$ (with n_f being the number of active quark flavour¹⁸). The parameter Λ_{QCD} is an intrinsic QCD scale. This is a dimensional parameter introduced by the coupling, which defines the scale at which the coupling becomes larger and leaves the perturbative regime. When interaction coupling α_s is small, it is possible to apply perturbative theory to study the partons. But α_s will become higher for larger distances, implying that perturbative theory is no longer possible and the partons are now in a nonperturbative regime. The scale Λ_{QCD} separates long distance regimes (soft processes) from short regimes (hard processes). The scale parameter is usually accepted to be on the order of a few hundred MeV:

$$\Lambda_{QCD} \sim 200 \text{ MeV} \quad (2.32)$$

As mentioned above, the quarks are in a asymptotic freedom regime when the momentum transfer is large ($Q \gg \Lambda_{QCD}$), so that the coupling is small, allowing to explain the interactions by perturbative QCD (pQCD). Outside this regime, perturbative theory is no longer possible and alternatives needs to be used, such as Gribov's Regge Theory.

Gribov's Regge Theory is a multi scattering theory and commonly used by hadronic interaction models to described soft processes (or low momentum transfer regimes). In this theory the interactions are described by quasi-particles called pomerons (with vacuum quantum numbers), since confinement does not allow partons to be exchanged.

2.7.5.2 Hadronic Models

There are several hadronic interaction models, with different input parameters, resulting in different outcomes. We shall divide them into two groups: low energy and high energy models. The division between this groups occurs around a few hundred GeV, in the center of mass energy.

Low energy models, for example FLUKA or GHEISHA, cover the lowest energies of air showers. From the main shower observables that were addressed before, X_{\max} and N_{μ} , only the latter shows a dependence on the low energy hadronic model used. The X_{\max} is mostly dominated by the first interactions, which have a center of mass energy out of the range of these models. However, the total number of secondary particles at the ground level is dependent on low energy interactions. A different transverse momentum distribution between the models results in different particle density for the lateral distribution at the ground. For example, the density of muons at a distance of 1 km or more from the shower axis is predicted to be 5 – 20% higher with the hadronic model GHEISHA than with FLUKA [73].

High energy models are described by pQCD, in asymptotic freedom regime (hard processes), and by Gribov Regge theory, when perturbative calculations are no longer valid (soft processes). When using Gribov Regge theory to treat soft processes, it is required to know the amplitude for pomeron exchange. This input is parametrized from experimental data at lower energies and, then, extrapolated to the highest energies. Since different models have different parametrization methods, it results in differences on the predictions. The most important and

¹⁸Flavour, in Particle Physics, is a property that distinguish different quarks and different leptons.

successful models for cosmic rays studies at the highest energies are QGSJET, EPOS and SYBILL. Due to their relevance and frequent references in this thesis, the models QGSJET and EPOS are describe below.

QGSJET

The hadronic interaction model QGSJET is based on Quark Gluon String models [74, 75]. From the QGSJET01 model to QGSJETII, non-linear effects arriving from pomeron-pomeron interactions were included and the model was updated according to HERA data. The most recent version of this model is QGSJETII-04. This latest version was tuned with LHC data. In the non-perturbative regime, this model applies Gribov Regge theory to hadrons.

EPOS

EPOS is a hadronic model based on Gribov Regge theory but, instead of being applied to hadrons, it is applied to partons: pomerons are exchanged between partons (quarks and gluons) instead of being exchanged by hadrons, as often used in other models. The most recent version of this model is EPOS-LHC, which is tuned to LHC data. When compared to other models, this one predicts a higher number of muons at the ground level. More details about on model can be found in [76].

A comparison of the predictions from the latest version of both models was made in [77].

2.7.5.3 Extensive Air Showers Simulations

The development of an air shower in the atmosphere is a very complex process to study. It is not possible to perform a detailed analytic analysis of experiments on air showers. Some analytic calculations are possible to be made using cascade equations, but they only give previsions for the average values of the variables. There are countless interactions occurring until the shower front reaches the surface and then the particles interact with the detectors. To analyse this long and complex development it is necessary to resort to simulations to process all the interaction of the particles in the atmosphere and the response of the detectors to the particles.

Monte Carlo simulations are a powerful and fundamental tool for the study of extensive air showers. The most common software for Monte Carlo simulations used in Cosmic Rays analyses are CORSIKA [78, 79], AIRES [80], CONEX [81], SENECA [82] and COSMOS. These simulations are processed in software frameworks, like, for example, the Offline Software Framework, which is the software framework developed by the Pierre Auger Collaboration, and will be described later in this thesis.

These Monte Carlo programs are used to simulate the particles propagation and interaction alongside the shower. For a certain set of given parameters, such as the energy, type and direction of the primary, the Monte Carlo simulations provide the longitudinal and lateral distributions of particles. These simulations are very complex. At each step, is necessary to determine the interaction and decay lengths, as well as the energy losses of each one of the particles. Since a shower has millions of particles, it consumes time and computational resources

to simulate the complete shower from the first interaction to the surface. Thinning methods [83] and cascade equations [84] are two techniques used in event generators (Monte Carlo simulations), in order to reduce the processing time.

The thinning method is based on the idea that given the size of the shower, it is redundant to follow all its particles. Initially, every particle is followed, since they carry large portions of energy and, therefore, are important for shower fluctuations. However, after the particle reached an energy limit, only some particles are followed and weighted in order to represent other similar particles. This reduces the particles to be followed by some orders of magnitude. CORSIKA (Cosmic Rays Simulations for KASCADE) is a four dimensional simulation that uses Monte Carlo and thinning methods to reduce the processing time.

Cascade equations are used as a technique where only some particles are tracked and the others are represented by cascade equations. By other words, particles which carry large fractions of energy are followed by the Monte Carlo simulation but particles with energy below a given threshold are not. Instead, the particles that would result from the ignored particles are described by cascade equations. These cascade equations are parametrizations related to the average values of the shower but hide natural fluctuations. Notwithstanding, since cascade equations are only applied to particles with smaller energy fraction, it is assumed that the total fluctuations would not suffer significant changes.

2.7.6 Radiation Emissions

Alongside the development of the shower in the atmosphere, radiation is emitted due to different effects and in different frequencies. Measurements of these radiations allow to analyse and quantify extensive air showers, especially during its development, since ground detectors of charged particles only collect information about the shower when these particles hit the surface. One of the most useful detection technique is the measurement of the fluorescence light emitted in the showers, as it was performed by Fly's Eye or the fluorescence telescopes of the Pierre Auger Observatory, as it was mentioned in Chapter 1. Cherenkov radiation is also another important radiation associated to cosmic rays studies, not only because the shower emits this radiation, but also because it is widely use as an indirect way to detect secondary charged particles at the ground level, as it was done at Culham, with photomultipliers inside a tank filled with water [15].

Another radiation emitted in air showers is Askaryan radiation, postulated by Gurgen Askaryan in 1962. The Askaryan effect is similar to the Cherenkov effect, since it results from charged particles travelling faster than the phase velocity of light in a given dielectric (in this case, the air). The particle travelling in a dense medium produces a shower of secondary particles which have a charge asymmetry, resulting in the emission of radiation of the radio and microwave bands. An example of an analysis of cosmic rays through Askaryan radiation can be seen in [85].

Radio radiation from air showers have also other sources. A common one is the influence of the geomagnetic field of Earth on the charge distribution of particles around the axis of the shower. The deflections of electrons by the magnetic field of the Earth results in synchrotron emissions (in order to preserve the momentum conservation) in the radio frequency regime. One of the biggest radio

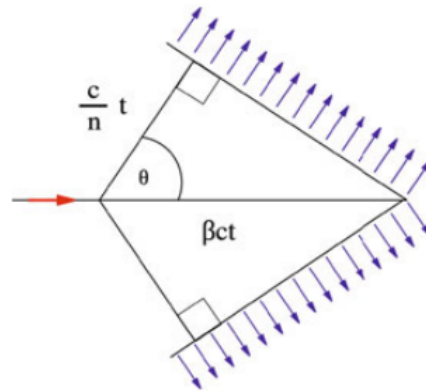


FIGURE 2.17: Schematic representation of Cherenkov effect [36].

detectors is LOFAR (Low Frequency Array), located in the Netherlands¹⁹. AERA (Auger Engineering Radio Array) is an upgrade of the Pierre Auger Observatory to measure radio waves emitted by ultra high cosmic rays and will be later described.

To perform measurements of the light arriving from air showers it is necessary to account for light attenuation during its propagation in the atmosphere until reaching the detectors. This is mainly necessary for fluorescence detection. The attenuation in the range of the fluorescence emissions (with wavelength between 300 and 400 nm) is mainly caused by air molecules (Rayleigh scattering) and aerosol particles (Mie scattering). This implies that fluorescence detection requires a permanent control over the atmospheric parameters.

2.7.6.1 Cherenkov Light

We have seen before what is Vavilov-Cherenkov radiation, or simply Cherenkov radiation [36, 42].

The photons are emitted with a certain angle θ_C , in relation to the motion of the particles, which is dependent on the refractive index of the medium n . It can be resumed as:

$$\cos(\theta_C) = \frac{ct/n}{vt} = \frac{1}{\beta n} \quad (2.33)$$

Where β is the ratio of the velocity v to the speed of light ($\beta = v/c$). Given the energies of the particles, assuming that $\beta \sim 1$ is a good approximation. Therefore, the Cherenkov angle shall be expressed as $\theta_C = \arccos(1/n)$. This effect is represented with a scheme in Figure 2.17.

The refractive index of water, air and standard glass are listed in Table 2.1, with the respective Cherenkov angles of the medium. These are the most important mediums to have in consideration when talking about Cosmic Rays. As one can see from Table 2.1, the refractive index of air is slightly higher than 1, which implies that Cherenkov radiation can also be emitted in air by charged particles. The Cherenkov photons can be found at a maximum shift of 1.3° from the particle direction but, due to transverse momentum, they can be found as far as 25° from the shower axis. Some experiments, mostly studying cosmic gamma rays like

¹⁹LOFAR has several scientific goals, including cosmic rays studies, but also deep extragalactic surveys, solar science and others.

HESS or VERITAS, use air Cherenkov (Cherenkov radiation in air) in their scientific research.

TABLE 2.1: Refractive index and Cherenkov angle in air, water and standard glass.

Medium	n	$\theta_{C,\max}$ [°]
Air	1.00029	1.38
Water	1.33	41.25
Glass	1.52	48.86

The surface array of the Pierre Auger Observatory is constituted by Water Cherenkov Stations, which are tanks filled with water and equipped with photomultipliers inside to detect Cherenkov radiation. Details of these stations will be addressed in the next Chapter, including particular effects that can occur, such as a direct intersection of the PMT by the charged particle and consequent Cherenkov radiation in the glass of the PMT.

By assuming that $\beta = 1$, the table above shows the values for the maximum angle of emission for the photons. However, that is not always the case. For Cherenkov emission it is required that the velocity v of the charged particle is higher than the speed of light in a certain medium. The refractive index n is given as the ratio between the speed of light in vacuum with the speed of light in a medium ($n = c/v$). This means that the speed of light in water is $\sim 2.25 \times 10^8 \text{ ms}^{-1} \sim 0.75c$. Muons and electrons will emit Cherenkov photons if travelling in water faster than this value. For electrons, the energy threshold in water is:

$$E_{e,\text{threshold}} = \frac{mc^2}{\sqrt{1 - \frac{1}{n^2}}} \sim \frac{0.51}{\sqrt{1 - 0.75^2}} \sim 0.771 \text{ MeV} \quad (2.34)$$

Analogously, for muons $E_{\mu,\text{threshold}} \sim 159.65 \text{ MeV}$ and for proton $E_{p,\text{threshold}} \sim 1.42 \text{ GeV}$. Protons of such energies are not common at the sea level, but electrons and muons arriving from air showers have often enough energy to produce Cherenkov light in water.

Through the Frank-Tamm²⁰ formula, one can determine how many photons are produced per unit of energy and per unit of path length:

$$\frac{d^2N}{dEdx} \approx \frac{\alpha Z_p^2}{\hbar c} \sin^2(\theta_C) \approx 370 Z_p^2 \sin^2(\theta_C) [\text{eV}^{-1} \text{cm}^{-1}] \quad (2.35)$$

Where α is the fine structure constant and Z_p is the charge of the particle.

The charged particle loses a very small fraction of energy due to this effect that can be neglected (usually the energy losses per Cherenkov radiation are 10^{-4} times smaller than due to ionization). The Cherenkov radiation is emitted in a large frequency range but is predominantly emitted near the ultraviolet region.

2.7.6.2 Fluorescence Light

Another light emission occurring in air showers due to charged particles is fluorescence light. This radiation is emitted by nitrogen molecules when excited

²⁰Ilya Frank (1908-1990) and Igor Tamm (1895-1971) were Russian physicists and shared with Pavel Cherenkov the Nobel Prize in Physics in 1958 for the discovery of the Cherenkov effect.

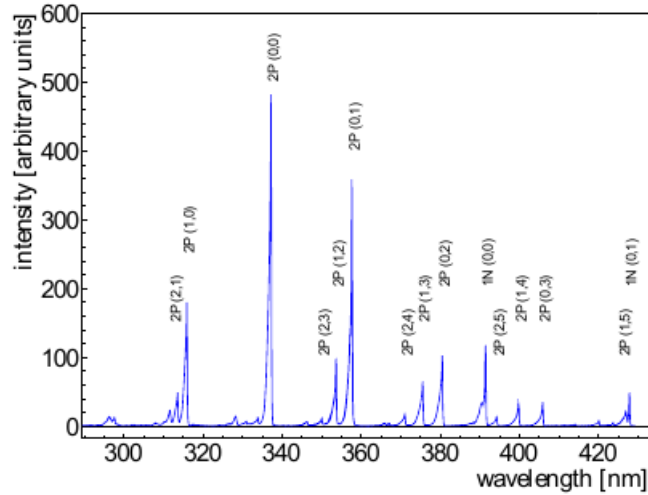


FIGURE 2.18: Fluorescence spectrum in air when excited by a current of $\sim 10 \mu\text{A}$, with 3 MeV electrons at a pressure of 800 hPa [87].

by charged particles.

Nitrogen is the seventh element of the Periodic Table, discovered in 1772 by Daniel Rutherford (1749-1819). This is the most abundant gas in our atmosphere, present as a diatomic molecule N_2 . Most energy losses of particles from an air shower occur from ionization and excitation of N_2 and N_2^+ . When nitrogen molecules return to their ground state, they emit photons with wavelength around the range 300 - 400 nm, addressed as fluorescence light. Most photons ($\sim 80\%$) come from the transition from the 2P band system of N_2 , while the photons emitted from N_2^+ ($\sim 20\%$) come from the 1N band system²¹ [86]. The fluorescence spectrum for N_2 is represented in Figure 2.18.

While Cherenkov radiation has a well established relation between the angle of emission, the medium and the velocity of the particle, fluorescence light is dependent on the nitrogen molecules being excited and then returning to the ground state, emitting photons in an isotropic way. This means that fluorescence light can be detected at large distances from the shower axis.

The number of fluorescence photons emitted during the shower development is proportional to the energy deposit in air, for the excitation of nitrogen. The number of emitted photons can be expressed as:

$$n_\gamma = \frac{\epsilon(P, T, \lambda) E_{\text{dep}}}{E_\lambda}, \quad (2.36)$$

Where $\epsilon(P, T, \lambda)$ is the fraction of energy emitted as fluorescence radiation from the total energy E_{dep} lost by the shower in the atmosphere. It is commonly referred to as fluorescence efficiency and is dependent on the pressure and temperature of the atmosphere and on the wavelength of the emitted photon.

The fluorescence light is often expressed in terms of the fluorescence light

²¹The electronic configuration of molecules is very complex. Nitrogen has 5 valence electrons and 4 valence orbitals. A stable configuration in the atmosphere is N_2 , which has a triple bond between the two atoms and a non-binding pair of electrons for each, accordingly to the Lewis structure. The orbitals of each atoms form new hybrid ones by mixing the 2s and 2p.

yield (FLY), which is the conversion factor between the number of emitted photons and the energy deposited in the atmosphere. It is usually defined as photons per meter (FLY/L) or as photons per energy deposited in the atmosphere (FLY/E_{dep}). This is:

$$\frac{FLY(P, T, \lambda)}{E_{\text{dep}}} = \frac{\epsilon(P, T, \lambda)}{E_{\lambda}} \left[\frac{\text{photons}}{\text{MeV}} \right], \quad (2.37)$$

$$\frac{FLY(P, T, \lambda)}{L} = \frac{\epsilon(P, T, \lambda)}{E_{\lambda}} \frac{dE}{dX} \rho_{\text{air}} \left[\frac{\text{photons}}{\text{m}} \right], \quad (2.38)$$

Where ρ_{air} is the atmospheric density and $\frac{dE}{dX}$ is the energy loss rate in the atmosphere. This value is, as well, dependent on the pressure and temperature of the atmosphere and on the wavelength of the emitted photon. Therefore, such measurements require good atmospheric conditions and constant monitoring.

The *modus operandi* of the Fluorescence Detector of the Pierre Auger Observatory will be described and explained in the next Chapter.

2.7.7 Inclined Showers

One reason to express the shower depth in terms of mass per unit area ($[g \text{ cm}^{-2}]$) instead of unit length is the fact that showers have different arrival directions. By other words, primary cosmic rays hit the Earth from all directions, implying that the axis of the shower will have a certain zenith and azimuthal angles. Therefore, at the same altitude crossed in the atmosphere, a vertical air shower will cross less matter than an inclined shower. For example, a shower with $\theta = 0^\circ$ that hits the Pierre Auger Observatory had crossed around 870 g cm^{-2} in the atmosphere, while a shower with $\theta = 60^\circ$ would have crossed around 1700 g cm^{-2} [18]. Assuming a flat Earth, the correlation between the depth of the shower X and the respective zenith angle θ is:

$$X = \int \frac{\rho(z)}{\cos(\theta)} dz \quad (2.39)$$

Where $\rho(z)$ is the atmospheric density. Figure 2.19 shows the variation of the atmospheric thickness with the zenith angle of the shower.

Due to electromagnetic absorption in the atmosphere, showers with zenith angles larger than 60° are mostly constituted by muons when they hit the ground.

In Figure 2.20, the variation with the atmospheric depth of the particles density is displayed. The differences between a vertical and an inclined shower lies in the quantity of crossed mass, i.e., atmospheric depth. The variation of the ratio density between muons and electrons with the atmospheric depth can be seen in this Figure. A larger atmospheric depth crossed implies a smaller fraction of electrons. This can be related with the zenith angle of the shower, since showers with larger angles crossed more matter in the atmosphere.

Counting the number of particles at the ground for such showers implies a very small (or nonexistent) electromagnetic contamination. This allows to perform a better analysis of the primaries' properties since, as we saw earlier, the number of muons is correlated with the type and energy of the primary.

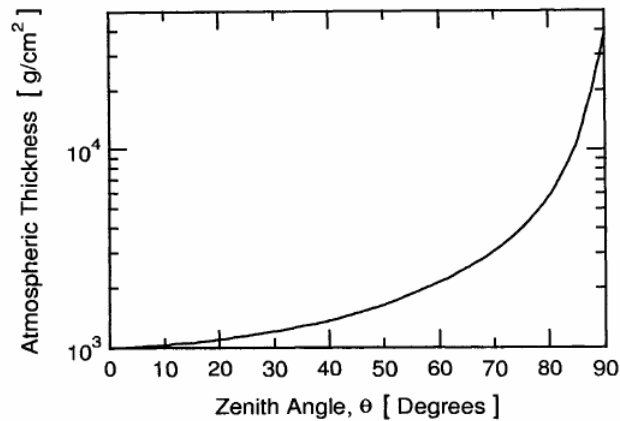


FIGURE 2.19: Variation of the atmospheric thickness at the sea level crossed by the shower as function of its zenith angle [18].

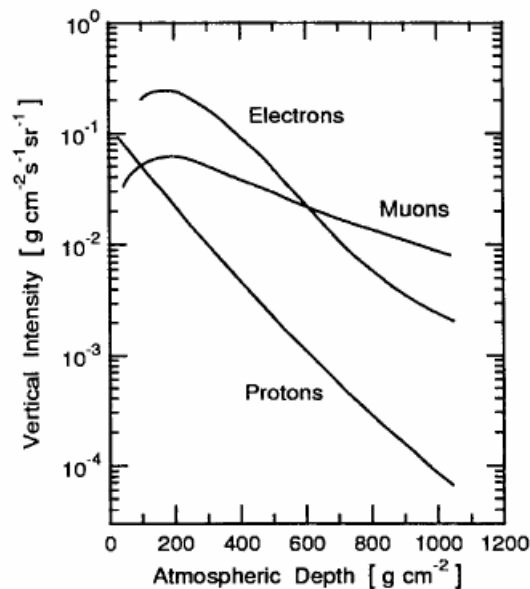


FIGURE 2.20: Variation of the particle densities with the atmospheric depth [18].

2.7.8 Muon Content in Inclined Showers

Recent studies have shown a muon deficit in simulations of 30% to 80%, depending on the hadronic model [88]. As we have seen before, the muon content of a shower (N_μ) is a parameter sensitive to the primary cosmic rays that induced the shower (their energy and mass composition) and to hadronic interaction properties. Understanding this parameter is fundamental to extensive air shower studies and to comprehend the mass composition of the primaries at the highest energies.

The muon content of inclined showers was recently studied in analyses about the total number of muons [88] and the muon production depth [89]. The possibility of hadronic and (or) energy rescaling was also tested [90].

2.7.8.1 Muon Number

As calculated in the Heitler's Models section (see Section 2.7.3), the number of muons in an air shower can be given in terms of the energy E_0 and the mass A of the primary:

$$N_\mu = \left(\frac{E_0}{\xi_c \pi} \right)^\beta \cdot A^{1-\beta}. \quad (2.40)$$

Where, as previously mentioned, $\beta \sim 0.9$. The number of muons is proportional to the energy and the mass of the primary, meaning that iron-induced showers should have more muons than proton ones (for the same energy). This means that N_μ is a good parameter to study the mass composition of primaries. Notwithstanding, detailed simulations of extensive air showers show dependencies of the muon content with the hadronic interaction properties, such as the multiplicity, inelasticity, baryon anti-baryon pair production and the charge ratio [91, 92].

The logarithmic gain of muons with energy can be obtained from deriving equation 2.40:

$$\frac{d \ln N_\mu}{d \ln E} = \beta + (1 - \beta) \frac{d \ln A}{d \ln E}. \quad (2.41)$$

This carries additional information about the muon content dependency on the charge and how much this value should increase per decade of energy (for showers induced by primaries of the same mass).

To correlate the number of muons with the mass of the primary it is necessary to measure the secondary particles at the ground. Such measurements are performed, for example, in Argentina by the Pierre Auger Observatory. However, at its current stage, the surface array of detectors do not have the capacity to disentangle the electromagnetic and the muonic components, making mass composition studies through the muon content very complicated.

Nonetheless, as mentioned above, this entanglement of the muonic and electromagnetic component is heavily attenuated for inclined showers. By crossing a larger quantity of mass in the atmosphere, showers with zenith angle larger than 60° have a smaller electromagnetic component, due to absorption on air. Only very energetic electrons or those which resulted from the muon decay will be found at the ground level. Usually, at the level of the Pierre Auger Observatory, it is expected that the influence of the electromagnetic component on the signal of the detectors is between 15% and 20% [93].

Hybrid events obtained by both detectors of the Pierre Auger Observatory, the surface detector (SD) and the fluorescence detector (FD), were selected to perform an analysis of the muon content of showers [88].

The sample of hybrid events was submitted to several conditions to filter the events which were not of interest for this analysis. Only events with zenith angles $62^\circ < \theta < 80^\circ$ and with energies above 4×10^{18} eV were accepted. A total of 174 events were accepted for this analysis.

To infer the mass composition of the primaries from these events it is necessary to reconstruct the number of muons for each shower.

The muon density ρ_μ can be described as a function of the distance to the shower axis \vec{r} , i.e.:

$$\rho_\mu(\vec{r}) = N_{19} \rho_{\mu,19}(\vec{r}, \theta, \phi), \quad (2.42)$$

Where $\rho_{\mu,19}$ is the parametrized ground density for a proton-induced shower simulated with an energy of 10^{19} eV with QGSJETII-03 and N_{19} is a scale factor which relates the observed muon densities at the ground level to the average muon density profile of simulated proton-induced showers of 10^{19} eV. This scale factor is

independent of the zenith angle and can be used as an estimator for the number of muons.

The fitted value for N_{19} gives the number of muons per unit area relative to the reference density. By other words, N_{19} is a relative measure of N_μ . A full description of the event reconstruction of inclined showers and how N_{19} is inferred from the measured signal can be found in [94].

This analysis was tested with Monte Carlo simulation by comparing N_{19} to the ratio $R_\mu = N_\mu/N_{\mu,19}$ ²². A deviation within 5% was obtained between N_{19} and R_μ . The uncertainty for R_μ was estimated to be around 11%, by combining the uncertainty of the hadronic models with the response of the tank to inclined muons [95]. This analysis of the response of the tank showed an agreement within 10% between the simulation and data to large angles.

Due to intrinsic fluctuations caused by statistics or randomly mixed samples of different mass composition, the average R_μ from these fluctuations, $\langle R_\mu \rangle$, is then considered for the comparisons.

From the equations derived from the Heitler's Models (equations 2.40 and 2.41) it is expected that the average number of muons can be related to the primary energy in terms of a power law. Consequently, the average muon content R_μ should be obtained by the same relation, since it is proportional to the average N_μ . Mathematically, this means:

$$\langle R_\mu \rangle = a \left(\frac{E}{10^{19} \text{ eV}} \right)^b. \quad (2.43)$$

This parametrization was fitted to the data, where a represents the average muon content at 10^{19} eV and b represents the logarithmic gain of muons with energy. The results from the fit to the data are:

$$a = \langle R_\mu \rangle = (1.841 \pm 0.029 \pm 0.324(\text{sys.})), \quad (2.44)$$

$$b = \frac{d\langle \ln R_\mu \rangle}{d \ln E} = (1.029 \pm 0.024 \pm 0.030(\text{sys.})). \quad (2.45)$$

The systematic uncertainties of $\sim 18\%$ for the absolute scale associated with $\langle R_\mu \rangle$ are dominated by the energy scale of Auger ($\sim 14\%$) and by the intrinsic uncertainty related to the measurements of R_μ ($\sim 11\%$, as mentioned above).

The results for ratio of the average R_μ to the energy are represented in Figure 2.21. This ratio softens the influence of the energy on the muon content and emphasizes the mass composition dependency²³. Together with the data (and the respective line fitted to the results), the theoretical curves for iron and proton are drawn, based on the hadronic models EPOS-LHC and QGSJETII-04 for $\theta = 67^\circ$ ²⁴.

The theoretical curves for proton and iron are well separated, which proves $\langle R_\mu \rangle$ as a good parameter to evaluate the mass of primaries.

The data, however, show values of $\langle R_\mu \rangle$ which would indicate a mass composition heavier than iron.

The results for X_{max} are expressed in Figure 2.21 (right) associated with the mean logarithmic muon content $\langle \ln R_\mu \rangle$. The theoretical expectations for this relation are also represented for four different hadronic interactions and for different

²² $N_{\mu,19}$ is the total number of muons and given by $N_{\mu,19} = \iint \rho_{\mu,19} dx dy$.

²³ However, there is still a small energy dependency which results from the index b of the power law. The lines on Figure 2.21 will have a inclination of $b - 1$, which should be close to zero. The inclination observed for the fits based on the hadronic models result from the energy dependency still entangle on the $\langle R_\mu \rangle / \frac{E}{10^{19} \text{ eV}}$ ratio. In both cases $0.9 < b < 1$.

²⁴ The showers are simulated with $\theta = 67^\circ$ because it is the average zenith angle of the data.

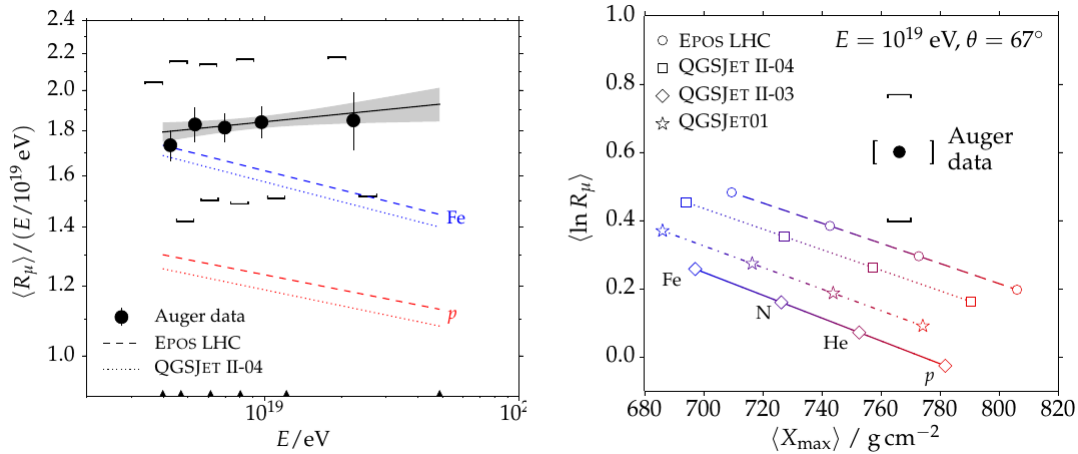


FIGURE 2.21: Left: Average muon content as a function of the shower energy, in double logarithmic scale. The data is represented in black circles and the black line is the respective fit. The grey band is the uncertainty associated with the fit. The brackets show the systematic errors of the measurements and their diagonal offset represents the correlated effect of systematic shifts in the energy scale. For comparison, the predictions for iron and proton are drawn (in both plots) to $E = 10^{19}$ eV and $\theta = 67^\circ$ using two different hadronic models. Right: $\langle R_\mu \rangle$ as a function of the $\langle X_{\text{max}} \rangle$ for the data and predictions from different models [88].

mass compositions, for showers at $E = 10^{19}$ eV and $\theta = 67^\circ$. While the X_{max} points to a composition lighter than iron, the $\langle R_\mu \rangle$ implies the opposite. There is a disagreement between the data and the hadronic models predictions, which can be seen by the lack of superposition of the data error bars and the model lines.

Finally, in Figure 2.22, the values of $\langle \ln R_\mu \rangle (10^{19} \text{ eV})$ and $d\langle \ln R_\mu \rangle / d \ln E$ are summarized for the models predictions and for the data.

None of the hadronic models predictions falls within the uncertainties bars of the value of $\langle \ln R_\mu \rangle$ of the Auger data. The minimum deviation is 1.4σ . This implies a muon discrepancy between 30% and 80% ($^{+17}_{-20}$ (sys.)%). Or, from a different perspective, if the predictions for the number of muons obtained by the hadronic models are correct, an increase, by the same factor, on the Auger energy scale would have to be made.

The measurement of the logarithmic gain $d\langle \ln R_\mu \rangle / d \ln E$ is also higher than the predictions but has a smaller discrepancy than in the case of $\langle \ln R_\mu \rangle$. In this case, contrary to the other parameter, the predictions show a better agreement within themselves. This might suggest that the logarithmic gain is well described by the simulations. In that scenario, the Auger data would favour a mixed composition situation, since the deviation for pure-induced case for proton and iron is 2.2σ and 2.6σ , respectively.

Analyses to showers with zenith angle $\theta < 60^\circ$ are compatible, within uncertainties, to this results, showing that the total number of muon is not well reproduced by the most recent hadronic models [96].

2.7.8.2 Muon Production Depth

Another observable related to muons which can be used to infer the mass composition of primary cosmic rays is the muon production depth.

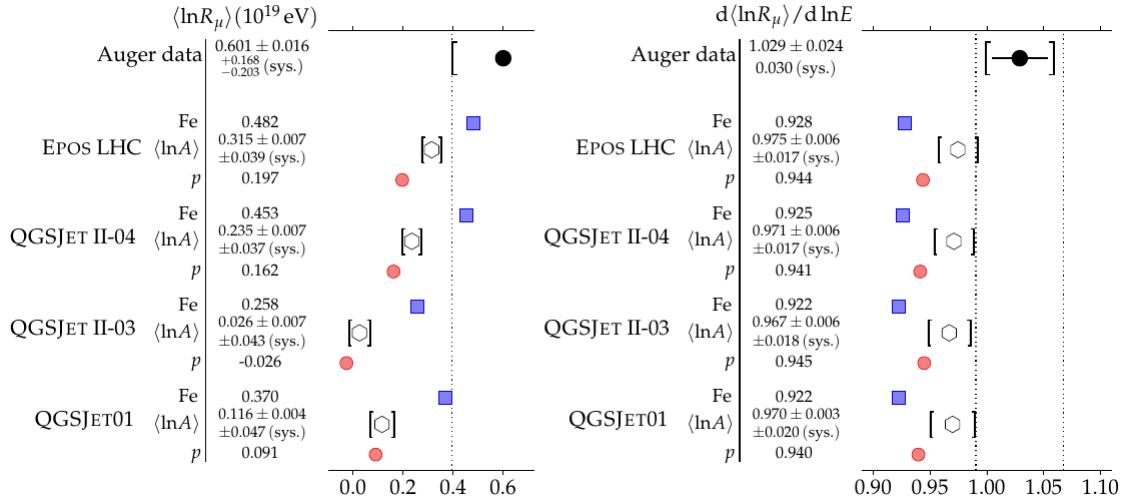


FIGURE 2.22: Left: Comparison between Auger data and different model predictions of the mean logarithmic muon content $\langle \ln R_\mu \rangle$, for $E = 10^{19}$ eV. The predictions are made at $\theta = 67^\circ$ for proton, iron and a shower with a mix composition that matches the $\langle X_{\max} \rangle$ of the data. The uncertainties are represented by the black brackets. Right: Analogous comparison as in the left figure but for $d\langle \ln R_\mu \rangle / d \ln E$ between 4×10^{18} eV and 5×10^{19} eV [88].

Contrary to electrons, the transverse momentum of muons is very small, so their trajectory in the atmosphere can be approximated to straight lines. Since muons are not as affected by *bremstrahlung* and multiple scattering as electrons, their propagation alongside the shower will not suffer many deflections. This means that the arrival directions of muons at the ground point to their production depth.

The phenomenological development of the time distribution of muons in an air shower can be found in [97, 98].

The muon production point along the shower axis can be described by:

$$z \simeq \frac{1}{2} \left(\frac{r^2}{c(t - \langle t_\varepsilon \rangle)} - c(t - \langle t_\varepsilon \rangle) \right) + \Delta - \langle z_\pi \rangle, \quad (2.46)$$

Where r is the distance at the ground to the shower axis and $t - \langle t_\varepsilon \rangle \approx t_g$, which represents the geometric delay, caused by deviations of muons trajectories from the shower axis, where t_ε is the kinematic delay, caused by energy loss of muons in the atmosphere. The parameter Δ is the distance between the muon impact point with the surface and the shower front plane. The last parameter of the equation, z_π , is related to the decay length of charged pions (which then decay to muons) such as $z_\pi = c\tau_\pi E_\pi \cos(\alpha) / (m_\pi c^2)$, where α is the angle between the muon trajectory and the shower axis.

To relate the distance of production with the depth, one has to integrate over the atmospheric density, i.e.:

$$X^\mu = \int_z^\infty \rho(z') dz'. \quad (2.47)$$

The muon production depth can be inferred from the arrival time of muons at the water Cherenkov stations at the ground level of the Pierre Auger Observatory.

The muonic shower maximum X_{\max}^{μ} , the point where the shower reaches its maximum production of muons, can be obtained by fitting the muon production depth with a Gaisser Hillas function.

There were 481 selected hybrid events at the Pierre Auger Observatory. The full description of the criteria for the event selection can be found in [89]. The events had a zenith angle close to 60° , which reduces the electromagnetic contamination of the shower at the surface.

In Figure 2.23, the results for the X_{\max}^{μ} determination are displayed together with the theoretical predictions for proton and iron, based on the hadronic models QGSJETII-04 and EPOS-LHC. While both models predict a similar development of X_{\max}^{μ} with energy, their absolute value has a large difference. The Auger data falls, within error bars, inside the iron prediction for QGSJETII but not for EPOS-LHC. By this analysis it is not only visible that X_{\max}^{μ} can be used as parameter to study the mass composition of primary cosmic rays, but also as a tool to test hadronic interaction models.

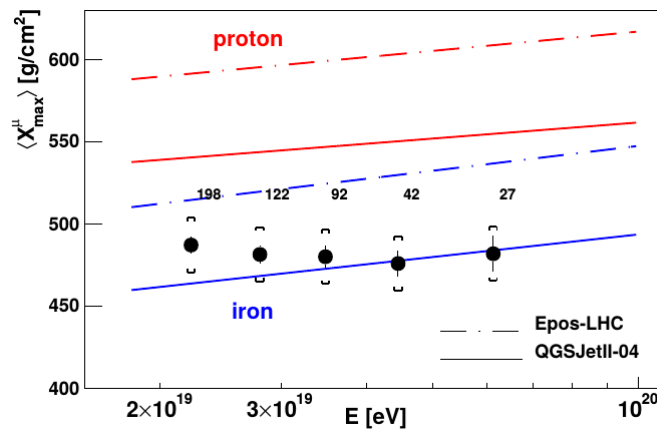


FIGURE 2.23: Average value of the maximum depth of the muon production $\langle X_{\max}^{\mu} \rangle$ as a function of the shower energy E . The data is represented in black dots and the numbers above represent the total number of events for each bin. For comparison, the predictions for proton and iron are drawn based on two different hadronic models [89].

The depth of the shower maximum X_{\max} and the maximum muon production depth X_{\max}^{μ} are variables of the shower which are strongly correlated [99]. Since both are also correlated with the mass composition of the primary, they can be converted into $\langle \ln A \rangle$ [100].

In Figure 2.24, the results for the $\langle \ln A \rangle$ evolution with the energy of the primary are shown. The values for $\langle \ln A \rangle$ are calculated, using the same interaction model, through the $\langle X_{\max}^{\mu} \rangle$ and the $\langle X_{\max} \rangle$ of the showers. In Figure 2.24 (left) the results are displayed for the hadronic model QGSJETII-04 and EPOS-LHC (right). The lines for proton ($\ln(A = 1) = 0$) and for iron ($\ln(A = 56) \sim 4$) are also shown in the figure.

In both cases, the calculations from X_{\max}^{μ} and X_{\max} are in disagreement. A deviation of, at least, 6σ was obtained for the EPOS-LHC model and 1.5σ for QGSJETII-04. Despite the comparison showing a better agreement for the QGSJETII-04, it needs to be mentioned that this model presents more uncertainties on the $\langle \ln A \rangle$ determination by X_{\max} [100, 101].

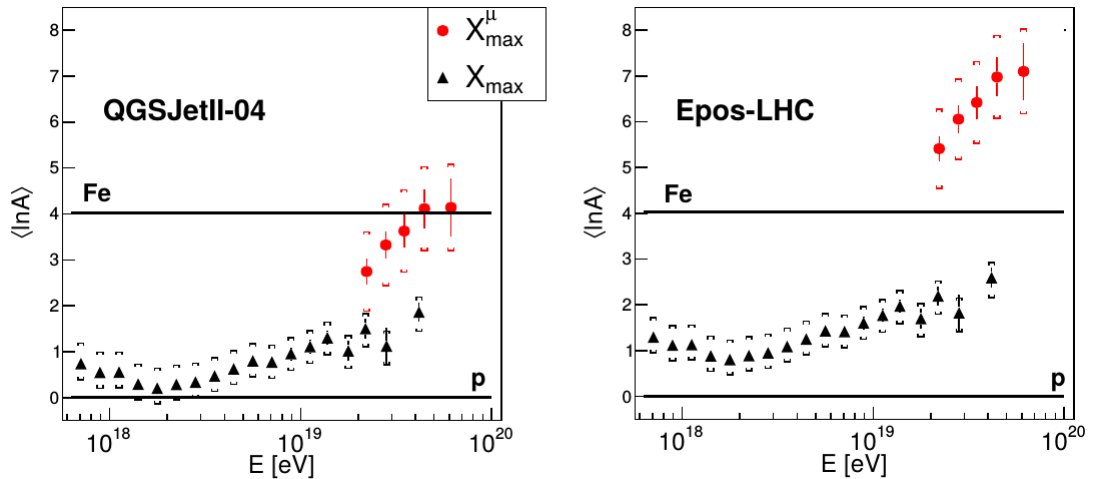


FIGURE 2.24: Results of $\langle \ln A \rangle$ from $\langle X_{\max}^{\mu} \rangle$ and $\langle X_{\max} \rangle$. The hadronic models QGSJETII-04 (left) and EPOS-LHC (right) are used as reference [89].

This study shows that, as the previous one, the muon content is in disagreement with X_{\max} for the current hadronic interaction models. None of the models shows a consistent description of the electromagnetic and muonic showers.

2.7.8.3 Testing Hadronic Interactions

The most recent hadronic interaction models, EPOS-LHC and QGSJETII-04, were tested in a recent analysis to hybrid events from Auger. 411 events were used, with energies between 6 EeV and 16 EeV and zenith angles smaller than 60° [90]. In order to analyse the hadronic interactions, an approach was introduced to remove the sensibility over the absolute energy calibration, which was a parameter of high uncertainty on the muon content determination (described above).

In Figure 2.25, the longitudinal profile (left) and the lateral distribution (right) are shown for a typical event of this analysis. In both graphics, the predictions for showers induced by proton and iron according to QGSJETII-04 are shown. The longitudinal profile for the data matches the theoretical curves but the lateral distribution for the simulated events is, systematically, smaller than the collected one. The description of the criteria used for the production of the simulated events can be found in [90].

The S_{1000} is a reference parameter, used by the Pierre Auger collaboration to characterize the lateral distribution of showers (as described above in section 2.7.4), and accounts for the signal at 1000 m from the shower core. To analyse the discrepancy between the simulation and the data, a new parameter S_{resc} , the rescale simulated S_{1000} , was used.

Two parameters were introduced in this analysis: R_E and R_{had} . The first is the energy rescaling parameter, to allow for a possible shift on the energy calibration from the fluorescence detectors of the Pierre Auger Observatory. The other parameter is a multiplicative rescaling of the hadronic component of the shower.

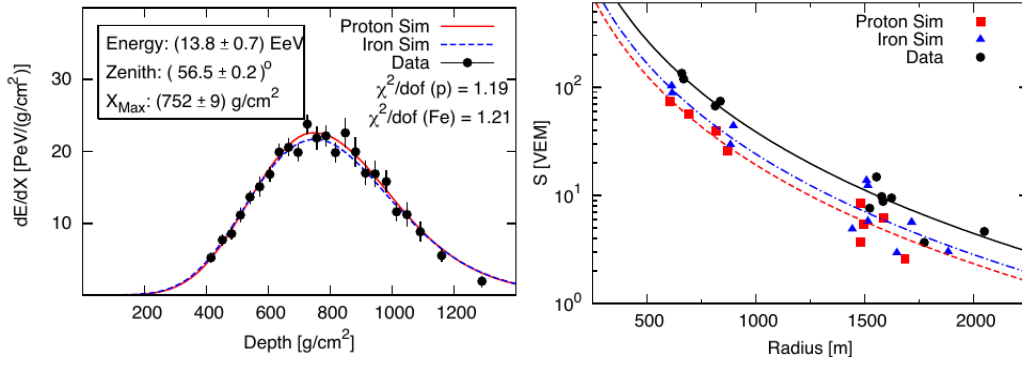


FIGURE 2.25: Left: Measured longitudinal profile and curves for iron and proton simulations with QGSJETII-04. Right: Observed and simulated lateral distribution function for the same events [90].

A given shower i has a certain signal S_{EM} , which accounts for the electromagnetic signal, and a signal S_{had} , for the hadronic part. Considering that the primary has a mass j , S_{resc} can be expressed as:

$$S_{resc}(R_E, R_{had})_{i,j} \equiv R_E S_{EM,i,j} + R_{had} R_E^\alpha S_{had,i,j}. \quad (2.48)$$

Where R_E^α is a factorization parameter for the hadronic signal, since it increases slower than linearly with energy. Most hadronic interaction models assume that $\alpha \sim 0.9$, changing very little with the mass.

The best fit values for R_E and R_{had} were determined through a likelihood

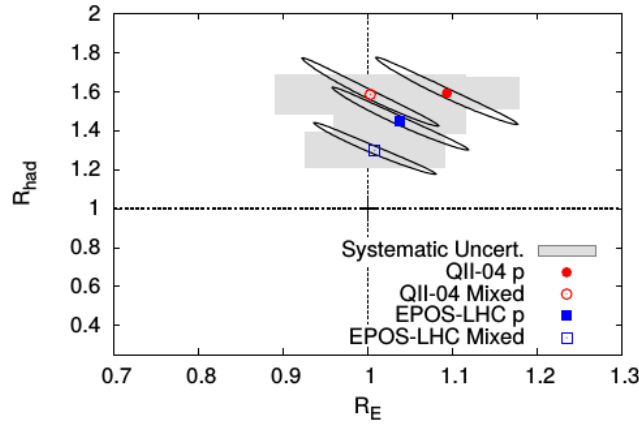


FIGURE 2.26: Best values fitted for R_E and R_{had} with the hadronic models EPOS-LHC and QGSJETII-04, for a pure proton (solid symbols) and mixed composition (open symbols). The grey area represents the systematic uncertainties and the black ellipse gives the area for the 1σ statistical uncertainties [90].

function, using the S_{resc} from the simulated events and the S_{1000} from the data.

The results for R_E and R_{had} are displayed in Figure 2.26. The results of this analysis show that no energy rescaling is needed. It follows also that, on average, a hadronic shower is 1.33 ± 0.16 times larger than the EPOS-LHC prediction and 1.61 ± 0.21 for QGSJETII-04.

2.7.8.4 Implications and Motivation

As discussed in this thesis in different occasions, the mass composition of primary cosmic rays is still unclear at the highest energies. The depth of the shower maximum (X_{\max}) and the number of muons (N_{μ}) are two properties of extensive air showers which depend on the mass and energy of the primary. While X_{\max} is currently obtained by the Pierre Auger Observatory with the fluorescence detectors, the value of N_{μ} has to be inferred from the showers by filtering the electromagnetic component, which carries large uncertainties. The current upgrade of the observatory, AugerPrime, aims to solve this issue.

However, studies to improve the understanding of muons can be already performed with the existing experimental setup of Auger, by having phenomenological analysis in consideration. Recent studies published by the Pierre Auger Collaboration show a disagreement on the muon content between data and simulations produced by hadronic interaction models. The results obtained for X_{\max} and N_{μ} in these analyses show a disagreement on the mass correlation for each parameter. The values of X_{\max} and N_{μ} were used for consistency analyses of the hadronic interaction models, which showed discrepancies on the predictions. In a hypothetical scenario, the hadronic tests made with N_{μ} suggested a mass composition heavier than iron, which, not only is unlikely to the the abundance of elements heavier than iron in the Universe, but is also in disagreement with the predictions from the X_{\max} values.

At the moment, the reason behind the discrepancy between data and simulation on the muon content is still unclear. Either there are features on the hadronic models which are not correct or there is new physics to be understood about hadronic interaction at extremely high energies.

The systematic uncertainties of the muon content are dominated by the absolute energy scale. To decrease these uncertainties is necessary to perform studies with the water Cherenkov stations, mainly to understand its response to muons and how well is its signal described by the simulations.

Chapter 3

Pierre Auger Observatory

“Any device in science is a window on to nature, and each new window contributes to the breadth of our view.” - C. F. Powell

As we have seen in Chapter 1, the knowledge about Cosmic Rays is closely linked to the development of new detectors and on the capacity to combine them to obtain more information. The study of extensive air showers requires the use of several detection techniques, in order to detect as much secondary particles as possible.

In Chapter 2, the state of the research field of Cosmic Rays and the open questions were reviewed. As we have seen, different ranges of energies require the use of different detectors and different configurations, be it balloons, satellites, surface or fluorescence detectors. The use of different detector configurations, for example, the covered area and the different distances between detectors in a surface array, dictates the range of energies where an observatory can operate efficiently. As mentioned in Chapter 1, the KASCADE experiment had a distance between stations of circa 13 meters and covered 0.04 km^2 , resulting in optimal performance for energies above 10^{14} eV and below 10^{17} eV . But for the case of Telescope Array, which is optimized to study the extremely high energies, the distance between the stations is 1.2 km and covers a total of 762 km^2 . The extremely high energies of Cosmic Rays require huge such observatories.

It became very clear in the early 1990s that to answer the questions about the extremely high energies, namely to confirm the existence of the suppression at the GZK threshold and to study the mass composition of such primaries and how they are accelerated, a surface array of detectors that covered an area larger than 1000 km^2 would be needed. Out of this need, at the International Cosmic Rays Conference (ICRC) of 1991, Jim Cronin, from the University of Chicago, and Alan Watson, from the University of Leeds, conceived the idea of the Pierre Auger Observatory, named after the physicist to whom the discovery of extensive air showers was attributed.

The Pierre Auger Observatory is located in the Province of Mendoza, Argentina (see Figure 3.1), in the high plains of the Cuyo region. Currently, it is maintained by a collaboration of 15 countries¹ and has been collecting data in Argentina since 2004 (fully operating since 2008). The observatory was designed to guarantee a high statistic of extremely high energy events.

With more than 1600 water Cherenkov stations, spread over 3000 km^2 , and with four stations for fluorescence measurements the Pierre Auger Observatory is the largest experiment ever build for ultra high energy cosmic rays detection².

Until now, the Auger data allowed to obtain some scientific results (most of

¹Argentina, Australia, Brazil, Czech Republic, France, Germany, Italy, Mexico, Netherlands, Poland, Portugal, Romania, Slovenia, Spain and USA.

²For comparison, Luxembourg has an area of $\sim 2600 \text{ km}^2$.

them were covered in the last Chapter). In 2008, the confirmation of the suppression region was published by the collaboration [102]. The latest results from the X_{\max} , mass composition and arrival directions were exposed in the first sections of Chapter 2. Other studies include measurements of the proton-air cross-sections [103] and upper limits analyses for exotic particles [104].

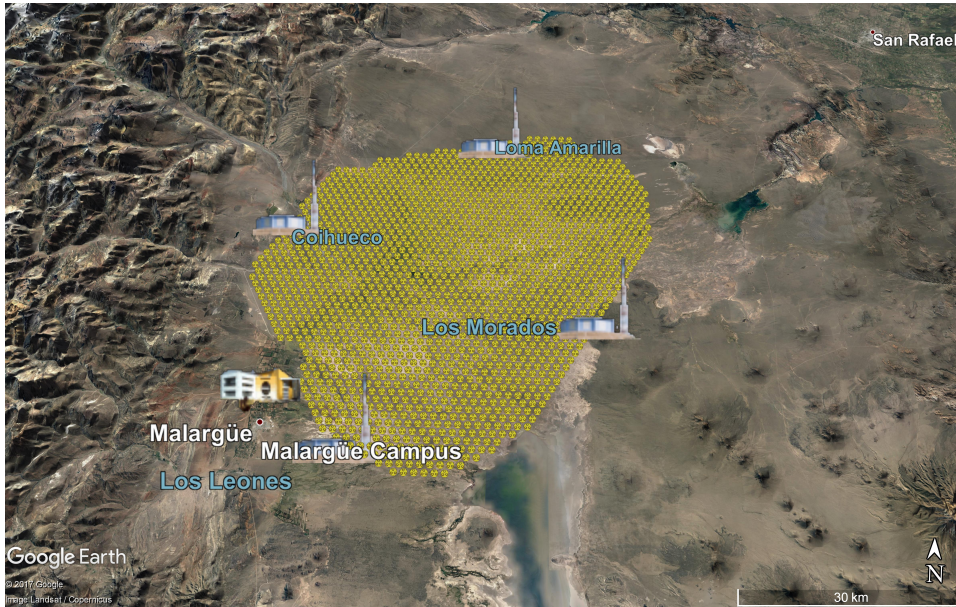


FIGURE 3.1: Google Earth view of the Pierre Auger Observatory. The scale and the north direction are displayed in the right down corner. The Auger Central Campus is located in Malargüe and the yellow points represent the default position of the water Cherenkov stations. The positions of the four fluorescence stations are also marked. The location of the cities of Malargüe and San Rafael can be seen in the left down corner and right upper corner, respectively. Developed by Stéphane Coutu in 2006.

In this Chapter, the surface and fluorescence detectors will be described, including how they operate. Other upgrades or smaller detectors will also be described, as well as MARTA, which was an upgrade proposed for the detection of the muonic component to the observatory with Resistive Chamber Plates (RPCs). RPCs will also be explored and explained later in this Chapter, since they are important for the following analyses in the next Chapters. Notwithstanding, the descriptions in this Chapter will be only a resume of the observatory apparatus, since neither the surface array nor the fluorescence telescopes were used in the analyses performed in this thesis. More details will be given about the water Cherenkov station and its features, in order to help to understand the analysis developed in the following Chapters. More detailed information about the design of the Pierre Auger Observatory can be found in [105].

3.1 Hybrid Design

The key feature of Auger is not only its dimensions but the usage of a hybrid technique to measure air showers. The Fluorescence Detector (FD) and the Surface Detector (SD) allow to perform different measurements from an air shower,

giving a more detailed information about its development. At the moment, only Telescope Array, in the USA, performs similar air shower measurements with a hybrid technique.

Figure 3.2 shows the flat lands of Mendoza with some water Cherenkov stations (on the left) and a fluorescence station (on the right). This region of Argentina was chosen for being a semi-desert, flat and high land. The altitude of the observatory varies from 1340 m to 1610 m, having an average altitude of 1420 m (which gives a crossed atmospheric depth of $\sim 875 \text{ g cm}^{-2}$). This altitude is optimal for analyses of air showers at the extremely high energies, since it is closer to the X_{max} than if it was placed at the sea level, but also low enough to allow for the full development of the shower (see Section 2.7.1). Not only it is a high and flat land, which optimize the analyses by the surface array, but it is also a semi desert area with low light pollution to contaminate the fluorescence light detections.

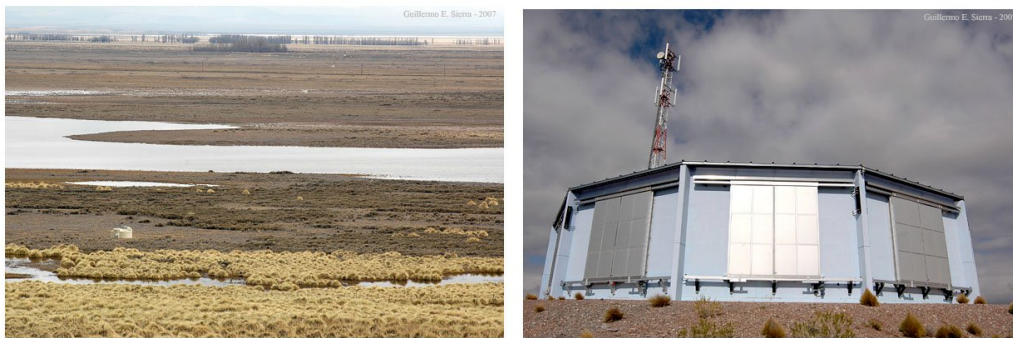


FIGURE 3.2: Left: Water Cherenkov station in high flat lands of the province of Mendoza, near Malargüe. Right: Picture of a fluorescence station of the observatory. The pictures were taken by Guillermo Sierra in 2007 and have public access at the Auger website [106].

3.1.1 Fluorescence Detector

The FD of the Pierre Auger Observatory consists of 24 air fluorescence telescopes, plus 3 additional ones of the HEAT enhancement, with the aim to measure the light emitted by nitrogen in the atmosphere, due to the interaction with charged particles from air showers (see Section 2.7.6.2).

The 24 telescopes are divided into four observation sites - Coihueco, Loma Amarilla, Los Morados and Los Leones - each one with 6 telescopes. The FD stations are located in the periphery of the SD array, pointing to the center of the observatory to assure that, when possible, both, FD and SD, measure the same air shower, in which case are called hybrid events. Each telescope has a field view of $30^\circ \times 30^\circ$. Additionally, in each station there are shutters in order to protect the telescopes, when necessary, from external adverse light or other conditions, and also an antenna for communication with the Central Data Acquisition System (CDAS).

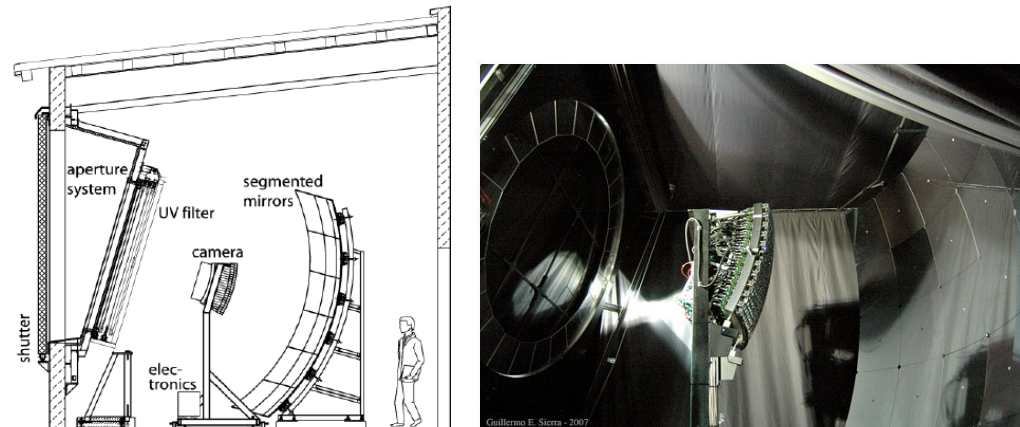


FIGURE 3.3: Left: schematic representation of the components of a telescope from the FD, with a person for scale. Right: picture from inside of one of the telescopes, with the aperture on the left side and the PMTs at the center and the mirrors on the right side [107].

In Figure 3.3, a schematic view and a photo of a telescope are shown. The fluorescence light passes through a corrector optic and a filter before being focused onto a camera by a $3.5 \times 3.5 \text{ m}^2$ segmented mirror. This camera contains 440 hexagonal pixels. Each pixel is a hexagonal XP3062 photomultiplier (built by Photonis) with side length of 40 mm. The corrector optic (or corrector ring) corrects spherical aberration and eliminates coma aberration. The UV bandpass filter transmits in the 280-430 nm band and absorbs visible light, reducing the background light that reaches the camera.

The fluorescence light produced from de-excitation of nitrogen travels through the atmosphere until it reaches the telescopes. This propagation will affect the measured light, so a continuous monitoring of the atmosphere is required to estimate the attenuation. Different measurements are performed, some which are redundant but they give a clear control over the atmospheric parameters necessary to understand the systematic errors present.

Two laser facilities are used to monitor the aerosols and clouds. At the center of the SD array, the CLF and XLF (Central Laser Facility and Extra Laser Facility) are located, which allow for atmospheric control and to monitor the geometrical reconstruction from FD. Each one of the FD facilities has a LIDAR (Laser Detection And Ranging) station which contains a laser and a telescope, which detects the backscattered signal from the laser's emission to the atmosphere, allowing for aerosols control. Other lasers are used, such as the HAM (Horizontal Attenuation Monitor), which measures the aerosol horizontal attenuation, and the APF (Aerosol Phase Function monitor) with the purpose to measure the cross section of the Mie scattering.

Due to being only operational during moonless nights, as well as the atmospheric conditions for clouds and aerosols, the FD has a short duty cycle. Roughly, the fluorescence detector has a duty cycle of only 15%.

The shower reconstruction from the FD is basically determined by analysing the directions from the camera's pixels and the time information. The reconstruction can be obtained with an angular resolution smaller than 1° .

With the data collected from the telescope, a longitudinal profile of the shower can be constructed (explained in Section 2.7.4). From the Gaisser Hillas function,

the X_{\max} value of the shower can be determined with a resolution of $\sim 20 \text{ g cm}^{-2}$. The energy deposited by the shower in the atmosphere can be estimated, with an uncertainty of $\sim 14\%$, by integrating the longitudinal profile.

A detailed description of the optical system, the calibration and the precision of the shower reconstructions of the Fluorescence Detector of Auger can be found in [107].

3.1.2 Surface Detector

The Surface Detector (SD) of the Pierre Auger Observatory is an array of 1660 water Cherenkov stations spread over 3000 km^2 as a triangle grid with 1.5 km as side dimensions. The array achieves full efficiency at energies higher than $3 \times 10^{18} \text{ eV}$.

Each one of the stations that creates the surface array has a water tank equipped with 3 photomultipliers, a GPS for time control and an antenna for communication with the CDAS. Each station is independent of the others and is powered by a battery charged by a solar panel. In Figure 3.4, a water Cherenkov station is displayed with its respective components.

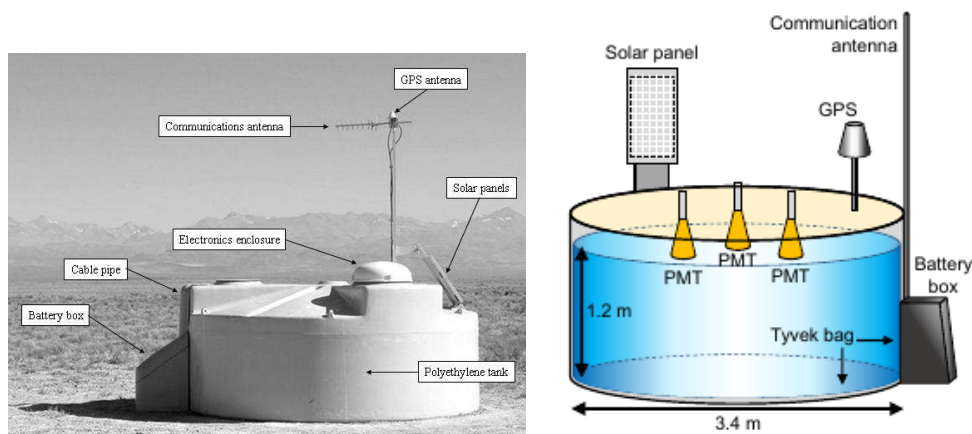


FIGURE 3.4: Water Cherenkov station and the respective components necessary for its autonomous operation [108].

The tanks are constantly bombarded with atmospheric particles which would result in huge amounts of data stored if the collaboration decided to save all the collected information. Most of the times, these particles were not originated from extremely high energy air showers, but from less energetic showers. In order to reduce the data to reasonable amounts, each one of the stations has local triggers, which are sent to the CDAS. For a full data transfer, it is required that at least three stations are triggered in the same time window, in order to achieve a high probability that we are in the presence of an air shower.

Contrary to the FD, the SD does not require special conditions to operate, which means that it has a duty cycle of nearly 100% and would only change if some type of communication failure occurs.

The shower is reconstructed by having the arrival times of the shower and the geographic position of the station in consideration. Combining the distance between stations with the time delays between those stations, it is possible to obtain

the geometry of the shower. After this, the lateral profile of the shower is fitted to a NKG-function (explained in Section 2.7.4) and the energy of the primary can be inferred by comparison of this distribution with simulations.

More information about the Surface Detector can be found in [108].

3.1.2.1 Water Cherenkov Station

The water Cherenkov tank is a cylinder of radius 1.8 m and height 1.2 m and filled with 12000 l of pure water [108]. The Cherenkov light (see Section 2.7.6.1) produced in the water is collected by three PMTs on the top of the tank, symmetrically distributed at a distance of 1.2 m from the center.

When triggered, the stations storage data in the form of electric signals detected by the three PMTs, as a function of time.

The Cherenkov light is reflected at the walls of the tank and well diffused before reaching the photomultipliers tubes. The signal is obtained in ADC but frequently expressed in terms of VEM (Vertical Equivalent Muon), where 1 VEM corresponds to the signal left by a muon crossing vertically the tank at its center. The conversion is obtained by dividing the ADC signal by the muon hump ADC charge in the calibration histograms ($Q_{\text{VEM}}^{\text{peak}}$) and multiplied by a conversion factor. The signal collected from the well diffused light has a linear dependence on the path of the particle inside the tank. I.e., the longer the path, the higher is the charge. The collect signal in VEM is proportional to the number of photons³ in the tank. However, in case of a charged particle crossing the PMT directly (producing Cherenkov light in the glass) or direct Cherenkov light emissions to the PMTs (i.e., no reflections inside the tank) the signal linearity is lost. This particularities will be addressed later.

The design and construction of the surface array of Auger faced several challenges. Besides budget issues, the water Cherenkov tanks had to be designed for a life time of 20 years and to resist the environment conditions, such as variations of temperature, floods or strong winds. The walls of the tank need to isolate the water from external light and to keep it bacteria free as long as the observatory is operational to assure that the Cherenkov light is uniformly diffused in all stations.

In order to address these issues, the tank was lined with five layers: one layer of Carbon black LDPE (low density polyethylene) between two layers of clear LDPE bounded to layer of Dupont Tyvek® 1025-BL by a layer of TiO₂ pigmented in LDPE. The polyethylene layers are opaque and guarantee that no external light enters the tank and the inside layer of Tyvek was chosen because it is a strong material and has an excellent diffuse reflectivity for Cherenkov light near the ultraviolet regime.

3.1.2.2 Photomultipliers

PMTs are detectors with the capability of converting light from a few hundred photons into a current pulse, without adding a large random noise. The outside of the tube is usually glass and serves as pressure boundary to assure that the

³By its turn, the number of photons inside the tank is not only dependent on the path of the particle in water but also on the number of charged particles inside the tank. Therefore, the signal is also proportional to the number of particles inside the tank.

vacuum conditions are maintained inside the tube. A vacuum environment is necessary to allow low energy electrons to be accelerated by the internal electric fields. Inside the tube, there is a photocathode, which is a photosensitive layer, and an electron multiplier structure [109].

Cherenkov photons reach the photocathode and, due to photoelectric effect, electrons are released inside the tube. The electron multiplier structure consists of several electrodes (called dynodes). This structure will amplify the signal by producing more electrons in the electrodes. The charge will then be collected by an anode at the end of the tube. In Figure 3.5, a photography and a schematic drawing of the XP1805 photomultiplier tube used in the water Cherenkov stations.

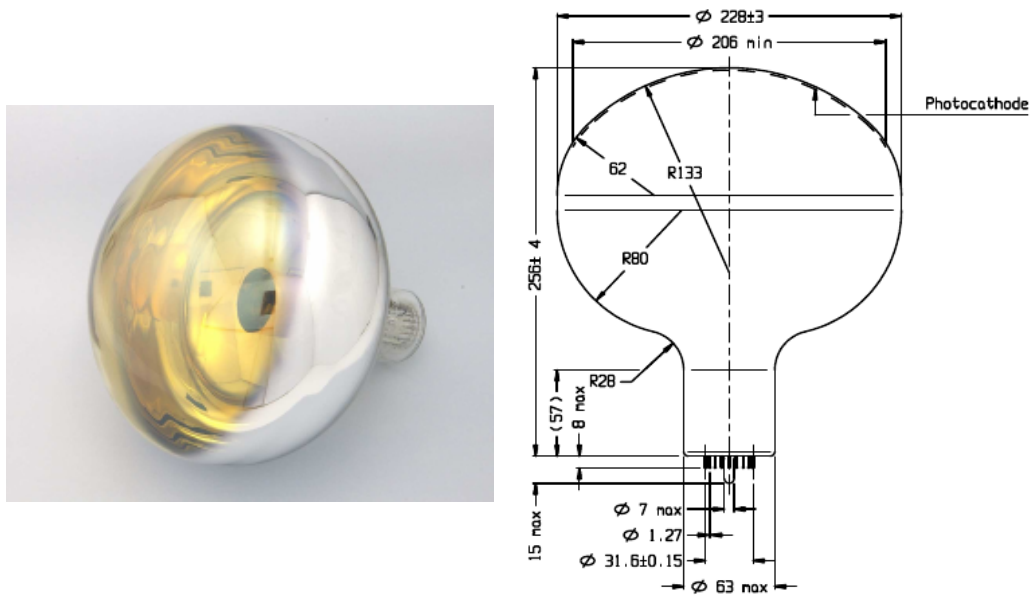


FIGURE 3.5: Photography and schematic drawing of the XP1805 PMT used on the water Cherenkov stations of the Pierre Auger Observatory. The measurements on the right are in mm. These PMTs are produced by Photonis. Pictures taken from HZC Photonis website [110].

3.1.2.3 Direct Cherenkov Effects

The energy measurement performed by the surface array of Auger relies on the linearity between the collected signal and the energy of the particle, since the energy of the primary is proportionally related with the number of particles of the shower. This requires that the light reaching the PMTs is well diffuse, otherwise the linearity will be lost. Particular phenomena can break this linearity by hitting the PMTs with non-diffused light. There are three main issues that can create this situation: intersection of the PMT, direct Cherenkov light to the PMT and semi direct light. The intersection of a PMT is exclusively dependent on the impact point of the particle in the tank. If a charged particle hits one of the PMTs (which has no dependency on the angles of the particle) it will produce Cherenkov light in the glass of the PMT. Direct Cherenkov light occurs when the light hits the PMT without suffering any reflections at the walls of the tank and the last one, semi

direct light, implies that the light have not made enough reflections (in order to be well diffused) before hitting the PMT. These last two cases are dependent on the angles of the particle and on the point of impact in the tank. Studying the angular dependency of semi direct light is a complex analysis but for the case of direct Cherenkov light, one only needs to have the Cherenkov cone in consideration.

We have seen in Section 2.7.6.1 that the Cherenkov angle is emitted is dependent on the refractive index. Inside the water Cherenkov tank, the muons and the electrons emit photons with a maximum angle of $\theta \sim 41.25^\circ$.

In Figure 3.6 a representation of the trajectory of a muon inside the tank is shown. The muon enters the tank with a zenith angle θ_μ and, if it is energetic enough, will emit Cherenkov photons with an angle of θ_C , relative to its path. If the sum of the angles is close to 90° , $(\theta_C + \theta_\mu) \sim 90^\circ$, it becomes very likely that one of the PMTs is hit with direct Cherenkov light.

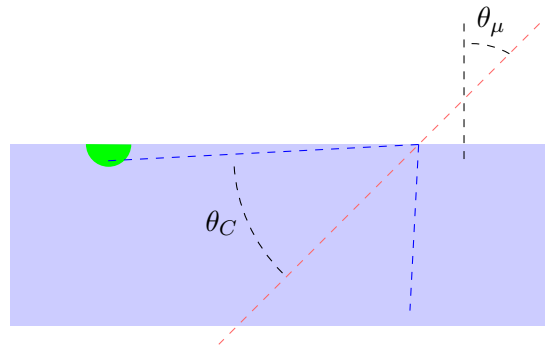


FIGURE 3.6: Schematic representation of the water Cherenkov tank, in blue, and a PMT, in green. A muon (path represented by a red dashed line) hits the tank with a zenith angle of θ_μ . If the muon is energetic enough, it will emit radiation in the form of Cherenkov photons, with an angle θ_C .

Since the Cherenkov angle is always very close to 41.25° , the probability of a PMT being hit, depends exclusively on the geometry of the path of the charged particle. This probability is, therefore, dependent on the intersection point of the muon in the tank and on its azimuthal and zenith angles.

A detail study of the dependencies of the direct and semi direct light on the impact parameters are described in [111], where a parametrization of these effects was also made. It also shows the influence of these effects on the PMT signal. The probability of direct light to the PMTs as a function of the zenith angle can be estimated by a numerical Monte Carlo calculation.

It is expected that the azimuthal distribution of muons is uniform and that all points of the top surface of the tank have an equal probability of being hit, while the zenith is correlated with the muon flux. Furthermore, these three parameters are independent from one another. Following these premises, we can define $P(\theta_\mu)$ as the probability to obtain direct light emission to at least one of the three PMTs.

Particles whose trajectory crosses the PMTs produce a different effect, due to Cherenkov light produced in the glass of the PMT. To avoid having both effects entangled in the determination of the probability P , all the situations where the PMTs are crossed are removed from the calculation. If the particle crosses the tank

close to one of the PMTs, without intersecting them, and with a favourable azimuth, it can produce direct Cherenkov light, even for short zenith angles. However, for the rest of the intersection points, it is required to have a zenith angle large enough such that $\theta_C + \theta_\mu \geq 90$. Therefore, the probability P should increase quickly after the zenith angle of the muon becomes larger than 48° .

By constructing a Monte Carlo simulation, one can determine $P(\theta_\mu)$. For simplicity, it is assumed that the PMT is a perfect semi-sphere with radius 11.39 cm. Several points were generated on the top of the tank, with the azimuthal uniformly distributed, $\phi_\mu \in [0, 360]^\circ$, and a fixed value for the zenith angle, repeating the process for all the possible natural numbers for the zenith, $\{\theta_\mu \in \mathbb{N} | 0^\circ \leq \theta_\mu \leq 90^\circ\}$. By studying the geometry of the path of the particle, it can be determined which ones shall produce direct Cherenkov light, without crossing the PMTs. The total number of events which produce this effect is then divided by the total number of generated events which do not cross the PMTs. By other words, the probability P , is given by the Monte Carlo calculation as a fraction between the events with direct Cherenkov light emission to the PMTs, n_C , and the total number of events, N :

$$P(\theta_\mu) = \frac{n_C}{N}. \quad (3.1)$$

In Figure 3.7 the results for the variation of P with θ_μ are shown. As expected, the value of P increases strongly after the zenith angle becoming larger than 48° , with values higher than 0.5. This means that a muon that hits the tank with an inclination larger than 48° , has a probability close to 60% to emit direct Cherenkov light to one of the PMTs. This result shows how important it is to study direct light emissions in studies of inclined particles, since this effect is very likely to occur and cannot be ignored. This thesis aims to discuss the response of the WSC to inclined muons ($> 60^\circ$). Given their angle, and following this calculation, it is expected that the analyses of inclined muons will include signal on the PMTs from direct effects.

This proceeding can be applied to individual PMTs, allowing to determine the value of P for each one of the PMTs. However, an azimuthal variation in this case, is also expected, due to the PMTs positioning in the tank (if a PMT would be in the center of the tank, no variation would be expected). Therefore, the variation of P with the zenith and azimuth angles were calculated for each PMT. For the first one, the exact same method described above was used. For the azimuth, an analogous method was created. The value of P was calculated for each value of ϕ_μ . As for the zenith angle, a distribution proportional to $\cos^2(\theta) \sin(\theta)$ was used (see Section 4.2.2), with $\theta \in [0, 90]^\circ$. The other steps are exactly the same as for the zenith calculation. In Figure 3.8, the results are shown in terms of $P(\theta_\mu)$ and $P(\phi_\mu)$.

3.2 Enhancements

The Pierre Auger Observatory is fully efficient for energies above 3×10^{18} eV. In order to lower this energy threshold, two new detectors were added to the observatory: HEAT [112] and AMIGA [113]. These two detectors allow to study air showers above 10^{17} eV, which is an important region to study (due to the transition from cosmic rays with galactic to extra-galactic source).

HEAT (short for High Elevation Auger Telescope) combines three telescopes located nearby the FD station Coihueco. The special feature of this telescope is

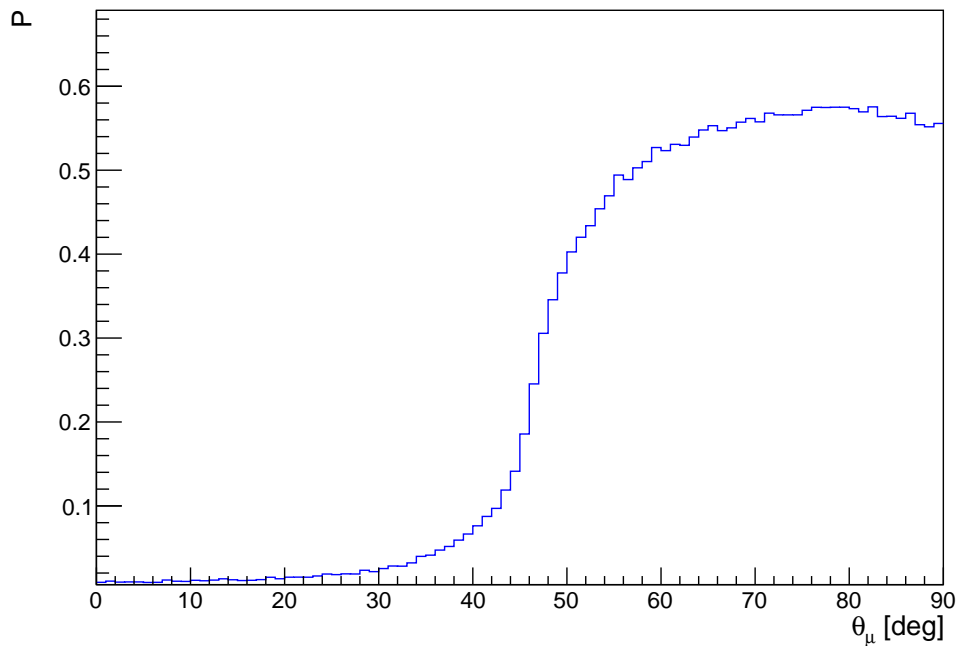


FIGURE 3.7: MC calculation. It represents the dependence of the probability of at least one of the three PMTs being hit with direct Cherenkov light as function of the zenith angle. The non-zero fraction below the critical angle results from particles which cross the tank close to a PMT (without intersecting it). A 1000000 points were simulated on the top of the tank for each integer number of θ_μ .

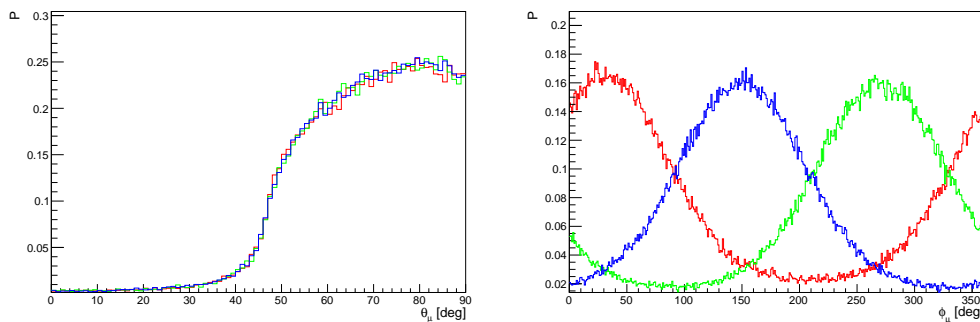


FIGURE 3.8: On the left: variation of the probability of having direct Cherenkov light emission for each PMT, P , with the zenith angle of the muons. On the right: variation of P for each PMT with the azimuth.

their elevation. Their field-of-view in the Vertical goes from 30° to nearly 60° . This allows the telescope to look higher in the atmosphere and collect fluorescence light from lower energy showers which reach their maximum upper in the atmosphere.

These telescopes overlook an infill array called AMIGA (Auger Muon Infill for the Ground Array). This array consists of 61 water Cherenkov stations combined with underground scintillators to measure the muonic component. Each station is at distance of 750 m to each other (comparing with the 1.5 km of the SD

array), in an area of approximately 25 km².

Another addition to the observatory is AERA [114] (Auger Engineering Radio Array) which is an antenna system to measure radio emissions from high energy air showers. Several antennas are continuously operating in the field and sensitive to the frequencies between 30 to 80 MHz.

3.3 AugerPrime

AugerPrime is the observatory's upgrade to respond to the need of obtaining a more accurate measurement of the muonic component of air showers. The idea behind this upgrade is to place two plastic scintillator models, of ~ 2 m² each, on the top of the existing 1660 water Cherenkov detectors. The Collaboration will have access to measurements of the showers independent from the water Cherenkov detectors. This will allow for a comparison of both signals. Particularly, the amplitude and time distributions of these signals will be different. This occurs because, while both detectors will be crossed by all types of particles, the scintillators will be dominated by the electrons, while the WCD will be dominated by muons and photons. The analysis to the signals will allow to obtain further information, particularly a more precise measure of the muonic component.

A photography and a schematic drawing of the AugerPrime setup are represented in Figure 3.9. The full design report of this new upgrade can be found in [115]. It is planned that all scintillators will be assembled on the top of the tanks by 2018.

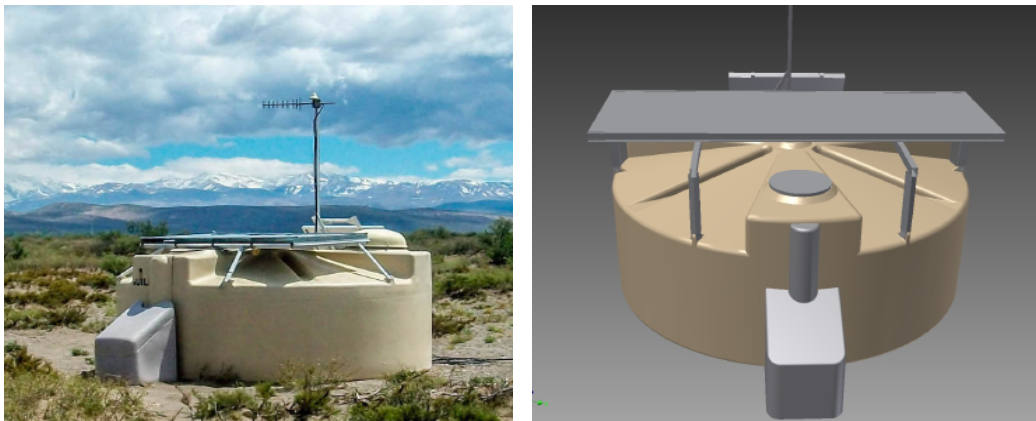


FIGURE 3.9: Picture and schematic representation of a water Cherenkov station with a scintillator detector at its top [115].

3.4 The MARTA Project

MARTA (Muon Array RPC for the Tank Array) was an upgrade proposal to the Surface Detector of Auger. The idea consisted in using four Resistive Plate Chamber under the Cherenkov station to measure the muon component in air

showers, by using the water of the tank as a shield for the electromagnetic component [116].

This proposal was not selected as the main upgrade to the observatory but some stations from the surface array will be equipped according to this design for complementary studies, in particular, due to the fast response and space resolution of the RPCs. Additionally, the RPCs are still used as a tool to study the response of the water Cherenkov tank to muons, as has been done with a test tank that we shall address in the following Chapters.

3.4.1 Resistive Plate Chambers

Developed in the 1980s by R. Santonico and R. Cardarelli [117, 118], the Resistive Plate Chambers are gas detectors for charged particles, with capacity for achieving high time accuracy and efficiency. RPCs are built by layers of gas separated by resistive plates which maintain an intense and uniform electric field.

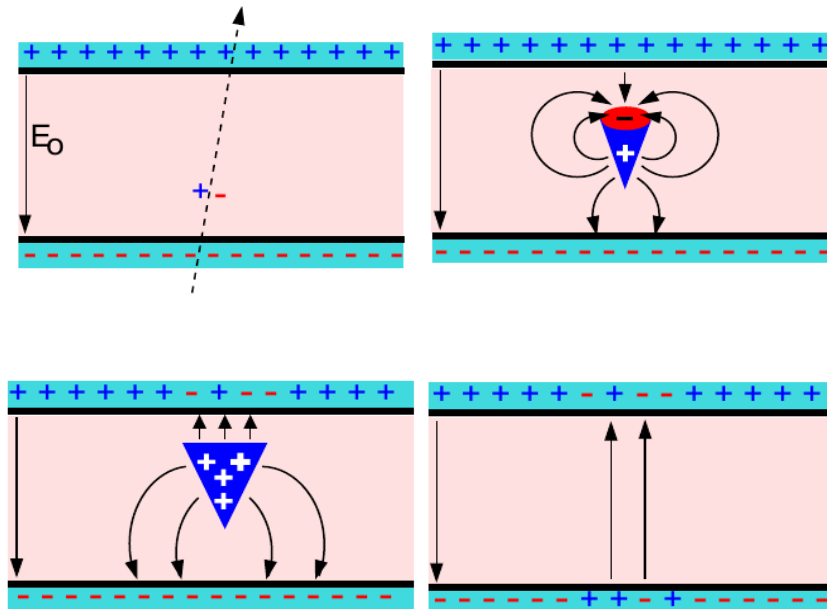


FIGURE 3.10: Particle detection by a RPC. The development being in the top left picture with the passage of a charged particle (dashed line) which provokes the ionization of the gas. The electrons will move in the opposite direction of the electric field E_0 (picture top right) while the positive ions will move in the direction of the electric field. The electrons will reach the anode (bottom left) before the ions reach the cathode (bottom right). When the electrons reach the anode, it will produce deformations in the electric field which can be measured and will confirm that a particle crossed the plates. After a few hundreds picoseconds the gas and the electric field will return to the initial stage [119].

Like other gas detectors, the functional principle of RPCs is the gas ionization (provoked by charged particles) which will then induce a signal in the electrode. This process is represented in Figure 3.10 and lasts a few hundreds picoseconds, making RPCs fast detectors. A review of the functioning of the RPCs can be found

in [120, 121].

RPCs are used in several experiments of Particle and Astroparticle Physics, such as muon trigger in LHC experiments [122]. Since they are built in small segments (called pads) and have a good time resolution, RPCs are good detectors for space and time tracking of particles.

In the test tank, RPCs are used as a hodoscope for tracking muons and infer their trajectory. This will be addressed later in this thesis, including a monitoring analysis of the used RPCs.

Chapter 4

Experimental Setup

“Many applications of the coincidence method will therefore be found in the large field of nuclear physics, and we can say without exaggeration that the method is one of the essential tools of the modern nuclear physicist.” - Walther Bothe

The Gianni Navarra¹ test tank is located at the Malargue central campus, disconnected from the surface array, but identical in construction. This test tank has been used for studies about the calibration and the response to muons of the water Cherenkov detectors.

By disposing detectors through a surface, close enough to each other, and having their time window in account, we can obtain coincidences. Thereby, several particles can be measured with different detectors, which are separated from each other, like it happens with the SD of the Pierre Auger Observatory, and, therefore, to detect extensive air showers. But instead of having a grid alignment, the detectors can also be orientated to each other, in a way that they can be used to have a perception of the track of the particle that crossed them.

By using two RPCs, one can make use of the coincidence technique to obtain information about the path of the particle. It is possible to obtain the angles of the particles (zenith and azimuth), the track length of the particle in the tank, the intersection points in the tank (both, when it enters and when it exits) and to determine analytically the intersections with the PMTs or direct Cherenkov-light emissions to them.

A picture of this test tank is shown in Figure 4.1, with one of the RPCs visible at the top.

This Chapter aims to discuss the principles of RPC hodoscope, in order to set the conditions for a new data acquisition. The electronics of this experiment will be briefly described, as well as the motivations for the studies about the response of the tank.

An important feature of the analyses is the production of simulations that include the RPC hodoscope. These were performed with the Offline Framework of the Pierre Auger Collaboration and will be explained, including the properties of the atmospheric muons and the description of the RPC’s simulation.

Until now, two main studies were performed with the test tank. One focusing on the response of the WCD to angle between 20° and 50° and the other focusing on the VEM calibration. Both will be briefly described, for a better understanding of the RPC hodoscope functioning and goals.

At last, the motivations for a new acquisition to inclined muons will be exposed. The geometry selected for the new analysis will be described, together with a discussion of the importance of having precise measurements and of the used reference frames. Other important parameters, such as the acquisition time

¹Named after the Italian physicist Gianni Navarra, which led the EAS-TOP group.

required to collect enough data, will also be addressed.



FIGURE 4.1: Picture of the experimental setup of Gianni Navarra in Malargue, Argentina. The large cylinder is the water Cherenkov station and the box on the top is one of the RPCs (the other one is not visible in this picture, since is located under the tank).

4.1 RPC Hodoscope

The RPC hodoscope was placed at the test tank in the context of the works of the MARTA project (see Section 3.4 and [123]). The tank has been used for studies of the WCD's response as a function of the trajectory of the traversing particles.

The analyses of the response of the tank to muons follow the need to have a better understanding of the tank's reaction to single muons and how well do the simulations describe it, which is fundamental to have a good estimative of the muon content of extensive air showers. Additionally, some studies in the collaboration raised the possibility of ageing effects (see, for example, [124]) adulterating the reflectivity of the liner of the tank or the attenuation length in water, which would impact the light propagation inside the tank.

The experimental setup consists of a water Cherenkov tank equipped with two RPCs, which were described in Section 3.1.2.1 and Section 3.4.1, respectively. A lateral schematic view is shown in Figure 4.2, representing a single muon (dashed red line) crossing the RPCs and the tank, allowing to reconstruct its trajectory by determining several geometric parameters: angles, impact point and track length inside the tank.

An analysis with the hodoscope is dependent on the combination of the data between the two RPCs and the three PMTs from the tank. To perform such data combination, one needs to store the data from the tank and from the RPCs and then to combine them.

The data acquisition (DAQ) system of this experimental setup has two different components: from the water Cherenkov station and from the RPCs. The DAQ of the tank is the standard used by the water Cherenkov stations but, instead of being connected to the CDAS (Central Data Acquisition System), the tank is directly linked by a serial cable to the console of the SDE (Surface Detector

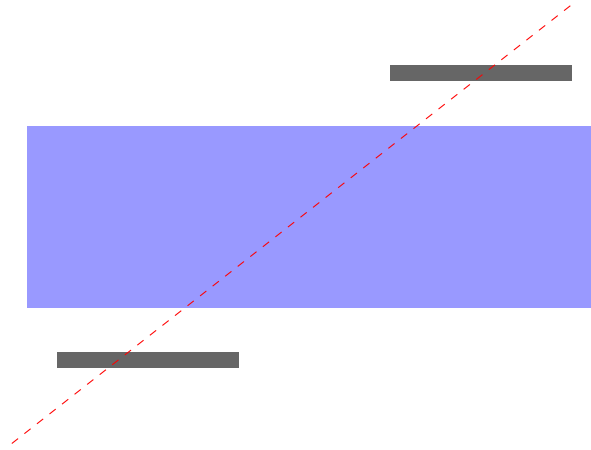


FIGURE 4.2: Lateral view of the experimental setup configuration. The blue rectangle represents the tank, while the grey ones represent the RPCs. The dashed red line represents the muon trajectory.

Electronics) microprocessor.

The hodoscope electronics consist of a discrete electronics systems developed for the readouts of the RPCs and uses front-end boards and one motherboard. Each front-end board has eight channels, one for each pad in a row. Each channel will amplify the signal induced in the pad and then the signal is converted to an 1-bit digitization by applying a threshold. The signal is then sent to the motherboard, which is responsible for managing the triggers, the signal and the time.

4.1.1 Triggers

The setup of the RPC hodoscope is configured to analyse single muons which cross the WCD and the RPCs. Since the setup uses a RPC hodoscope and its goal is to obtain single hits on both RPCs, it is natural to use them to trigger the data storage. The triggers could, however, also be given by the tank. Notwithstanding there are two main reasons to oppose this choice.

A single muon, travelling at the speed of light, needs ~ 10 ns to cross the complete setup. A tank-based trigger, however, has a delay of the order of ~ 800 ns, due to delays on the light generation, propagation in water and collection, from the response of the PMTs and then from the delay in the SDE electronics. This would require to extract the information from the RPC signals prior to the trigger signal.

Moreover, the RPCs represent an area lower than 10% of the tank area, which means that a sample collected with a tank-based trigger would be dominated by events that have not crossed the hodoscope.

Therefore, a hodoscope-based trigger suits this configuration better. A trigger is then generated when at least one hit on both RPCs is detected, within a time window of 100 ns. Given the positioning of the RPCs, the vast majority of the events when using a hodoscope-based trigger will produce signal in all detectors.

A detailed description of the DAQ and the trigger systems of this setup can be found in [125, 126].

4.2 Simulation of Atmospheric Particles

As it was mentioned before, simulations are a fundamental tool for cosmic rays studies, given how complex it would be to analyse the information analytically. The simulations of the Pierre Auger Collaboration are produced with the Offline Software Framework, which is optimized to analyse air showers. The analyses with the hodoscope, however, are performed with data collected from atmospheric muons, which is then used to study the response of the WCD.

This requires to have in account two new features: atmospheric muons and the simulation of the RPCs. A simulation of the RPC hodoscope needs to have in consideration the flux and angular dependencies of the atmospheric muons and to reproduce the conditions at which the data collection was performed, such as the geometric positioning of the detectors and their efficiencies.

The simulations will then be compared with the data and from it, it will be inferred how similar the results and how trustworthy are the simulations.

To clarify the structure of the simulations and to explain the differences between showers and atmospheric muons, a discussion about the Offline Software Framework, the atmospheric muons and the simulation of the RPCs will follow.

4.2.1 Offline Software Framework

The Offline Software Framework is a software framework developed by the Pierre Auger collaboration for air shower studies, such as event simulation and reconstruction.

The software is constituted by three main parts, outlined in Figure 4.3: processing modules which can be assembled and sequenced by instructions written in XML files; an event data structure which is used by the models to deliver data to one another and that accumulates reconstruction and simulation information; and a detector description which gives descriptions of the atmospheric conditions as a function of time and the performance of the observatory [127].

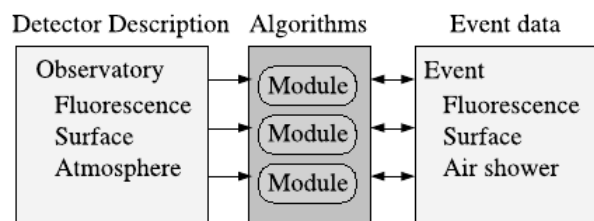


FIGURE 4.3: Representation of the main structures of the Offline Software Framework [127].

4.2.2 Atmospheric Muons

Earth is constantly bombarded with primary cosmic rays, from all directions and with different energies (as discussed in Chapter 2). This implies that there is a constant flux of particles reaching the surface, especially muons since their angular dependency to reach the surface is smaller, since they interact less with matter when compared, for example, with electrons. This creates a flux of atmospheric muons, which can be used for several studies of cosmic rays or even for

detector calibrations or other studies related to detectors.

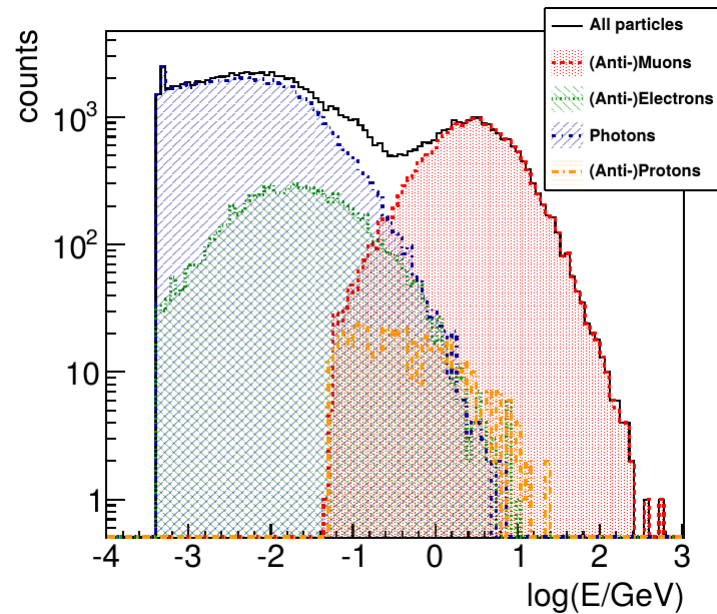


FIGURE 4.4: Energy distribution for atmospheric particles at Pierre Auger Observatory used to produced the simulation [125].

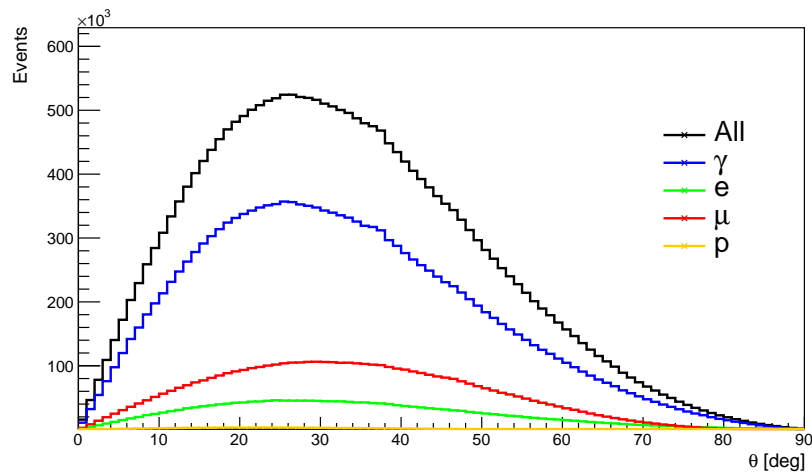


FIGURE 4.5: Zenith distribution of the flux of atmospheric particles used in the simulation.

A file was created to be used as particle injector for the simulations. Figures 4.4 and 4.5 show, respectively, the energy distribution for atmospheric particles and their zenith angle dependency used to create this file [125]. The energy distribution for muons ranges from hundreds of MeV to hundreds of GeV. The average energy for muons at the sea level is 4 GeV. Muons result from decays of charged pions and kaons (mostly pions) at an height of about 15 km (in relation to the sea level) and have an energy around 6 GeV. After crossing the atmosphere, which has a depth of around 1000 g cm^{-2} , the muons lose $\sim 2 \text{ GeV}$, given an energy loss

for muons of $2 \text{ MeV per g cm}^{-2}$ [18, 36].

The flux of muons has a zenith angle dependency which is proportional to $\cos^n(\theta)$. Recent analysis [128] to the muon flux implied that $n = 2.00 \pm 0.04(\text{stat.})$. To complement the flux dependency it is necessary to address the solid angle, resulting in an additional dependency with $\sin(\theta)$. A good approach to the flux of muons is then $\cos^2(\theta) \sin(\theta)$.

Since the flux of muons is constant and muons barely interact with matter (until decaying into electrons), they are an optimal particle to the analysis of the response of a detector.

4.2.3 Detector Simulation

To complete the structure necessary to simulate the hodoscope setup, it was also required to implement a module to simulate the RPCs. A full description of the detector simulation can be found in [125].

The passage of particles through the RPCs and the water Cherenkov station is simulated using Geant4. The tank simulation was already included but the RPCs had to be implemented, setting its functioning, dimensions, pad segmentation, position and orientation related to the tank.

The signal in the RPC was parametrized by measurements made at LIP Coimbra. The probability of observing a charge x is described by the gamma function:

$$G(x; \alpha, \beta) = \frac{\beta^\alpha}{\Gamma(\alpha)} x^{\alpha-1} e^{-\beta x}, \quad (4.1)$$

where $\alpha \equiv \alpha(\theta)$ is a shape parameter and $\beta \equiv \beta(\theta)$ is the inverse of a scale parameter. The parameter θ is the angle between the particle trajectory with the plane perpendicular to the RPC surface. More inclined angles have a higher probability for producing a signal, since the particle will cross a longer distance inside the pad segment of the RPC. The particle is only detected by the RPC if the charge produced in the detector is higher than the chosen threshold (2.75 pC, chosen to obtain a 90% efficiency in the RPCs, for particles crossing with a zenith angle of 38°).

4.3 Previous Analyses

Understanding the response of a detector is essential to reduce systematic uncertainties in the measurements. As we have seen, to perform such studies, the Gianni Navarra test tank has a RPC hodoscope, which triggers the storage of events and allows to control the particle's trajectory. The collected data can then be compared to a simulation with the same geometric parameters to analyse how compatible they are with each other.

Some studies were already performed with this hodoscope, namely to the response of the WCD to single muons in a certain zenith angle range and to the VEM calibration of the PMTs.

In these two different analyses, which will be briefly described below, the zenith angles below 13° (VEM calibration [129]) and between 20° and 55° (first results [125]) were covered. In both cases, the linearity between the charge and the track length of the particles was study and the data and simulation results were compared. Neither of the analysis found a significant disagreement between data

and simulation. In both analyses, this comparison showed that, for the angles at study, the Offline Software Framework produces a trustworthy simulation, with a maximum deviation of $\sim 3\%$.

4.3.1 First Results

The first analysis performed with the RPC hodoscope is very similar to the one that this thesis aims to describe. While in the context of this thesis, we aim to study the response of the water Cherenkov detector to inclined muons ($> 60^\circ$), these first studies covered smaller angles [125], more precisely, with a zenith angle range spawned between 20° and 55° .

From the RPC positioning, the particles' track length in water, L , was lim-

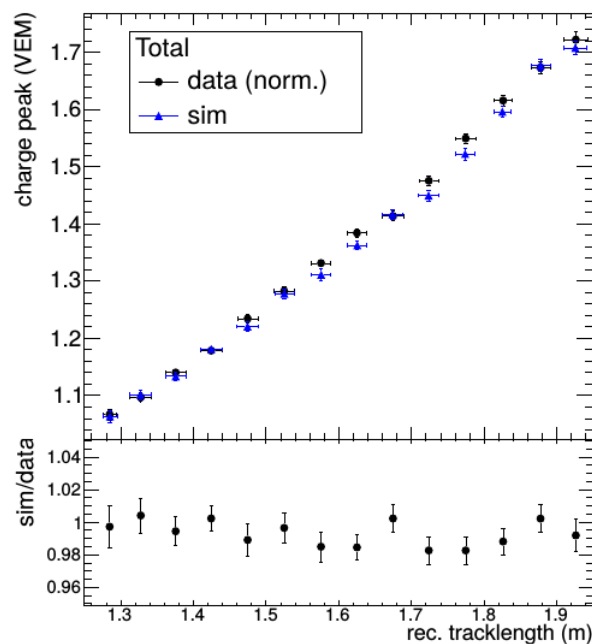


FIGURE 4.6: Results of the total charge peak variation with the reconstructed track length for the data and for the respective simulation for muons with a zenith distribution within $[20^\circ, 55^\circ]$ [125].

ited between $[1.25, 1.95]$ m. It is expected that the charge signal is proportional to the track length of the particles in water. As discussed in Section 3.1.2.3, longer track lengths imply higher charge detected by the PMTs, since more Cherenkov photons are emitted. This linearity between charge and the length of the particle's path on the tank was studied and confirmed by the data and the respective simulation. A similar analysis will later be performed to inclined muons and explained in detail in Chapter 6. The results for the total charge peak² as a function of the track length can be consulted in Figure 4.6.

The results obtained from the analysis of the data show that the charge distribution has a linear correlation with the track length of the muons in water. The same correlation was observed in the simulation produced with the Offline Framework. A maximum deviation of $\sim 2\%$ was found between the acquired

²Sum of all the PMTs signals.

data and the simulation, either for the sum of the PMT signals and for each individual PMT signal.

4.3.2 VEM Calibration

The second analysis performed at the test tank was made to nearly vertical muons, with $\theta \in [0, 13]^\circ$ [129].

The main goal of this analysis was to study the VEM calibration of the water Cherenkov detector. Measurements of muons which crossed the tank as close as possible to vertical angles (with vertical being $\theta = 0^\circ$) and as near the center of the tank as possible were studied. Since the analysis was based on nearly vertical muons, the track length of the particles was close to the height of the tank, such as $L \sim 1.2$ m.

In Figure 4.7 the variation of the total charge peak with the distance to the center of the tank is shown for the analysis of nearly vertical muons.

As one can see in Figure 4.7, the differences between the simulation produced

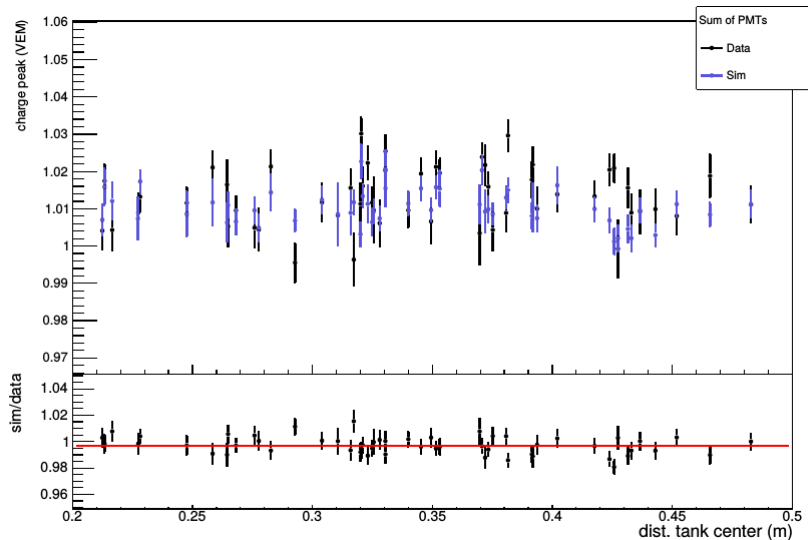


FIGURE 4.7: Variation of the total charge peak (sum of all PMTs) with the distance to the center of the tank for nearly vertical muons [129].

by the Offline Framework and the data are, on average, smaller than 1%. These results show that the simulation describes well the response of the tank to muons for the geometrical configuration used in this study. Additionally, the analysis to the VEM calibration to the PMT average charge, PMT sum charge and PMT average peak agree with the original calibration experiments (within uncertainties). This result leads to conclude that no possible ageing effect is adulterating the VEM calibration (for the particular case of the Gianni Navarra tank).

4.4 New Acquisition

So far, the studies with the RPC hodoscope were performed to single muons with zenith angles smaller than 55° , and showed an agreement between data and

simulation. From a complementary point of view, it comes naturally the need to increase the studies to inclined muons. But there are more motivations for the importance of studying the response of the WCD to inclined muons.

As discussed in the end of Chapter 2, in Section 2.7.8, an excess of muons was found in data, in relation to the simulations, for analysis of hybrid events of Auger with zenith angles larger than 60° . The analysis, however, had large uncertainties associated, namely systematic uncertainties arriving from the uncertainty of the response of the tank to inclined muons. This uncertainty was based on studies about the response of the WCD to inclined angles, with discrepancies between data and simulation up to 10% [95].

A problem which is also more frequent at these angles is direct light effects, as was explained and calculated in Section 3.1.2.3. The light reaches the PMT is not well diffused, which will produce higher signals on the PMTs.

A new acquisition to muons with zenith angles higher than 60° is then needed to study how well the simulation reproduces the response of the WCD, and to analyse the consequential uncertainties, to reduce the systematic uncertainties in measurements of muon content at these angles. As explained, the muon content at angles higher than 60° assumes a greater importance due to the electromagnetic absorption in the atmosphere. This implies that measurements at the surface of showers with this inclination detect mostly to muons, allowing for a more precise study of this component of the showers.

To reach such angles with the RPC hodoscope, the bottom RPC was shifted to the side of the tank and inclined. This new setup was implemented in the Offline Software Framework and a schematic drawing, obtained by the viewer of Offline, is shown in Figure 4.8. In the following sections, the geometry of the new setup will be described and an explanation of how one can estimate the acquisition time is provided. It is also addressed why these two points are important for the analysis that will follow.

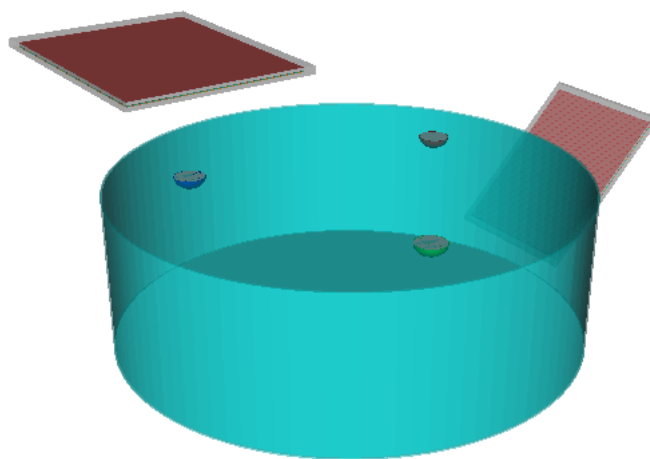


FIGURE 4.8: Three-dimensional representation of the experimental setup configuration for the inclined muons analysis.

4.4.1 Geometric Description

By imposing that a particle crosses both RPC it becomes possible to access the trajectory of the measured particle, through determining its direction, which is very important for this study. But, to do so, it is crucial to have a precise measurement of the position of the RPCs and the distance between them and to the tank. Also, precise measurements about the geometry of the configuration were required in order to have correct values of the angles. These parameters will be used as inputs for Monte Carlo simulations, for the Offline Software and also used to determine the path of the particles in water needed for the analysis. It is then crucial to understand the geometry of the setup and to assure the precision of the measurements to be applied in the different parts of the analysis.

To represent the configuration, there are three different reference frames, that were created for previous analyses: Theodolite, Offline and a reference frame presented in an internal GAP note of the Pierre Auger Observatory, further referred to as "GAP-2015-033". The first is a referential where measurements were taken with a theodolite, the second is the referential implemented in Offline Framework and the latter was used in the fist report note of the Gianni Navarra test tank.

In all frames, the bottom of the tank is placed on the xy -plane and the center of the tank is aligned with the intersection of the x - and y -axes, $(0, 0, 0.6)$ m. The differences between the reference frames are related to which PMT crosses the y -axis, as it is illustrated in Figures 4.9, 4.10 and 4.11, which represent a top view of each referential. In table 4.1 the rotation angles, over the z -axis, required to change from one referential to the other are expressed.

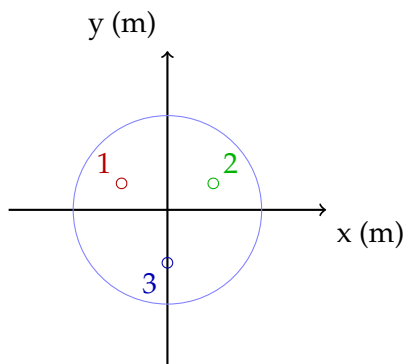


FIGURE 4.9:
Theodolite referential.

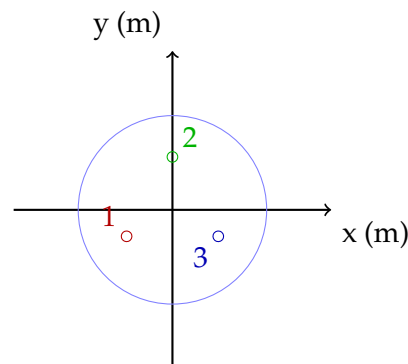


FIGURE 4.10:
GAP-2015-033 referential.

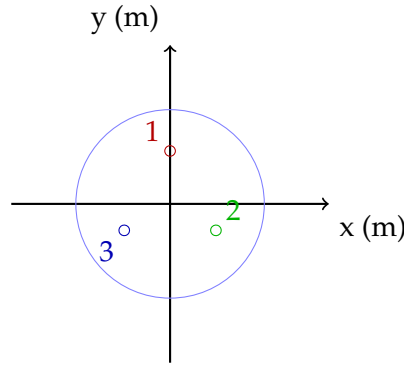


FIGURE 4.11: Offline referential.

TABLE 4.1: Rotation angles to change between the different referential. (Consult horizontally. For example, to go from the Offline referential to Theodolite, one must rotate 60° over the z axis).

	Theodolite	Offline	GAP-2015-033
Theodolite	-	-60°	60°
Offline	60°	-	120°
GAP-2015-033	-60°	-120°	-

Despite having three reference frames, the relative distances between the detectors do not change. The tank, at the middle for all frames, has cylinder shape with a height of 1.2 m and a diameter of 3.6 m. The top RPC is 1.17 m above the top of the tank, while the bottom one is at the tank's side, and the distance to the tank varies from 0.51 m to 1.84 m, due to its inclination. Given this geometric configuration, the muons will exit the tank from the lateral side, which are commonly called clipping muons.

In order to find the correct coordinates for each RPC in any available referential, we must first clarify the geometry of the RPCs. The RPCs used at Gianni Navarra have dimensions of $1.285 \times 1.65 \text{ m}^2$. Each one is segmented in a matrix of 8×8 pads of size $0.14 \times 0.18 \text{ m}^2$. Each pad is separated from the others, vertically and horizontally, by 0.01 m wide guard-rings. In Figure 4.12 a schematic representation of a RPC is shown, with the 64 pads and the border segments. The red dot represents the center of the active area of the RPC, which is the reference parameter to determine the coordinates of the RPC. The measurements were performed with a theodolite, which measured the RPCs positions relatively to the tank, returned the center of the RPCs (in this referential) and the angles of inclination and rotation.

TABLE 4.2: Dimensions of the segments of the RPC, defined in Figure 4.12.

	L	R	B	T	d	a	b	ξ	κ
Size [m]	0.055	0.04	0.11	0.03	0.01	0.18	0.14	1.285	1.65

For RPC one, its center, the rotation over the z axis (related to its center) and the inclination were measured. The RPC above the tank is parallel to the tank and the to xy-plane, which means it has no inclination. The other RPC has an inclination (related to the xy-plane, the surface) of 45.9° . The centers of each RPC

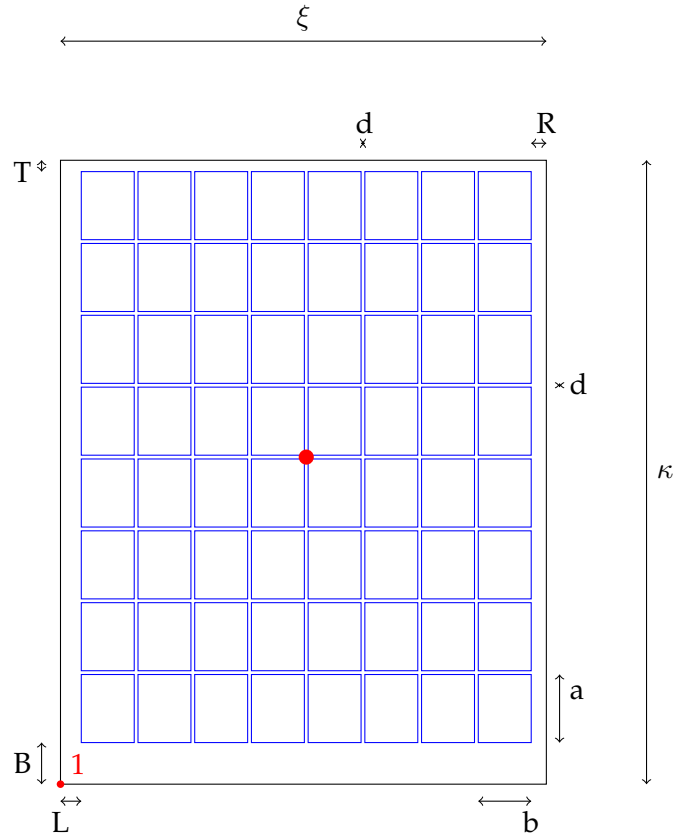


FIGURE 4.12: Graphic representation of a RPC. Each RPC, $\xi \times \kappa \text{ m}^2$, contains 64 pads, distributed in a 8×8 matrix. Each pad (of dimensions $a \times b$) is separated from each other, vertically and horizontally, by d . L , R , B and T represent the borders. Those are sections of the RPC without pads (non active space). The dimensions of each segment can be seen in Table 4.2. The red dot in the center represents the center of the active area of the RPC. The number 1 represents the Corner 1, also used as reference.

are given in the Theodolite referential and we need to perform a rotation over the z -axis to move to a different referential. Since the RPCs' sides are not aligned with the axes, also the rotation (over z) that each RPC has in relation to its center has been measured. This is summarized in Table 4.3.

TABLE 4.3: Measured values for center of the RPC (in Theodolite referential), the rotation angle for the each RPC (over its center) and the inclination angle relatively to the xy -plane. The rotation angles are defined in Figure 4.13.

	Center of the RPC [m]	Rotation Angle (z-axis)	Inclination
Top	(0.89, -1.17, 2.37)	$\phi_t = 70.3^\circ$	$\varphi_t = 0^\circ$
Bottom	(-2.46, 1.79, 0.39)	$\phi_b = 68.2^\circ$	$\varphi_b = 45.9^\circ$

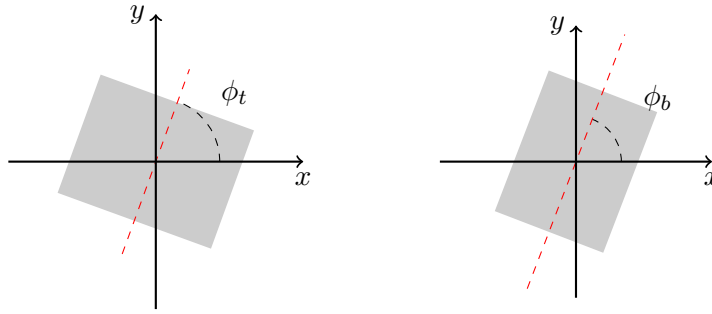


FIGURE 4.13: Definition of the top (left) and bottom (right) RPCs rotation over the z -axis. The smaller side of the top RPC is parallel to the x -axis before being rotated by an angle of ϕ_t . While in the bottom RPC the longer side is parallel to the x -axis before being rotated by an angle of ϕ_b .

We pretend to determine the coordinates for the RPC in the Offline referential. To start, one must impose a rotation over the z axis of -60° to the center point. The equation 4.2 gives the new coordinates, according to a rotation $\theta = -60^\circ$ over z of the coordinates of the Theodolite referential. The coordinates for the center of the RPCs in the Offline referential are expressed on table 4.4.

$$\begin{cases} x' = x \cos(\theta) - y \sin(\theta) \\ y' = x \sin(\theta) + y \cos(\theta) \\ z' = z \end{cases} \quad (4.2)$$

TABLE 4.4: Coordinates for the center of the RPCs, in the Offline referential.

Center of the RPC [m]	
Top	(-0.57, -1.37, 2.37)
Bottom	(0.32, 3.02, 0.39)

To obtain any point of the RPCs, such as its limits or the center of a specific pad, we need to determine the distance of that point to the center of the RPC. We note that, in the top RPC, the longer side is aligned with the y -axis and the shorter with the x -axis in the Offline referential. We determine the variation in x and y from the center to the selected point, defined as Δx and Δy , respectively, and then we impose a rotation (over the z -axis) of 70.3° to obtain the correct coordinates in the Offline referential frame. For example, for the Corner 1 (see figure 4.12) we have: $\Delta x = -(4b + 3.5d + L)$ and $\Delta y = -(4a + 3.5d + B)$. After imposing a rotation by ϕ_t we obtain the values for $\Delta x'$ and $\Delta y'$, i.e.:

$$\begin{cases} \Delta x' = \Delta x \cos(\phi_t) - \Delta y \sin(\phi_t) \\ \Delta y' = \Delta x \sin(\phi_t) + \Delta y \cos(\phi_t) \end{cases} \quad (4.3)$$

For the bottom RPC, we note that the longer side is aligned with the x -axis and the shorter with the y -axis. If we consider that the bottom RPC is parallel to the xy -plane (placed at the same z as its center), we can determine the distance to the Corner 1 by $\Delta x = -(4a + 3.5d + B)$ and $\Delta y = 4b + 3.5d + L$. However, this RPC does not have only a rotation over z in relation to its center, but also an

inclination of 45.9° , over y , in relation to one of its shorter sides (represented as ξ in Figure 4.12), which needs to be done first. It follows that,

$$\begin{cases} \Delta x' = \Delta x \cos(\varphi_b) \\ \Delta y' = \Delta y \\ \Delta z' = -\Delta x \sin(\varphi_b) \end{cases} \quad (4.4)$$

Now, one must do a rotation of the variations $\Delta x'$ and $\Delta y'$, over z , of 68.2° to obtain the correct value for the corner 1 coordinates of the RPC bottom, in the Offline referential. I.e.,

$$\begin{cases} \Delta x'' = \Delta x' \cos(\phi_b) - \Delta y' \sin(\phi_b) \\ \Delta y'' = \Delta x' \sin(\phi_b) + \Delta y' \cos(\phi_b) \\ \Delta z'' = \Delta z' \end{cases} \quad (4.5)$$

In Table 4.5, the values for the four corners of each RPC are represented in the Offline referential. Figure 4.14, both RPCs and the tank are illustrated from the top view. In each RPC, the pads in trigger mode selected for the acquisition are represented by red dots: 9 at the top and 6 at the bottom one. The blue dots represent the intersections of the muons with the top of the tank. The exit points of the particles from the tank are represented in Figure 4.15, by the red dots.

The collected data will then result from muons which crossed a pad in trigger mode at the top RPC and a pad in the bottom one. There are 54 pads combinations available for muons' trajectories. From this, a zenith angle for particles between 62° and 68° is expected.

TABLE 4.5: Coordinates of each corner for both RPC, in the Offline referential. The Corner 1 is represented in Figure 4.12, the others were randomly chosen.

	Corner 1 [m]	Corner 2 [m]	Corner 3 [m]	Corner 4 [m]
Top	(-1.16, -0.45, 2.37)	(0.39, -1.01, 2.37)	(-1.59, -1.66, 2.37)	(-0.04, -2.22, 2.37)
Bottom	(1.11, 3.47, 0.96)	(0.61, 2.23, 0.96)	(0.07, 3.88, -0.19)	(-0.43, 2.65, -0.19)

4.4.2 Acquisition Time Estimative

In order to increase the control over the performance of the acquisition and, therefore, having a better knowledge about the data we are collecting, we estimate the acquisition time. This estimative is important because it allows us to have a perception of the required time to collect enough data to study. Choosing an arbitrary number could result in lack of data to perform the studies or could give us so much data that it would not make any difference if we have less statistic. Since the tank is needed for other studies and it wastes resources while operating, we have to calculate a decent estimate of the acquisition time, so we do not have too less statistics neither much more than the required for the analysis.

To estimate the acquisition time we need to have the setup geometry in consideration. There are two RPC available and we want to obtain coincidences of atmospheric muons between them. The probability of having a coincidence depends on the muons' zenith-angle distribution, and on the positions of the RPCs.

For the new acquisition we plan to study inclined angles. We used as reference a pack of data collected in the end of May 2015 with a range of angles from

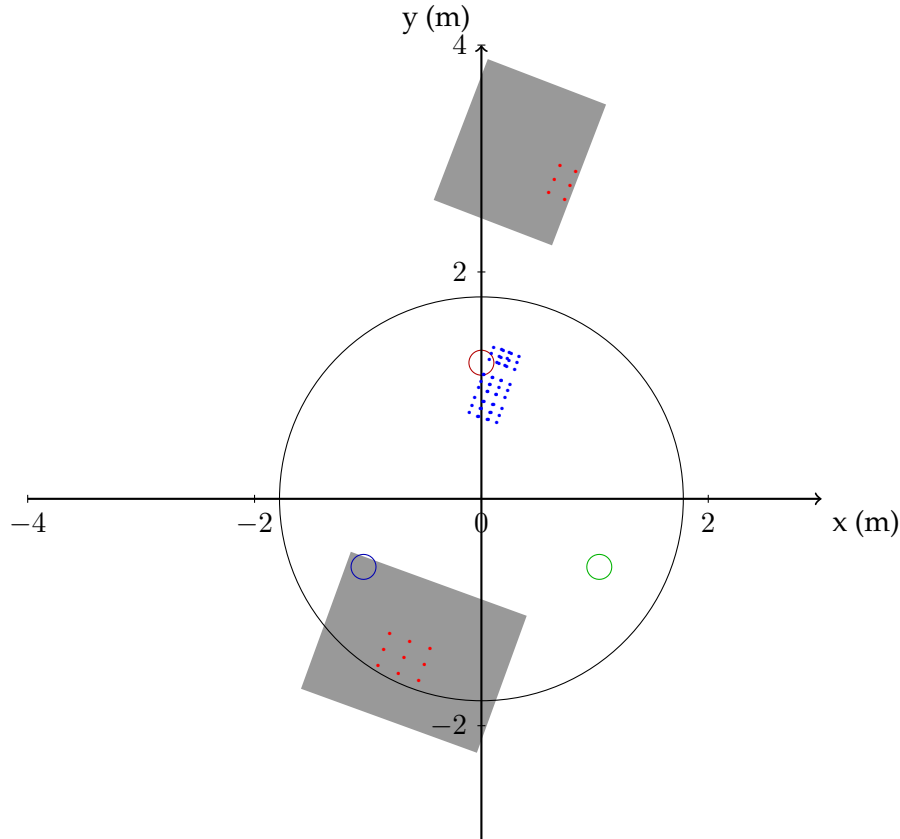


FIGURE 4.14: Top view of the test tank configuration for the study of higher angles ($> 50^\circ$). The PMTs are represented inside the tank accordingly to the Offline referential. The red dots over the grey areas mark the center of the used pads. At the upper side, the bottom RPC is drawn, with 6 active pads. At the lower of the picture, the top RPC is shown, with 9 active pads. The blue dots represent the intersections with the top surface of the tank ($9 \times 6 = 54$).

around 50 to 70 degrees, which is the same range that is wanted for the new acquisition. To obtain such angles, these data were obtained with the bottom RPC inclined $\sim 45^\circ$ but the inclination the of other RPC was not changed, so that is parallel to the ground. Having this configuration in consideration, a semi-analytical Monte Carlo simulation was developed to calculate a geometric efficiency.

To estimate the geometric efficiency $\varepsilon_{geometric}$, also called geometric acceptance, we pretend to calculate, from all particles that cross one pad of the top RPC, how many will cross a specific pad of the bottom RPC. Let i and j represent a pad of the bottom and top RPCs, respectively, such that $\varepsilon_{geometric}^{ij}$ is the fraction value for the coincidences between the pad i and the pad j . $\varepsilon_{geometric}^{ij}$ will represent the probability of the muon crossing pad i , knowing that it also crossed the pad j .

To do this, random points were generated in a pad from the top RPC and azimuth and zenith angles were associated to each point. A distribution in zenith proportional to $\cos^2(\theta) \sin(\theta)$ was considered to simulate the atmospheric flux of muons and the azimuthal angles were uniformly distributed over 2π . Then, having the angles in account and by geometric calculation (intersection of a line and a plane, in Appendix C), the fraction that reaches a pad in the bottom RPC was determined.

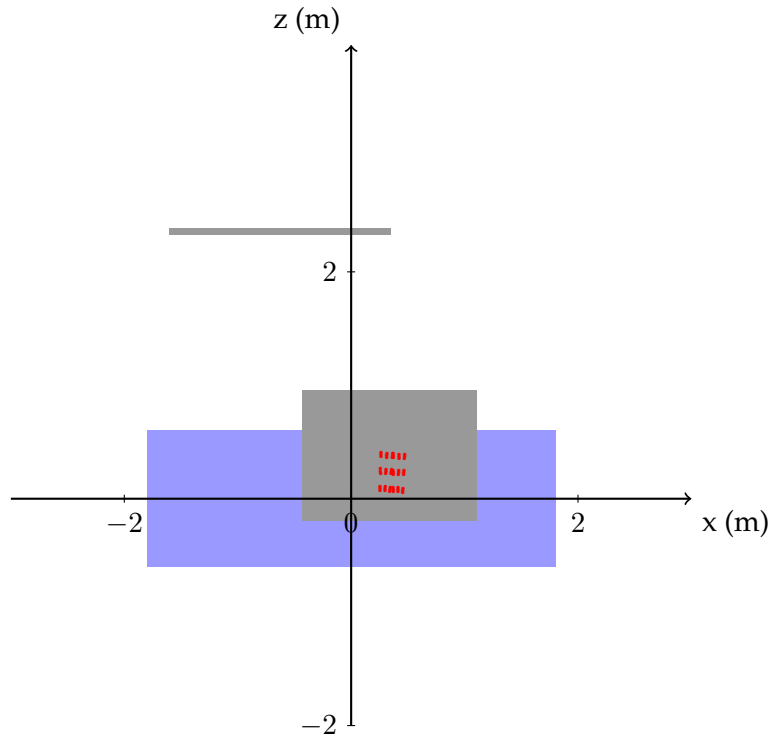


FIGURE 4.15: Lateral view over the RPC hodoscope. The tank is represented by the blue rectangle and the RPC by the grey ones. The red points represent the exit points of the particles from the tank.

Now, this calculation can be used to determine the fraction of coincidences for the RPCs.

$$\varepsilon_{geometric} = \sum_{i=1}^{N_b} \sum_{j=1}^{N_t} \varepsilon_{geometric}^{ij} \quad (4.6)$$

Where N_t and N_b give respect to the number of pads in trigger mode in each RPC (top and bottom, respectively). For this setup, $N_t = 9$ and $N_b = 6$, as referred above.

The hodoscope total efficiency also depends on the intrinsic efficiency of each RPC. We considered that both RPC have the same value and we attribute to them 85% of intrinsic efficiency, since it is a typical value for the RPC's efficiency, as we will see in the next Chapter. It follows that,

$$\begin{aligned} \varepsilon_{hodoscope} &= \sum_{i=1}^{N_b} \sum_{j=1}^{N_t} \varepsilon_{geometric}^{ij} \times \varepsilon_{RPC}^i \times \varepsilon_{RPC}^j \\ &= \varepsilon_{geometric} \times \varepsilon_{RPC}^2 \end{aligned} \quad (4.7)$$

To obtain an estimated rate of triggers that should occur in this setup configuration, one must have into account the rate of atmospheric muons in one pad, f_μ , which was estimated to be 6 Hz [123].

$$f_{trigger} = \varepsilon_{hodoscope} \times f_\mu \quad (4.8)$$

To perform the analysis, we pretend to collect events that trigger both RPCs and leave a trail inside the tank. From all the events that trigger the RPCs, roughly

only 40% of the events are available due to the alignment between the detectors, $\varepsilon_{alignment}$. Since the RPCs and the WCD have different time responses, the number of events will be different. By aligning the events from each detectors, through an analysis of their time, several events of the RPCs will be lost, since they are much faster than the WCD. From these, in general, 50% of the events end up being excluded, ε_{cut} , due to different types of cuts that are made in order to have clear events to analyse. This means that only $\sim 20\%$ of the events that trigger the RPCs will be used for the analysis. Therefore,

$$f_{acquisition} = f_{trigger} \times \varepsilon_{alignment} \times \varepsilon_{cut} \quad (4.9)$$

This estimative gives a rate of ~ 0.01 Hz, which would give more than 25000 events to analyse after one month.

Chapter 5

Data Acquisition and Monitoring

“Observation, reason, and experiment make up what we call the scientific method.” - Richard Feynman

Once the test tank and the RPCs were in their correct position and operational, the data collection was initiated. To assure that the analysis will be performed to single muons, it is necessary to monitor the quality and stability of the acquired data.

The experimental setup is complex and each detector gives different information. The water Cherenkov detector operates in a similar way as the ones from the SD of Auger. Then it has to assured that the tank is storing the PMTs data, and their respective calibration, correctly, so that it can be later analysed. The RPC hodoscope plays a fundamental role to filter the charged particles that reach the tank. It allows to have a sample of muons limited to a certain geometric range (inclined muons, in this case). Therefore, assuring that the behaviour of each RPC is under normal conditions is crucial for the quality of this study, in particular since, as mentioned before, the triggers are given by these detectors.

Moreover, the exposed location of the RPCs, especially the top one, makes external conditions more likely. This will result on the time variation of the RPCs response and requires a selection of stable data acquisition time.

Thus, this Chapter aims to discuss the procedure used for the monitoring of the data collected by each detector. It is explained how the data was monitored during the acquisition and how each parameter and its variation with time were analysed. Each RPC will be scrutinized to assure that the acquisition is stable and the data is reliable, so that it is possible to proceed to its analysis.

5.1 Monitoring Data

A set of functions was developed in C for ROOT [130] to monitor the acquisition and the data collected by the RPC hodoscope and the test tank.

A frequent verification of the data storage from the PMTs and of the variation of several RPC's monitored parameters is necessary to assure that the setup is collecting the data correctly and that it is stable over time to allow to perform a good analysis. This verification requires, for example, to analyse the stability of the PMTs calibration or the background variation of each RPC's pad, to guarantee that some background noise (from electronics) is not influencing the results. Frequently monitoring of both RPCs and the three PMTs of the tank is then essential in this setup, so that a set of functions to automate the process has been developed.

This set of functions allows to study the acquired data and its behaviour with time. It is then possible to have a simplified diagnosis of the data and to perform an almost real-time monitoring of the acquisition.

In the case of one of the detector is not working as it should, a frequent verification will allow to detected the malfunctioning quickly and solve it, which would not be possible to do if the data was only checked after its full acquisition. A periodic check control will guarantee that the data is as stable as possible, without, for example, long periods of background noise domination at the RPCs.

The monitoring analysis also includes calculating the rates for measured events, estimating the signal on the RPCs due to atmospheric muons and the rate due to random coincidences.

Additionally, the monitored parameter of the RPCs (temperature, pressure, current, relative humidity and applied voltage) can be used to have a deeper knowledge about their efficiency. With these parameters it is possible to calculate the reduced electric field (on each RPC) which is correlated with their efficiency.

The developed functions were used daily to monitor the stability of the data. The explanation that follows illustrates a random and stable period of acquisition to show which parameters were used, and how much they could vary.

The setup has a complex configuration, since there are two resistive plate chambers and three photomultiplier tubes. The focus is on events which provoke a single hit on each RPC and are detected by the PMTs. However, given the triggers of the setup and the external conditions, such as temperature variation and background due to electronics, the storage of data is not always constant. This requires to verify several parameters to assure the quality of the data sample.

From the tank, the acquired data is similar to a water Cherenkov station of the SD. The ADC traces from the PMTs and the calibration histograms are the types of data available. Calibration histograms are recorded every 50 minutes and used to convert the signal from ADC to VEM, as explain in Section 3.1.2.1. An example of a calibration histogram is displayed in Figure 5.1. A fit is adjusted to the second peak of the histogram and the obtained value is the muon hump charge used for the conversion. A detail description of this fitting process can be found in [131].

Figure 5.2 shows the muon hump charge of the calibration histograms, Q_{VEM}^{peak} , for all three PMTs for a certain time of acquisition. This period of acquisition is very stable, since there are no failures of data storage and the variations are very smooth and small. Discrepancies between PMTs might be caused by small differences in their gain.

From the RPCs, the data informs about the pad segment which was triggered and at which time. In time intervals of fifteen minutes, the acquisition is stopped to measure the background rates, which refer to the stability of each pad. These rates are obtained by counting the number of hits in a pad over 10 seconds. With these values it is possible to evaluate the status (dead, noisy or valid) of each one of the pads. A pad is considered dead if no signal is detected. When a pad registers a rate over 1000 Hz, it is considered noisy and becomes inactive until it registers a background below this threshold in the measurements to follow. This high noise rate can occur due to electronics noise in the pads or in the DAQ chain. During this period of inactivation, the pad is not considered for data acquisition. For a stable sample of events, it is important to assure that the pads are active during most of the acquisition time.

Due to technical restrictions, only 9 pads were available for the top RPC and only 6 for the other one (red points in Figure 4.14). In Figure 5.3, the number of active pads in each RPC is shown (bottom figure) and, for the same period, the mean value for the background rates (top figure). With the exception of a few

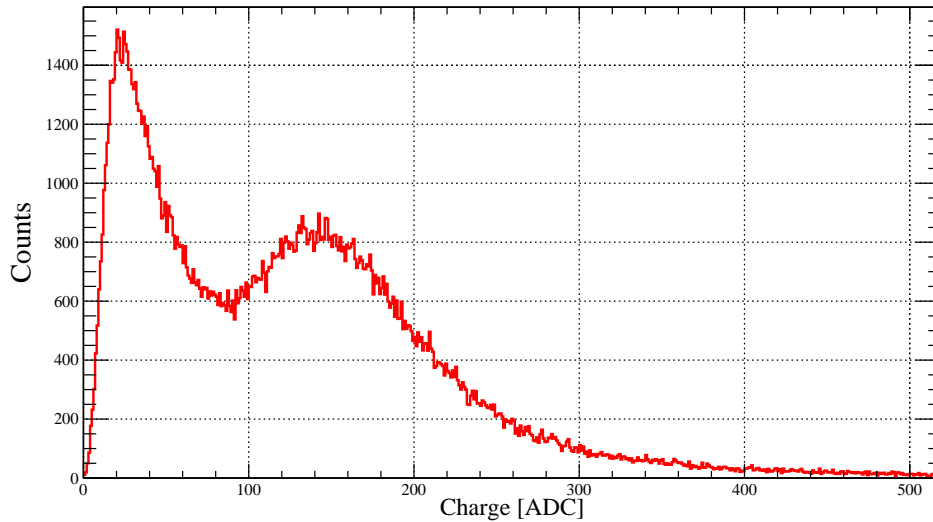


FIGURE 5.1: Example of a calibration histogram.

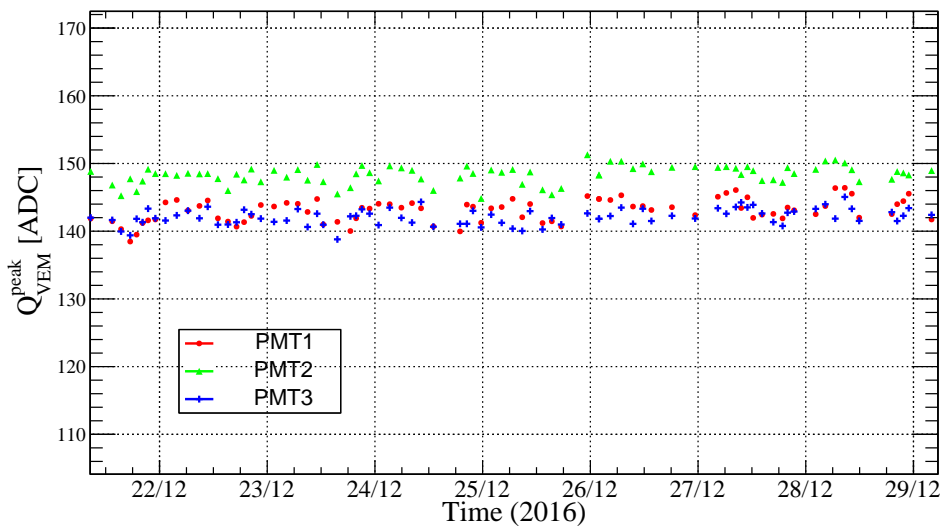


FIGURE 5.2: Calibration values of the PMTs 1,2 and 3 during a week of data acquisition tank.

peaks in the background levels, the values are stable and low, with all the pads active for those periods. In the last Chapter, it was mentioned that the muon rate at a pad of the RPC should be around 6 Hz. Notwithstanding, the background rates are determined by counting the number of hits, be them provoked by muons, electrons or detector/electronic noise.

In both graphics of Figure 5.3, the top RPC shows more variations than the bottom one. This will be later explored in detail but it is important to mention that, contrary to the bottom RPC, the top one has been constantly placed above the tank, which made it more exposed to external factors (like weather conditions). Even if in this setup none of them is completely shielded by the tank, the top one still remains more exposed, since the bottom RPC is placed at the side and inclined, which might produce some shielding from background effects.

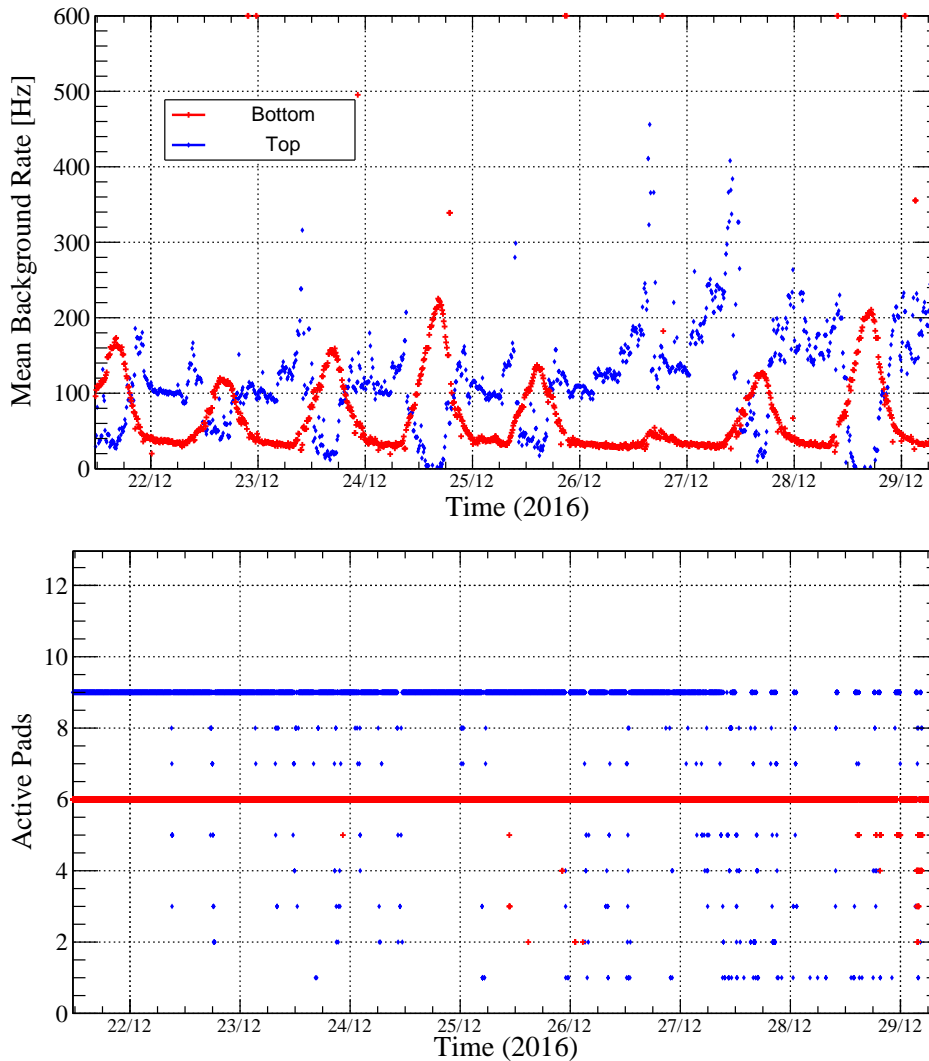


FIGURE 5.3: Up: Mean values for the background rates of the top and bottom RPCs. Down: Number of active pads for both RPCs, from a total of 9 at the top and 6 at the bottom RPC, for the same period of acquisition.

Despite the values being low, there are still peaks which need to be understood. The bottom RPC shows oscillations of the mean background rate related to the hours of more solar exposition, as it is expected since a rise of the temperature provoke an increase of the background, as we will see later in this Chapter. The top RPC requires a more detail analysis in order to be fully explained. At first sight, it might be perceived that the RPCs show an anti-correlation, which is not the case. The night hours are the most stable hours for both detectors. Since it is more exposed, the mean values for the top RPC will be higher. When the temperature rises with the daily hours, the background in the bottom RPC firmly increases and then falls when the temperature also falls. This increase is also found in the top RPC, with a tight peak that is followed by a fast fall to nearly zero. This could be explained by a loss of efficiency of the top RPC.

5.2 RPC Monitoring and Analysis

A deeper analysis of the RPCs behaviour can be performed in order to understand the variations observed in Figure 5.3. The RPC has five constantly monitored parameters: current I [nA], applied voltage HV [V], pressure P [mbar], relative humidity [%] and temperature T [°C], which are stored each minute. The current is one of the most important parameters to monitor and accounts for the sum of several currents: ionization currents (provoked by the charged particles in the gas) and leakage currents. The HV is an applied voltage to the RPC, which is adjusted each 5 minutes to compensate the variations of temperature and pressure, in order to stabilize the efficiency of the RPCs.

The variations of these parameters can be compared with the background variations in order to understand them. In Figures 5.4 and 5.5, the variations as a function of time for these monitoring parameters¹ are shown for the same time period used above. Each point in these graphics shows the average value of the parameters in 15 minutes (i.e., between measurements of the background rates).

The variation of the temperature inside the RPCs is, as one would expect, associated with the solar exposition and with the wide amplitude of daily thermal variations in Malargue. The other parameters vary at the same time, as one can compare in Figures 5.4 and 5.5. The variations on the pressure are very small and the variations on the applied voltage are introduced, as mentioned above, to counter the variations of temperature and pressure.

The reduced electric field is a parameter correlated with the efficiency of the RPC. By determining its variation with time, which can be done with the monitored parameters of the RPC, we can understand the efficiency variations of these detectors. This is discussed by *L. Lopes et al* [132], in their article from 2014 about this type of detectors. The reduced electric field, $\frac{E}{N}$, is expressed in Townsend [Td] or $V \cdot m^2$, and can be determined by:

$$\frac{E}{N} = \kappa \cdot \frac{V_{\text{eff}} \times T_K}{d \times P}. \quad (5.1)$$

In this equation, κ is a constant, T_K is the temperature but has to be converted from Celsius to Kelvin, V_{eff} is the effective potential difference across the gas gap and d is the gap thickness. The effective potential can be calculated by using the applied voltage (HV) and the current (I), that is:

$$V_{\text{eff}} = HV - R_{cm^2} \cdot I_{cm^2} \quad (5.2)$$

We can determine the values of R_{cm^2} and I_{cm^2} knowing the geometric parameters of the RPCs and the temperature. The variable R_{cm^2} is the resistance per square centimetre seen by the current and can be determined with the volume resistivity $\rho(T)$ and expressed as a function of the temperature (in Celsius):

$$R_{cm^2}(T) = \rho(T) \times t \times l \quad (5.3)$$

Where $\rho(T) = 10.5 \times 10^{12} \times 10^{\frac{20-T}{24.3}} \Omega \text{ cm}^{-1}$, t is the amount of glass plates and l is the glass thickness. As for I_{cm^2} , it was determined by dividing the measured current I by the RPC area in cm^2 , A_{RPC} .

By this, the equation 5.1 can be rearranged as:

¹The relative humidity is not included in this analysis because it is not expected to affect the performance of the RPCs.

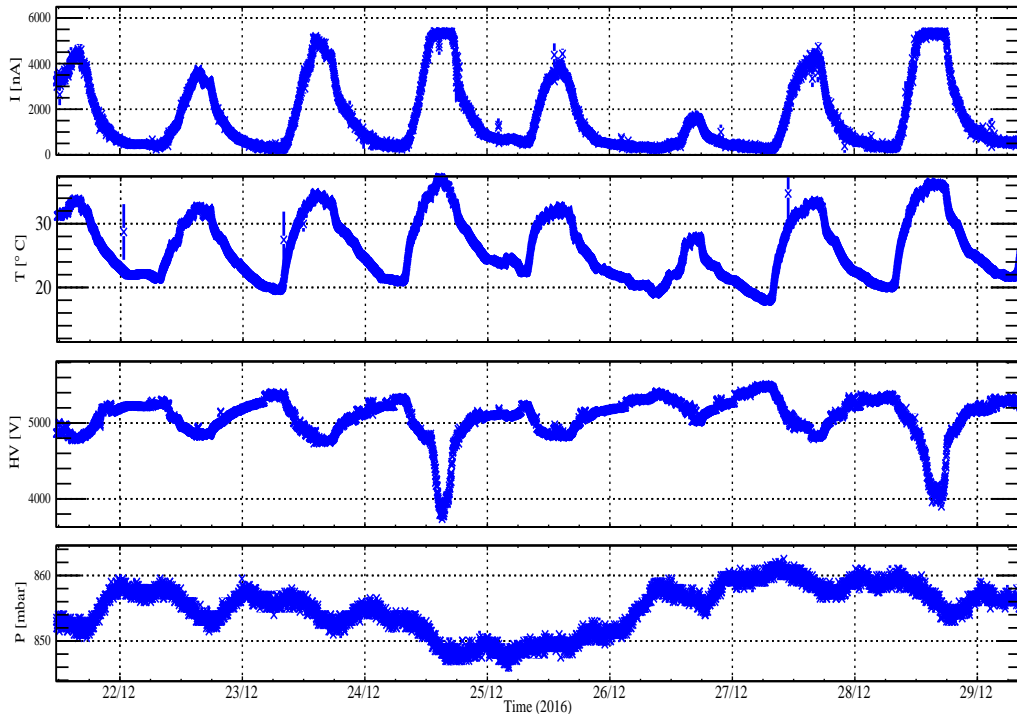


FIGURE 5.4: Variation of the monitored parameters of the top RPC as a function of time. From the upper to the lower picture: current, temperature, applied voltage and pressure.

$$\frac{E}{N} = \frac{\kappa \times T_K}{d \times P} \times \left(HV - (\rho(T) \times t \times l) \cdot \frac{I}{A_{RPC}} \right) \quad (5.4)$$

Where the variables T , I , P and HV are directly extracted from the monitoring, and T_K is, as explained, the conversion of T to Kelvin. The values of the constants κ , d , l , A_{RPC} and t are expressed in Table 5.1.

TABLE 5.1: Values of the constants of Equation 5.4.

Constant	Value
κ	$0.0138068748 \text{ K}^{-1} \text{ mbar cm}^3$
l	0.19 cm
d	0.1 cm
t	1.5
A_{RPC}	$2.12 \times 10^4 \text{ cm}^2$

By using this expression and the respective values of I , T , HV and P from Figures 5.4 and 5.5, the variation of E/N as a function of time can be determined. This parameter can be correlated with the efficiency of the RPCs, as done in [133]. In Figure 5.6, the relation between the reduced electric field and the RPC's efficiency is illustrated. A plateau of efficiency is observed for values of E/N above 245 Td. For values beneath this value, the efficiency of the RPC drops quickly. The graphic was parametrized and used to estimate the efficiency on both RPCs, to better understand the variation of the background rates.

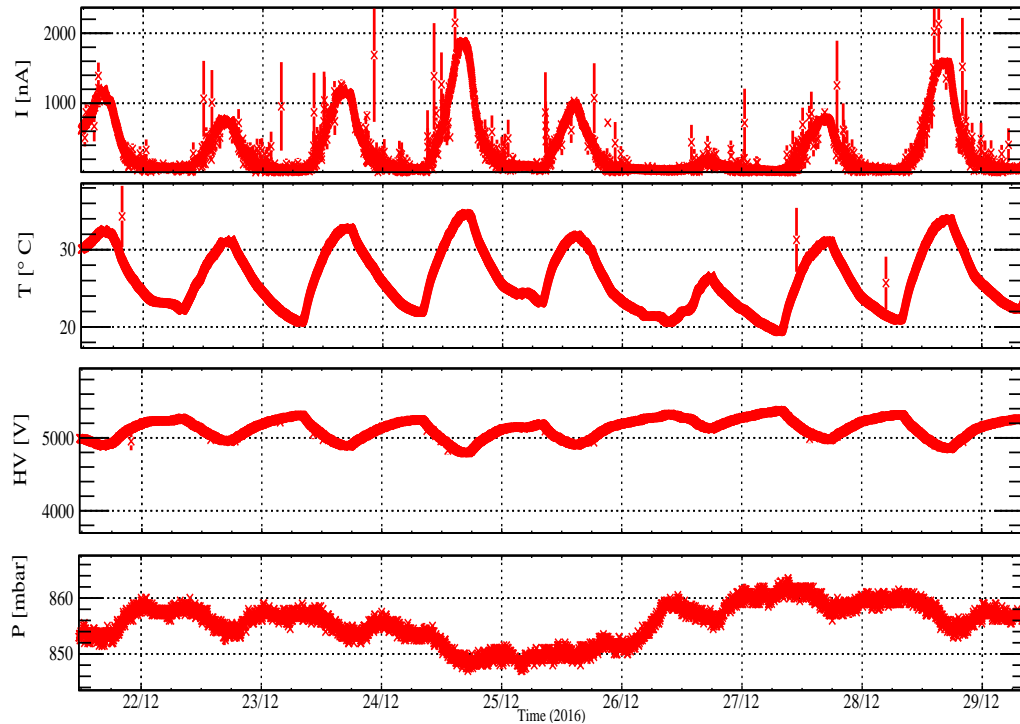


FIGURE 5.5: Variation of the monitored parameters of the bottom RPC as a function of time. From the upper to the lower picture: current, temperature, applied voltage and pressure.

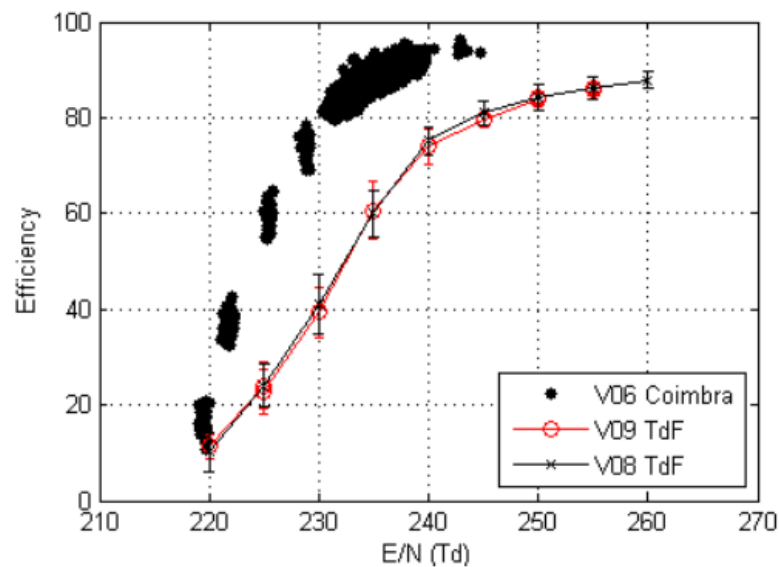


FIGURE 5.6: Correlation between the reduced electric field and the efficiency in a RPC [133]. In the legend, TdF means "Terra del Fogo", which is in Argentina. The differences between the curves from Coimbra and from Terra del Fogo arrive from different atmospheric conditions (mostly the pressure).

Figures 5.7 and 5.8 show the variations of the mean background rate, the reduced electric field and the efficiency for RPCs (top and bottom, respectively). In

both cases, the efficiency remains in the plateau for the majority of the time, with efficiency values close to 80%. Nonetheless, the variations of the reduced electric field are different among both detectors. These variations occur for different reasons, influencing differently the behaviour of the RPCs, as it can be seen in the background rates.

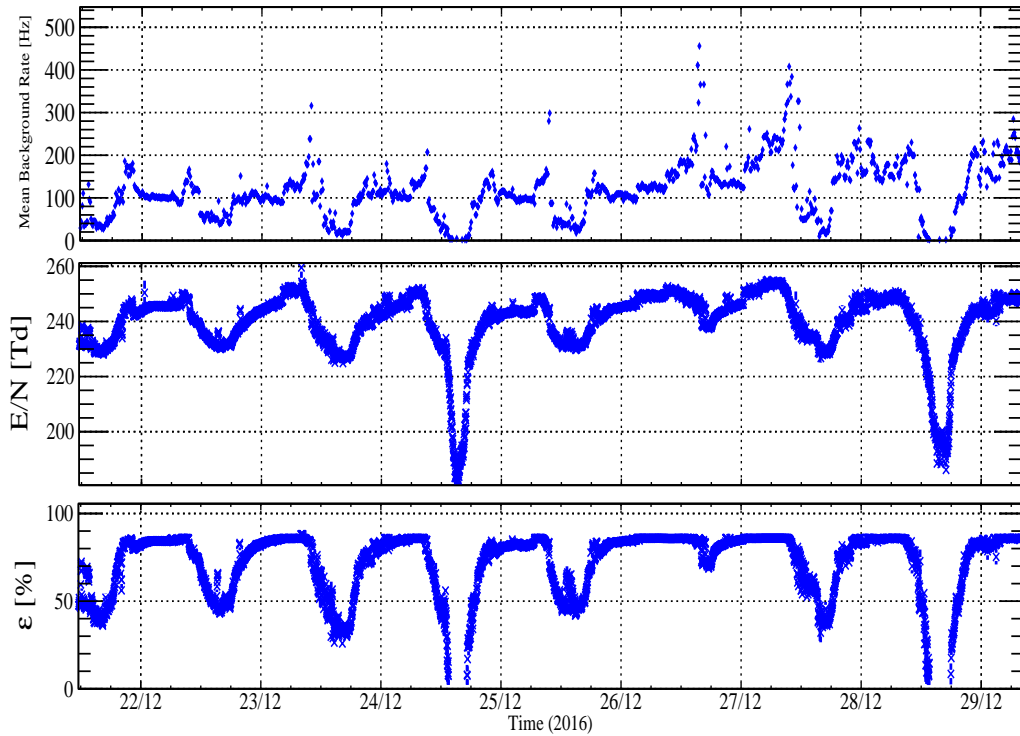


FIGURE 5.7: Comparison of the time variation of the mean background rate, the reduced electric field and the efficiency on the top RPC.

Close to the midday of each day, the E/N of the top RPC starts to drop due to the increase of the current. This fall also reduces the efficiency of the detector compared to the plateau, assuming values below 50%. This results in a fast decay of the background rates, going down to zero in the most extreme cases. However, the minimum values of the E/N in the bottom RPC are higher than in the top RPC. As it can be seen in Figure 5.8, the bottom RPC is almost constantly above 70% efficiency. This explains the apparent anti-correlation (which does not exist) between the background rates of the RPCs. When both RPCs are at their maximum efficiency, the mean background is ~ 40 Hz in the bottom one and ~ 100 Hz in the top detector. At daily hours, the background rises in both detectors, but then drops quickly in the top one, since it is no longer operational. A more detailed analysis of the reduced electric field explain the different behaviours of the RPCs.

Equation 5.4 can be divided in two different contributions for E/N : one for the applied voltage and a negative contribution from the current. Let them be respectively defined as $(E/N)'$ and $(E/N)''$, such that $E/N = (E/N)' - (E/N)''$, where:

$$\left(\frac{E}{N}\right)' = \frac{\kappa \times T_K}{d \times P} \times HV, \quad (5.5)$$

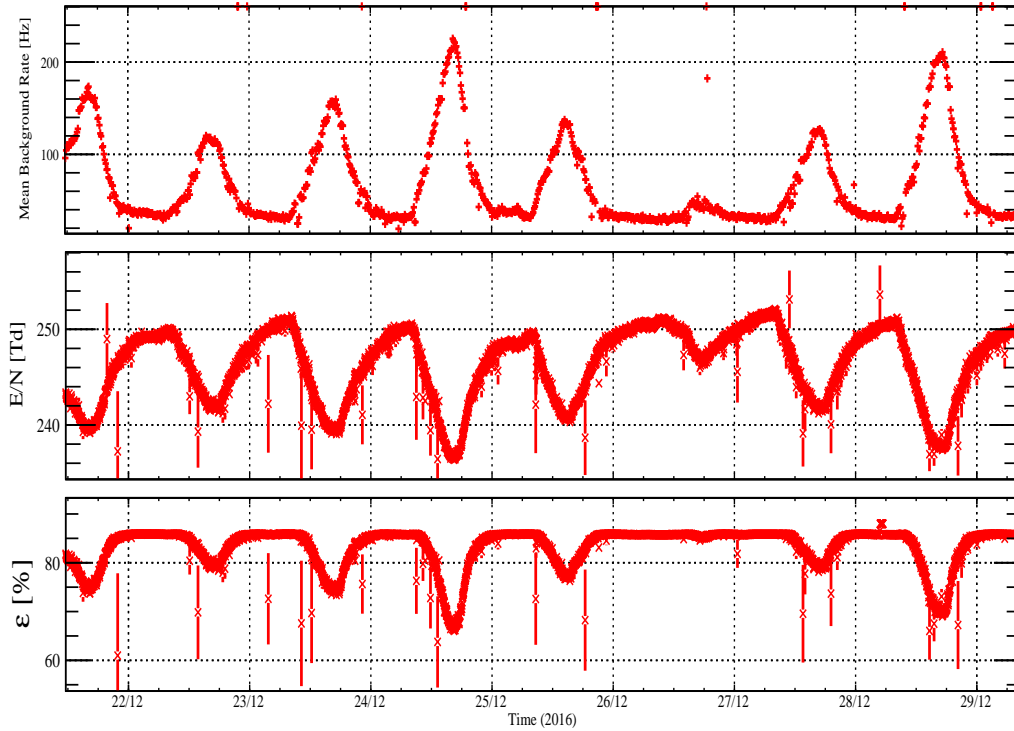


FIGURE 5.8: Comparison of the time variation of the mean background rate, the reduced electric field and the efficiency on the bottom RPC.

$$\left(\frac{E}{N}\right)'' = \frac{\kappa \times T_K}{d \times P} \times (\rho(T) \times t \times l) \cdot \frac{I}{A_{RPC}}. \quad (5.6)$$

The temperature and the pressure will influence both contributions. Therefore, the applied voltage and the current will settle the final E/N .

Figure 5.9 (up) shows the relation between the mean background rates and the temperature values for both RPCs. An increase of the background rates with the temperature inside the pads is expected, since the particles in the gas will be more excited, increasing the likeliness of gas ionization. This behaviour is well represented by the bottom RPC, where the increase of the temperature is followed by an increase of the mean background rates.

However, in the top RPC, the case is different. The temperature will still increase the background rates, as it can be seen in Figure 5.9 (up), with a few points of higher rate visible above 24°C, but not below it. The temperature will, nonetheless, not only increase the background rate but also charge generated per ionization, Q_{ion} , which implies an increase of the current. Let the background rate be defined as f_{back} . The current I can be expressed as the product of the ionization rates in the gas (i.e, background rates) with the charge per ionization. That is:

$$I(T) = f_{\text{back}}(T) \times Q_{\text{ion}}(T). \quad (5.7)$$

This means that an increase of the temperature, since it increases both f_{back} and Q_{ion} , will produce an increase of the current. The same is valid for the bottom RPC, but the values of the background rate are always lower, in comparison to the top RPC. Figure 5.9 (down) shows the variation of the current with temperature for both detectors. In both cases, I increases with the temperature but much faster

for the top RPC. The bottom RPC hits its limit with ~ 2000 nA, at 34°C , while the top one surpasses this limit at 28°C . It is, therefore, expected that $(E/N)''$ is higher for the top RPC, which will result in a higher decay of the efficiency and, as a consequence, the background rates will also drop.

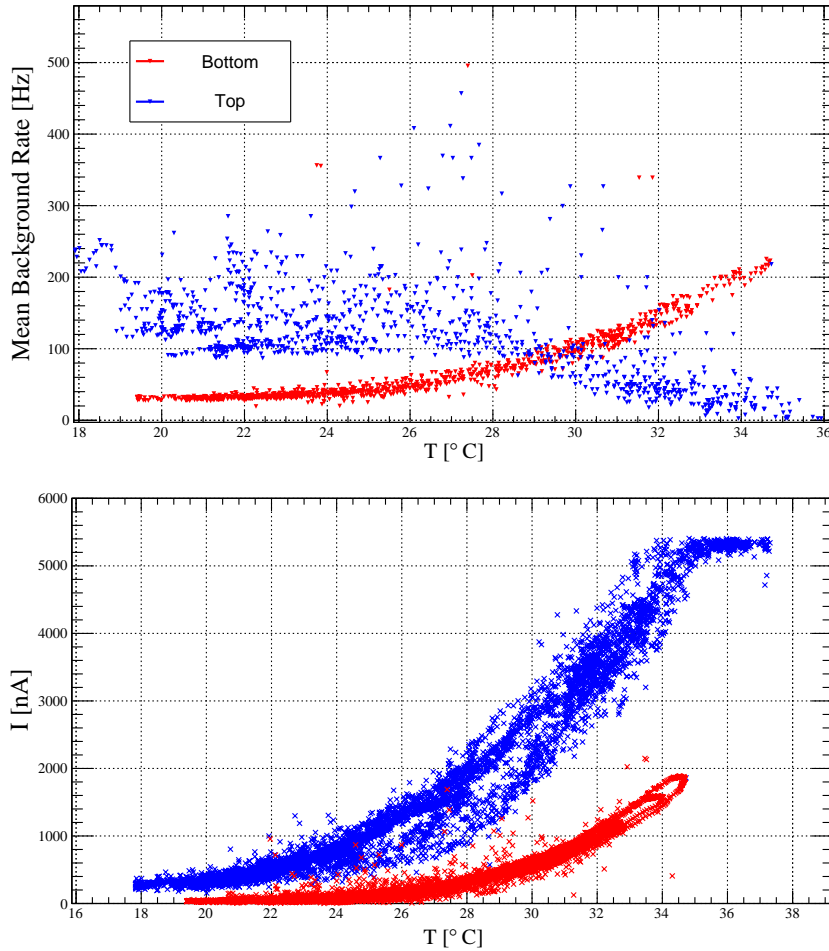


FIGURE 5.9: Up: Relation between the temperature and the mean background rates for both RPCs. Down: Relation between the temperature and the current values for RPC top (blue) and bottom (red).

As for $(E/N)'$, it would be expected that it would suffer small variations, since HV is adjusted to compensate the variations of T and P .

Figure 5.10 shows $(E/N)'$ (up) and $(E/N)''$ (down) as a function of time.

The graphic of $(E/N)'$ is not constant, which means that an additional drop of E/N also arrives from a decrease of HV , suggesting that the adjustments on the applied voltage were not working correctly. However, while there is a variation in $(E/N)'$ in both detectors, it is above 240 Td, which means that the RPCs will not move away from their efficiency plateau. There are, nonetheless, two moments when $(E/N)'$ drops in the top RPC that result in a complete loss of the efficiency, which might arrive from problems with the power supply.

The influence of $(E/N)''$ is small for both detectors but the top one still has some peaks which are enough to move the RPC from its efficiency plateau. As it can be seen in Figure 5.6, if the RPC has a reduced electric field of 240 Td, a decrease of 10 Td is enough to reduce the efficiency from 80% to 40%.

This is the case for the top RPC. Since the increase of $(E/N)''$ is coincident with the decrease of $(E/N)'$, when adding both contributions, the total E/N drops enough, so that the RPC's efficiency left the plateau. Since in the bottom RPC, the value of $(E/N)'$ is always higher than the value of the top one and the $(E/N)''$ never surpasses 4 Td, the drops in the efficiency will be very small and the RPC does not stop being operational.

This drop in the efficiency occurring for the top RPC might be explained by issues with the gas (such as reductions in its flux). Furthermore, since it is more subjected to external factors than the bottom RPC, which was shielded under the tank for most of the experiments performed until now, it is more worn out.

It is important to mention that these RPCs were originally developed for the MARTA project, which assumed that the detectors would be under the tank (therefore, more protected).

However, as we will see in the end of this Chapter, the majority of the events selected for the analysis were collected at periods with a high reduced electric field and, respectively, a high efficiency, which assures the stability and quality of the data.

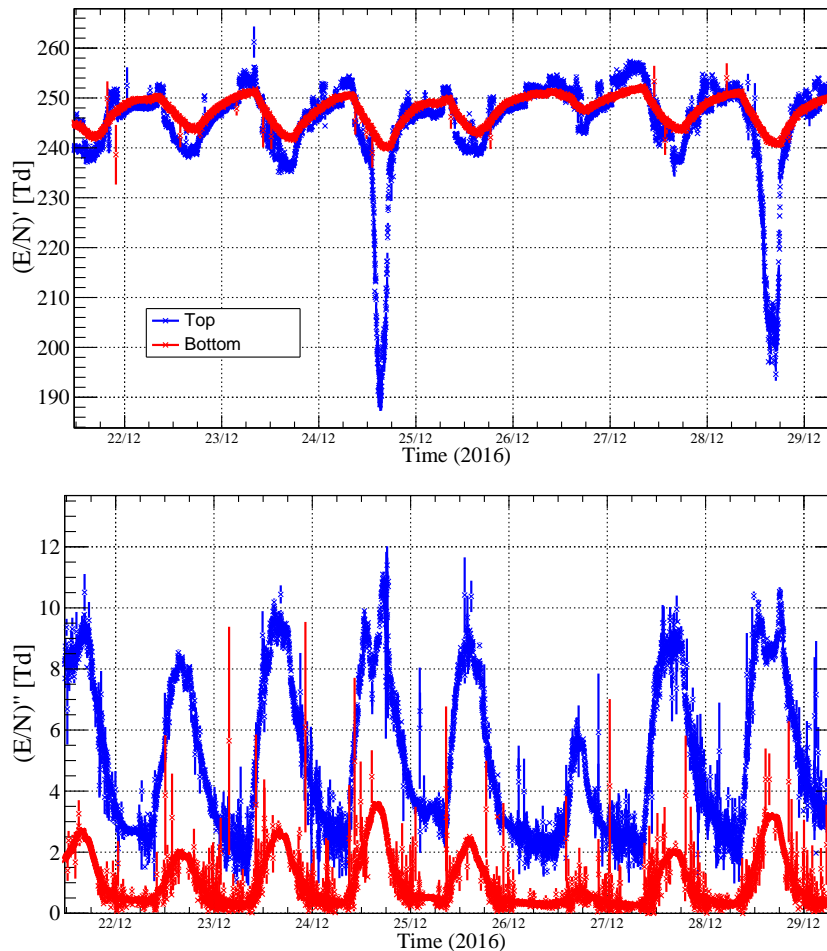


FIGURE 5.10: Up: Variation $(E/N)'$ as a function of time for RPC top (blue) and bottom (red). Down: Variation $(E/N)''$ as a function of time for both RPCs.

5.3 Rates Analysis

A further analysis that can be made to assure the quality of the data, is to analyse the different rates involved in the experiment, to fill the gaps between the acquired and expected data. This allows, for example, to characterize and understand the raw data.

Four different rates can be estimated and compared to understand the data collection - expected rate of random coincidences, expected rate for single muon hits, and measured trigger rates before and after the cuts.

Random coincidences

The setup of the test tank is based on the coincidence technique, to allow the tracking of the particle's path. However, random coincidences may occur, resulting in unwanted data.

As explained above, we want to focus in the analysis on particles that crossed both RPCs. To do that, events where both RPCs detected one particle were selected, requiring that a pad on each RPC was activated in the same time window. But it can happen that the pads activated on the RPCs were inducted by different particles or by some background effect. These events do not fulfil the criteria of a particle crossing both detectors. However, there is no direct way to separate these events from the others (unless we use the tank data, as we will see in next Chapter). What can be done, is studying the expected rate for these events, using the background data of the RPCs.

Let the rate for random coincidences be expressed as $f_{\text{background}}$ and the background rate values as ν_i^b and ν_j^t for the pad i of the bottom RPC and for the pad j of the top RPC. The rate of random coincidences can be expressed as:

$$f_{\text{background}} = \sum_{i=1}^{N_b} \nu_i^b \times \sum_{j=1}^{N_t} \nu_j^t \times \tau, \quad (5.8)$$

Where τ is the coincidence time window and, in this case, $\tau = 100$ ns [125]. By other words, to determine this rate, one must sum over all of the possible pad combinations between the two RPCs. For a given time, these measured values can be combined, as stated in equation 5.8, and an estimate for the random coincidences can be obtained. This can be done for all measurements of background data so that the variation of this rate can be analysed. It can be verified if there is any specific time where these random coincidences are more probable or if there is a combination of pads that is more propitious to these events.

Expected rate of single muon hits

The estimation for the expected rate of single muon hits was explained in the last Chapter, in Section 4.4.2. To determine this value, the equation 4.8 was used, where the parameter that changes with time is $\varepsilon_{\text{hodoscope}}$, since it depends on the number of active pads at a given moment.

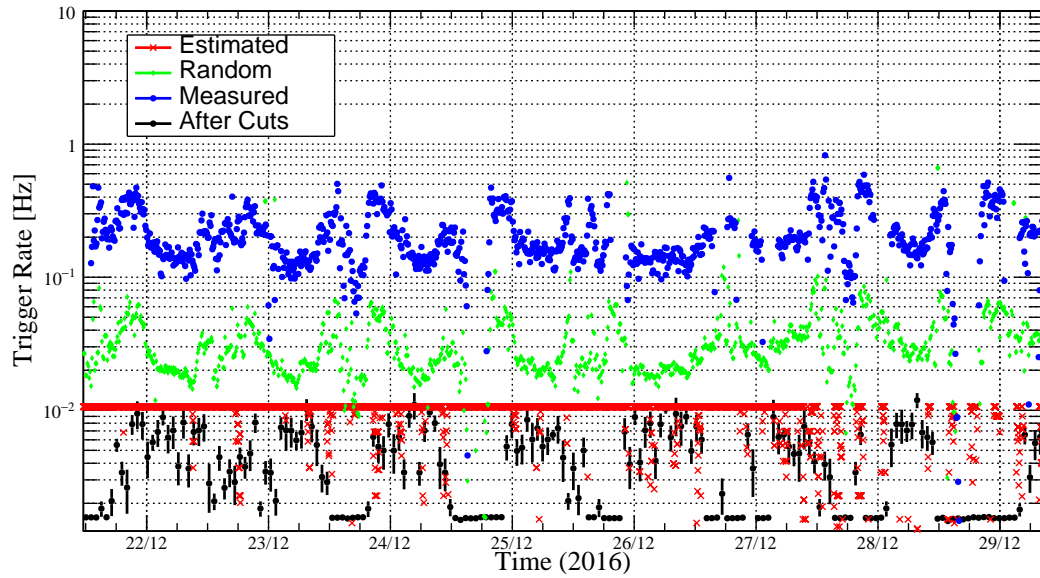


FIGURE 5.11: Estimated random coincidences rate (in green), estimated rate for muons (in red), measured trigger rate before cuts (in blue) and the rate after the data selection (in red) as a function of time.

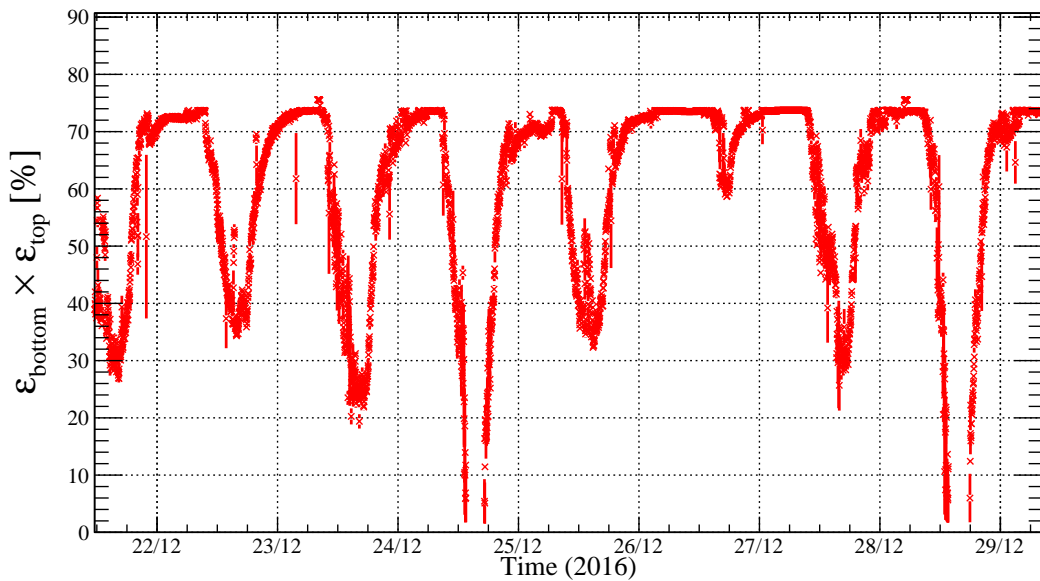


FIGURE 5.12: Hodoscope efficiency variation as a function of time.

Measured Trigger Rate

The last two rates to determine are related to the measured trigger rates for the complete data and for the data after the selection. To obtain this rate, one must simply count the number of single hits collected by the RPCs and normalize it to the considered time (for our case, the time gaps between background measures of the RPCs, ~ 15 min, was the chosen time window). This was done for the data before and after the cuts (which will be explained in Chapter 6).

Figure 5.11 compares all four rates for the period of time at analysis since the beginning of this Chapter. In an ideal scenario, it would be expected that the sum

of the expected rate of muons with the random coincidences rate would be equal to the measured rate. This is not verified because the measured rate is dominated by false triggers.

In the next Chapter, the false triggers will be described together with the data selection. Roughly 75% of the events were generated by electronic noise in the RPCs, since no signal trace was detected by the PMTs on these events. In previous analyses this value was lower, where about 50% of the events were originated by electronic noise. This increase is explained by the shifting of the bottom RPC, since it is no longer under the tank, and therefore more exposed.

However, these calculations allow to demonstrate that most of the selected events for the analysis were collected in more stable hours (lower exposition to the sun) and the rate is compatible to the estimated rate for muons.

Figure 5.12 shows the efficiency of the hodoscope system of the RPCs. It is determined by multiplying the efficiency of both RPCs. The variations of rate of measured muons (after cuts) follows the hodoscope efficiency trend. Lower efficiency of the RPCs provoked, as expected, a lower detection of single muons. This shows, once again, that most of the selected events were collected in stable periods.

5.4 Overview

Only a week of data was selected to explain the behaviour of the RPCs in this Chapter. However, as it can be seen from all plots, there is a daily periodicity in the acquisition, which is present during the full acquisition time. The background rates are more stable during the evening hours. With the increase of the temperature, the background rises at the bottom RPC and the top one loses its efficiency, due to a high increase of the current. This results in more triggers by the hodoscope during sunny hours, most of which are false ones.

The hodoscope efficiency is then also higher at evening hours and the events that are used in the analysis were mostly collected during these periods, which guarantees the quality of the data.

The reduced electric field is a powerful variable to understand the behaviour of a RPC and to determine the efficiency of the hodoscope. However, a precise determination of this value requires a constant and careful measurement of the RPC parameters. The current in particular is a parameter that highly influences the efficiency of the RPC, since a variation of just a few Td in the E/N is enough to move the efficiency from its plateau. Also a current above ~ 2000 nA can move the detector away from its efficiency plateau. Including the current in the adjustments of the applied voltage could be a future solution to keep the reduced electric field always above 240 Td, to guarantee that the RPCs will remain in the efficiency plateau.

Despite the periodic peaks in the rates leading to an absence of good events during more than a third of the day, it still was possible to reunite a decent sample of events to analyse the response of the WCD.

The RPCs were developed under the MARTA project to be placed below the tank and shielded from external conditions, such as weather conditions. Previous studies with the Gianni Navarra test tank had already shown that it was possible to perform experiments without the RPCs being shielded by the tank but this experiment in particular goes even further, by having both RPCs exposed. With

constant monitoring of the RPCs and a careful data selection it is possible to perform an analysis, which shows the potential of the RPCs, even in not optimized conditions.

Given the behaviour of the RPCs at hours of more solar exposition, it is redundant to collect data during these periods, since all events will end up being rejected. Therefore, to protect the RPCs from being worn out, it would be better to turn them off and to cover them to shield them from external factors. However, such task would be hard to automate and would require a permanent presence of a researcher to control it. Alternatively, a thin shielding of the RPCs, to protect them from thermal variations, could solve the issue and would not affect the measurement of muons.

Chapter 6

Analysis of inclined atmospheric muons

*"You can have data without information, but you cannot have information without data." -
Daniel Keys Moran*

In the last two Chapters, the geometric configuration of the experimental setup was described and the monitoring of the data was explained. The analysis of the response of the tank to inclined muons can be performed with the collected data, after filtering a sample of single muons.

The analysis that follows can be divided in three main stages: data selection, geometric reconstruction and the results discussion by comparison with the simulation.

Firstly, the criteria and the motivations for the data selection will be explained in detail, in order to prove that the sample to be analysed consists of single muons, within uncertainties.

Next, the muon trajectories reconstruction will be described, as well as the distributions resulting from it, such as the track length and the zenith and azimuth angles.

After these early descriptions, the data will be analysed and compared to the simulation. The discrepancies are characterized and possible explanations for their origin are provided.

6.1 Data

By the end of Chapter 5, the stability and quality of the data were confirmed, especially of the selected events, allowing to proceed with the analysis.

Before moving forward, it is important to understand the information provided by each one of detectors of the test tank experiment and which parameters will be used for the analysis in this Chapter.

We have seen already in the last two Chapters that the RPC hodoscope has a complex configuration. There are three main groups of acquired data to analyse: RPC, Tank and Tank Calibration. More specifically:

- RPC data: status (hit or not-hit) of each pad of each RPC, together with the timestamp given by the tank GPS.
- Tank data: high-gain and low-gain traces of each PMT of the WCD, as well as the GPS time.

- Tank Calibration data: current and charge histograms of each PMT.

Additionally to these, there are also the RPC background data and the RPC monitoring parameters, as we discussed in Chapter 5. Notwithstanding, they were used to monitor the acquisition and understand the RPC's behaviour. Therefore, they will not be mentioned again in this Chapter.

The data from the RPC is very simple to describe: when a particle is detected by a pad, the identification of the pad and the respective time will be saved. As we have seen, the storage of data from the test tank is triggered if both RPCs detected at least one hit. Therefore, all single hit events will have a registered position in each RPC, which will be later use to reconstruct the trajectories of the muons (which is a simple geometric calculation, since the pad's positions were already settled in Chapter 4).

The tank information consists on the PMT traces and their calibration. The later was already discussed in Chapter 5 and it is used to perform the ADC to VEM conversion. As for the traces there are high-gain and low-gain. The later will not be addressed in this analysis, since we are measuring single particles, therefore their amplitude in low-gain traces will be too small to be analysed. On the other side, high-gain traces are not suitable for shower analyses, since their trace will saturate with just a few particles inside the tank.

The high-gain traces were read and analysed with software especially developed for the test tank, instead of using the Offline Framework, as it happens with the WCD from the Auger SD. This removes any possible bias, making the analysis completely independent from the Offline Framework, which increases the quality of the comparisons.

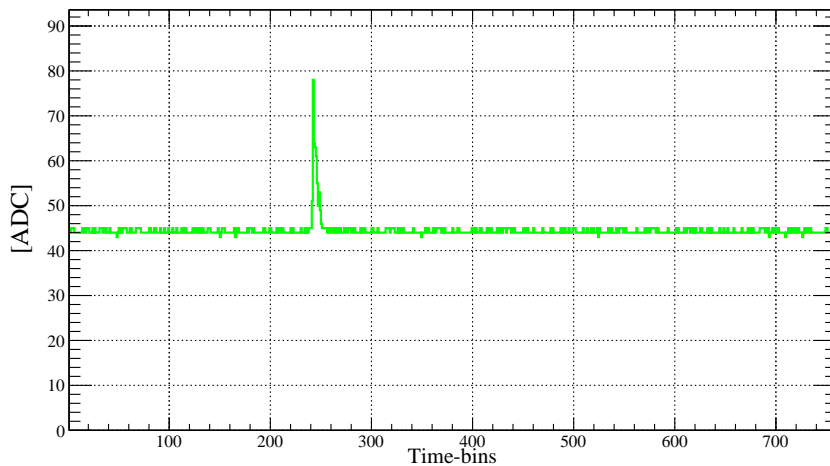


FIGURE 6.1: Example of a high-gain trace (from PMT 2).

Figure 6.1 shows an example of a high-gain trace, with 768 time-bins, each corresponding to 25 ns time-interval. The high-gain traces are analysed to infer their respective average baseline values and number of signals. For each signal, the start and stop time-bins are registered and the charge and its peak are calculated (in ADC and then converted to VEM), and also the Area over Peak (AoP). Each one of these quantities required a different analysis. In detail:

- **Baseline:** to determine the average value of the trace baseline (and respective RMS), the 12 consecutive time-bins before the trigger region are selected (where no signal was found) and their average value is considered.
- **Number of signals:** an increase of 2.5 ADC, in relation to the baseline, was used as threshold for the signal search in the traces.
- **Peak time-bin:** the start time-bin is defined as the first time-bin above the threshold and the stop one is given by 10 time-bins after the baseline recovering to normal values.
- **Charge:** the charge, in ADC, is determined by integrating the trace above the baseline, between the start and stop time-bins of the signal. The conversion to VEM requires the calibration histograms and a conversion factor, as explained before in Chapters 3 and 5. An uncertainty of 1.5 ADC (or ~ 0.01 VEM) is attributed to this calculation [129].
- **Area over Peak:** or VEM Area to Peak Ratio, or just AoP, is an indirect measure of the signal duration and a key indicator of the performance of the Cherenkov station. The AoP, as the name suggests, is the ratio between the area that results in the integrated charge and the peak obtained in a signal. This parameter is important to study possible ageing effects on the tank. A smaller AoP might imply a higher light absorption due to impurities in water or diminished reflectivity of the liners of the tank [134]. Studies about the long term performance of the water stations were described in [135, 136]. The signal peak is determined by searching for the maximum amplitude of the signal (which, in most cases is either the start time-bin or the one after it) and subtracting the baseline value. The AoP of each signal is then obtained by determining the ratio between the charge and the signal peak.

Each one of these parameters contributes for the characterization of each event, which can be used to filter the ones which fit into the category that we pretend to analyse.

6.1.1 Data Alignment

The data available was collected between 30th of November 2016 and 15th of January 2017. Table 6.1 summarizes the number of events collected by the RPCs and the tank. Additionally, is also shown the number of events after the time-alignment between them.

The RPCs store data faster than the tank, due to a higher acquisition dead time in the tank, which implies that the RPC data will contain more events than tank data, as it can be seen in Table 6.1.

Each event, either from the tank or from the RPCs, has a timestamp associated, which can be used to synchronize the data, so then we have a single group of events with information from the tank PMTs and from the RPC hodoscope. A small inefficiency of this process results in losses up to 2% of the tank data.

TABLE 6.1: Statistics of the data collected by the different detectors and the alignment between them.

Data File	Events	Percentage [%]
RPC	807182	100
Tank	295083	36.6
Alignment	289026	35.8

After this alignment of the different types of data available, the sample is reduced to 289026 events where, for each one, it is known how many hits were produced in the RPCs and the signal in each one of the PMTs is well characterized.

6.1.2 Data Selection

As previously explained, before starting the analysis to inclined muons, the data must be filtered to eliminate different sources of background (which was already guaranteed in Chapter 5). Several cuts were imposed over the data to assure that the sample is composed of single atmospheric muons. This data selection is summarized in Table 6.2.

TABLE 6.2: Number of events after each cut and respective percentage left in relation to the aligned data.

Selection	Events	Percentage [%]
Alignment	289026	100
Signal in the trigger region	43379	15.0
Single hits	15891	5.5
No Saturation/Oscillations	14619	5.05
Charge Error	12391	4.3

Starting with a sample of events with the data between the tank and the RPC hodoscope aligned, there were imposed four different cuts: signal in the trigger region, single hits, no saturation/oscillations and the charge error. Each one of the cuts pretends to eliminate different contaminations, by imposing limits in the different variables available for each event. The purpose and criteria applied in each cut is summarized below.

- **Signal in the trigger region:** we concluded in Chapter 5 that a big part of triggered events were produced by false triggers. If we rely only in the RPC events, it is not possible to disentangle false triggers from the others. However, the problem can be overcome by analysing the traces of the PMTs. False triggers given by the RPC hodoscope will not give any signal in the PMTs. Therefore, by simply imposing that at least one signal was found in each trace (of each PMT), $\sim 75\%$ of the events were eliminated. Additionally to this restriction, it was also required that the signal was detected in the trigger region, by removing all events where the peak signal was not located between the time-bins 242 and 245. Figure 6.2 shows the distribution of the position of the peak signal for the sum of all PMTs traces. A signal produced by a RPC-triggered muon peaks, by definition, in this region.

Events with peak signals in a different time-bin were removed.

- **Single hits:** to study the geometry of the path of the particle, it is required to know which pads of the RPCs were activated. This means that the data used can only consist on single hits events. I.e., this cut is imposed to guarantee that one and only one hit in each RPC was registered. This removes small showers and showers produced inside the tank, towards the direction of the bottom RPC, from the data.
- **No Saturation/Oscillations:** not all showers are eliminated with the single hits cut. It is expected that a fraction smaller than 5% of the events after the single hits cut are showers [125]. Some might be big enough to saturate the high-gains PMT traces. Such events are filtered by analysing the saturation of the trace. Baseline oscillations are also removed from the data. Traces with at least 3 ADC counts below the baseline and followed by a rise of at least 5 ADC counts in the next two time bins are removed.
- **Charge Error:** events with an error on charge larger than 5 ADC are removed from the data.

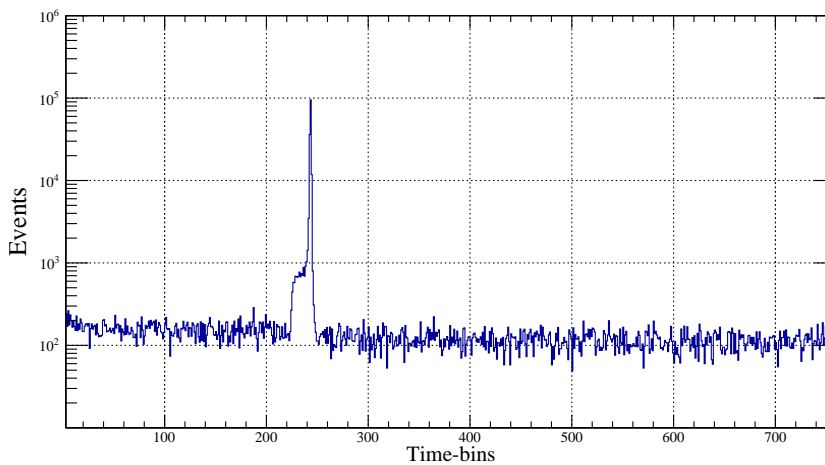


FIGURE 6.2: Distribution of the time-bin position of the peak signal for sum of all PMTs traces.

After all cuts, the selected data is resumed into 12391 events.

To verify the impact and the importance of this selection, we can compare some parameters before and after the cuts.

In Figure 6.3, the charge distribution for PMT 3 is compared for the non-filtered data with the impact of successive cuts until the final distribution after all cuts. Given the purpose of this analysis and the geometric configuration of this experiment, PMTs 2 and 3 are optimal for this verification, since the light reaching them is well diffused (no direct light effects). It is expected for PMTs 2 and 3 to show a similar signal (as we will see later), meaning that only PMT 3 is shown, to avoid redundant verifications.

The first cut applied (Signal in the trigger region, in blue in Figure 6.3), eliminates the false triggers, which is well visible by the absence of a peak at 0 VEM. The losses of events on the peak slightly below 1 VEM is due to events with a peak signal outside the trigger region.

The restriction to single hits (in green in Figure 6.3) removes the events of higher charge, since these are events with more than one particle. It is verified by a decrease of the tail's distribution for higher charges.

The cut to remove the saturated signals (in purple) shows a small impact, which implies that most showers were already removed by the single hits filter. The most visible implication of this cut is, as well, a diminishing of the tail of high charges. Likewise, the verification of the charge error also barely provokes any changes in the charge distribution.

Above all, these cuts allow to remove most false triggers and small showers from the data, in order to have a sample composed of single hits that fulfil the criteria expected for muon signals.

In Figure 6.4, the AoP distributions are shown, analogously to the charge

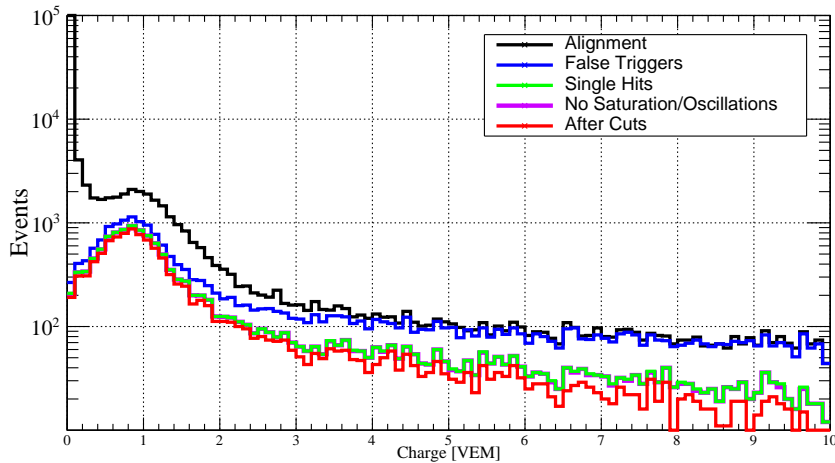


FIGURE 6.3: Charge distributions for PMT 3 before the data selection (in black), the signal in the trigger cut (in blue), the restriction to signal hits (in green), no saturation and no baseline oscillations (in purple) and the final distribution, after the charge errors (in red).

distributions explained above. Since AoP is a characteristic of the signal, it is expected that the distribution of the AoP for single muons is not too wide. This is verified in this distribution, where the width of the distribution becomes smaller after the cuts. Smaller values of AoP (< 1) are expected for electromagnetic particles [137], while large AoP values result from non single hits (i.e, more than one particle), which is exactly what Figure 6.4 indicates. Removing the false triggers (and signals outside the trigger region) reduces the lower AoP values. Eliminating events with more than one hit in each RPC removes small showers, therefore, the events with higher AoP values are removed. In the end, the distribution is more concentrated around the expected AoP values for muon signals (~ 3).

As it was shown at the end of Chapter 5, the selected events were collected mostly at stable periods of the detectors. Now it was also demonstrated that this selection assures that the analyses to be performed afterwards are done, as much as possible, over single muons.

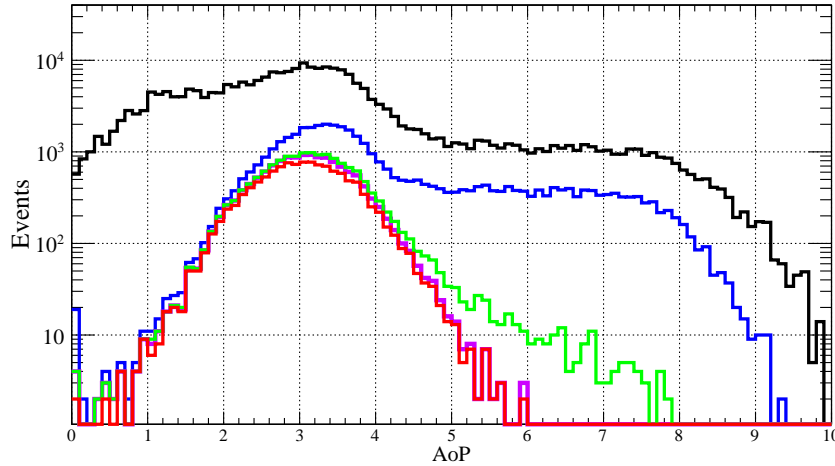


FIGURE 6.4: Area over Peak distributions for PMT 3 before the data selection (in black), the signal in the trigger cut (in blue), the restriction to single hits (in green), no saturation and no baseline oscillations (in purple) and the final distribution, after the charge errors (in red).

6.1.3 Muon Trajectory Reconstruction

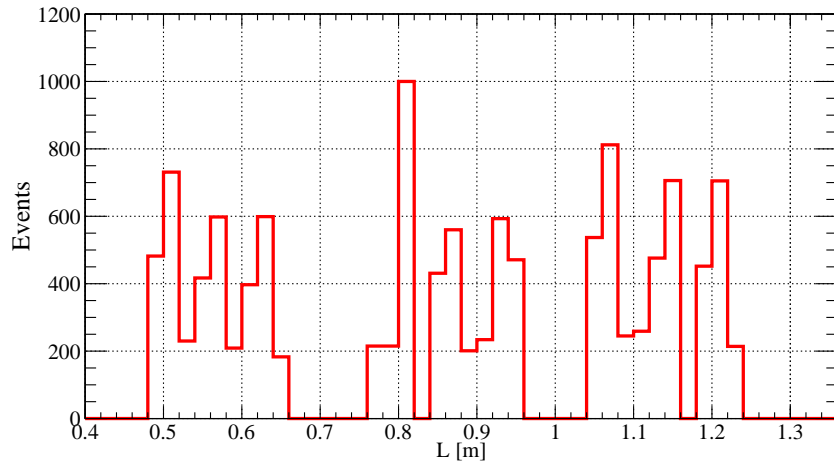
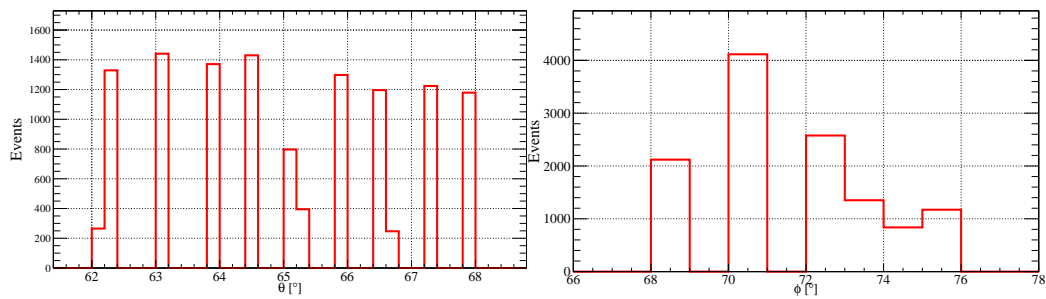
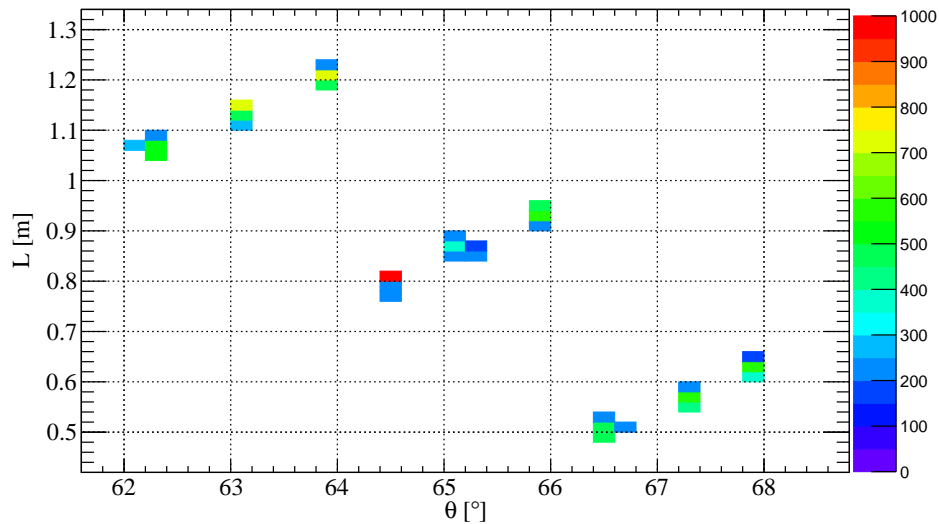
Before initiating the analysis of the charge distribution, the geometry of the data was verified.

The particles cross the top RPC, then enter the tank from the top and exit it from the side (clipping muons), and finally hit the bottom RPC. Each one of these trajectories has a track length, a zenith and an azimuth angles associated. These parameters were calculated through the pad combinations (54, in this case), by using the center of each pad. Therefore, each determination of the particle intersection of the RPC has an maximum uncertainty of 0.11 m, which is related to fact that each pad had been resumed to a single point.

The track length of the particles inside the tank (see Figure 6.5), L [m], is distributed in the interval $[0.48, 1.24]$ m, with a propagated uncertainty of 0.02 m for each value. The zenith angle distribution, θ , (see Figure 6.6 left) varies between 62° and 68° . Using the simulation from Offline Framework, the angular resolution was estimated to be $\sim 1^\circ$. The azimuth angle distribution, ϕ , is less important for the analysis, since it is dependent on the chosen referential and the atmospheric muons flux have no relevant dependency on the azimuth. The distribution of this parameter is shown in Figure 6.6 (right), with an angular resolution of $\sim 1^\circ$, and its variation and limits is a consequence of the RPC positioning selected to obtain large zenith angles.

In Figure 6.7, the relation between the track length and the zenith angle is displayed. The discontinuous variations emerged from the reconstruction together with the segmentation in rows and columns of the RPCs, that is, due to the detector granularity. More inclined trajectories have a smaller track length inside the tank, due to the relative positioning of the RPCs. Trajectories with higher zenith angle result from pads which are more distant from the tank center, in each RPC. Such trajectories, however will exit the tank by the lateral side at a higher height, having, therefore, a shorter L .

The track length and the zenith angle have a similar distribution for all discreet points. This is also verified by the number of events of each one of the 54

FIGURE 6.5: Track Length (L) distribution.FIGURE 6.6: Left: Zenith angle (θ) distribution. Right: Azimuth angle (ϕ) distribution.FIGURE 6.7: Relation between the zenith angle and the track length of the particles trajectories of this setup. The color represents the number of events that have the respective L and θ relation.

pads combinations. Each combinations has a number of events close to 200.

Figure 6.8 shows the intersections of the muons' trajectories with the tank at

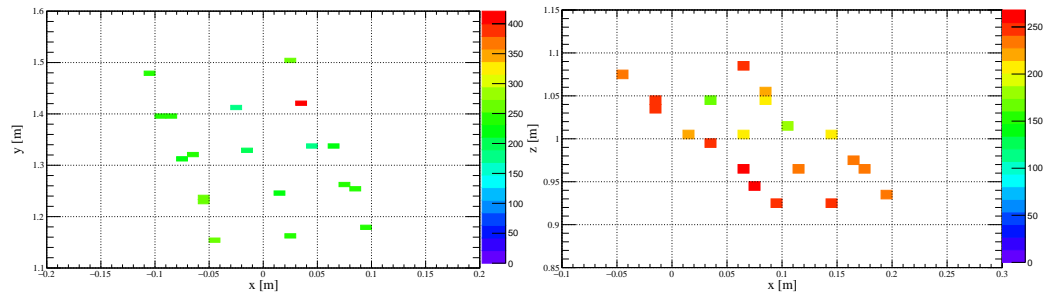


FIGURE 6.8: Left: Coordinates of the points of intersection of the muons when entering the tank at its top (see Figure 4.14 for reference). Right: Coordinates of the points of intersection of the muons when exiting the tank, from the side (see Figure 4.15 for reference).

the entry (left) and at the exit (right). The color represents the number of events at each bin. Figures 4.14 and 4.15 should be consulted for reference to the tank and detectors positions.

6.1.4 Features on the Data Signal

The zenith angle dependence of direct light to the PMTs was discussed in Section 3.1.2.3 and, through a numerical calculation, it was estimated that these effects become more likely to occur for angles higher than 48° , which is the case of this experiment. In Figure 4.14, it became clear that the trajectories of the particles intersect the top surface of the tank near the PMT 1, or even cross it. This has a direct impact on the charge distribution of this detector.

Figure 6.9 shows the charge distributions of PMT 1, while Figure 6.10 shows the distributions for PMTs 2 and 3.

Once the particles cross the tank close to PMT 1, their trajectories are roughly at the same distance from PMT 2 and from PMT 3. Then, a similar charge distribution is expected from these two PMTs. Figure 6.10 shows precisely this, since the charge distributions of PMT 2 and 3 are almost completely overlapping one another. Both illustrate a single signal peak, which would be expected. The peaks occur in these distributions for values close to 1 VEM, which is slightly above the expected value (as we will see later).

However, the distribution of PMT 1 shows a different behaviour, by presenting an additional peak for higher charges due to direct light effects. Since this PMT is hit by non-diffused light, the shape of this distribution is expected.

Two unexpected features are present in all distributions: a long tail for high charges and a small peak for small charges at ~ 0.2 VEM.

It would be expected, especially in PMTs 2 and 3, that the signal would not have higher values of charge, with the exception of some fluctuations. This is also observed in PMT 1 and raises the possibility that the data sample is not composed exclusively of single muons.

An additional peak for small charges was also found in PMT 1. This is a hidden peak in PMTs 2 and 3, but one can observe that these two distribution have roughly the same amount of events for this charge range as the small peak in PMT 1.

Each one of these observations in the distributions will be analysed in detail.

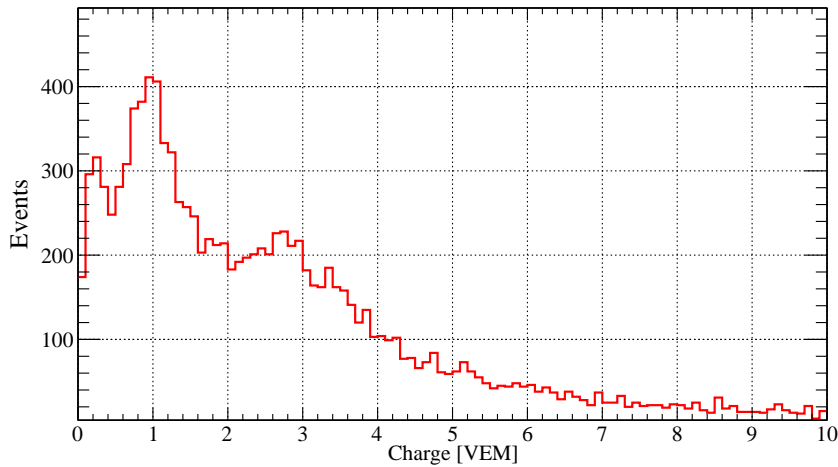


FIGURE 6.9: Charge distribution for PMT 1.

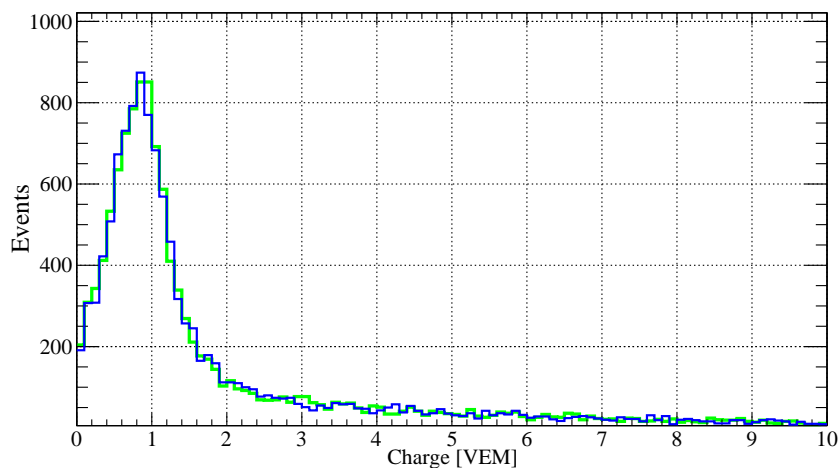


FIGURE 6.10: Charge distribution for PMTs 2 and 3.

6.1.5 AoP and Charge relation

To complement the understanding of the data it is necessary to explore the influence of intersections of the PMT and direct Cherenkov light emission. The intersection of a PMT by a particle can result in Cherenkov light production in the glass (which has a different refractive index than water) resulting in an unusual signal. Direct emission of Cherenkov photons to the PMT will also result in a higher signal. Both cases adulterate the charge distribution of a PMT, since the light is not well diffused when it reaches the PMT's surface.

As it was explained earlier, these direct light effects to the detector are dependent on the particle's trajectory. By knowing the trajectory of the particle, it can be calculated if there were any effect to the detector or not. However, there is an ambiguity associated with the trajectories' calculations by the hodoscope, which arrives from the pads dimensions. We know when a particle crosses a pad segment of a RPC, but we do not know where exactly. Therefore, it can be estimated

a probability that a pads combination between the top and bottom RPCs has to produced these effects.

A Monte Carlo simulation can be used to generate random points across the two pads of a combination. Using these results, several trajectories can be organised but all belonging to the same pads combination. Then it can be analytically determined if those trajectories crossed the PMT or if they produced direct Cherenkov light (as it was done in Section 3.1.2.3). Finally, by counting the trajectories that produced this effects, a probability of both effects can be estimated for each pads combination.

This can be used as a way to compare combinations which have zero probability of originating these effects with the other ones. A good way to study these different combinations is looking at the different relations that occur between the charge and the AoP. We can use the other two PMTs as a control sample.

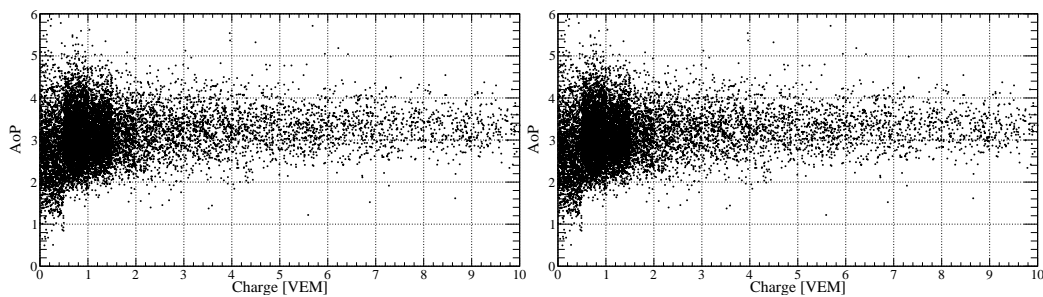


FIGURE 6.11: Charge vs AoP for PMTs 2 (Left) and 3 (Right).

PMTs 2 and 3 give a relation between charge and AoP for well diffused light, since direct effects are geometrically impossible to hit any of them. Figure 6.11 shows the Charge vs AoP for both PMTs. The majority of the events have an AoP between 2 and 4 and a charge between 0.6 and 1.2 VEM. This can then be compared to PMT 1 to disentangle the different effects.

To represent this relation for PMT 1, the events were divided in three groups: no effects, direct Cherenkov light and intersection of the PMT. From the estimation above, each pads combination has a certain probability of producing direct Cherenkov or intersecting the PMT. In some pads combinations, these two probabilities were zero, meaning that none of these effects are geometrically expected¹. All events that crossed a pads combination that had zero likelihood of producing direct light effects were included in the groups of no effects and the Charge vs AoP relation for these events are represented in Figure 6.12 (up). These results are similar with the distributions for PMT 2 and 3 from Figure 6.11, although the average AoP value is smaller in PMT 1. This is related with the fact that the calculation used for pad selection cannot account for semi-diffused light.

There were no pads combinations with 100% probability of intersecting the PMT. Given how close from the PMT 1 the trajectories intersect the top of the tank, there are pads combinations where is likely to occur only direct Cherenkov light and others which is likely to occur direct light or a trajectory intersection

¹This calculation, however, does not allow to assure that the light is well diffused, which requires that the Cherenkov light suffer a few deflections before hitting the PMT. The calculations do not account for semi-diffused light, since that would require a more complicated analysis.

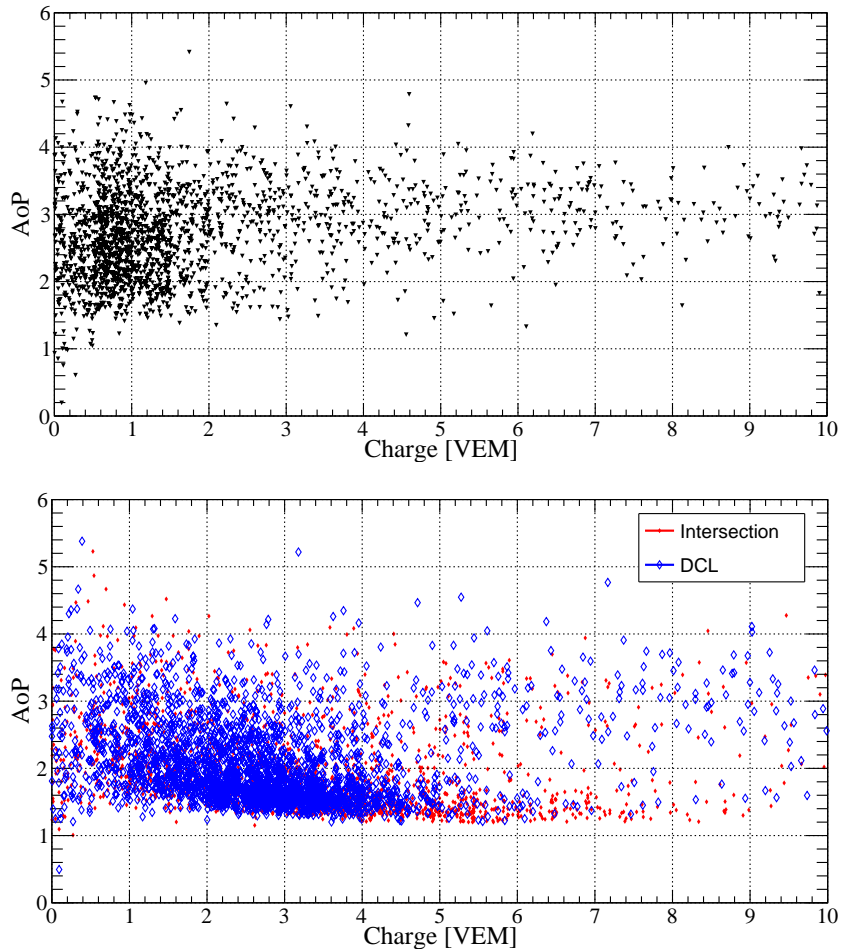


FIGURE 6.12: Charge vs AoP for PMTs 1.

of the detector. Therefore, the pads combinations with a non-zero probability of resulting in direct Cherenkov light were divided in two groups: intersection and no intersection of the PMT. An additional filter to the peak position being at the time bin 242 was introduced, since direct light effects are expected to hit the PMTs first bins of the trigger region. These effects will produce a higher peak in the signal than well diffused light. Consequently, the AoP value will diminish, since the latter is inversely correlated with the former. Figure 6.12 (down) shows the Charge vs AoP distributions for events that crossed pads combinations with a non-zero probability of producing direct Cherenkov. In red there are represented events from pads combinations which can result on the intersection of the PMT and in blue are represented events from pads combinations where only direct Cherenkov light is likely to occur. Both effects have similar distributions, as demonstrated by Figure 6.12 (down). Even by having in consideration that direct Cherenkov light is present in both groups, the differences in the distributions are too small to imply that Cherenkov in the glass would have a complete different AoP vs Charge correlation.

The comparison of this results with the PMTs 2 and 3, and the filtered ones without effects from PMT 1, it becomes clear a long tail for high charges and low AoP values, which has to be originated by direct light effects.

The AoP is a characteristic of the signal, being related with the time that it takes for the trace return to baseline levels. If we compare two signals with the

same charge but different AoP values, the one with the lower AoP has a higher amplitude signal but with a thinner width. Therefore, a different signal trace is expected for well diffused light and non-diffused light.

From this analysis of the AoP vs Charge correlation, a large number of events with charge higher than 3 VEM and AoP values between 2 and 4 was found, for all PMTs, including in the different filtered samples of PMT 1. Before moving forward, it is important to discuss why events higher than 3 VEM are not expectable.

As mentioned before, 1 VEM is the signal equivalent to a vertical muon crossing at the center of the tank. Since the tank has a height of 1.2 m, and a linearity with L of the signal is expected, it can be assumed that if the particle's trajectory had a length inside the tank of ~ 1.2 m, then the charge should be ~ 1 VEM.

Since in this experiment, the analysis is performed to single muons, a linearity of the charge with the track length is expected. Having in consideration the dimensions of the tank, with a diameter of 3.6 m, the longest possible trajectory for a single particle is the diagonal of the tank, which has a length of ~ 3.8 m. From this, it can be estimated that the highest signal for a single muon would ~ 3.16 VEM. Therefore, it is a reasonable assumption to consider that, if there are no direct effects, a single particle would not have a signal higher than 3 VEM.

For the specific case of this setup, a 3 VEM signal as the highest value for a single muon is a very conservative estimation, since the maximum L of this experiment is ~ 1.25 m. This means that events with more than 2 VEM would already be very unlikely (excluding PMT 1).

The fact that these events have an AoP distribution similar to events with smaller charge, implies that the signal shapes are similar. This was observed in the traces of these events, where their shapes appeared to be very similar to events with smaller charge, but with higher amplitude (as expected, since they have high charge values).

The existence of these features in the data points to the presence of a background contamination, which is not accounted for in the simulation that follows.

6.2 Simulation

The main goal of this analysis is to understand how well does the simulation recreates the response of the tank at large angles. Assuring that the simulations are reproducing well the behaviour of the detectors is fundamental for cosmic rays physics, since they are used to infer several properties of the showers and the primaries.

In Chapter 4, the previous analysis with the test tank were explained and concluded that, until 55° , the Offline Software Framework recreates well the response of the water Cherenkov detector. In a similar way as described in Section 4.2, the Offline was used to produce simulation samples to compare with the collected data from the test tank.

6.2.1 Geometry verification

Verifying that the geometry introduced as input in Offline describes well the experimental setup is essential for a good analysis. Since the signal on the PMTs is dependent on the track length and the occurrence of direct effects is related with the geometry, assuring that the experimental positions of the RPCs are correctly set in the simulation is fundamental.

The geometry was carefully implemented in Offline Framework, such that a good agreement between the experimental calculations and the simulation was verified. Therefore, the Offline inputs are correct and a trustworthy simulation is possible to be created.

6.2.2 Simulation Procedure

The input file used for Offline Framework to simulate atmospheric muons was explained in Section 4.2.2. Particles are randomly selected from this file and inserted in Offline to proceed with the simulation. Given the conditions imposed, only data from particles which activate the hodoscope are stored. Photons, since they are neutral, do not trigger the RPCs. Additionally, given the hodoscope configuration, inclined muons will activate it. In Figure 4.5 it was shown that the flux of muons is low for muons with angles larger than 60° . If the complete file is introduced in Offline, the simulation will produce the output information for each particle but the fast majority will not activate the hodoscope. The processing time for these simulations is long, therefore some conditions were introduced to reduce it and make it more efficient.

To overcome this time efficiency issue a geometric condition was imposed. This condition aims to reduce the processing time by stopping the simulation of a particle if a certain criteria is not confirmed. The particle is simulated at the top RPC, with a certain energy and momentum. Since the particles at study are muons, it is unlikely that many deflections will occur inside the tank. Therefore, at the top RPC, the trajectory of the particle is analytically calculated by using its momentum. If the calculated trajectory does not hit the one of the six selected pads of the bottom RPC, the simulation is stopped and a new particle is randomly chosen from the input file. Otherwise, the simulation of the particle goes on until the end.

However, it was soon realized that this restriction had an influence of $\sim 10\%$ in a pure muon simulation, which will be demonstrated later. Therefore, the simulation samples had to be produced without any condition. Nonetheless, this geometric condition was still used for quantifying the possible deflections in this experiment.

6.2.3 Charge distribution for single muons

Since it is expected that muons are the dominant type of particles in the data, due to the electromagnetic absorption in water, the analysis was initiated with a simulation sample consisting exclusively of muons. This sample was identified as Sample A. Table 6.3 shows the restrictions of this sample, including the zenith angle limits of the particles.

Although the muons barely interact with matter (i.e., deflections are unlikely) not all the muons injected have enough energy to pass the threshold for both RPCs. This means that, even if geometrically all the injected muons cross the RPCs, some will not be detected due to their low energy², or due to the intrinsic efficiency of the RPC.

To perform an analogous analysis to the simulation as it was done to the data,

²If the particle does not have enough energy to cross the tank, it will not reach the bottom RPC.

TABLE 6.3: Restrictions of the input file used to produce Sample A.

Sample	Type of Particles	θ [°]
A	μ^\pm	[55 – 75]

it is necessary to assure that the events are as much alike as possible. It is fundamental to assure that data and simulation passed through the same filters. Given the organization of simulated events, only two cuts are necessary to consider: single hits and pads in trigger mode.

Although the initial conditions for particle injection include only one hit on both RPCs, this does not account for possible particle productions, which will mainly affect the bottom RPC. Contiguous pads to the selected ones (9 and 6 for top and bottom RPC, respectively) could also result in the storage of an event in case of a deflection. Therefore, events with more than one hit on the bottom RPC and(or) with pads triggered that do not belong to the selected for the data analysis were removed.

These two cuts reduced the number of events in the simulation to 10%. The dominant cut imposed on the simulation was the verification of the pads in trigger mode.

To overcome statistical issues, a sample of ~ 12000 would be optimal for a good comparison with the data. However, a large part of the injected into Offline will not even trigger the RPC hodoscope. About 4 million muons were necessary to injected into Offline to have a sample, post-cuts, of 10799. Table 6.4 resumes the statistics of events selections of Sample A.

TABLE 6.4: Events statistics for Sample A.

Sample Selection	Events
Injected	4×10^6
Simulated	1×10^5
After Cuts	10799

The track length and zenith angle distributions, normalized, are represented in Figure 6.13 for the Sample A in comparison with the data (with a different binning that Figure 6.5). A small difference on these distributions was found between the simulation and data, despite both distributions showing similar shapes. The structures found in these distributions are the same, however the discrepancies point towards a larger θ in the data.

The pad combinations have a similar up time so do not explain the differences, which raises the possibility for events with more than one particle triggering the hodoscope and that survive the cuts imposed on the data as an explanation for these differences. A presence of a background contamination from such events with a distribution without angular correlations, i.e., with an uniform zenith angle distribution would help explaining these differences.

Figure 6.14 shows the charge distributions for PMTs 1, 2 and 3 for the Sample A, in comparison with the distributions of the data. The distributions present several differences, even at the peaks of charge.

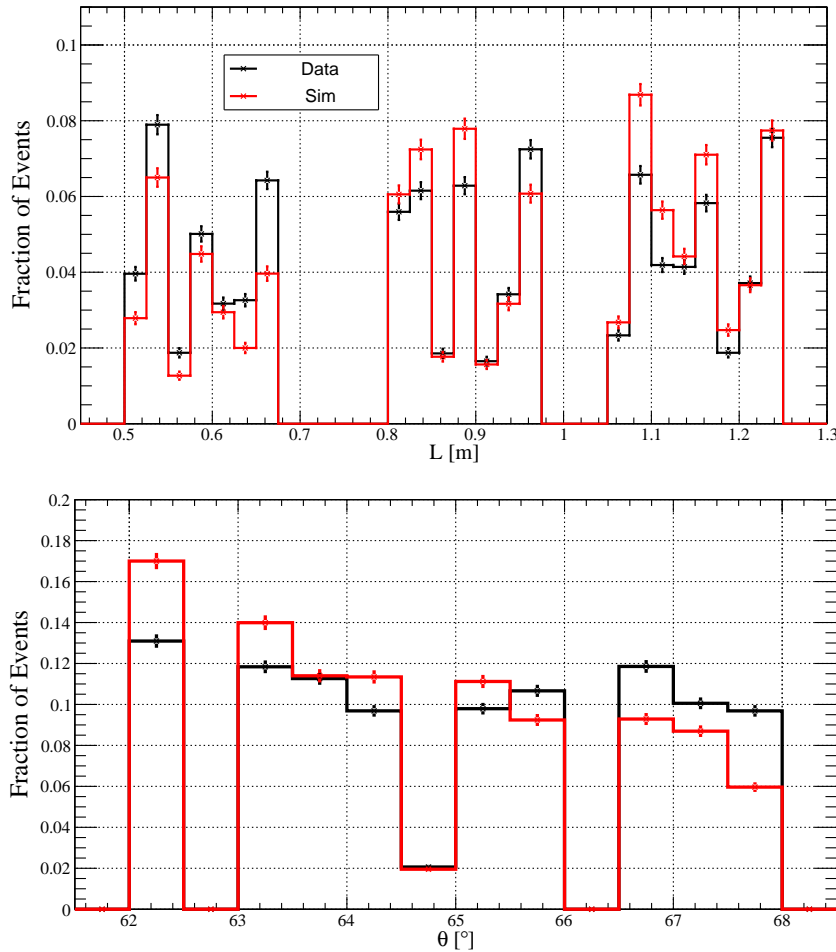


FIGURE 6.13: Up: Track length distributions for the simulated Sample A in comparison with the data. Down: Zenith angle distributions for the simulated Sample A in comparison with the data.

Starting with PMT 1, the data shows three peaks, while in the simulation there are only two, missing a peak for smaller charges. The first peak of the simulation occurs for the same values as the data but the other one occurs for smaller values (in comparison with the data). Additionally, for values higher than 4 VEM, the data distribution shows a tail that is not visible in the simulation.

Given the similarity, PMTs 2 and 3 can be analysed simultaneously. The peak of charge occurs for different values but also the peak is much higher in the simulation and a long tail for higher charges does not exist in the simulations. For comparison, in these PMTs, roughly 89% of the events in the simulations have a charge smaller than 1 VEM, while in the data only $\sim 46\%$ are under this value.

In Figure 6.15, the AoP distributions for PMTs 1, 2 and 3 are displayed as a comparison between the data and the simulation. The simulation's distribution of PMT 1 confirms the previous suspicion of a background contamination in the data, by showing only one peak, while the data shows two. It becomes clear by comparison with the other two PMTs, that the second AoP peak of the data is due to a background contamination and the first one is related with direct Cherenkov effects.

The AoP distributions for PMTs 2 and 3 are, once more, similar as expected. The data and simulation distributions are very similar. Since, as we have seen

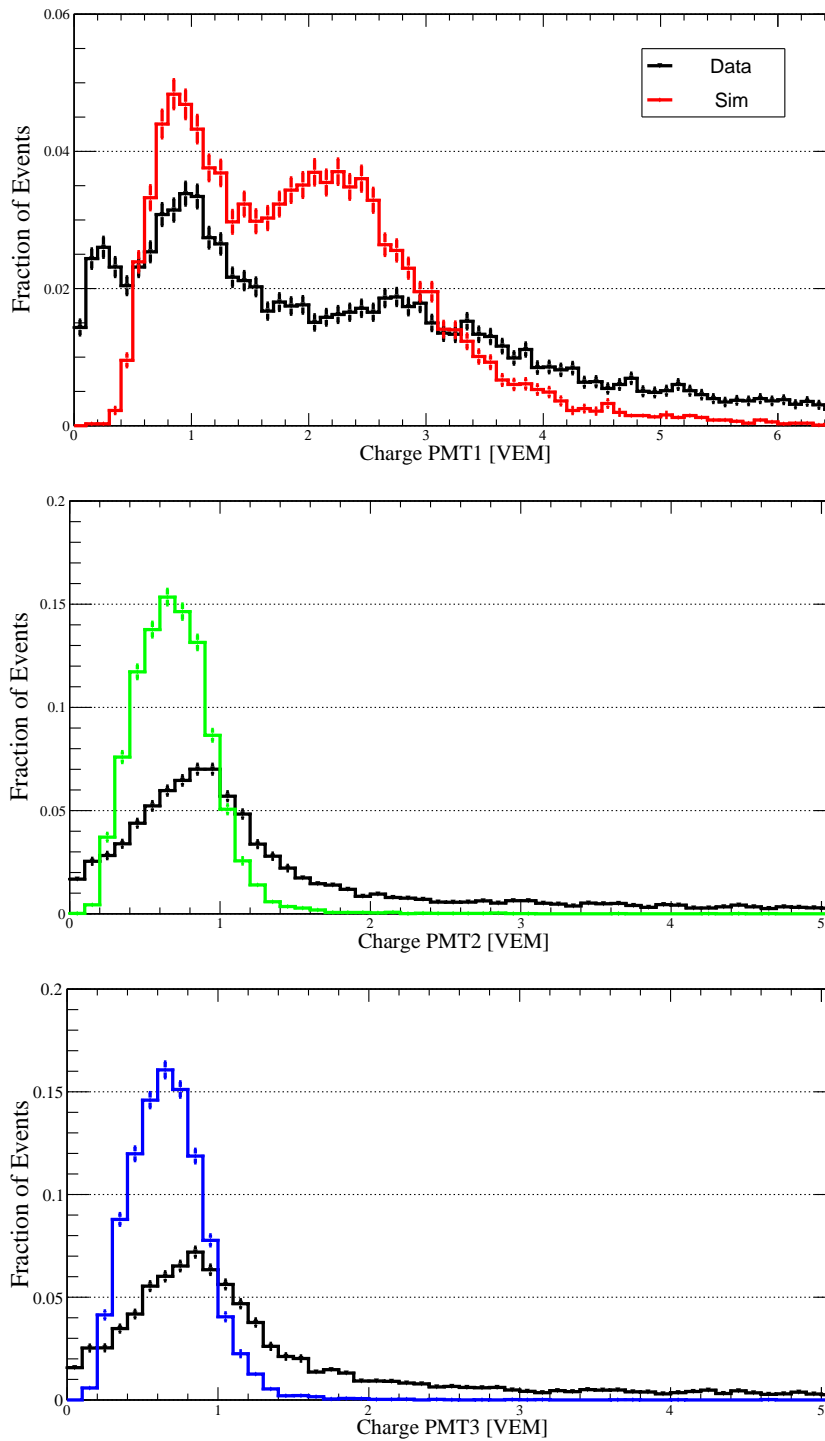


FIGURE 6.14: Comparison between data (in black) and simulation (in color) of the charge distributions for PMTs 1 (up), 2 (middle) and 3 (down).

before, the high charge events follow a tight AoP distribution between 2 and 4, it is more likely that the discrepancies shown in this Figure between data and simulation are due to ageing effects on the tank, which imply a decrease in the AoP with respect to the nominal simulation.

A deeper analysis is needed to understand this differences. From these comparisons, a low peak of charges and a long tail for high charges for all detectors

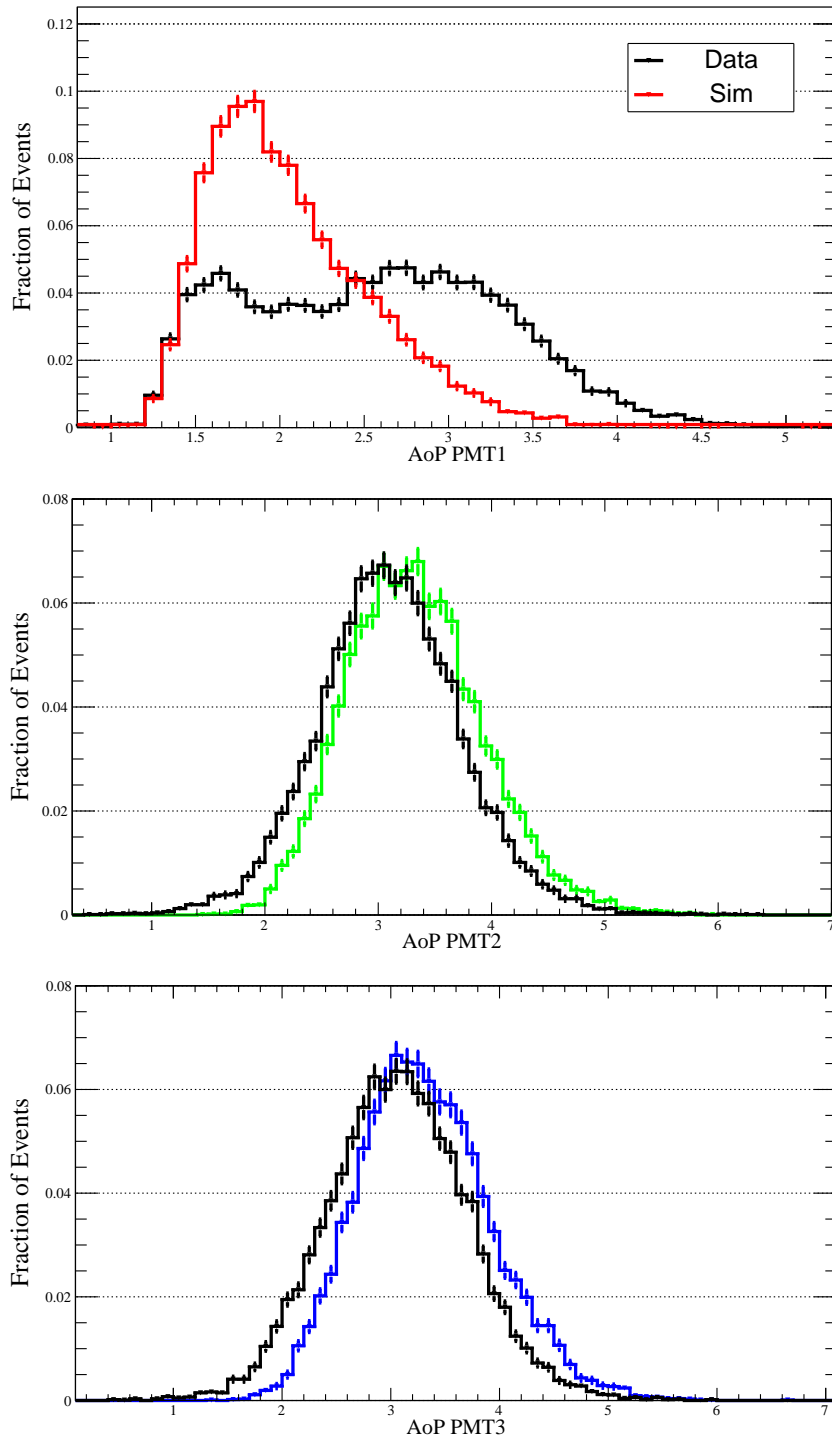


FIGURE 6.15: Comparison between data (in black) and simulation (in color) of the AoP distributions for PMTs 1 (up), 2 (middle) and 3 (down).

remain to be explained.

6.3 Discussion

From the analyses described above, it becomes clear there are discrepancies between the data and the (pure muon) simulation. Even before the comparison with the simulation, the charge distributions of the data appear show to existence of two background contaminations of the data sample, either at small charges, either at high charges.

We pretend now to discuss both contaminations and to address possible explanations for each one. Furthermore, possible solutions to filter these effects from the data are given, so that a comparison with the simulation is possible, namely with respect to direct light effects.

Electrons are the most likely explanation for the small peak in the data. Below are addressed three different possibilities for small charge in the PMTs: electrons triggering the RPC hodoscope, muons decaying into electrons inside the tank and electrons hitting only one RPC and the other hit resulting from a coincidence (or another particle that does not cross the tank).

As for the long tail of events for high charges, it is firstly addressed how much the deflections inside the tank are likely to occur (which would produce higher charge), as well as the influence of the angular restriction used on muons. After this, it will be discussed the likelihood of these events resulting from small showers.

6.3.1 Peak of events for low charge

The peak for small charges found in the data more visible in PMT 1, which has well defined peak. However, this sample of low charge events is present in all PMTs, such that roughly 10% of events have a charge below 0.4 VEM.

No specific pads combination was responsible for these events, with the events spread over all combinations. Therefore, no dependency on L or θ was found.

A time dependency was neither found, implying that the effect is constant and ruling out possible time variation effects.

The smallest possible track length is ~ 0.4 m, therefore, the corresponding signal (~ 0.33 VEM) would be the smallest of the distribution. Apart from fluctuations, events with charge smaller than 0.3 VEM would be very unlikely. In the case of the PMT 1, since it is dominated by direct light effects, the lower limits of charge should even be higher. This was verified in the simulation, where just a negligible fraction of events ($< 0.5\%$) have a charge smaller than 0.4 VEM in PMT 1 (see Figure 6.14).

Three different hypotheses were raised: hodoscope triggers by single electrons, muons decaying into electrons and a combination of a random hit in one RPC and an electron hitting the other.

6.3.1.1 Hodoscope triggers from single electrons

In order to study the possible influence from electrons on the data, the restriction of the injected particles in the simulation was lifted. Instead of injecting only muons, all types of particles were injected³. This sample was called Sample B and

³Photons were not added to the simulation to save processing time, given the fact that they cannot be detected by the RPCs.

the inputs into Offline are characterized in Table 6.5).

Lifting the restriction on the type of particle, implies that the fraction of particles which do not trigger the hodoscope increases, since electrons are more likely to be absorbed in water and, therefore, do not hit the bottom RPC, therefore, even more injected particles will end up not triggering the hodoscope.

TABLE 6.5: Restrictions of the input file used to produce Sample B.

Sample	Type of Particles	θ [°]
B	All (except γ)	[55 – 75] for μ^\pm [0 – 90] for e^\pm

To estimate a possible contamination by a through-going electromagnetic component a large number of particles were injected. A total of 3×10^6 particles were injected over the top RPC. The overwhelming part of the particles do not trigger the hodoscope. Only $\sim 0.9\%$ of the events were stored. After cuts, the number of events was resumed to 3472, of which only 67 were single hits produced exclusively by electrons. This gives a percentage of electrons smaller than 2%. This is summarized in Table 6.6.

TABLE 6.6: Events statistics for Sample B.

Sample Selection	All Particles
Injected	3.8×10^6
Simulated	34245
After Cuts	3472
N_μ	3405
N_e	67

With a maximum of 2% of the events, the through-going electromagnetic component does not hold enough statistics to change the shape of the charge distributions. This shows that, even with a minimum value for L of ~ 0.5 m, which is smaller than half of the tank height, nearly all of the electrons will be absorbed in water. This is also a value too small to be able to justify the small peak of charge, since that peak holds roughly 11% of the events of that distributions. A small value of triggers from the through-going electromagnetic component was already expected since electrons are usually absorbed after crossing 20 cm in water.

6.3.1.2 Muon Decay in the Tank

Events with small charge (< 0.2 VEM) are usually attributed to electrons or to muons decaying into electrons in the tank. However, neither of the scenarios is likely to trigger the hodoscope, since, as stated above, electrons are easily absorbed in the tank.

Assuming that a muon decays near PMT 1 and the electron follow the trajectory on the direction of RPC bottom, the signal detected at PMTs 2 and 3 should be very small. However, this is not the case. The average trace for events with

a charge < 0.4 VEM in PMT 1 is shown in Figure 6.16, for all PMTs. Since there was no restriction for PMTs 2 and 3, they have a higher amplitude due to fluctuations. However, this shows that the signal is also present for the same range in PMTs 2 and 3, which excludes the hypotheses of muons decaying into electrons triggering the RPC hodoscope.

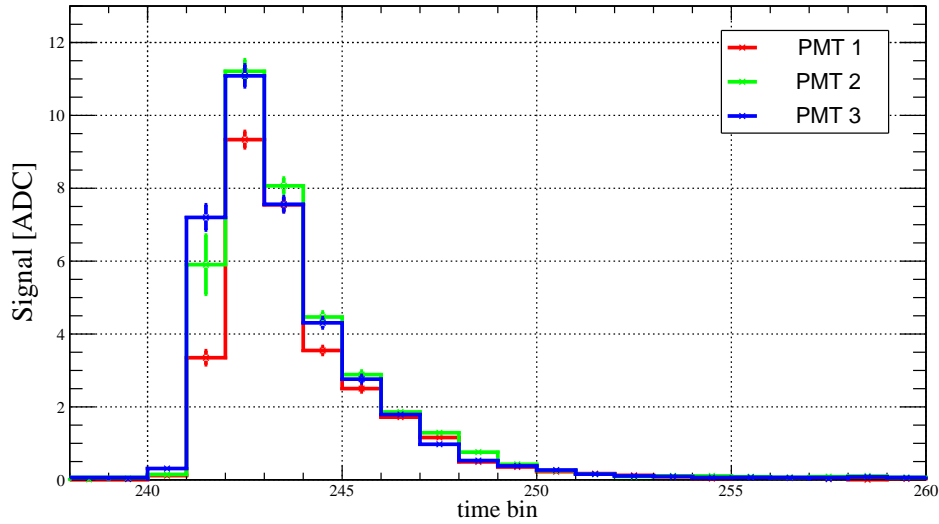


FIGURE 6.16: Average trace for events with less than 0.4 VEM in PMT1, in comparison with the average traces (of the same events) for PMTs 2 and 3. The baseline was removed in all traces for a better perception.

6.3.1.3 Random triggers and single electrons

An explanation for the low charge events are electrons hitting only one of the RPCs and, in the same time window, a muon hitting the other (or some other source). Due to time limitations, it was only possible to study the signal produced by electrons crossing the top RPC. Figure 6.17 shows the charge distribution for all PMTs for the electrons simulation (in color) in comparison with the data distribution for this range. All displayed distributions are normalized to the peak of charge of PMT 1 for small charges for a better comparison.

A peak between 0.2 and 0.3 VEM was found in the electrons distributions. This could be a good explanation for the small peak of charge in PMT 1 (which also present in PMTs 2 and 3, but more attenuated). However, the data charge distributions still shows a high number of events below 0.2 VEM, contrary to this simulation.

It could, however, be explained by the electrons crossing the tank from the corner and hitting the bottom RPC. Given the geometry of the setup, an electron could, for example, cross the tank through the corner in the direction of the RPC Bottom. This would result in a small track length, such that the electron is not absorbed (so it can hit the bottom RPC). Therefore, a very small signal would be sent to the PMTs.

A combination of both scenarios would explain this contamination for small charges.

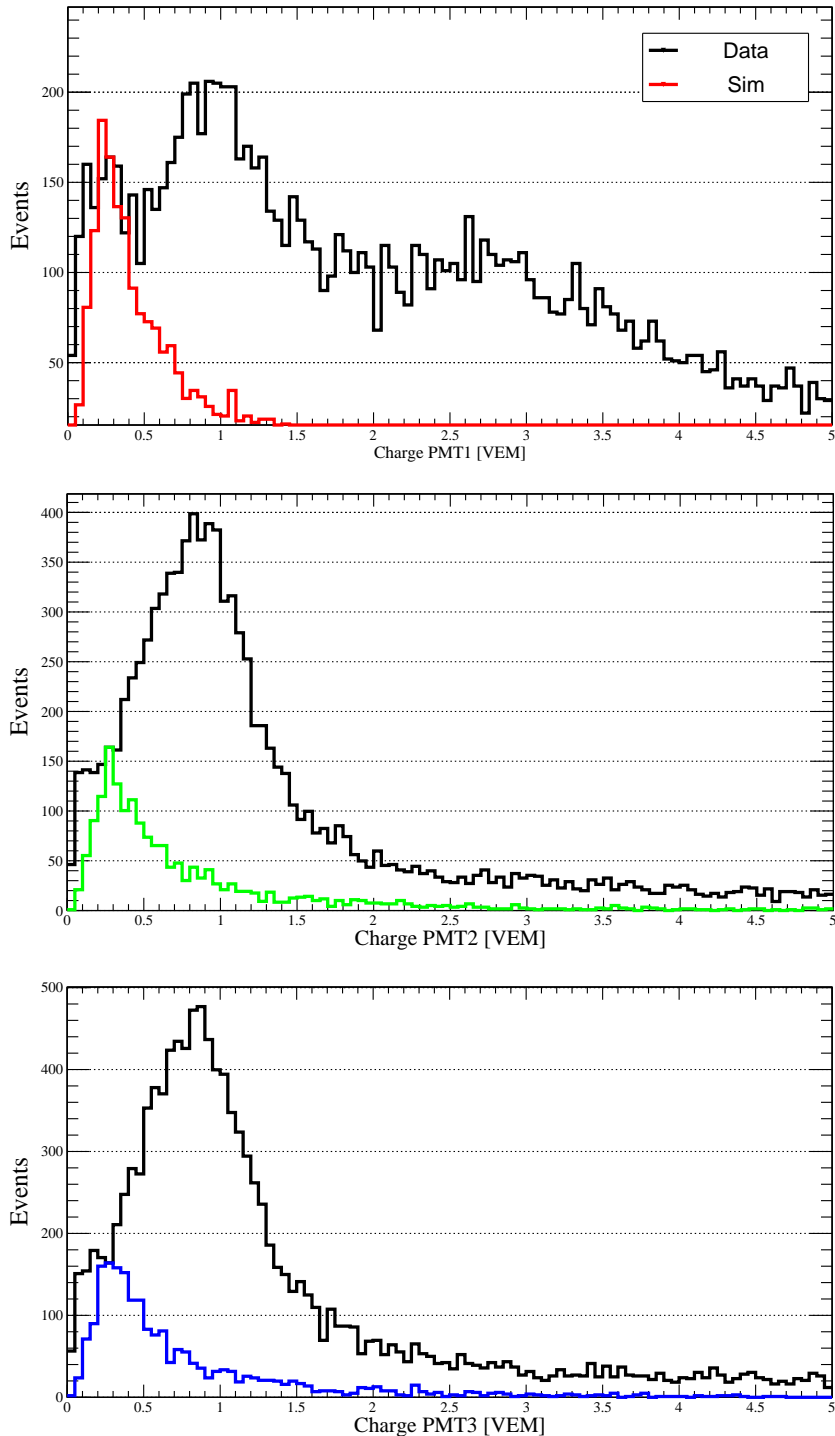


FIGURE 6.17: Charge distributions (normalized to PMT1's first peak of charge) for electrons crossing the top RPC (in color) in comparison with the data (in black) for PMTs 1 (up), 2 (middle) and 3 (down).

6.3.2 High Charge Events

The other feature found in the data and not present in the single muons simulation is the large amount of events with a higher charge than expected, specially higher than 3 VEM. About 2400 events have a charge higher 3 VEM on PMTs 2 and 3, which is nearly 20% of the data.

Figure 6.18 shows, for high charge events, the number of events of each pads combinations. No specific pads combination appears to trigger these events. Therefore, no correlation with L or any other geometric parameter is expected in this data sample. No time dependency was either found on the distribution of these events.

It is, however, worthy to mention that, contrary to high charge events, the muon simulation shows a dependency on the pad combinations, such that it promotes combinations with shorter angles (as we have seen before). Following

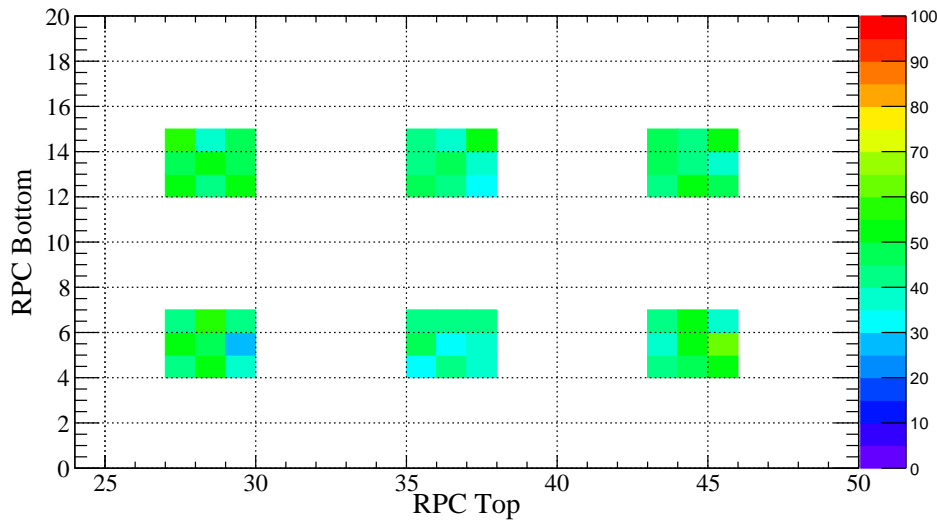


FIGURE 6.18: Number of events for each pads combination. The numbers in the axis give respect to the pads identification. The vertical axis marks the identification of the bottom pads and the horizontal axis marks it for the top pads. The color points the number of events of each combination.

that no correlation with the track length, nor with the pads neither with the time was found, the traces of events with similar characteristics, except for the charge value, can be compared.

In Figure 6.19, two different traces are displayed (one normalized to the peak of the other, for a better trace comparison). Both result from the same pads combination (therefore, have the same reconstructed track length, ~ 1 m) and have a similar AoP value (~ 3.5). However, one has a charge of 0.86 VEM and the other has 6.9 VEM. The traces are very similar. If the high charge trace results from several particles in the tank, this comparison demonstrates that they must arrive in the same time window.

6.3.2.1 Zenith Angle Dependency

No dependency was found in any variable of the data for this setup. However, by using data from previous setups, the angular distribution can be enlarged, allowing for a deeper study of a possible dependency. A correlation with the zenith angle was found and it is displayed in Figure 6.20. Two different groups of data were used, with different angular distributions. One with $\theta \in [20, 50]^\circ$ and another with $\theta \in [50, 70]^\circ$. In data at the analysis in this thesis, with $\theta \in [60, 70]^\circ$, the percentage of high events was about 20%. For a setup with angles in the range $[50, 70]^\circ$, this percentage was $\sim 18\%$ and for the group of data with the

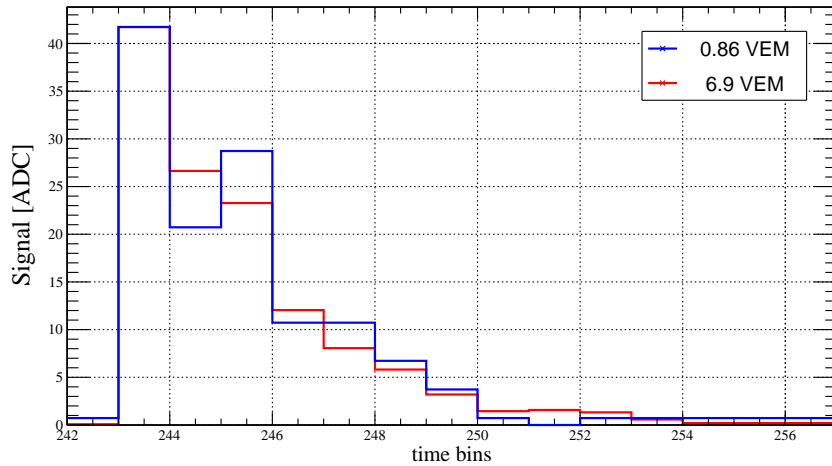


FIGURE 6.19: Comparison of a trace of 6.9 VEM and a trace with 0.86 VEM (normalized to the peak of the former).

shorter angles it was less than 5%. A clear dependency on the zenith angle was found, nonetheless, high charge events are always present.

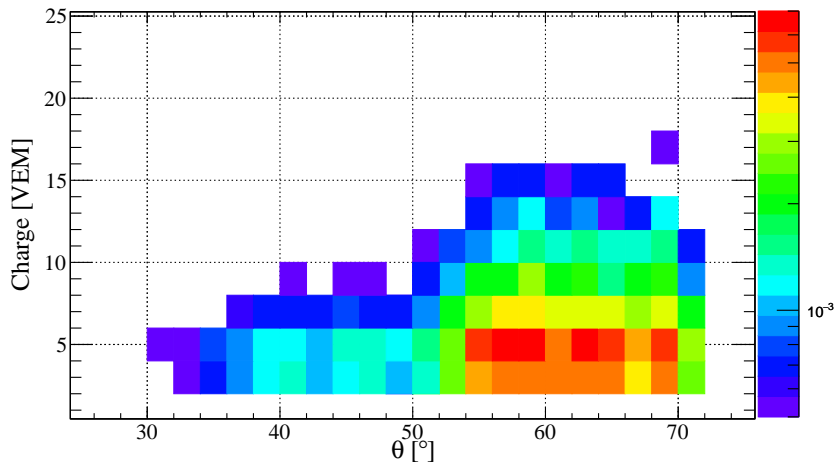


FIGURE 6.20: Variation of the frequency of high charge events with the zenith angle. The color shows the fraction that each angle and charge combination occurred in the data samples.

This dependency, however, could be explained by the dependency on the zenith angle of the flux of atmospheric muons. Assuming a scenario where this flux of high charge events is uniform and non-correlated with any angular parameter, its relevance would change with the flux of muons.

Since for shorter angles the flux of muons is high, this flux of high charge events would remain unnoticed (even if present). However, at inclined angles, the flux of muons suffers a large decay and, therefore, increasing the perception of high charge events.

6.3.2.2 The influence of large deflections

An additional study was performed with the simulation to quantify the deflections suffered by muons and how much it affects the charge distributions. It is expected that few muons suffer significant deflections inside the tank. However, some still occur and this can be quantified by using the geometric condition that was explained in Section 6.2.2.

One can analyse the variation of a component of the momentum. In a situa-

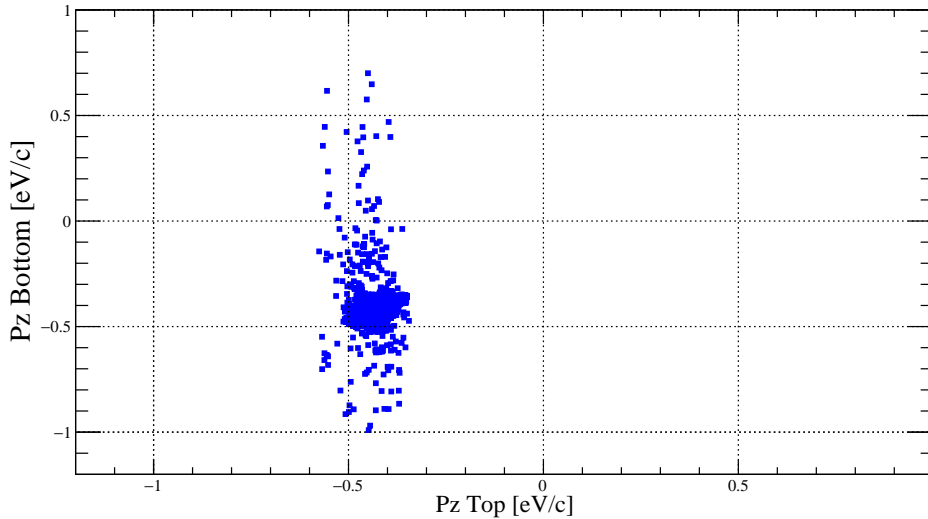


FIGURE 6.21: P_z variation between bottom and top RPCs in Sample A.

tion with no deflections, the values of a component of the momentum should be equal at both RPCs. Otherwise, if the values are different, then some deflection occurred.

Figure 6.21 shows the variation of the values of the component z of the momentum for Sample A. A larger distribution of the values at the bottom RPC was noticed. This confirms the existence of the deflections. More than that, this Figure tells that some deflections occurred at the bottom of the tank. The muons had, initially, a negative value for p_z but ended up with a positive value when they reached the bottom RPC. By another words, this tells that the muons suffered a deflection at the bottom of the tank, shifting their trajectory upwards, in the direction of the bottom RPC.

Using the Offline Framework and the detailed information about each particle, we conservatively estimated that $\sim 10\%$ of the muons suffer large deflections. Lifting the angular restriction does not have a significant impart in this estimation.

However, and as conclusion, the most is more important for this work is that the charge distributions show very small changes if the contributions from these deflections were removed.

6.3.2.3 Possible contamination by Small Showers

These discrepancies between the data and the simulation should be explained by some unaccounted background source. The events of high charge described above are an evidence of these differences. These contaminations introduce a

shift in the charge peak towards higher charges.

We study there are three possibilities which could justify this background: malfunctioning of the PMTs, single muons with high charge or small showers.

If a PMT was not working properly in a way that would justify an increase of the charge, in principle that would also be visible in of the calibration histograms. As we have seen in Chapter 5, the calibration was stable. Not only this but a malfunctioning of the PMT would not be able to justify the zenith angle dependency of high charge events, since it is impossible for the PMTs to infer the trajectories of the muons (except for the case of direct effects).

The energy range of atmospheric muons and their interaction with the water, as well as the diffusion of the Cherenkov light are well studied. It is not expected for a single muon to produce a charge inside the WCD as high as 7 VEM. Even more, there seems to be no immediate explanation to explain why would these muons with high charge be less likely at shorter angles.

From the hypotheses that we raise, small showers is the likely one. A few charged particles from a shower could produce a high signal at the tank. Furthermore, there are several possible justifications to explain the zenith angle dependency found for high charge events. Given the dependency of atmospheric muons with the zenith angle, the larger the angles we study are, the smaller is the flux and, therefore, more relevant would the contribution of the background from small showers become. By another words, if we assume that small showers triggers are stored by the test tank with no zenith angle dependency and have a constant rate through time or any other geometric parameter, the rate of these showers would be enhanced when the flux of atmospheric muons became much lower. It was also noticed that the geometric efficiency of the hodoscope increases with the number of particles (see Appendix D).

Furthermore, the high charges occur simultaneously for all PMTs, corroborating the possibility for several particles inside the tank. This relation is demonstrated in Figure 6.22. Finally, the trace analysis described above (see Figure 6.19) suggests that, in the case high charge results from several particles, they arrived in the same time window. This points to a shower of particles (which, by definition, have the same origin) instead of random coincidences of atmospheric particles.

A detailed simulation would be necessary to surpass these issues (which

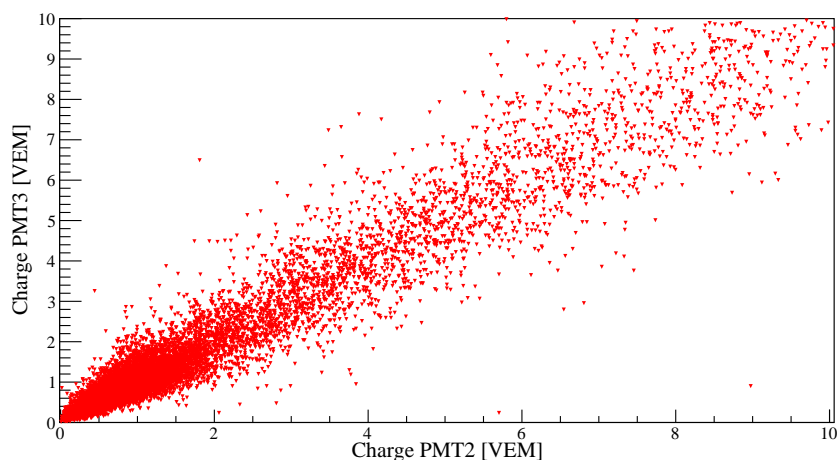


FIGURE 6.22: Correction between the charge distribution of PMTs 2 and 3.

it was not done due to time limitations). To quantify the background contaminations with the simulation, the Offline Software Framework would have to account for small showers triggering the hodoscope, and also consider the electrons contributions described above. Only a full simulation would allow for a precise quantification of both background effects, so that a proper study of the response of the WCD could be performed.

6.3.3 Response of the water-Cherenkov detector

Following the previous assumptions, we can try to analyse the response of the tank in these conditions, by either trying to account for how much should these backgrounds affect the distributions, or by selecting a sample of events which should be free from the contaminations.

This was used to analyse how should the charge peaks in the data be after by the contaminations, how they vary with L and how different they are from the simulation.

Another point addressed and described below, is an attempt to filter a sample of events composed only by muons provoking direct effects, so that it can be compared to the simulation.

6.3.3.1 WCD Response to Inclined Muons

The variation of the charge peak with the length of the particles in the water is a good approach to study the response of the WCD to inclined muons. As discussed in Chapter 3, a linear dependence of the charge with the track length is expected. However, as stated before, this can only be verified for well diffused light, which is not the case when direct light effects occur.

Since filtering well diffused light from non-diffused light is a complicated task, the analysis of the linearity between the track length and the charge has been performed only to PMTs 2 and 3.

To analyse the variation of the charge with the track length, the data was separated in several groups, according to their reconstructed trajectories' length inside the water tank. From Figure 6.5 (up) it is observed that the data can be easily separated in nine different groups. Such segmentation on the track length distribution occurs due to the pad segmentation of the RPCs.

There are nine different charge distributions, each one of them associated with a different reconstructed track length value. As explained in the first experiment with this test tank [125], the amplitude of the signal collected by a PMT is proportional to length of the muon inside the tank. This is replicated in Figure 6.23, which shows traces from PMT 2 for different intervals of track length. As expected, there is an increase of the amplitude with L .

Each one of the nine groups had an average of 1300 events. Each charge distribution was analysed and a Gaussian function was fitted around its peak of charge. The fit range was chosen dynamically in order to avoid fluctuations that introduce a high error. Several intervals around the peak were analysed and the one with the best χ^2 value and the smallest error in the peak determination was selected. Figure 6.24 shows a charge distribution for muons with trajectories between 0.8 m and 0.9 m. The adjusted fit and the output parameters are also displayed.

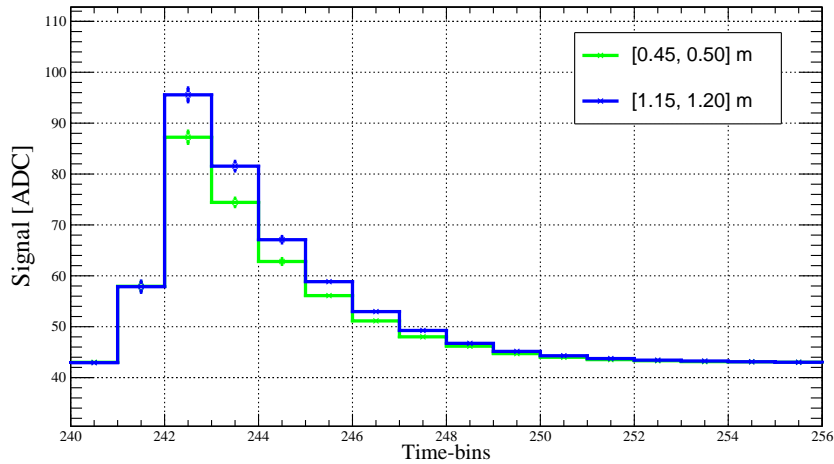


FIGURE 6.23: Average trace signal of PMT 2 for different intervals of track length.

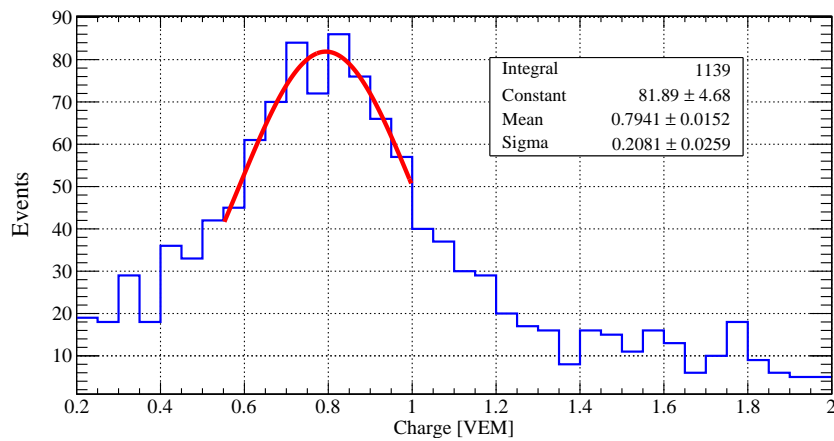


FIGURE 6.24: Example of a charge distribution of PMT 2 for a track length range between 0.8 and 0.9 m and the adjusted fit.

The value of the peak of charge can be obtained from the Gaussian fit and, by replicating the same procedure to all track length groups, the dependence of this peak with L can be determined.

The same proceeding as described above for the data was applied to the simulation, step by step. Figure 6.25 displays the results of all fits adjusted to the peak of charge for the different distributions for PMTs 2 and 3, for the data and for the simulation.

Despite the contaminations found in the data, two expectations that match a single muon distribution were verified: PMTs 2 and 3 show similar distributions and the peak of charge increases with L . This could suggest that the contaminations are only shifting the charge peaks and that it might be possible to overcome this discrepancy by using some conversion factor.

As expected, the distributions for the data and simulation show different behaviours. In a hypothetical scenario, the disagreement implies that either there is a track length shift of 0.2 to 0.35 m, or there is a charge discrepancy up to 0.2 VEM. The geometry was carefully measured and implemented in the simulation,

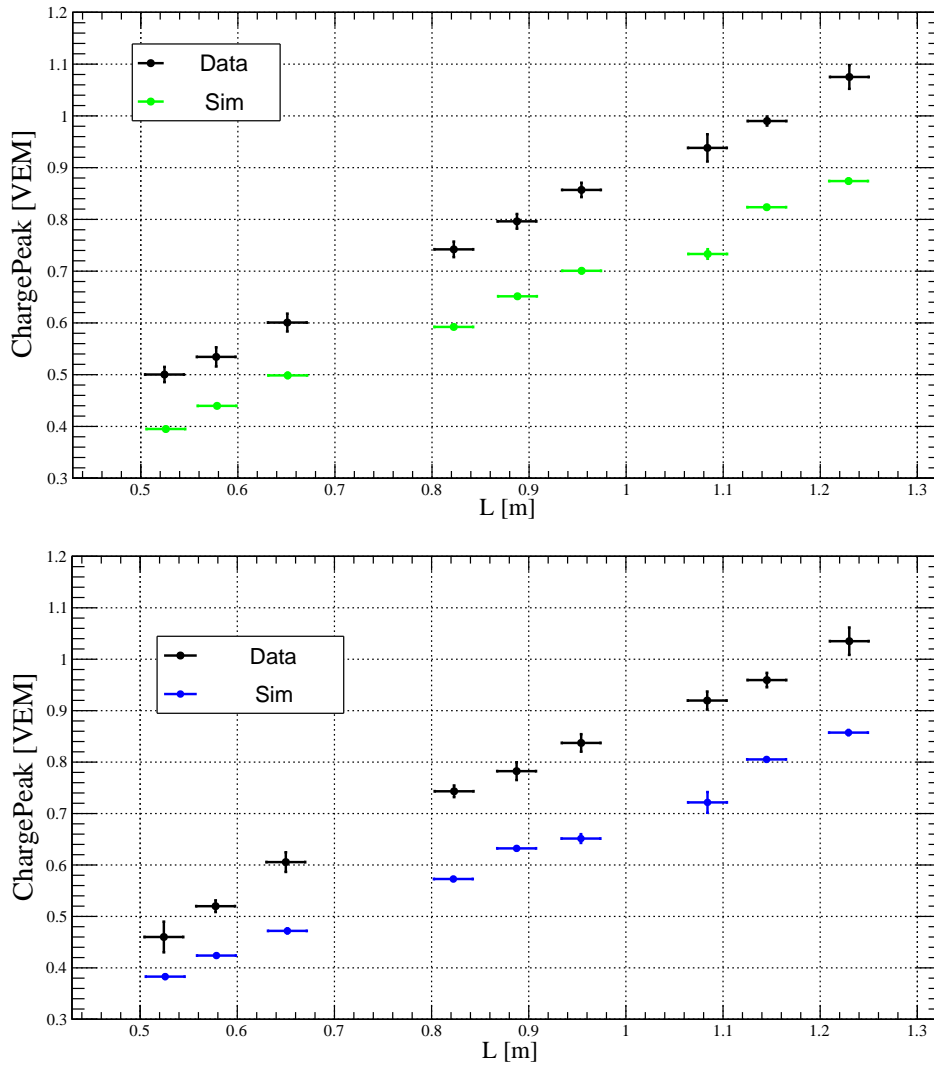


FIGURE 6.25: Variation of the peak of charge with the length reconstructed track inside the WCD for data (in black) and simulation (in color) for PMTs 2 (up) and 3 (down).

which excludes the first hypothesis. A difference up to 0.2 VEM also seems unlikely, since nothing was noticed in previous analyses for shorter angles.

A new approach was taken to overcome this issue. A rescaling factor was introduced in the data, so that it could be compared with the simulation without the possible contribution by the contamination. The points of the data were normalized to the first point of the simulation.

The result is displayed in Figure 6.26 for PMTs 2 and 3. Within uncertainties, this results points to an agreement between simulation and the data calibrated to the first point. This could suggest that the simulation is describing well the response of the tank, despite the disagreements found, on the premise that the bias introduced by the showers background is eliminated by the re-normalization procedure. However, further analysis are required to support this argument, namely to either quantify with more precision the possible contaminations or by using a new sample, free from any contamination.

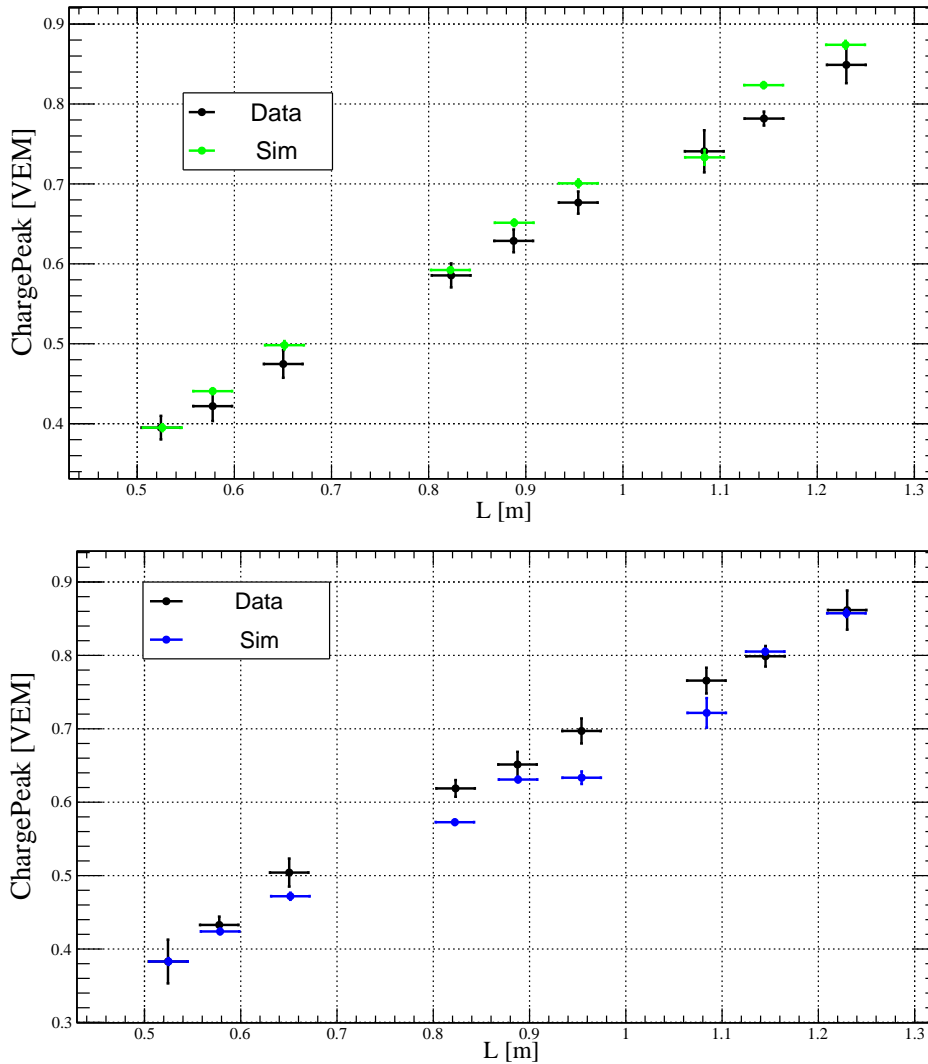


FIGURE 6.26: Comparison between data and simulation of the charge peak's variation with the reconstructed length of the path inside the WCD for PMT 2 (up) and 3 (down), with the data normalized to the first point of the simulation.

6.3.3.2 WCD Response to Direct Cherenkov Effects

The relation between charge and AoP can be used to characterize the discrepancies between data and simulation, as it was done in Section 6.1.5 to characterize direct light effects.

Figure 6.27 compares the data and simulation's values of the charge vs AoP relation for PMT 1. The simulation's values for PMT 1 confirm the analysis performed in Section 6.1.5, and allows to conclude that the tail of high charges and low AoP values belongs to direct effects, as demonstrated by the simulation.

From the analysis of these distributions, a last study that can be made to the response of the WCD is its response to direct light effects.

From the normalized AoP distributions for data and simulation of PMTs 1, 2 and 3, displayed before in Figure 6.15, it becomes clear that direct effects have a low AoP.

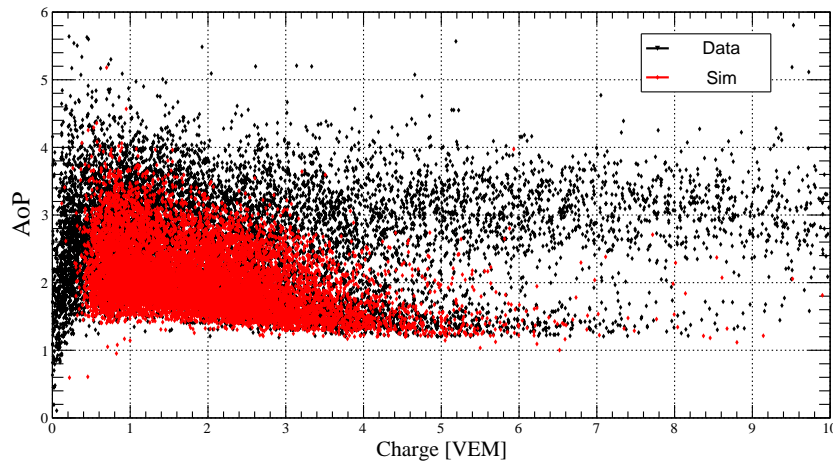


FIGURE 6.27: Comparison between Data and Simulation of the Charge vs AoP distributions of PMT 1.

The data distribution for PMT 1 shows a peak compatible with the simulation, which is expected to be the result of direct light effects, plus a second contribution which might arrive from the showers background. It would be expected that the second peak in PMT 1 results from the small showers contamination. , the normalized distributions for data and simulation of PMT 1 are compared with the data distribution for PMT 2. This represents a possible explanation of PMT 1's AoP behaviour.

Then, a way to compare the data and simulation of PMT 1 is to impose a cut in the AoP at 2 and ignore events with a higher AoP in both data and simulation. Additionally, the charge was also restricted to values higher than 2 VEM. This would select a sample of single muons whose trajectories imply direct effects and also free of background, either the peak for low charges, either the tail for high charges, as it can be seen in Figure 6.27.

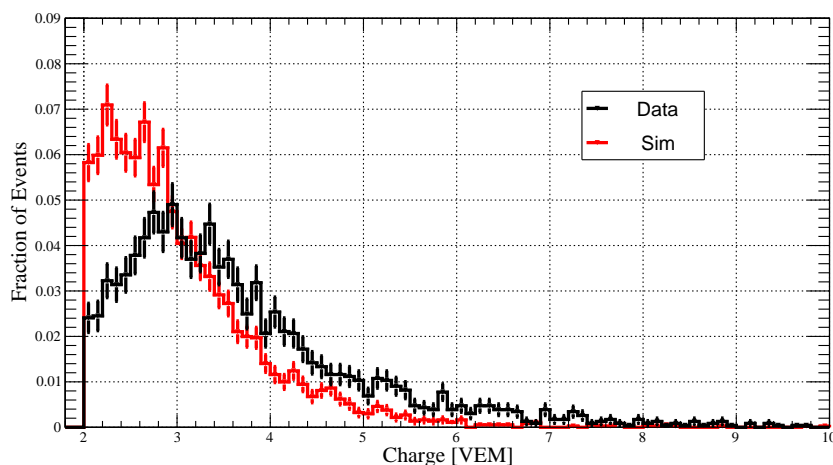


FIGURE 6.28: Normalized charged distributions for PMT1 for events with AoP < 2 and Charge > 2 VEM.

Figure 6.28 shows the normalized charge distribution for PMT 1 of the events which survived the AoP cut. A shift to higher charges was observed and we

found no immediate explanation. Using the full simulation (in order to simulate the Cherenkov in the glass) does not change significantly the charge distributions.

6.4 Final Notes

Due to background contaminations in the data was not possible to perform a precise analysis of the response of the WCD to inclined muons. A detailed simulation which allows to account for the contributions from small showers and electrons paired with uncorrelated hits would be required to quantify these backgrounds.

Additionally, a new acquisition might be useful for a full study of the response of inclined muons. From this study it becomes clear the difficulties that such measurements face. The experimental setup has a very complex configuration and requires a good control of all aspects.

The study of the response of the water Cherenkov detector to muons according to their trajectory is based on reconstructions performed through the RPC hodoscope. However, this reconstruction assumes that the singles hits in the RPCs were provoked by single muons which is not always the case, as we have seen in this analysis.

When the flux of atmospheric muons is high, as it occurred from the previous analyses with the Gianni Navarra test tank, this extra effects are statistically negligible. However, inclined muons have a lower flux, so that these effects can no longer be ignored. This can be easily noticed in the data selection analysis, where only $\sim 4\%$ of the aligned events were used for the analysis.

A possible future acquisition should increase the number of the pads in both RPCs, so that the angular range is increased, allowing an angular study with the same experimental setup.

One would gain with the recently developed RPCs electronics which allows to store the time. Having access, with precision, to the time from hits in the RPC would be an easy solution to assure that the single hits are originated by the same muon. Since most of them travel very close to the speed of light, they do not take more than 10 ns to cross the hodoscope. Time discrepancies higher than this value (or smaller, although, statistically unexpected) would imply that the hits were not provoked by the same muon.

Conclusion

In the last one hundred years, the field of Cosmic Rays went from non-existent to one of the most intriguing areas to study the mysteries of the Universe. The studies of Cosmic Rays opened the way for Particles and Astroparticles Physics. Their importance is well recognized by the scientific community, such that their discoverer was awarded with the Nobel Prize in 1936.

The dynamics of this field have been constantly changing. The works of the first half of the last century were mostly confined to small experiments, with just some detectors and led to the discovery of several particles, such as the positron and the muon. After WWII, Particles and Astroparticles Physics start to disentangle due to the invention of particles accelerators. Gradually, due the discovery of extensive air showers, the studies of Cosmic Rays became more focused in large observatories.

One of the most remarkable features of Cosmic Rays is their range of energies, especially at the highest energies, where collisions in the atmosphere occur at center of mass energies, nearly 100 times higher than currently possible at LHC. Nowadays, Telescope Array and the Pierre Auger Observatory are the biggest experiments at the extremely high energies. Both operate with a hybrid design, combining a surface array of detectors with fluorescence telescopes, which allows for a more complete understanding of air showers.

Recent analyses performed to hybrid events collected, with zenith angles larger than 60° , by the Pierre Auger Collaboration showed disagreements between data and simulations, with a deficit on the muon content up to 80% in the simulation. However, large uncertainties were associated with these measurements, namely uncertainties on the energy scale of the Auger SD and in the WCD response to inclined muons. Further analyses are required to decrease them.

A test tank was equipped with a RPC hodoscope to track the trajectories of charged particles crossing it. This hodoscope allows to perform a proper analysis of the response of the WCD to muons and how much it varies with the muons' trajectories (i.e., angles and track length in water). Additionally, ageing effects in the tank can also be studied. Previous analyses with this test tank to muons with zenith angles smaller than 55° showed that the simulations produced by the Offline Software Framework are describing well the response of the water Cherenkov detector, with uncertainties not higher than 2%.

In this work, in order to address the uncertainties associated with the muon content measurements at inclined angles and as a sequence from the studies with the test tank, the RPC hodoscope was positioned to collect muons with angles $> 60^\circ$.

After a careful monitoring of the detectors and a selection of the data, a sample of ~ 12000 events was collected, with $\theta \in [62, 68]^\circ$. Due to the impact point at the surface of the tank and the inclination of the particles, one of the PMTs was subjected to direct Cherenkov light effects.

The comparison with the (pure muon) simulation showed two main disagreements: a peak for small charges and a long tail for high charges. Both cases can be explained by different sources of unaccounted background.

The peak for small charges can be explained by electrons in coincidence with uncorrelated hits. The electrons can hit the top RPC while a random hit (from a muon, for example) hits the bottom one, leaving a small charge in the PMTs, peaking between 0.2 VEM and 0.3 VEM. Another situation are electrons crossing the tank from the corner and hitting the bottom RPC (while the top one suffers a random hit). This would produce a smaller charge than the first situation, since the electrons would travel a short distance inside the tank.

The long tail for high charges is possibly due to small showers reaching the tank and producing single hits in the RPC hodoscope. An analysis to the signal traces showed that, in case this high signals are the result of several particles inside the tank, they must arrive simultaneously. This would be expected for showers and not for random particles in the tank. Additionally, a comparison with previous experimental setups revealed a zenith angle variation in the fraction of these events. This could be explained by the zenith angle dependency of the flux of muons. Since in previous setup experiments the angle was shorter, the flux was higher than in this experiment, making this high charge events statistically less relevant.

The analysis to the charge peak variation as a function of the reconstructed track length showed an agreement, within uncertainties, between data and simulation, if the bias introduced by background contamination in the charge distributions can be eliminated by renormalization of the data by a calibration factor.

By applying some filters in charge and AoP, the response of the tank to direct Cherenkov light effects was also addressed. The results showed a disagreement between data and simulation and no immediate explanation was possible to obtain.

A more detailed simulation, including small showers, would be required to quantify the background contamination. Additionally, a new acquisition, with an enlarged angular range, could help overcoming the issues found in this analysis, so that the open questions about the response of the WCD to inclined muons can be answered.

Appendix A

Kolhörster and Bothe's Coincidence Experiment: probability of two electrons to be produced by a gamma ray

In 1929, Kolhörster and Bothe performed an experiment which allowed them to conclude that cosmic rays are corpuscular [4]. Through the use of the coincidence technique in two Geiger-Müller tubes, they argued that cosmic rays could not be gamma rays. They defended that the probability of a gamma ray to produce two electrons is too small to justify the number of coincidences that they measured.

The coincidence fraction is the number of coincidences over the total particles detected by the lower counter, and it is proportional to the probability of a single ray to produce one electron per each counter.

In their experiment, the two German physicists, had a shield of thickness X and then two Geiger-Müller counters, separated by an absorber. A gamma ray must produce an electron, by Compton effect, on the shield and then it must be detected by the upper counter. By the same process, another electron needs to be produced in the absorber and be detected by the lower counter. Figure A.1 illustrates this process.

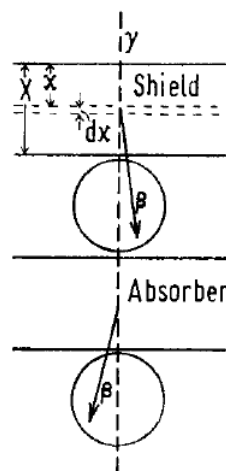


FIGURE A.1: Illustration of a γ ray producing two electrons [4].

One can define the scattering coefficient of the γ rays as μ and the absorption coefficient of the secondary rays in the shield by α . The probability of a vertical gamma ray produces a secondary electron is given by:

$$w_1 = \int_0^X \mu e^{-\mu x - \alpha(X-x)} dx \quad (\text{A.1})$$

Analogously, the same can be obtained for the emission of an electron to the second counter. Let us define that probability by w_2 . The probability of obtaining a coincidence, i.e., an electron in both counters, is given by $w_1 w_2$. Therefore, the coincidence fraction, r , is:

$$r = \frac{w_1 w_2}{w_2} = w_1 \quad (\text{A.2})$$

This implies that the probability that a single gamma ray produces a coincidence on the counters is proportional to w_1 . In the experiment performed by Bothe and Kolhörster, the upper limit for w_1 is 0.01. The measured coincidence fraction was $r_{measured} = 0.095$. Since $r_{measured} \gg w_1$, then one can conclude that the coincidences cannot have origin on gamma rays.

Appendix B

Calculation of the GZK energy limit

In 1964, Penzias and Wilson discovered the CMB which had repercussions over the Cosmic Rays field. In 1966, Greisen and, apart, Kuzmin and Zatsepin, proposed a limit to the energy spectrum of Cosmic Rays, due to the interaction of these with the CMB. One can summarize this process, such as:

$$p + \gamma_{CMB} \rightarrow p + \pi^0 \quad (\text{B.1})$$

The 4-vector relating the momentum and energy of a particle is given by $P^\mu = (E, \vec{p})$. The dot product of two 4-vectors is invariant:

$$P_\mu P^\mu = EE - \vec{p} \cdot \vec{p} = E^2 - p^2 = m^2 = s \quad (\text{B.2})$$

where m is the rest mass.

Considering now the case of photopion production in interactions between cosmic rays protons and γ_{CMB} , we have that the center of mass energy squared is:

$$s = (E_\gamma + E_p)^2 - (\vec{p}_\gamma \cdot \vec{p}_p)^2 \quad (\text{B.3})$$

Since $s = (m_\pi + m_p)^2$, once the squares are developed, it follows:

$$E_\gamma^2 + E_p^2 + 2E_\gamma E_p - p_\gamma^2 - p_p^2 - 2\vec{p}_\gamma \cdot \vec{p}_p = m_\pi^2 + m_p^2 + 2m_\pi m_p \quad (\text{B.4})$$

From equation B.2, $E_\gamma^2 - p_\gamma^2 = m_\pi^2 = 0$ and $E_p^2 - p_p^2 = m_p^2$. Replacing this in equation B.4, one can obtain that:

$$2E_\gamma E_p - 2|\vec{p}_\gamma||\vec{p}_p| \cos(\theta) = m_\pi^2 + 2m_\pi m_p \quad (\text{B.5})$$

The minimum energy required for this interaction would occur in a frontal collision ($\theta = 180^\circ$), which follows that $2|\vec{p}_\gamma||\vec{p}_p| \cos(\theta) = E_\gamma E_p$. The threshold energy to produce a pion is, then, given by:

$$E_{p(threshold)} = \frac{m_\pi^2 + 2m_\pi m_p}{4E_\gamma} \quad (\text{B.6})$$

According to last PDG report (2016) [64] $m_p \sim 938.27 \text{ MeV}/c^2$ and $m_{\pi^0} \sim 134.97 \text{ MeV}/c^2$. For a relativistic gas, the energy per particle is given by $E = 3k_B T$, where k_B is the Boltzmann's constant. Since the temperature for CMB photons is 2.725 K, it follows that $E_\gamma \sim 7 \times 10^{-4} \text{ eV}$. Finally, replacing all the values in the previous equation, we obtain:

$$E_{p(threshold)} \sim 9 \times 10^{19} \text{ eV} \quad (\text{B.7})$$

It would be expected that protons with an energy above this limit would lose energy through pion production, due to the interaction with CMB. Nonetheless there are some photons from the CMB more energetic than the mean value used for this calculation.

The mean free path for photo-pion production is given by:

$$\lambda_{p\gamma} = \frac{1}{\langle N_{CMB} \rangle \sigma_{p\gamma}} \quad (\text{B.8})$$

With N_{CMB} being the average photons density of the CMB and $\sigma_{p\gamma}$ is the cross-section for proton-photon interaction. The value for N_{CMB} lies between 400 and 500 photons per cm^3 and $\sigma_{p\gamma} \sim 2.4 \times 10^{24} \text{ cm}^2$. Following this, $\lambda_{p\gamma} \sim 10$ Mpc, which is the mean path that protons travel until they interact. On average, a proton should lose around 20% of its energy on each interaction, which means that after ~ 10 interactions (or ~ 100 Mpc) the energy of the proton should be lower by at least an order of magnitude.

Appendix C

Semi-Analytical Monte Carlos simulation for the hodoscope geometric efficiency determination

In order to estimate a value for the geometric efficiency for the configuration of the RPC hodoscope, a Monte Carlo simulation was created. For that, points between the limits of a pad were uniformly generated in the top RPC and the goal is to determine the fraction that reaches a specific pad in the bottom RPC. To determine the trail, angles θ and ϕ were associated to each point. Uniform values between 0 and 2π were generated for the azimuthal, while the zenith angle needs to recreate the atmospheric flux of muons, so it was generated between 0 and π , since muons arriving from the ground are very unlikely, but with a distribution proportional to $\cos^2(\theta) \sin(\theta)$ (see Section 4.2.2).

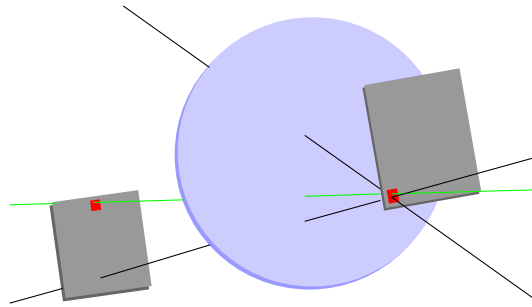


FIGURE C.1: Representation of the Gianni Navarra configuration, by a top view. In the right is represented the top RPC and in the left the bottom one. The blue circle represents the Water-Cherenkov Tank. We considered trajectories that cross a pad on the top RPC and we will determine the fraction that reaches a selected pad of the bottom RPC.

The next step is to determine the plane equation for our bottom RPC and to determine the line equation of the trajectory. Starting with the plane equation, we can determine the equation by using three point of the RPC. Let them be $A(A_x, A_y, A_z)$, $B(B_x, B_y, B_z)$ and $C(C_x, C_y, C_z)$. Using these points, the vectors \vec{AC} and \vec{AB} can be calculated, as well as the vector $\vec{n} = (n_x, n_y, n_z) = \vec{AC} \otimes \vec{AB}$, which is the normal vector to the plane. The plane equation is, then, given by:

$$\vec{n} \cdot (\vec{P} - \vec{P}_0) = 0 \quad (\text{C.1})$$

Where $\vec{P} = (x, y, z)$ and \vec{P}_0 is a point of the plane. Randomly choosing the point A, follows that $n_x(x - A_x) + n_y(y - A_y) + n_z(z - A_z) = 0$. Defining a constant d such as $d = -(n_x A_x + n_y A_y + n_z A_z)$, the final plane equation is:

$$n_x x + n_y y + n_z z = d \quad (\text{C.2})$$

For the line equation, we need to find a new point to determine our vector director. One shall start with the random point obtained by the Monte Carlo simulation, $\vec{P}_1 = (P_{1x}, P_{1y}, P_{1z})$, that is restricted by the geometry of the RPC. Using the angles that were generated, another random point \vec{P}_2 that belongs to the same line as \vec{P}_1 . By trigonometric calculations, follows that $\vec{P}_2 = (P_{2x}, P_{2y}, P_{2z}) = (r \cos(\phi) \tan(\theta) + P_{1x}, r \sin(\phi) \tan(\theta) + P_{1y}, P_{2z})$ where $r = P_{2z} - P_{1z}$ and P_{2z} is the z coordinate of the point P_2 , which can be randomly chosen. So, the line equation is given by:

$$\vec{r}(t) = (P_{1x}, P_{1y}, P_{1z}) + t(P_{2x} - P_{1x}, P_{2y} - P_{1y}, P_{2z} - P_{1z}). \quad (\text{C.3})$$

Now, one needs to substitute the equation C.3 in the equation C.2, such that:

$$n_x(P_{1x} + t(P_{2x} - P_{1x})) + n_y(P_{1y} + t(P_{2y} - P_{1y})) + n_z(P_{1z} + t(P_{2z} - P_{1z})) = d \quad (\text{C.4})$$

The next step is to solve equation C.4 for t:

$$t = \frac{d - \vec{n} \cdot \vec{P}_1}{\vec{n} \cdot (\vec{P}_2 - \vec{P}_1)} \quad (\text{C.5})$$

To end the calculation, one only needs to replace the value of t in the line equation to find the point of intersection between the plane and the line. Let the intersection point be defined by I:

$$\begin{aligned} I = & (P_{1x} + \frac{d - \vec{n} \cdot \vec{P}_1}{\vec{n} \cdot (\vec{P}_2 - \vec{P}_1)} \cdot (P_{2x} - P_{1x}), \\ & P_{1y} + \frac{d - \vec{n} \cdot \vec{P}_1}{\vec{n} \cdot (\vec{P}_2 - \vec{P}_1)} \cdot (P_{2y} - P_{1y}), \\ & P_{1z} + \frac{d - \vec{n} \cdot \vec{P}_1}{\vec{n} \cdot (\vec{P}_2 - \vec{P}_1)} \cdot (P_{2z} - P_{1z})) \end{aligned} \quad (\text{C.6})$$

To finish the Monte Carlo simulation, it is verified if the intersection point I is between the limits of the pad (in the bottom RPC), in order to determine the fraction of particles that reach it.

Appendix D

Monte Carlo Calculation: Hodoscope geometric efficiency with small showers

To estimate the probability of single hits in the RPC hodoscope, a Monte Carlo calculation was produced. The goal is to obtain the trigger probability as a function of the number of particles considered. The procedure was very similar to the estimated rate for single muons, described in Section 4.4.2. It was assumed that the particles arrive at the experimental setup in the same 100 ns time window.

Given the test tank configuration, there are four different situations which can produce a trigger. Therefore, there are four different geometric efficiencies to determine. Let them be defined as ε_1 , ε_2 , ε_3 and ε_4 , such that:

- ε_1 - The particles that enter the tank also trigger the hodoscope, producing single hits.
- ε_2 - The particles that enter the tank produce a hit in the top RPC and the hit at bottom RPC is produced by particles that do not enter the tank.
- ε_3 - The particles that enter the tank produce a hit in the bottom RPC and the hit at top RPC is produced by particles that do not enter the tank.
- ε_4 - None of the single hits produced at the hodoscope are provoked by particles crossing the tank.

The sum of these efficiencies gives the total geometric efficiencies provoked by small showers. Let n be the number of particles, from 1 to 15. For each value of n , each probability ε was determined.

To do that, several events, with a particle density of n per tank volume, were generated with random zenith and azimuth angles, such that $\theta \in [0, \pi/2]^\circ$ and $\phi \in [0, \pi]^\circ$. For events with $n > 1$, the particles have a angular distribution within 10° to each other, since particles from a shower have similar angles. Using these generated particles, it was determined if the RPC hodoscope was triggered by a hit and a hit only in each RPC. It was then determined how likely it is for the hodoscope to be triggered for each n .

The results of this calculation are displayed in Figure D.1, for each ε , where the total sum is represented by the black dots. This estimative suggests that having ten particles (in the same time window) in the tank increases the probability of

having single hits triggers by a factor of ~ 100 in relation to having only one particle.

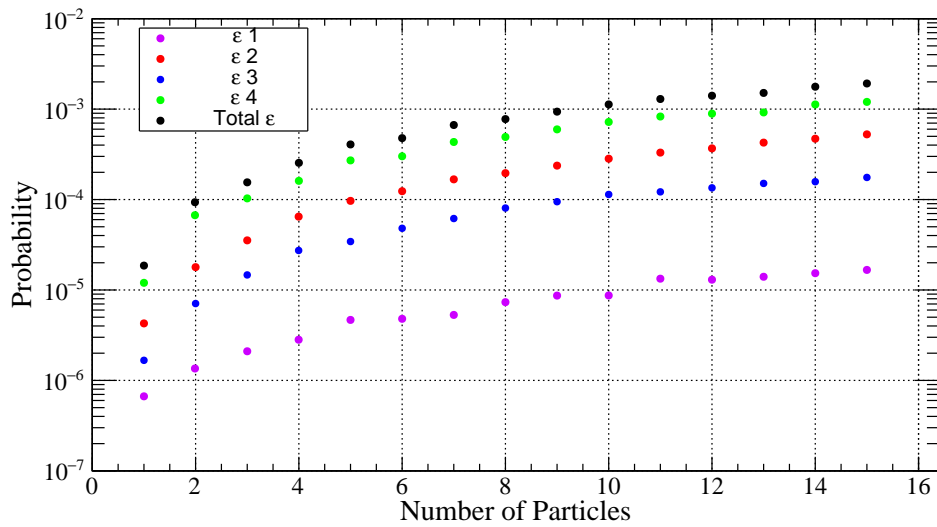


FIGURE D.1: Single hits trigger efficiency of the hodoscope as a function of the number of particles. The total hodoscope geometric efficiency is represented in black.

Bibliography

- [1] Alessandro De Angelis. "Atmospheric ionization and cosmic rays: Studies and measurements before 1912". In: *Astroparticle Physics* 53.C (2014), pp. 19–26. ISSN: 09276505. DOI: 10.1016/j.astropartphys.2013.05.010. URL: <http://dx.doi.org/10.1016/j.nuclphysbps.2013.05.001>.
- [2] Per Carlson and Alessandro De Angelis. "Nationalism and internationalism in science: The case of the discovery of cosmic rays". In: *European Physical Journal H* 35.4 (2010), pp. 309–329. ISSN: 21026459. DOI: 10.1140/epjh/e2011-10033-6. arXiv: 1012.5068.
- [3] Vitalii L. Ginzburg. "Cosmic ray astrophysics (history and general review)". In: *Physics-Uspeski* 39.2 (1996), pp. 155–168. ISSN: 1063-7869. DOI: 10.1070/PU1996v039n02ABEH000132. URL: <http://stacks.iop.org/1063-7869/39/i=2/a=A03>.
- [4] W. Kolhörster W. Bothe. "2. The Nature of the High-altitude Radiation". In: 777.1929 (1929), pp. 148–167.
- [5] Arthur H. Compton. "A Geographic Study of Cosmic Rays". In: *Physical Review Letters* 56.January (1933), pp. 2419–2422. ISSN: 0031-9007. DOI: 10.1103/PhysRevLett.3.32.
- [6] Bruno Rossi. "Directional Measurements on the Cosmic Rays Near the Geomagnetic Equator". In: *Physical Review* 45.3 (1934), pp. 212–214. ISSN: 0031899X. DOI: 10.1103/PhysRev.45.212.
- [7] Marcel Schein, William P. Jesse, and E. O. Wollan. "The nature of the primary cosmic radiation and the origin of the mesotron [4]". In: *Physical Review* 59.7 (1941), p. 615. ISSN: 0031899X. DOI: 10.1103/PhysRev.59.615.
- [8] David Darling. *Cloud Chamber*. 2016. URL: http://www.daviddarling.info/encyclopedia/C/cloud_chamber.html.
- [9] Carl D. Anderson. "The positive electron". In: *Physical Review* 43.6 (1933), pp. 491–494. ISSN: 0031899X. DOI: 10.1103/PhysRev.43.491.
- [10] Seth H. Neddermeyer and Carl D. Anderson. "Note on the nature of Cosmic Ray Particles". In: *Physical Review* 51.1936 (1937), pp. 1–7. ISSN: 0033-2941. DOI: 10.2466/pr0.1969.24.2.487.
- [11] C. M. G. Lattes et al. "Processes Involving Charged Mesons". In: *Nature* 159.4047 (1947), pp. 694–697. ISSN: 0028-0836. DOI: 10.1038/159694a0. URL: <http://www.nature.com/doifinder/10.1038/159694a0>{\% }5Cn<http://www.wendelsantos.com.br/sistema/download/ArtigoLattes.pdf>{\% }5Cn<http://www.nature.com/doifinder/10.1038/159694a0>.
- [12] V. D. Hopper and S. Biswas. "Evidence Concerning the Existence of the New Unstable Elementary Neutral Particle". In: *Physical Review* (1950), pp. 1099–1101.

- [13] Luisa Bonolis. "From cosmic ray physics to cosmic ray astronomy: Bruno Rossi and the opening of new windows on the universe". In: *Astroparticle Physics* 53.C (2014), pp. 67–85. ISSN: 09276505. DOI: 10.1016/j.astropartphys.2013.05.008. arXiv: arXiv:1211.4061v1.
- [14] H. Bethe and W. Heitler. "On the Stopping of Fast Particles and the Creation of Positive Electrons". In: *Proceedings of the Royal Society of London Series A* (1934). ISSN: 1364-5021. DOI: 10.1098/rspa.1983.0054.
- [15] Karl-Heinz Kampert and Alan A. Watson. "Extensive Air Showers and Ultra High-Energy Cosmic Rays : A Historical Review". In: *Flying* (2012), pp. 1–56. DOI: 10.1140/epjh/e2012-30013-x. arXiv: arXiv:1207.4827v1.
- [16] Paolo Maestro. "Cosmic rays: direct measurements". In: (2015). arXiv: 1510.07683. URL: <http://arxiv.org/abs/1510.07683>.
- [17] R. Sparvoli. "Direct measurements of cosmic rays in space". In: *Nuclear Physics B - Proceedings Supplements* 239-240 (2013), pp. 115–122. ISSN: 09205632. DOI: 10.1016/j.nuclphysbps.2013.05.019. URL: <http://linkinghub.elsevier.com/retrieve/pii/S0920563213003964>.
- [18] Peter K.F. Grieder. *Cosmic Rays at Earth*. Elsevier, 2001.
- [19] W. D. Apel et al. "Ankle-like feature in the energy spectrum of light elements of cosmic rays observed with KASCADE-Grande". In: *Physical Review D - Particles, Fields, Gravitation and Cosmology* 87.8 (2013), pp. 1–5. ISSN: 15507998. DOI: 10.1103/PhysRevD.87.081101. arXiv: 1304.7114.
- [20] Andreas Haungs. "Cosmic Rays from the Knee to the Ankle". In: *Physics Procedia* 61 (2015), pp. 425–434. ISSN: 1875-3892. DOI: <http://dx.doi.org/10.1016/j.phpro.2014.12.094>. URL: <http://www.sciencedirect.com/science/article/pii/S187538921400707X>.
- [21] ScienceDaily. *Karlsruhe Institute of Technology*. "Cosmic rays: Galactic knee and extragalactic ankle." 2013. URL: www.sciencedaily.com/releases/2013/06/130603113350.htm.
- [22] Cern Timelines. *Fly's Eye detects record-breaking cosmic ray*. 2016. URL: <http://timeline.web.cern.ch/fly%E2%80%99s-eye-detects-record-breaking-cosmic-ray-32-x-1020-ev>.
- [23] Pierre Auger Observatory. *Internal Report Gap 2015-092*. 2015.
- [24] R. Battiston et al. "Cosmic ray physics from low to extreme energies: Status and perspectives". In: *Advances in Space Research* 37.10 (2006). Astrophysics, pp. 1834–1840. ISSN: 0273-1177. DOI: <https://doi.org/10.1016/j.asr.2006.03.015>. URL: <http://www.sciencedirect.com/science/article/pii/S0273117706001438>.
- [25] T. Antoni et al. "KASCADE measurements of energy spectra for elemental groups of cosmic rays: Results and open problems". In: *Astroparticle Physics* 24.1–2 (2005), pp. 1–25. ISSN: 0927-6505. DOI: <https://doi.org/10.1016/j.astropartphys.2005.04.001>. URL: <http://www.sciencedirect.com/science/article/pii/S0927650505000691>.

- [26] Roberto Aloisio. "The Physics of UHECRs: Spectra, Composition and the Transition Galactic-Extragalactic". In: *2016 Conference on Ultrahigh Energy Cosmic Rays (UHECR2016) Kyoto, Japan, October 11-14, 2016*. 2017. arXiv: 1704.07110 [astro-ph.HE]. URL: <https://inspirehep.net/record/1594696/files/arXiv:1704.07110.pdf>.
- [27] R. Aloisio, V. Berezhinsky, and A. Gazizov. "Transition from galactic to extragalactic cosmic rays". In: *Astropart. Phys.* 39-40 (2012), pp. 129–143. DOI: 10.1016/j.astropartphys.2012.09.007. arXiv: 1211.0494 [astro-ph.HE].
- [28] V. Berezhinsky, A. Z. Gazizov, and S. I. Grigorieva. "On astrophysical solution to ultrahigh-energy cosmic rays". In: *Phys. Rev. D* 74 (2006), p. 043005. DOI: 10.1103/PhysRevD.74.043005. arXiv: hep-ph/0204357 [hep-ph].
- [29] R. U. Abbasi et al. "Study of Ultra-High Energy Cosmic Ray composition using Telescope Array's Middle Drum detector and surface array in hybrid mode". In: *Astropart. Phys.* 64 (2015), pp. 49–62. DOI: 10.1016/j.astropartphys.2014.11.004. arXiv: 1408.1726 [astro-ph.HE].
- [30] R. U. Abbasi et al. "First observation of the Greisen-Zatsepin-Kuzmin suppression". In: *Physical Review Letters* 100.10 (2008), pp. 1–5. ISSN: 00319007. DOI: 10.1103/PhysRevLett.100.101101. arXiv: 0703099 [astro-ph].
- [31] Inés Valiño. "The flux of ultra-high energy cosmic rays after ten years of operation of the Pierre Auger Observatory". In: *PoS (ICRC 2015)* (2015).
- [32] K. Greisen. "End to the cosmic-ray spectrum?" In: *Physical Review Letters* 16.17 (1966), pp. 748–750. URL: <http://www.scopus.com/inward/record.url?eid=2-s2.0-4243270502&partnerID=40&md5=0c304a6111fd377ab03c210d779be7ea>.
- [33] G. T. Zatsepin and V. A. Kuzmin. "Upper Limit of the spectrum of cosmic rays". In: *JEPT Lett.* 4 (1966), p. 78.
- [34] Valerio Verzi, Dmitri Ivanov, and Yoshiki Tsunesada. "Measurement of Energy Spectrum of Ultra-High Energy Cosmic Rays". In: (2017). arXiv: 1705.09111 [astro-ph.HE].
- [35] J.W. Cronin. "Cosmic rays: The most energetic particles in the universe". In: *Reviews of Modern Physics* 71.SUPPL. 2 (1999), S165–S172. URL: <http://www.scopus.com/inward/record.url?eid=2-s2.0-0033098370&partnerID=40&md5=4f181a64129f55bf0be5971d6cb7bcc1>.
- [36] Alessandro De Angelis and Mário João Martins Pimenta. *Introduction to particle and astroparticle physics: Questions to the universe*. Springer, 2015, pp. 1–661. ISBN: 9788847026889. DOI: 10.1007/978-88-470-2688-9.
- [37] J. J. Beatty, J. Matthews, and S.P. Wakely. "Review of Particle Physics: Cosmic Rays". In: *Chin. Phys.* 4.August 2015 (2016), pp. 1–22.
- [38] Pierre Auger Observatory. *Internal Report Gap 2016-029*. 2016.
- [39] Alessio Porcelli. "Measurements of X_{max} above 10^{17} eV with the fluorescence detector of the Pierre Auger Observatory". In: *PoS (ICRC 2015)* (2015).
- [40] Dmitri Ivanov. "TA Spectrum Summary". In: *PoS ICRC2015* (2016), p. 349.

- [41] R. Abbasi et al. "Report of the Working Group on the Composition of Ultra High Energy Cosmic Rays". In: *Proceedings of International Symposium for Ultra-High Energy Cosmic Rays (UHECR2014)*. DOI: 10.7566/JPSCP.9.010016. eprint: <http://journals.jps.jp/doi/pdf/10.7566/JPSCP.9.010016>. URL: <http://journals.jps.jp/doi/abs/10.7566/JPSCP.9.010016>.
- [42] M. S. Longhair. *High Energy Astrophysics*. Cambridge University Press, 2011. ISBN: 9780521756181.
- [43] Enrico Fermi. *On the Origin of the Cosmic Radiation*. 1949.
- [44] R. D. Blandford and J. P. Ostriker. "Particle Acceleration by Astrophysical Shocks". In: *Astrophysical Journal* 221 (1978), pp. L29–L32.
- [45] R J Protheroe. *Acceleration and Interaction of Ultra High Energy Cosmic Rays*. 1998. arXiv: 9812055v1 [arXiv:astro-ph].
- [46] Pijushpani Bhattacharjee and Günter Sigl. "Origin and propagation of extremely high-energy cosmic rays". In: *Physics Reports* 327.3–4 (2000), pp. 109–247. ISSN: 0370-1573. DOI: [https://doi.org/10.1016/S0370-1573\(99\)00101-5](https://doi.org/10.1016/S0370-1573(99)00101-5). URL: <http://www.sciencedirect.com/science/article/pii/S0370157399001015>.
- [47] Daniel Kuempel. "Search for Ultra-High Energy Photons with the Pierre Auger Observatory". In: *AIP Conf. Proc.* 1792.1 (2017), p. 070012. DOI: 10.1063/1.4969009. arXiv: 1611.08110 [astro-ph.HE].
- [48] A. M. Hillas. "The Origin of Ultra-High-Energy Cosmic Rays". In: *Annual Review of Astronomy and Astrophysics* 22.1 (1984), pp. 425–444. DOI: 10.1146/annurev.aa.22.090184.002233. eprint: <http://dx.doi.org/10.1146/annurev.aa.22.090184.002233>. URL: <http://dx.doi.org/10.1146/annurev.aa.22.090184.002233>.
- [49] Luis Anchordoqui et al. "Ultrahigh Energy Cosmic Rays: The state of the art before the Auger Observatory". In: *Int. J. Mod. Phys. A* 18 (2003), pp. 2229–2366. arXiv: 0206072v3 [arXiv:hep-ph].
- [50] Julien Aublin. "Arrival directions of the highest-energy cosmic rays detected with the Pierre Auger Observatory". In: *PoS (ICRC 2015)* (2015).
- [51] R. Abbasi et al for IceCube Collaboration. "Measurement of the Anisotropy of Cosmic-ray Arrival Directions with IceCube". In: *The Astrophysical Journal Letters* 718.2 (2010), p. L194. URL: <http://stacks.iop.org/2041-8205/718/i=2/a=L194>.
- [52] A. A. Abdo et al. "The Large-Scale Cosmic-Ray Anisotropy as Observed with Milagro". In: *The Astrophysical Journal* 698.2 (2009), p. 2121. URL: <http://stacks.iop.org/0004-637X/698/i=2/a=2121>.
- [53] B. R. Dawson et al. *Past, Present and Future of UHECR Observations*. 2017. arXiv: arXiv:1703.07897v2.
- [54] Alexander Aab et al. "Multi-resolution anisotropy studies of ultrahigh-energy cosmic rays detected at the Pierre Auger Observatory". In: *JCAP* (2016). arXiv: 1611.06812 [astro-ph.HE].
- [55] O. Deligny. "Cosmic-Ray Anisotropies: A Review". In: *25th European Cosmic Ray Symposium (ECRS 2016) Turin, Italy, September 04-09, 2016*. 2016. arXiv: 1612.08002 [astro-ph.HE]. URL: <https://inspirehep.net/record/1505720/files/arXiv:1612.08002.pdf>.

- [56] Alexander Aab et al. "Observation of a Large-scale Anisotropy in the Arrival Directions of Cosmic Rays above 8×10^{18} eV". In: *Science* 357.6537 (2017), pp. 1266–1270. DOI: 10.1126/science.aan4338. arXiv: 1709.07321 [astro-ph.HE].
- [57] S. Abdollahi et al. "Cosmic-ray electron-positron spectrum from 7 GeV to 2 TeV with the Fermi Large Area Telescope". In: *Phys. Rev. D* 95.8 (2017), p. 082007. DOI: 10.1103/PhysRevD.95.082007. arXiv: 1704.07195 [astro-ph.HE].
- [58] A. D. Panov. "Electrons and Positrons in Cosmic Rays". In: *J. Phys. Conf. Ser.* 409 (2013), p. 012004. DOI: 10.1088/1742-6596/409/1/012004. arXiv: 1303.6118 [astro-ph.HE].
- [59] Francesco Nozzoli. "Precision measurement of antiproton to proton ratio with the Alpha Magnetic Spectrometer on the International Space Station". In: *25th European Cosmic Ray Symposium (ECRS 2016) Turin, Italy, September 04-09, 2016*. 2016. arXiv: 1701.00086 [astro-ph.HE]. URL: <https://inspirehep.net/record/1507423/files/arXiv:1701.00086.pdf>.
- [60] Nicola Tomassetti. "AMS-02 in space: physics results, overview, and challenges". In: *Nucl. Part. Phys. Proc.* 265-266 (2015), pp. 245–247. DOI: 10.1016/j.nuclphysbps.2015.06.063. arXiv: 1511.00052 [astro-ph.HE].
- [61] K Greisen. "Cosmic Ray Showers". In: *Annual Review of Nuclear Science* 10.1 (1960), pp. 63–108. DOI: 10.1146/annurev.ns.10.120160.000431. eprint: <https://doi.org/10.1146/annurev.ns.10.120160.000431>. URL: <https://doi.org/10.1146/annurev.ns.10.120160.000431>.
- [62] Antoine Letessier-Selvon and Todor Stanev. "Ultrahigh energy cosmic rays". In: *Rev. Mod. Phys.* 83 (3 2011), pp. 907–942. DOI: 10.1103/RevModPhys.83.907. URL: <https://link.aps.org/doi/10.1103/RevModPhys.83.907>.
- [63] Claus Grupen. *Astroparticle Physics*. Springer Science and Business Media, 2005.
- [64] C. Patrignani et al. "Review of Particle Physics". In: *Chin. Phys.* C40.10 (2016), p. 100001. DOI: 10.1088/1674-1137/40/10/100001.
- [65] Ralph Engel, Dieter Heck, and Tanguy Pierog. "Extensive air showers and hadronic interactions at high energy". In: *Ann. Rev. Nucl. Part. Sci.* 61 (2011), pp. 467–489. DOI: 10.1146/annurev.nucl.012809.104544.
- [66] J. Matthews. "A Heitler model of extensive air showers". In: *Astroparticle Physics* 22.5-6 (2005), pp. 387–397. ISSN: 09276505. DOI: 10.1016/j.astropartphys.2004.09.003.
- [67] Pierre Auger Collaboration. "Plans for a Proposal to Upgrade the Pierre Auger Observatory". Auger Internal Report. 2013.
- [68] T. K. Gaisser and A. M. Hillas. "Reliability of the method of constant intensity cuts for reconstructing the average development of vertical showers". In: *Proceedings of the International Cosmic Ray Conference* 8 (1977), pp. 353–357.

- [69] “The Pierre Auger Cosmic Ray Observatory”. In: *Nuclear Instruments and Methods in Physics Research Section A: Accelerators, Spectrometers, Detectors and Associated Equipment* 798 (2015), pp. 172–213. ISSN: 0168-9002. DOI: <http://dx.doi.org/10.1016/j.nima.2015.06.058>. URL: <http://www.sciencedirect.com/science/article/pii/S0168900215008086>.
- [70] D. Barnhill et al. “Measurement of the lateral distribution function of UHECR air showers with the Pierre Auger Observatory”. In: *29th International Cosmic Ray Conference (ICRC 2005) Pune, India, August 3-11, 2005*. [7,291(2005)]. 2005, p. 291. arXiv: astro-ph/0507590 [astro-ph]. URL: http://lss.fnal.gov/cgi-bin/find_paper.pl?conf-05-302-E-TD.
- [71] David J Griffiths. *Introduction to elementary particles; 2nd rev. version*. Physics textbook. New York, NY: Wiley, 2008. URL: <https://cds.cern.ch/record/111880>.
- [72] S. Bethke. “Determination of the QCD coupling α_s ”. In: *J. Phys. G26* (2000), R27. DOI: 10.1088/0954-3899/26/7/201. arXiv: hep-ex/0004021 [hep-ex].
- [73] T. Pierog and K. Werner. “EPOS Model and Ultra High Energy Cosmic Rays”. In: *Nuclear Physics B - Proceedings Supplements* 196 (2009). Proceedings of the XV International Symposium on Very High Energy Cosmic Ray Interactions (ISVHECRI 2008), pp. 102–105. ISSN: 0920-5632. DOI: <http://dx.doi.org/10.1016/j.nuclphysbps.2009.09.017>. URL: <http://www.sciencedirect.com/science/article/pii/S0920563209006537>.
- [74] S. Ostapchenko. “Non-linear effects in high energy hadronic interactions”. In: *INFN Eloisatron Project 44th Workshop on QCD at Cosmic Energies: The Highest Energy Cosmic Rays and QCD Erice, Italy, August 29-September 5, 2004*. 2005. arXiv: hep-ph/0501093 [hep-ph].
- [75] Sergey Ostapchenko. “Monte Carlo treatment of hadronic interactions in enhanced Pomeron scheme: I. QGSJET-II model”. In: *Phys. Rev. D* 83 (2011), p. 014018. DOI: 10.1103/PhysRevD.83.014018. arXiv: 1010.1869 [hep-ph].
- [76] T. Pierog et al. “EPOS LHC: Test of collective hadronization with data measured at the CERN Large Hadron Collider”. In: *Phys. Rev. C* 92.3 (2015), p. 034906. DOI: 10.1103/PhysRevC.92.034906. arXiv: 1306.0121 [hep-ph].
- [77] Sergey Ostapchenko. “LHC results and hadronic interaction models”. In: *25th European Cosmic Ray Symposium (ECRS 2016) Turin, Italy, September 04-09, 2016*. 2016. arXiv: 1612.09461 [astro-ph.HE]. URL: <https://inspirehep.net/record/1507284/files/arXiv:1612.09461.pdf>.
- [78] J. Engel et al. “Nucleus-nucleus collisions and interpretation of cosmic-ray cascades”. In: *Phys. Rev. D* 46 (11 1992), pp. 5013–5025. DOI: 10.1103/PhysRevD.46.5013. URL: <https://link.aps.org/doi/10.1103/PhysRevD.46.5013>.
- [79] D. Heck et al. *CORSIKA: a Monte Carlo code to simulate extensive air showers*. Feb. 1998.

- [80] S. J. Sciutto. *AIRES: A System for air shower simulations. User's guide and reference manual. Version 2.2.0.* 1999. arXiv: astro-ph/9911331 [astro-ph].
- [81] T. Pierog et al. "First results of fast one-dimensional hybrid simulation of EAS using CONEX". In: *Nucl. Phys. Proc. Suppl.* 151 (2006), pp. 159–162. DOI: 10.1016/j.nuclphysbps.2005.07.029. arXiv: astro-ph/0411260 [astro-ph].
- [82] Jeferson A. Ortiz, Gustavo A. Medina Tanco, and V. de Souza. "Longitudinal development of extensive air showers: Hybrid code SENECA and full Monte Carlo". In: *Astropart. Phys.* 23 (2005), pp. 463–476. DOI: 10.1016/j.astropartphys.2005.02.007. arXiv: astro-ph/0411421 [astro-ph].
- [83] A. M. Hillas. "Two interesting techniques for Monte-Carlo simulation of very high energy hadron cascades". In: *International Cosmic Ray Conference 8* (1981), pp. 193–196.
- [84] Hans-Joachim Drescher and Glennys R. Farrar. "Air shower simulations in a hybrid approach using cascade equations". In: *Phys. Rev. D* 67 (2003), p. 116001. DOI: 10.1103/PhysRevD.67.116001. arXiv: astro-ph/0212018 [astro-ph].
- [85] Krijn D. de Vries et al. "The cosmic-ray air-shower signal in Askaryan radio detectors". In: *Astroparticle Physics* 74 (2016), pp. 96–104. ISSN: 0927-6505. DOI: <http://dx.doi.org/10.1016/j.astropartphys.2015.10.003>. URL: <http://www.sciencedirect.com/science/article/pii/S0927650515001437>.
- [86] B V Sreekantan M V S Rao. *Extensive Air Showers*. Singapore : World Scientific, c1998., 1998.
- [87] M. Boháčová. "Study of the Air Fluorescence by AIRFLY". In: *Nuclear Physics B - Proceedings Supplements* 190 (2009). Proceedings of the Cosmic Ray International Seminars, pp. 266–271. ISSN: 0920-5632. DOI: <http://dx.doi.org/10.1016/j.nuclphysbps.2009.03.098>. URL: <http://www.sciencedirect.com/science/article/pii/S0920563209003375>.
- [88] Alexander Aab et al. "Muons in air showers at the Pierre Auger Observatory: Mean number in highly inclined events". In: *Phys. Rev. D* 91.3 (2015). [Erratum: *Phys. Rev. D* 91, no. 5, 059901 (2015)], p. 032003. DOI: 10.1103/PhysRevD.91.059901, 10.1103/PhysRevD.91.032003. arXiv: 1408.1421 [astro-ph.HE].
- [89] Alexander Aab et al. "Muons in air showers at the Pierre Auger Observatory: Measurement of atmospheric production depth". In: *Phys. Rev. D* 90.1 (2014). [Erratum: *Phys. Rev. D* 92, no. 1, 019903 (2015)], p. 012012. DOI: 10.1103/PhysRevD.92.019903, 10.1103/PhysRevD.90.012012, 10.1103/PhysRevD.90.039904. arXiv: 1407.5919 [hep-ex].
- [90] Alexander Aab et al. "Testing Hadronic Interactions at Ultrahigh Energies with Air Showers Measured by the Pierre Auger Observatory". In: *Phys. Rev. Lett.* 117.19 (2016), p. 192001. DOI: 10.1103/PhysRevLett.117.192001. arXiv: 1610.08509 [hep-ex].
- [91] T. Pierog and Klaus Werner. "Muon Production in Extended Air Shower Simulations". In: *Phys. Rev. Lett.* 101 (2008), p. 171101. DOI: 10.1103/PhysRevLett.101.171101. arXiv: astro-ph/0611311 [astro-ph].

- [92] Ralf Ulrich, Ralph Engel, and Michael Unger. “Hadronic Multiparticle Production at Ultra-High Energies and Extensive Air Showers”. In: *Phys. Rev. D* 83 (2011), p. 054026. DOI: 10.1103/PhysRevD.83.054026. arXiv: 1010.4310 [hep-ph].
- [93] I. Valiño et al. “Characterisation of the electromagnetic component in ultra-high energy inclined air showers”. In: *Astroparticle Physics* 32 (Jan. 2010), pp. 304–317. DOI: 10.1016/j.astropartphys.2009.09.008. arXiv: 0910.2873 [astro-ph.HE].
- [94] Alexander Aab et al. “Reconstruction of inclined air showers detected with the Pierre Auger Observatory”. In: *JCAP* 1408.08 (2014), p. 019. DOI: 10.1088/1475-7516/2014/08/019. arXiv: 1407.3214 [astro-ph.HE].
- [95] Piera L. Ghia. “Testing the surface detector simulation for the Pierre Auger Observatory”. In: *Proceedings, 30th International Cosmic Ray Conference (ICRC 2007): Merida, Yucatan, Mexico, July 3-11, 2007*. Vol. 4. [4,315(2007)]. 2007, pp. 315–318. arXiv: 0706.1212 [astro-ph]. URL: http://lss.fnal.gov/cgi-bin/find_paper.pl?conf-07-380.
- [96] Alexander Aab et al. “The Pierre Auger Observatory: Contributions to the 33rd International Cosmic Ray Conference (ICRC 2013)”. In: *Proceedings, 33rd International Cosmic Ray Conference (ICRC2013): Rio de Janeiro, Brazil, July 2-9, 2013*. 2013. arXiv: 1307.5059 [astro-ph.HE]. URL: <http://lss.fnal.gov/archive/2013/conf/fermilab-conf-13-285-ad-ae-cd-td.pdf>.
- [97] Lorenzo Cazon, R. A. Vazquez, and E. Zas. “Depth development of extensive air showers from muon time distributions”. In: *Astropart. Phys.* 23 (2005), pp. 393–409. DOI: 10.1016/j.astropartphys.2005.01.009. arXiv: astro-ph/0412338 [astro-ph].
- [98] L. Cazon et al. “A model for the transport of muons in extensive air showers”. In: *Astropart. Phys.* 36 (2012), pp. 211–223. DOI: 10.1016/j.astropartphys.2012.05.017. arXiv: 1201.5294 [astro-ph.HE].
- [99] S. Andringa et al. “The Muonic longitudinal shower profiles at production”. In: *Astropart. Phys.* 35 (2012), pp. 821–827. DOI: 10.1016/j.astropartphys.2012.03.010. arXiv: 1111.1424 [hep-ph].
- [100] Pedro Abreu et al. “Interpretation of the Depths of Maximum of Extensive Air Showers Measured by the Pierre Auger Observatory”. In: *JCAP* 1302 (2013), p. 026. DOI: 10.1088/1475-7516/2013/02/026. arXiv: 1301.6637 [astro-ph.HE].
- [101] Alexander Aab et al. “Depth of maximum of air-shower profiles at the Pierre Auger Observatory. I. Measurements at energies above $10^{17.8}$ eV”. In: *Phys. Rev. D* 90.12 (2014), p. 122005. DOI: 10.1103/PhysRevD.90.122005. arXiv: 1409.4809 [astro-ph.HE].
- [102] The Pierre Auger Collaboration. “Observation of the Suppression of the Flux of Cosmic Rays above 4×10^{19} eV”. In: *Phys. Rev. Lett.* 101 (6 2008), p. 061101. DOI: 10.1103/PhysRevLett.101.061101. URL: <https://link.aps.org/doi/10.1103/PhysRevLett.101.061101>.
- [103] Pedro Abreu et al. “Measurement of the proton-air cross-section at $\sqrt{s} = 57$ TeV with the Pierre Auger Observatory”. In: *Phys. Rev. Lett.* 109 (2012), p. 062002. DOI: 10.1103/PhysRevLett.109.062002. arXiv: 1208.1520 [hep-ex].

- [104] Alexander Aab et al. "Search for photons with energies above 10^{18} eV using the hybrid detector of the Pierre Auger Observatory". In: *JCAP* 1704.04 (2017), p. 009. DOI: 10.1088/1475-7516/2017/04/009. arXiv: 1612.01517 [astro-ph.HE].
- [105] Alexander Aab et al. "The Pierre Auger Cosmic Ray Observatory". In: *Nucl. Instrum. Meth.* A798 (2015), pp. 172–213. DOI: 10.1016/j.nima.2015.06.058. arXiv: 1502.01323 [astro-ph.IM].
- [106] Guillermo Sierra. *Pierre Auger Observatory Photos Gallery*. 2007. URL: <https://www.auger.org/index.php/gallery/photos>.
- [107] The Pierre Auger Collaboration et al. "The Fluorescence Detector of the Pierre Auger Observatory". In: *ArXiv e-prints* (July 2009). arXiv: 0907.4282 [astro-ph.IM].
- [108] I. Allekotte et al. "The Surface Detector System of the Pierre Auger Observatory". In: *Nucl. Instrum. Meth.* A586 (2008), pp. 409–420. DOI: 10.1016/j.nima.2007.12.016. arXiv: 0712.2832 [astro-ph].
- [109] Glenn F. Knoll. *Radiation Detection and Measurements*. 3rd Edition. John Wiley & Sons, Inc., 2000.
- [110] HZC Photonics. *XP1805 PMT*. 2017. URL: http://www.hzcphotonics.com/en_index.html.
- [111] Pierre Auger Observatory. "Internal Report GAP-2004-026 Direct Light impact parameter dependence in a Cherenkov water tank." In: (2004).
- [112] C. Meurer, N. Scharf, and Pierre Auger Collaboration. "HEAT - a low energy enhancement of the Pierre Auger Observatory". In: *Astrophysics and Space Sciences Transactions* 7 (May 2011), pp. 183–186. DOI: 10.5194/astra-7-183-2011. arXiv: 1106.1329 [astro-ph.IM].
- [113] B Daniel and Pierre Auger Collaboration. "The AMIGA enhancement of the Pierre Auger Observatory". In: *Journal of Physics: Conference Series* 632.1 (2015), p. 012088. URL: <http://stacks.iop.org/1742-6596/632/i=1/a=012088>.
- [114] Frank G. Schröder. "Radio detection of high-energy cosmic rays with the Auger Engineering Radio Array". In: *Nucl. Instrum. Meth.* A824 (2016), pp. 648–651. DOI: 10.1016/j.nima.2015.08.047. arXiv: 1601.00462 [astro-ph.IM].
- [115] Alexander Aab et al. "The Pierre Auger Observatory Upgrade - Preliminary Design Report". In: (2016). arXiv: 1604.03637 [astro-ph.IM].
- [116] Pierre Auger Collaboration. "MARTA - Muon Auger RPC for the Tank Array - Design Report". Auger Internal Note GAP-2013-020. 2013.
- [117] R. Santonico and R. Cardarelli. "Development of resistive plate counters". In: *Nuclear Instruments and Methods in Physics Research* 187 (Aug. 1981), pp. 377–380. DOI: 10.1016/0029-554X(81)90363-3.
- [118] R. Cardarelli et al. "Progress in resistive plate counters". In: *Nuclear Instruments and Methods in Physics Research A* 263 (Jan. 1988), pp. 20–25. DOI: 10.1016/0168-9002(88)91011-X.
- [119] C. Lippmann. "Detector physics of resistive plate chambers". PhD Thesis. Johann-Wolfgang-Goethe-University, 2003. URL: https://www.uni-frankfurt.de/46491283/thesis_christian_lippmann_pdf.pdf.

- [120] P. Fonte. "Applications and new developments in resistive plate chambers". In: *IEEE Transactions on Nuclear Science* 49.3 (2002), pp. 881–887. ISSN: 0018-9499. DOI: 10.1109/TNS.2002.1039583.
- [121] P. Fonte. "Review of RPC simulation and modelling". In: *PoS RPC2012* (2012), p. 033.
- [122] Y. Haddad et al. "High Rate Resistive Plate Chamber for LHC detector upgrades". In: *Nucl. Instrum. Meth.* A718 (2013), pp. 424–426. DOI: 10.1016/j.nima.2012.11.029. arXiv: 1211.5698 [physics.ins-det].
- [123] MARTA Muon Auger RPC Tank Array. "Second report on the Auger Data Challenge". 2014.
- [124] Pierre Auger Observatory. "Internal Report GAP-2004-018 Summary of Tests Towards Understanding the VEM Area over Peak Evolution." In: (2004).
- [125] Pierre Auger Observatory. "Internal Report GAP-2015-33 Measurements with the RPC Muon Hodoscope Installed at the Gianni Navarra Tank: First Results v1.1". In: (2015).
- [126] L. Lopes et al. "Outdoor field experience with autonomous RPC based stations". In: *Journal of Instrumentation* 11.09 (2016), p. C09011. URL: <http://stacks.iop.org/1748-0221/11/i=09/a=C09011>.
- [127] S. Argiro et al. "The Offline Software Framework of the Pierre Auger Observatory". In: *Nucl. Instrum. Meth.* A580 (2007), pp. 1485–1496. DOI: 10.1016/j.nima.2007.07.010. arXiv: 0707.1652 [astro-ph].
- [128] S. Pethuraj et al. "Measurement of Cosmic Muon angular distribution and vertical integrated flux by 2m×2m RPC stack at IICHEP-Madurai". In: (2017). arXiv: 1706.00901 [physics.ins-det].
- [129] Pierre Auger Observatory. "Internal Report GAP-2017-27 Results on the Gianni Navarra tank VEM calibration using a RPC muon hodoscope". In: (2017), pp. 1–18.
- [130] CERN. "ROOT Data Analysis Framework". 2017. URL: <https://root.cern.ch/>.
- [131] Pierre Auger Observatory. "Internal Report GAP-2015-50 Never Too Late to Change the SD VEM Calibration". In: (2015).
- [132] L. Lopes et al. "Resistive plate chambers for the Pierre Auger array upgrade". In: *Journal of Instrumentation* 9.10 (2014). DOI: 10.1088/1748-0221/9/10/C10023. URL: <https://www.scopus.com/inward/record.uri?eid=2-s2.0-84908336487&partnerID=40&md5=157658bcd3373f1afe7e665e742c3a88>.
- [133] L. Lopes et al. "Outdoor field experience with autonomous RPC based stations". In: *Journal of Instrumentation* 11.09 (2016), p. C09011. URL: <http://stacks.iop.org/1748-0221/11/i=09/a=C09011>.
- [134] Pierre Auger Observatory. "Internal Report GAP-2005-028 Direct Observation of the Long Term Stability of Water Tanks in the Pierre Auger Surface Detector." In: (2005).
- [135] Pierre Auger Observatory. "Internal Report GAP-2011-085 On the Area over Peak of the single muon traces from the Surface." In: (2005).

-
- [136] Ricardo Sato. "Long Term Performance of the Surface Detectors of the Pierre Auger Observatory". In: *Proceedings, 32nd International Cosmic Ray Conference (ICRC 2011): Beijing, China, August 11-18, 2011*. 2011. arXiv: 1107.4806 [astro-ph.IM]. URL: <https://inspirehep.net/record/919728/files/arXiv:1107.4806.pdf>.
- [137] Pierre Auger Observatory. "Internal Report GAP2005-101 Calibration Analysis: CAPISA data". In: (2005).